Comprehensive Investigations into CO_2 Hydrogenation over Cu-based Catalysts: Catalyst Design, Mechanistic Insights, and Kinetic Modeling

Aakash Bhardwaj



DEPARTMENT OF CHEMICAL ENGINEERING

INDIAN INSTITUTE OF TECHNOLOGY DELHI

APRIL 2026

© Indian Institute of Technology Delhi (IITD), New Delhi, 2026

Comprehensive Investigations into CO_2 Hydrogenation over Cu-based Catalysts: Catalyst Design, Mechanistic Insights, and Kinetic Modeling

by

Aakash Bhardwaj

Department of Chemical Engineering

Submitted

In fulfilment of the requirements for the award of the degree of

DOCTOR OF PHILOSOPHY

to the



Indian Institute of Technology Delhi

April 2026

Certificate

This is to certify that the thesis entitled **"Comprehensive Investigations into CO_2 Hydrogenation over Cu-based Catalysts: Catalyst Design, Mechanistic Insights, and Kinetic Modeling"** submitted by **Mr. Aakash Bhardwaj** to the Indian Institute of Technology Delhi for the award of the degree of **Doctor of Philosophy** in Chemical Engineering is a record of original and bonafide research work carried out by him under my supervision. He has fulfilled all the requirements, which to the best of my knowledge, have reached the requisite standard for the submission of the thesis.

The results embodied in this thesis have not been submitted, either in part or in full, to any other University or Institute for the award of any degree or diploma.



Prof. Sreedevi Upadhyayula
Supervisor
Department of Chemical Engineering
IIT Delhi



Prof. Shantanu Roy
Co-Supervisor
Department of Chemical Engineering
IIT Delhi-Abu Dhabi



Prof. Kamal Kishore Pant
Co-Supervisor
Department of Chemical Engineering
IIT Delhi

Acknowledgements

I offer a note of heartfelt devotion to Almighty GOD for bestowing upon me blessings, patience, strength, and peace throughout life's journey.

Every scientific endeavour represents a synthesis of collective knowledge, continuous learning, and the unwavering support of mentors and collaborators. The successful completion of this doctoral work would not have been possible without the guidance, encouragement, and wisdom of many individuals to whom I owe my deepest gratitude.

First and foremost, I would like to express my sincerest appreciation to my supervisors, **Prof. Sreedevi Upadhyayula, Prof. Shantanu Roy,** and **Prof. K. K. Pant** for their invaluable mentorship throughout my Ph.D. journey. Prof. Sreedevi Upadhyayula's constant guidance in heterogeneous catalysis and reaction engineering shaped my scientific thinking and experimental rigor. Prof. Shantanu Roy's expertise in multiphase reactor modeling enriched my understanding of transport phenomena and reactor-scale interpretation. Prof. K. K. Pant's deep insights into sustainable chemical processes and reactor engineering consistently motivated me to broaden the scope of my research. Their collective support, constructive criticism, encouragement, and trust were instrumental in shaping this work. I consider myself extremely fortunate to have worked under such inspiring mentors.

I also sincerely acknowledge Prof. Divesh Bhatia, a valued member of my Student Research Committee (SRC), for providing continuous encouragement, valuable feedback, and opportunities to work in the Energy and Environment Laboratory, which significantly enhanced the interdisciplinary depth of my research. I want to extend my sincere gratitude to my SRC members, Prof. Anil Verma and Prof. Hemant Kumar Kashyap, for their insightful suggestions, careful evaluation, and unwavering academic support throughout my doctoral program.

I am grateful to the Head of the Department of Chemical Engineering at IIT Delhi and all the esteemed faculty members of the department for providing an excellent academic environment and for their insightful interactions during coursework, seminars, and research discussions. I also extend my sincere thanks to the staff of the Departmental Characterization Laboratory and

the Central Research Facility (CRF) for their technical assistance and cooperation during various experimental studies.

I want to express my sincere gratitude to the senior researchers of the Heterogeneous Catalysis and Reaction Engineering Laboratory, Dr. Shashank Bahri, Dr. Komal Kumar, Dr. Gul Afreen, Dr. Kaisar Ahmad, Dr. Shailesh Pathak, Dr. Sachin Tomar, Dr. Surya Chandra Tiwari, and Dr. Ambreen Aziz Niazi for their valuable guidance, discussions, and support that significantly enriched my research experience. I am grateful to my colleagues Dr. Aloka Kumar Sahu and Mrs. Chitrangda Singh, and my juniors Mr. Shushant Yadav, Mr. Debarun Banerjee, Mr. Swagat Sabyasachi Sahoo, Mrs. Rupali Gautam, Ms. Hansa Muvel, and part-time scholars Mr. Srivardhan Grandhi, Mr. Rakesh Vankayala, Mrs. Minaz Makhania, Mr. Vineet Venunath, Mr. Ameya Dhok, Mr. Vikash Bharti, and several master's and undergraduate students including Mr. Akshdeep Singh Ahluwalia, Mr. Rohit Sahu, Ms. Biduru Gayathri Priya, Ms. Shriya Sharma, and Mr. Bhavya Jangid for their cooperation and support. I also extend my thanks to Mr. Sanjeev Mittal (Lab Manager) and special thanks to Dr. Meenakshi Pokhriyal for their constant technical guidance and fruitful discussions.

I also express my sincere gratitude to the senior researchers of the CRE Laboratory, Dr. Rajan Singh, Dr. Sagar Dhanuskar, Dr. Komal Tripathi, Dr. Snigdha Mishra, Dr. Shreya Singh, Dr. Vallari Chaurasiya, and Dr. Akshata Ramteke for their valuable suggestions and encouragement. My heartfelt thanks go to my colleagues, Mr. Shashank Shekhar, Mr. Pranit Samanta, Mr. Venkanna, Dr. Iqra, Dr. Deepti Mishra, Dr. Marut Jain, and Dr. Sadaf, and my juniors, Mrs. Shally Gupta, Mr. Abhishek Sahoo, Ms. Nidhi Kushwaha, Mr. Abdul Rafey, and Mr. Kaushik Kundu, for their continuous support. I would like to express special thanks to Dr. Vaibhav Pandey for his constant assistance with doubts, discussions, and technical problem-solving throughout my studies.

I further acknowledge the support and encouragement from the Multiphase Reactor Modeling Laboratory and Energy and Environment Laboratory, especially Dr. Pranav Kherdekar, Mr. Kuldeep Singh, Dr. Prateek Khatri, Dr. Dwijraj Mhatre, and Dr. Manoj Kumar Beriya, along with my colleague Mr. Illiyas Yusuf Mir and junior Syed Saif Ali, whose interactions were always stimulating and motivating.

I sincerely thank all the supporting staff at IIT Delhi, including Mr. Vishesh Kumar, Mr. Gautam, Mr. Krishna Kumar, Mr. Suchit Kumar, Mr. Ashish (U.G. Lab), Mr. Mohit (Library In-charge), Mrs. Anita (Office In-charge), Mr. Yogesh (Office Staff), and all technical and administrative personnel for their continuous assistance during my doctoral tenure. I also gratefully acknowledge the support of the Karakoram Hostel and Mess staff, seniors, colleagues, and juniors, as well as the security in-charges and guards, who directly or indirectly made my stay and work at IIT Delhi smooth and comfortable.

I extend my heartfelt gratitude to all my dear friends at IIT Delhi, including Dr. Sanjay Singh, Dr. Prakash Joshi, Mr. Shashank Shekhar, Dr. Lalit Kandpal, Ms. Apurva Mishra, Mrs. Ib Singh Deo, Mrs. Ankita Kumari, Dr. Deepak Seth, and Ms. Garima Singhal, for their friendship, emotional support, motivation, and companionship throughout this journey.

Finally, I would like to express my deepest gratitude to my beloved parents, Mr. Devendra Sharma and Mrs. Saroj Sharma, for their unwavering love, sacrifices, and blessings. I am also thankful to my siblings, Mr. Shrayans Bhardwaj and Mrs. Shweta Sharma, for their constant encouragement and support. I remain immensely grateful to my decade-long best friend, Ms. Armeena Irshad, for her unwavering faith in me and for being a constant source of moral support during the most challenging phases of this journey.

I want to conclude by sincerely thanking everyone who, directly or indirectly, contributed to the successful completion of this work and supported me throughout this remarkable academic journey.

Aakash Bhardwaj

Aakash Bhardwaj

Abstract

The ever-increasing global energy demand and the associated rise in anthropogenic CO_2 emissions necessitate the development of sustainable carbon capture and utilization technologies. Among various CO_2 valorisation pathways, catalytic hydrogenation of CO_2 to methanol is particularly attractive due to methanol's role as a clean fuel, hydrogen carrier, and industrial feedstock. However, the efficient and stable conversion of CO_2 to methanol remains a challenge due to thermodynamic limitations, catalyst deactivation, and an incomplete understanding of both the mechanistic and kinetic aspects of the process. This thesis addresses these challenges through a multi-layered strategy integrating machine learning-assisted catalyst design, precursor-engineered catalyst synthesis, advanced physicochemical characterization, in-situ mechanistic investigations, and rigorous kinetic modeling.

A Principal Component Analysis (PCA)-assisted machine learning framework was first developed using a curated dataset of 227 literature data points for Cu-based binary and ternary catalysts. Artificial Neural Networks (ANN), Support Vector Machine Regression (SVR), and Gaussian Process Regression (GPR) were implemented to simultaneously predict CO_2 conversion, methanol selectivity, CO selectivity, and methanol space-time yield (STY). Among these, the ANN model demonstrated the highest predictive reliability ($R^2 > 0.9$ for multiple outputs) with the lowest overall prediction error. Experimental validation using 30 independent data points over a laboratory-synthesized $Cu/ZnO/ZrO_2$ catalyst confirmed excellent predictive accuracy, particularly for methanol and CO selectivity.

Guided by these ML-derived insights, precursor-engineered Cu-based catalysts were systematically developed. A hydrothermal synthesis route was successfully established for stabilizing a phase-pure Mg-rich McGuinnessite precursor for Cu/MgO catalysts, demonstrated for the first time. The optimized Cu/MgO catalyst achieved a 15.2% CO_2 conversion, 68.5% methanol selectivity, and a MeOH STY of 98 $mg_{MeOH}/g_{cat}.hr$ at 240°C and 40 bar, along with excellent stability of 100 hours. *In-situ* DRIFTS confirmed a formate-methoxy reaction pathway, while enhanced oxygen vacancy concentration and strong Cu-Mg interaction were identified as key structure-activity drivers.

To further advance toward industrially relevant systems, a scalable mechano-chemical ball milling (MCBM) route was developed for synthesizing phase-pure zincian malachite

precursors and high-performance Cu/ZnO/ZrO_2 catalysts (CZZ-MCBM). This approach ensured superior metal dispersion, enhanced oxygen vacancy density, and a strong synergy between ZnO and ZrO_2. The optimized CZZ-MCBM catalyst exhibited 14.4% CO_2 conversion, 73% methanol selectivity, and a MeOH STY of 187 mg_{MeOH}/g_{cat}.hr at 260°C and 40 bar, along with outstanding long-term stability over 184 hours with ~4.2% performance deviation. A direct correlation between oxygen vacancy concentration and methanol productivity was established.

A comprehensive kinetic and mechanistic investigation was subsequently performed over the optimized CZZ-MCBM catalyst. *In-situ* DRIFTS conclusively established the dominance of the formate-mediated CO_2 hydrogenation pathway, with negligible participation of the indirect CO route. Intrinsic kinetics were described using multiple Langmuir-Hinshelwood-Hougen-Watson (LHHW) models, among which a dual-site three-reaction model provided the best statistical fit ($R^2 > 0.97$) and mechanistic consistency. The hierarchy of rate constants, $k_1(CO_2 \rightarrow MeOH) > k_2(RWGS) > k_3(CO \rightarrow MeOH)$, together with a low apparent activation energy of 23.1 kJ/mol, quantitatively confirmed the high intrinsic activity of the CZZ-MCBM catalyst.

Overall, this thesis establishes a comprehensive and experimentally validated workflow for CO_2-to-methanol catalysis, encompassing data-driven catalyst screening, precursor-controlled synthesis, defect and metal-support engineering, *in-situ* mechanistic elucidation, and kinetic model development. The integrated ML-experiment-kinetics strategy presented here provides a powerful platform for the rational design, scale-up, and industrial deployment of next-generation Cu-based catalysts for sustainable methanol production and advanced carbon utilization.

सार

वैश्विक ऊर्जा मांग में निरंतर वृद्धि तथा मानवजनित CO_2 उत्सर्जन में हो रही तीव्र बढ़ोतरी, सतत कार्बन कैप्चर एवं उपयोग (Carbon Capture and Utilization, CCU) तकनीकों के विकास की अनिवार्यता को रेखांकित करती है। CO_2 के विभिन्न उपयोगी रूपांतरण मार्गों में, CO_2 का उत्प्रेरक हाइड्रोजनीकरण द्वारा मेथनॉल में रूपांतरण विशेष रूप से आकर्षक है, क्योंकि मेथनॉल एक स्वच्छ ईंधन, हाइड्रोजन वाहक तथा औद्योगिक कच्चे माल के रूप में महत्वपूर्ण भूमिका निभाता है। तथापि, ऊष्मागतिकीय सीमाएँ, उत्प्रेरक का निष्क्रिय होना तथा अभिक्रिया की यांत्रिकी एवं गतिकी की अपूर्ण समझ के कारण CO_2 से मेथनॉल का कुशल एवं स्थिर रूपांतरण अब भी एक चुनौती बना हुआ है। यह शोध प्रबंध इन चुनौतियों का समाधान मशीन लर्निंग-सहायित उत्प्रेरक डिजाइन, प्रीकर्सर-आधारित उत्प्रेरक संश्लेषण, उन्नत भौतिक-रासायनिक लक्षणन, इन-सिटू यांत्रिकीय अध्ययन तथा कठोर गतिकीय मॉडलिंग को समेकित करते हुए प्रस्तुत करता है।

प्रारंभ में, तांबा-आधारित द्विघटक एवं त्रिघटक उत्प्रेरकों के लिए 227 साहित्यिक डेटा बिंदुओं के एक सुव्यवस्थित डेटासेट का उपयोग करते हुए प्रिंसिपल कंपोनेंट एनालिसिस (PCA) आधारित मशीन लर्निंग ढाँचा विकसित किया गया। इसमें आर्टिफ़िशियल न्यूरल नेटवर्क (ANN), सपोर्ट वेक्टर मशीन रिग्रेशन (SVR) तथा गॉसियन प्रोसेस रिग्रेशन (GPR) का उपयोग करके CO_2 रूपांतरण, मेथनॉल चयनात्मकता, CO चयनात्मकता तथा मेथनॉल स्पेस-टाइम यील्ड (STY) का एक साथ पूर्वानुमान किया गया। इन मॉडलों में ANN ने सर्वाधिक विश्वसनीय पूर्वानुमान क्षमता (कई आउटपुट के लिए $R^2 > 0.9$) तथा न्यूनतम समग्र त्रुटि प्रदर्शित की। प्रयोगशाला में संश्लेषित $Cu/ZnO/ZrO_2$ उत्प्रेरक पर 30 स्वतंत्र प्रायोगिक डेटा बिंदुओं द्वारा

किए गए सत्यापन से विशेष रूप से मेथनॉल एवं CO चयनात्मकता के लिए उत्कृष्ट पूर्वानुमान सटीकता की पुष्टि हुई।

इन मशीन लर्निंग से प्राप्त निष्कर्षों के आधार पर प्रीकर्सर-आधारित तांबा-आधारित उत्प्रेरकों का प्रणालीबद्ध विकास किया गया। पहली बार एक हाइड्रोथर्मल संश्लेषण पद्धति द्वारा Cu/MgO उत्प्रेरकों के लिए चरण-शुद्ध (phase-pure) Mg-समृद्ध मैकगिनेसाइट (McGuinnessite) प्रीकर्सर का सफलतापूर्वक स्थिरीकरण किया गया। अनुकूलित Cu/MgO उत्प्रेरक ने 240°C तथा 40 bar पर 15.2% CO_2 रूपांतरण, 68.5% मेथनॉल चयनात्मकता तथा 98 $mg_{MeOH}/g_{cat}.hr$ का मेथनॉल STY प्राप्त किया, साथ ही 100 घंटे तक उत्कृष्ट स्थायित्व भी प्रदर्शित किया। इन-सिटू DRIFTS विश्लेषण द्वारा फॉर्मेट-मेथॉक्सी अभिक्रिया मार्ग की पुष्टि हुई तथा ऑक्सीजन रिक्तियों की बढ़ी हुई सघनता एवं प्रबल Cu-Mg अंतःक्रिया को संरचना-क्रियाशीलता (structure-activity) के प्रमुख प्रेरक तत्व के रूप में पहचाना गया।

औद्योगिक रूप से अधिक प्रासंगिक प्रणाली की दिशा में आगे बढ़ते हुए, चरण-शुद्ध जिंकियन मैलाकाइट प्रीकर्सर तथा उच्च प्रदर्शन वाले Cu/ZnO/ZrO_2 उत्प्रेरकों के संश्लेषण हेतु एक स्केलेबल मैकेनो-केमिकल बॉल मिलिंग (MCBM) पद्धति विकसित की गई। इस विधि से धातु विसरण में श्रेष्ठता, ऑक्सीजन रिक्तियों की उच्च सघनता तथा ZnO और ZrO_2 के मध्य मजबूत सहक्रियात्मक प्रभाव सुनिश्चित हुआ। अनुकूलित CZZ-MCBM उत्प्रेरक ने 260°C तथा 40 bar पर 14.4% CO_2 रूपांतरण, 73% मेथनॉल चयनात्मकता तथा 187 $mg_{MeOH}/g_{cat}.hr$ का मेथनॉल STY प्रदर्शित किया। इसके अतिरिक्त, 184 घंटे के दीर्घकालिक परीक्षण में ~4.2% से कम प्रदर्शन ह्रास के साथ इसकी असाधारण स्थिरता भी सिद्ध हुई। ऑक्सीजन रिक्तियों की सघनता और मेथनॉल उत्पादकता के मध्य प्रत्यक्ष सहसंबंध स्थापित किया गया।

अनुकूलित CZZ-MCBM उत्प्रेरक पर एक व्यापक गतिकीय एवं यांत्रिकीय अध्ययन किया गया। इन-सिटू DRIFTS द्वारा निर्णायक रूप से यह स्थापित हुआ कि CO_2 के हाइड्रोजनीकरण की प्रक्रिया मुख्यतः फॉर्मेट-आधारित मार्ग से संचालित होती है, जबकि अप्रत्यक्ष CO मार्ग की भूमिका नगण्य है। आंतरिक गतिकी को विभिन्न लैंगमुइर-हिन्शेलवुड-हौगेन-वॉटसन (LHHW) मॉडलों के माध्यम से वर्णित किया गया, जिनमें द्वि-साइट तीन-अभिक्रिया मॉडल ने सर्वश्रेष्ठ सांख्यिकीय सामंजस्य (R^2 **>** 0.97) तथा यांत्रिकीय संगति प्रदर्शित की। दर स्थिरांकों का अनुक्रम $k_1(CO_2 \rightarrow MeOH)$ **>** $k_2(RWGS)$ **>** $k_3(CO \rightarrow MeOH)$ तथा 23.1 kJ/mol की निम्न प्रकट सक्रियण ऊर्जा ने CZZ-MCBM उत्प्रेरक की उच्च आंतरिक सक्रियता की मात्रात्मक पुष्टि की।

समग्र रूप से, यह शोध प्रबंध CO_2 से मेथनॉल में रूपांतरण हेतु एक पूर्णतः सत्यापित और एकीकृत कार्यप्रवाह प्रस्तुत करता है, जिसमें डेटा-आधारित उत्प्रेरक स्क्रीनिंग, प्रीकर्सर-नियंत्रित संश्लेषण, दोष (defect) तथा धातु-समर्थन अंतःक्रिया अभियांत्रिकी, इन-सिटू यांत्रिकीय विवेचना तथा गतिकीय मॉडल विकास सम्मिलित हैं। यहाँ प्रस्तुत मशीन लर्निंग-प्रयोग-गतिकी का एकीकृत दृष्टिकोण, सतत मेथनॉल उत्पादन एवं उन्नत कार्बन उपयोग के लिए अगली पीढ़ी के तांबा-आधारित उत्प्रेरकों के विवेकपूर्ण डिजाइन, स्केल-अप तथा औद्योगिक अनुप्रयोग हेतु एक शक्तिशाली मंच प्रदान करता है।

Contents

Certificate I

Acknowledgements II

Abstract V

सार VII

Contents X

List of Figures XV

List of Tables XXI

Chapter 1 Introduction 1

1.1 Overview 1

1.2 Global Scenario of CO_2 emissions from anthropogenic sources 3

1.3 History of methanol production 5

1.3.1 Early History (Pre-20^{th} Century) 5

1.3.2 CO Hydrogenation Era (1900s-1960s) 5

1.3.3 Emergence of CO_2 hydrogenation (1990s - Present) 7

1.4 Methanol Economy and World Methanol Demand 7

1.5 Thermodynamics and challenges in synthesizing methanol via CO_2 hydrogenation 8

1.6 Reaction kinetics of CO_2 hydrogenation to methanol 11

1.7 Current possible approaches to overcome limitations 12

1.8 Data-driven and machine learning approaches in catalyst design 13

1.9 Summary and Future Outlook 14

1.10 Thesis Organisation 14

Chapter 2 Literature Review 16

2.1 Overview 16

2.2 Green routes to produce hydrogen 17

2.3 Heterogeneous catalytic system for the direct hydrogenation of CO_2 to methanol 20

2.3.1 Catalytic Systems 21

2.3.2 Machine learning approaches in catalyst design for CO_2 hydrogenation to methanol 33

2.3.3 Reaction Pathways and Mechanisms in CO_2 Hydrogenation to Methanol 35

2.3.4 Kinetic Modeling 42

2.3.5 Reactor Aspects 48

2.4 Summary 51

2.5 Research gaps and motivation 52

2.6 Research Objectives 52

Chapter 3 Material and Methods 54

3.1 Overview 54

3.2 Methodology for machine learning 54

3.2.1 Machine Learning Models 57

3.3 Experimental Methods 63

3.3.1 Catalyst Synthesis 63

3.3.2 Catalyst Characterization Techniques 67

3.3.3 Catalytic Activity Tests Setup 71

3.4 DFT Computational details 73

3.5 Kinetic modelling and parameter fitting 74

3.5.1 Selection of a kinetic model framework 74

3.5.2 Model assumptions and elementary reaction mechanisms 75

3.5.3 Reactor Model and Assumptions 78

3.5.4 Assessment of Transport Limitations 78

3.5.5 General Rate Law Formulation 79

3.5.6 Model-Specific Rate Expressions 80

3.5.7 Parameter Estimation and Optimization 81

3.5.8 Model Validation 82

Chapter 4 Catalyst design using principal component analysis machine learning approach in methanol formation from direct CO_2 hydrogenation 83

4.1 Overview 83

4.2 Results and Discussion 84

4.2.1 Final Evaluation 84

4.2.2 Dimensionality reduction using Principal Component Analysis (PCA) 86

4.2.3 Performance Comparison of the Applied Algorithms 89

4.2.4 Experimental validation on the best optimized model 95

4.3 Summary and Future Outlook 98

Chapter 5 Enhanced methanol formation over Cu/MgO catalyst derived from Mg-rich hydroxycarbonate precursor 100

5.1 Overview 100

5.2 RESULTS AND DISCUSSION 101

5.2.1 Structural identification of precursor phase 101

5.2.2 Physical and Chemical Properties of the final catalyst 103

5.2.3 Catalytic activity results 111

5.2.4 Structure-activity relationship 115

5.2.5 Mechanistic insights into CO_2 hydrogenation to methanol over the CM-HT catalyst 117

5.3 Summary and Future Outlook 118

Chapter 6 CO_2 hydrogenation to methanol over mechano-chemically synthesized phase-pure Cu-based catalysts 120

6.1 Overview 120

6.2 Results and Discussion 121

6.2.1 From hydroxycarbonate precursors to active Cu/ZnO phases: A structural and nanoscale investigation 121

6.2.2 Engineering $Cu/ZnO/ZrO_2$ catalysts: Synthesis route comparison and structural insights 124

6.2.3 Comparative catalytic performance studies of Cu-based catalysts 136

6.2.4 Property-activity relationship 139

6.2.5 Catalyst Stability Studies 142

6.2.6 Post-catalytic characterization studies 143

6.3 Summary and Future Outlook 144

Chapter 7 Parameter-driven performance, reaction kinetics, and mechanistic modeling in CO_2 hydrogenation to methanol over the ternary Cu/ZnO/ZrO_2 catalyst 146

7.1 Overview 146

7.2 Results and Discussion 147

7.2.1 Parameter-driven performance: Uncovering the role of temperature, pressure, and WHSV in methanol synthesis 147

7.2.2 Mechanistic Insights 151

7.2.3 Kinetic Studies 153

7.2.4 Final Discussion and Industrial Implications 162

7.3 Summary 162

Chapter 8 Overall Conclusion and Future Recommendations 164

8.1 Conclusion 164

8.1.1 Overall Significance of the Thesis Work 165

8.2 Future Recommendations 166

Response to Examiner Comments 168

References 169

Appendix A i

CURRICULUM VITAE vi

List of Figures

Figure 1.1. Schematic of the major components covered during the present work. 3

Figure 1.2. Global greenhouse gas emission sources, warning scenarios, consequences, and possible solutions to mitigate the carbon footprint. (Adapted from source: www.methanol.org International Renewable Energy Agency Report [36,39,48,50]). 4

Figure 1.3. Schematic representation of CO_2 utilization pathways for producing value-added chemicals and global methanol demand distribution across key industrial applications. 8

Figure 1.4. Influence of thermodynamic conditions (T and P) on equilibrium conversion and product yield. Adapted from ref [16]. 11

Figure 2.1. Various routes for the production of hydrogen. 18

Figure 2.2. Various catalyst combinations have been used in the methanol synthesis reaction via CO_2 hydrogenation in the last decade. 23

Figure 2.3. Microstructural transformation of Cu/ZnO catalyst precursors during meso-structuring, nano-structuring, calcination, and activation steps. Adapted from Behrens et al. [85,104] 24

Figure 2.4. Structure-performance correlation for Cu-based methanol synthesis catalysts, demonstrating how SMSI effects, defect density, and Cu surface area integrates to produce the highest catalytic activity. Modified from ref [85]. 25

Figure 2.5. Comprehensive summary of catalyst design parameters for Cu-based catalysts, illustrating the interrelation between catalyst structure, active site features, and catalytic activity, along with corresponding synthesis methodologies. Modified from ref [16]. 27

Figure 2.6. Illustration of the four elementary methanol synthesis pathways (I-IV), showing the hydrogenation of CO_2 and CO and the reverse transformations among these species. 43

Figure 3.1. Illustrative ANN regression model. 58

Figure 3.2. General scheme to calculate the optimum number of neurons in the hidden layer. 59

Figure 3.3. Scheme for Support Vector Regression Evaluation. 61

Figure 3.4. The general scheme used for model assessment for Gaussian Process Regression (GPR). 62

Figure 3.5. Discrete sections of experimental work. 63

Figure 3.6. Schematic diagram of catalyst characterization techniques during this work. 67

Figure 3.7. Schematic diagram of the high-pressure fixed-bed tubular reactor setup with an inline gas analyzer. 71

Figure 3.8. Most stable configurations of $(Cu_{1-x}Mg_x)_2(OH)_2CO_3$ systems, (a) x = 0, (b) x = 0.125, (c) x = 0.25, (d) x = 0.375, and (e) x = 0.50. The orange, green, red, grey, and white colours represent Cu, Mg, O, C, and H atoms, respectively. 74

Figure 4.1. Scheme for model evaluation on testing data. 85

Figure 4.2. Scores plot for the input parameters onto the first two principal components. 86

Figure 4.3. Bar plot for variance explained for each principal component for input variables. 87

Figure 4.4. Loadings for the first two Principal Components for input variables. 87

Figure 4.5. Projection of test data onto the previous scores plot of the training dataset. 88

Figure 4.6. PCA plot for input descriptors of the training dataset characterized by the presence of promoters. . 88

Figure 4.7. (a) Scores plot for the output parameters onto the first two principal components, **(b)** Loadings plot for the first two principal components for output variables. 89

Figure 4.8. Bar plot for variance explained for each principal component. 89

Figure 4.9. (a) *Contribution pie chart for CO_2 Conversion* ***(b)*** *Contribution pie chart for MeOH Selectivity* ***(c)*** *Contribution pie chart for CO Selectivity* ***(d)*** *Contribution pie chart for MeOH STY.* 91

Figure 4.10. Optimal kernel function selection based on MSE and R values. 93

Figure 4.11. Parity plots comparing experimental and ANN-predicted values for **(a)** CO_2 conversion, **(b)** MeOH selectivity, **(c)** CO selectivity, and **(d)** MeOH STY using the independent laboratory validation dataset. The solid lines represent ideal parity (y = x), and the corresponding R^2 values indicate the predictive accuracy of the optimized ANN model. 97

Figure 5.1. (a) PXRD patterns of Cu-Mg hydroxycarbonate precursor with nominal substitution of Mg to be 50% (CM50) and no substitution (CM0), in comparison to the line diagrams of standard Malachite (PDF No. (PDF No.-41-1390) and McGuinnessite (AMCSD-0011133) structures, and **(b)** FTIR of Cu-Mg hydroxycarbonate precursor in comparison with the standard data (Extracted from RRUFF database No. R050508 (malachite), R050294 (rosasite)). 103

Figure 5.2. (a) PXRD patterns, and **(b)** N_2-adsorption-desorption isotherms of calcined samples prepared via different methods. Inset in (b) shows the pore size distribution curve for the CM-HT sample. 104

Figure 5.3. High-resolution XPS spectrum of **(a)** Cu 2p, **(b)** Mg 2p, **(c)** O 1s, and **(d)** C 1s of the calcined catalyst samples. 105

Figure 5.4. H_2 -TPR profiles of calcined catalyst samples **(a)** CM-HT, **(b)** CM-CP, **(c)** CM-IMP. 107

Figure 5.5. (a) CO_2-TPD profiles of the reduced catalyst samples compared to commercial MgO, **(b)** mode of CO_2 adsorption over weak, medium, and strong basic sites. 109

Figure 5.6. FESEM images of **(a, d)** CM-HT, **(b, e)** CM-CP, and **(c, f)** CM-IMP calcined catalyst samples... 110

Figure 5.7. (a, b, c) TEM and **(d, e, f)** HRTEM images of CM-HT, CM-CP, and CM-IMP, respectively. 110

Figure 5.8. (a) Effect of reactor temperature (at P = 40 bar, WHSV = 2600 ml/g_{cat}.hr, and H_2:CO_2 = 3:1), **(b)** Effect of pressure (at T = 240°C, WHSV = 2600 ml/g_{cat}.hr, and H_2:CO_2 = 3:1) on the CO_2 conversion and methanol selectivity of CM-HT sample, **(c)** Effect of pressure with the varying temperature range on the MeOH STY (at WHSV = 2600 ml/g_{cat}.hr, and H_2:CO_2 = 3:1), **(d)** Effect of WHSV on the catalytic performance (at T = 240°C, P = 40 bar, and H_2:CO_2 = 3:1), **(e)** Effect of temperature on the product distribution (at P = 40 bar, WHSV= 2600 ml/g_{cat}.hr, and H_2:CO_2 = 3:1), **(f)** Effect of pressure on the product distribution (at T = 240°C, WHSV = 2600 ml/g_{cat}.hr, and H_2:CO_2 = 3:1). 112

Figure 5.9. (a) Bar chart illustrating the comparative catalytic performance (CO_2 conversion and methanol selectivity) of Cu/MgO catalysts at optimized reaction conditions (T = 240°C, P = 40 bar, WHSV = 2600 ml/g_{cat}.hr, and H_2:CO_2 = 3:1), **(b)** Overall comparison of methanol STY at optimized reaction conditions. 113

Figure 5.10. (a) PXRD patterns, and **(b)** N_2-adsorption desorption isotherm of the spent samples. 114

Figure 5.11. Catalyst stability test (TOS) for CM-HT catalyst at optimized reaction conditions (T = 240°C, P = 40 bar, WHSV = 2600 ml/gcat.hr, and H_2:CO_2 = 3:1)..... 114

Figure 5.12. Radar plot illustrating the structure-activity relationship of Cu/MgO catalysts. 115

Figure 5.13. Characterization of the surface species on the Cu-MgO (CM-HT) sample. In-situ DRIFT spectra of Cu-MgO (CM-HT) with feed gas CO_2:H_2 (1:3) with a flow rate of 50 ml/min under atmospheric pressure and different temperatures. The bottom last spectra show the spectra with CO_2 activation over the catalyst surface before switching the feed gas to H_2. 118

Figure 6.1. (a) PXRD patterns illustrating the stepwise formation of hydroxycarbonate precursor via the MCBM method, **(b)** PXRD plot of calcined CZ-MCBM catalyst. 122

Figure 6.2. N_2-adsorption-desorption isotherms of Cu-ZnO calcined catalyst prepared via the MCBM method. The inset shows the pore size distribution curve for the CZ-MCBM sample. 123

Figure 6.3. Radar representation of the catalytic performance of the CZ-MCBM catalyst under varying temperature and WHSV at 40 bar. 124

Figure 6.4. (a) PXRD patterns of CuZnZr containing precursors synthesized via the MCBM, CPUSI, and SPUSI methods, illustrating phase evolution and precursor crystallinity after ZrO_2 incorporation, **(b)** PXRD patterns of the corresponding calcined $CuO/ZnO/ZrO_2$ (CZZ) catalysts prepared by MCBM, CPUSI, and SPUSI methods, showing the formation of mixed metal oxide phases. 126

Figure 6.5. N_2-adsorption-desorption isotherms of $CuO/ZnO/ZrO_2$ calcined catalyst prepared via the MCBM, CPUSI, and SPUSI preparation methods. The inset shows the corresponding pore size distribution curve for the $CuO/ZnO/ZrO_2$ sample. 128

Figure 6.6. HRTEM images of calcined **(a)** CZ-MCBM, **(b)** CZZ-MCBM, **(c)** CZZ-CPUSI, and **(d)** CZZ-SPUSI catalysts showing lattice fringes of CuO, ZnO, and ZrO_2 phases, highlighting the effect of synthesis route on crystallinity and metal dispersion. 129

Figure 6.7. (a) H_2-TPR profiles of CZ and CZZ calcined catalysts, (b) H_2-TPD profiles of CZ and CZZ calcined catalysts. 131

Figure 6.8. CO_2-TPD profiles of CZ and CZZ calcined catalysts. 132

Figure 6.9. Comparative high-resolution XPS spectra of Cu 2p, Zn 2p, and Zr 3d core levels for calcined CZ and CZZ catalysts. 134

Figure 6.10 (a) O 1s XPS spectra of calcined CZ and CZZ catalysts prepared via different synthesis routes, highlighting variations in lattice oxygen, surface oxygen species, and oxygen vacancy-related components **(b)** EPR spectra of calcined CZ and CZZ catalysts prepared via different synthesis routes, illustrating the variation in paramagnetic species and oxygen vacancy concentration. 136

Figure 6.11. Radar plot illustrating the comparative catalytic performance of CZ-MCBM and CZZ-MCBM catalysts at optimized reaction conditions (T = 260°C, P = 40 bar, WHSV = 5200 ml/g_{cat}·hr). 137

Figure 6.12. Radar plot illustrating the comparative catalytic performance of CZZ catalysts at optimized reaction conditions (T = 260°C, P = 40 bar, WHSV = 5200 ml/g_{cat}·hr). 138

Figure 6.13. (a) Comparative catalytic performance of all in-house synthesized Cu-based catalysts evaluated at T = 240°C, P = 40 bar, and WHSV = 5200 ml/g_{cat}.hr, **(b)** Benchmark comparison of the CZZ-MCBM catalyst with representative state-of-the-art Cu-Zn-based catalysts reported in the literature under comparable operating conditions [114,121,137,214,232–235]. 139

Figure 6.14. Spider plot illustrating the structure-property-activity relationship of CZ-MCBM and CZZ catalysts synthesized via different preparation routes. 140

Figure 6.15. (a) Comparative bar plot between relative oxygen vacancy concentration and CO_2 conversion for CZ-MCBM and CZZ-MCBM calcined catalysts, **(b)** Comparative bar plot between relative oxygen vacancy concentration and STY methanol for CZ-MCBM and CZZ-MCBM calcined catalysts. 141

Figure 6.16. (a) Comparative bar plot between relative oxygen vacancy concentration and CO_2 conversion for CZZ calcined catalysts, **(b)** Comparative bar plot between relative oxygen vacancy concentration and STY methanol for CZZ calcined catalysts. 141

Figure 6.17. (a) Catalyst stability test (TOS) of CZZ-MCBM catalyst on varying reaction conditions, **(b)** Catalyst stability test (TOS) of CZZ-MCBM catalyst at optimized reaction conditions (T = 260°C, P = 40 bar, WHSV = 5200 ml/g_{cat}·hr). 143

Figure 6.18. (a) PXRD pattern of CZZ-MCBM-S spent catalyst, **(b)** N_2 adsorption-desorption isotherm and PSD plot of CZZ-MCBM spent catalyst. 144

Figure 7.1. Effect of temperature on **(a)** CO_2 conversion and methanol selectivity, and **(b)** methanol space-time yield (STY) at 40 bar and WHSV = 5200 ml/g_{cat}.hr over the CZZ-MCBM catalyst during CO_2 hydrogenation to methanol. 148

Figure 7.2. Effect of pressure on **(a)** CO_2 conversion and methanol selectivity at T = 260°C and WHSV = 5200 ml/g_{cat}.hr, and **(b)** methanol space-time yield (STY) at varying temperatures and WHSV = 5200 ml/g_{cat}.hr over the CZZ-MCBM catalyst during CO_2 hydrogenation to methanol. 149

Figure 7.3. Effect of WHSV on **(a)** CO_2 conversion and methanol selectivity, and **(b)** methanol space-time yield (STY) at T = 260°C and P = 40 bar over the CZZ-MCBM catalyst during CO_2 hydrogenation to methanol. ... 150

Figure 7.4. Effect of **(a)** temperature and **(b)** pressure on product distribution (CO and CH_3OH) over the CZZ-MCBM catalyst during CO_2 hydrogenation to methanol. Plot **(a)** corresponds to P = 40 bar and WHSV = 5200 ml/g_{cat}.hr, and plot **(b)** corresponds to T = 260°C and WHSV = 5200 ml/g_{cat}.hr. 151

Figure 7.5. (a) In-situ DRIFTS analysis of surface species formed during CO_2 hydrogenation over the catalyst, **(b)** schematic representation of the proposed reaction mechanism showing the transformation pathways of surface intermediates leading to methanol formation. 153

Figure 7.6. Parity plots comparing experimental and predicted molar flow rates of **(a)** methanol (MeOH) and **(b)** carbon monoxide (CO) for Model A. 155

Figure 7.7. Parity plots comparing experimental and predicted molar flow rates of **(a)** methanol (MeOH) and **(b)** carbon monoxide (CO) for Model B. 155

Figure 7.8. Parity plots comparing experimental and predicted molar flow rates of **(a)** methanol (MeOH) and **(b)** carbon monoxide (CO) for Model C. 156

Figure 7.9. Experimental vs. model-predicted methanol formation rate for the single-site two-reaction model under varying process conditions. 161

Figure 7.10. Experimental vs. model-predicted methanol formation rate for the dual-site two-reaction model under varying process conditions. 161

Figure 7.11. Experimental vs. model-predicted methanol formation rate for the dual-site three-reaction model under varying process conditions. 161

List of Tables

Table 2.1. Overview of literature-reported Cu-containing catalysts and their performance in CO_2 hydrogenation to methanol as a function of synthesis route, operating parameters, and productivity indicators. 28

Table 2.2. Key surface intermediates and their associated active sites in the CO_2 hydrogenation to methanol process. 36

Table 2.3. Overview of literature-reported kinetic models describing CO_2 hydrogenation to methanol on Cu-based catalytic systems. 44

Table 3.1. Reactions involved during the hydrogenation reaction of CO_2 to methanol. 56

Table 3.2. Optimized analytical conditions for the GC-5800 model. 72

Table 3.3. Thermodynamic equilibrium constant of all the reactions as a function of temperature (Adapted from Graaf et al. 1988 [149]). 79

Table 3.4. Physicochemical constraints of the kinetic parameters [144,145,149]. 82

Table 4.1. Statistics for Input parameters. 85

Table 4.2. Statistics for Output parameters. 85

Table 4.3. Laboratory evaluation of catalytic performance and physicochemical properties of the CZZ-UARCP catalyst. 86

Table 4.4. 10-Fold results for ANN Algorithm. 90

Table 4.5. 10-fold results for SVM regression. 93

Table 4.6. 10-fold results for GPR. 94

Table 4.7. Evaluation of ANN and GPR performance based on MSE values. 94

Table 4.8. Comparison of the R^2 score for ANN, SVM, and GPR algorithms. 95

Table 4.9. Comparative R^2 scores of output variables for the training and validation datasets obtained using 10-fold cross-validation with the optimized ANN model. 97

Table 5.1. Structural and textural properties of the catalysts. 104

Table 5.2. Quantitative data of H_2-TPR analysis of Cu/MgO catalysts. 107

Table 5.3. Quantitative data of CO_2-TPD analysis of Cu-MgO catalysts. 108

Table 6.1. Physicochemical properties of CZ-MCBM catalyst. 123

Table 6.2. Physicochemical properties of the calcined CZZ catalysts. 127

Table 6.3. Quantitative data of H_2-TPR analysis of CZ and CZZ catalysts synthesized via the MCBM, CPUSI, and SPUSI preparation methods. 130

Table 6.4. Quantitative data of CO_2-TPD analysis of CZ and CZZ catalysts synthesized via the MCBM, CPUSI, and SPUSI preparation methods. 133

Table 6.5. Physicochemical properties of CZZ-MCBM spent catalyst. 143

Table 7.1. Statistical Goodness-of-Fit Metrics for the Kinetic Models. 154

Table 7.2. Estimated Parameters for the Single-Site Two-Reaction Model (Model A). 156

Table 7.3. Estimated Parameters for the Dual-Site Two-Reaction Model (Model B) 157

Table 7.4. Estimated Parameters for the Dual-Site Three-Reaction Model (Model C). 157

Table 7.5. Comparison of rate constants (mol/kg_{cat}.sec) with literature in the temperature range of 200-260°C. 158

Table 7.6. Comparison of Adsorption Constants with Literature at 200°C and 260°C. 159

Chapter 1 Introduction

1.1 Overview

The global energy demand is rising rapidly, driven by population growth and industrial expansion. This surge has triggered a sharp increase in anthropogenic CO_2 emissions, elevating atmospheric CO_2 levels and intensifying global warming. As a potent greenhouse gas, CO_2 is a significant contributor to emissions from industrial and vehicle sources. The accumulation of harmful greenhouse gases, such as CO_2, in the atmosphere is primarily linked to fossil fuel consumption, which has already raised the Earth's average temperature by approximately 1.5°C [1,2]. For decades, societies have relied heavily on coal, natural gas, and oil to produce fuels and chemicals essential for development. However, these conventional energy sources release enormous amounts of greenhouse gases (GHGs). In response to the current climate crisis, researchers stress the urgent need to develop efficient carbon capture technologies. Such innovations are crucial in mitigating CO_2 emissions from both stationary sources (e.g., power plants) and diffuse sources (e.g., transportation), thereby preventing further environmental damage [3–8].

To achieve a carbon-neutral future, reducing reliance on fossil fuels and advancing modern carbon capture technologies are crucial steps in stabilizing and ultimately lowering atmospheric CO_2 levels. Transitioning to renewable energy sources, such as solar, wind, hydrothermal, geothermal, and biomass, can significantly reduce greenhouse gas (GHG) emissions while easing dependence on conventional energy [9,10]. However, deploying carbon capture systems faces multiple challenges, including high solvent costs, energy-intensive solvent regeneration, and thermodynamic limitations during the conversion of CO_2 into value-added chemicals [10–14]. A particularly pressing issue arises when implementing these technologies in thermal power plants, which are major CO_2 emitters. Effective capture systems must minimize the substantial energy demands of desorption (CO_2 release) and compression processes. Despite these hurdles, carbon capture and storage (CCS) has emerged as a promising solution in both scientific and industrial fields [11,12,15,16]. Rather than treating CO_2 as mere waste, CCS reframes it as an affordable and abundant resource for producing energy carriers and industrial chemicals. While CCS alone cannot eliminate global warming, it represents a vital tool for mitigating climate change and fostering sustainable development [8,15–17].

Over the past decade, researchers have developed various technologies to reduce greenhouse gas emissions, including atmospheric CO_2 [18–20]. Among the primary carbon capture methods, absorption, adsorption, and membrane separation are widely used to capture CO_2 from flue gases and ambient air [18,19,21,22]. Once captured, the CO_2 can be desorbed, compressed, and either stored permanently or converted into high-calorific-value fuels [8,20,21]. Among different value-added chemicals derived from CO_2, methanol stands out as particularly promising due to high energy density, compatibility with existing fuel infrastructure, serves as a viable alternative to gasoline, and acts as a key feedstock in the petrochemical industry [3,4,8,13,14,22–24]. It also has paramount use in various valorisation sectors, such as fuel and fuel additives, and represents a discipline for reducing carbon footprint. In addition, methanol has a wide range of applications in the chemical industry as a raw material for producing formaldehyde, fatty acids, light olefins, and dimethyl ether (DME) [3,8,13,14,16,22,24–26]. Its energy and chemical production versatility underscore its importance in advancing sustainable industrial practices [3,8,24].

Conventional production relies on syngas processed via gas-solid reactions using $Cu/ZnO/Al_2O_3$ catalysts under high temperatures (250-300°C) and pressures (50 bar) [7,8,22,26–29]. While modern methods prioritize CO_2 as the carbon source, persistent challenges include catalyst deactivation (via sintering) [16,26,30,31], inefficient heat management [30,32], and high energy demands associated with CCS integration [18,30]. Emerging solutions, such as integrated CO_2 capture and utilization (ICCU), which employ homogeneous catalysts for streamlined conversion, show promise but remain in their early stages of development [33,34].

Current research focuses on optimizing gas-solid systems by developing advanced heterogeneous catalysts, particularly Cu-based binary and ternary variants, synthesized through innovative methodologies. These catalysts undergo rigorous characterization to assess stability, activity, and selectivity under operational stress [26]. Complementary strategies include machine learning for predictive analysis in catalyst design, in-situ mechanistic studies to decode reaction pathways and intermediates, and kinetic modeling for reactor design. This work aims to advance sustainable methanol production by enhancing catalyst durability and process efficiency, bridging energy needs with climate objectives. The integration of CCS with renewable energy and catalytic innovation underscores methanol's dual role in reducing carbon

footprints and supporting a circular economy. The major components of this work are schematically illustrated in **Figure 1.1.**

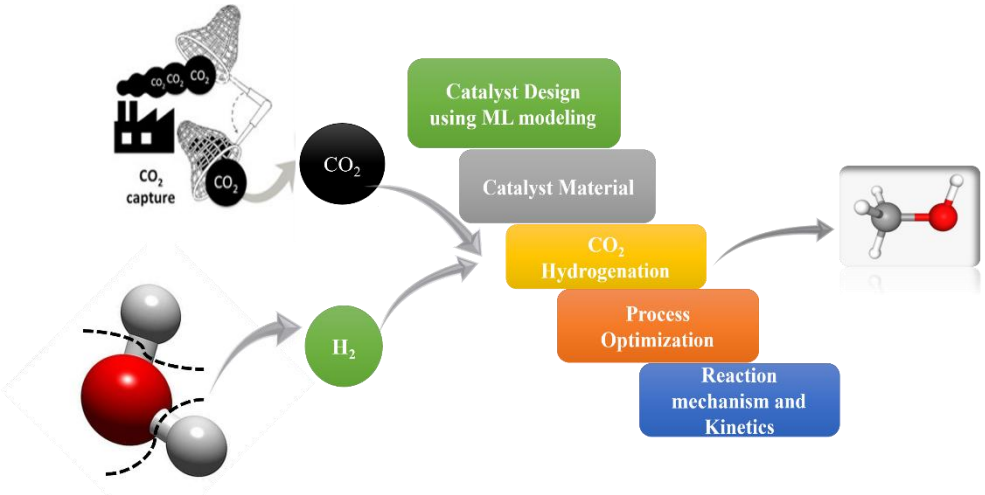


Figure 1.1. *Schematic of the major components covered during the present work.*

1.2 Global Scenario of CO_2 emissions from anthropogenic sources

The escalating concentration of CO_2 in the Earth's atmosphere has been widely acknowledged in recent years due to the implications of global warming [10,35,36]. This has raised significant environmental concerns globally, particularly about the reliance on carbon-based fuels [9,37,38]. Based on the prevailing circumstances, the current atmospheric concentration of CO_2 is at an all-time high, reaching 420 parts per million (ppm) in 2023 [35,36,39]. Multiple experts have documented that the concentration of CO_2 in the atmosphere has not experienced such a significant increase in the last century [10,36,40].

Over the past few decades, the increase in global energy demand, resulting from the rapid processes of globalization and industrialization, has contributed to the disruption of atmospheric CO_2 levels [9,10,36,38,39,41–44]. Therefore, it has been observed that the anthropogenic sources of CO_2 have been significantly influenced by global industrial development in recent decades, resulting in a sudden increase in atmospheric CO_2 content that surpasses what would be expected due to natural changes [9,18,21,37,39,42–44]. As depicted in **Figure 1.2**, a significant proportion of the worldwide greenhouse gas emissions can be attributed to the combustion of fossil fuels, namely in the context of coal-based thermal power plants, as well as other businesses involved in petroleum refining and petrochemical production [9,36,38,39]. Coal-fired thermal power plants are expected to gain increasing significance due to their substantial reserves exceeding 100 years and the growing global energy demand [45–

47]. Nevertheless, the vast magnitude of coal and gas combustion for power generation is a crucial concern [36,39]. Worldwide, CO_2 emissions have risen by almost 80% between 1970 and 2023. Anticipated growth in global energy demands is projected to lead to a further escalation in CO_2 emissions in the coming decades [9,36,38,39]. The establishment of the Intergovernmental Panel on Climate Change (IPCC) and the Environmental Protection Agency (EPA) occurred between 1970 and 1990 with the primary objective of evaluating the impact of greenhouse gas emissions on the Earth's climate, forecasting potential future consequences, and proposing appropriate corrective measures [36,38,39,48,49].

Based on the latest IPCC report, released in 2023 [36,39], the average global temperature increase is expected to surpass the 1.5°C threshold by 2040, even under low-emission scenario [36,39,48,50]. The average increase in global temperature is expected to be around 2.4°C by 2100 if global GHG emissions are met by the protocols, as illustrated in **Figure 1.2** [9,36,37,39,51]. From 2010 to 2019, the average yearly GHG emissions were more than in any other past decade on record [36,39,44,51]. The Global Carbon Budget (2023) [36,44] reported that emissions growth in 2018 was the highest since 2011, driven primarily by increased coal consumption in India (+8.7%), China (+0.9%), and Russia (+4.9%) [44].

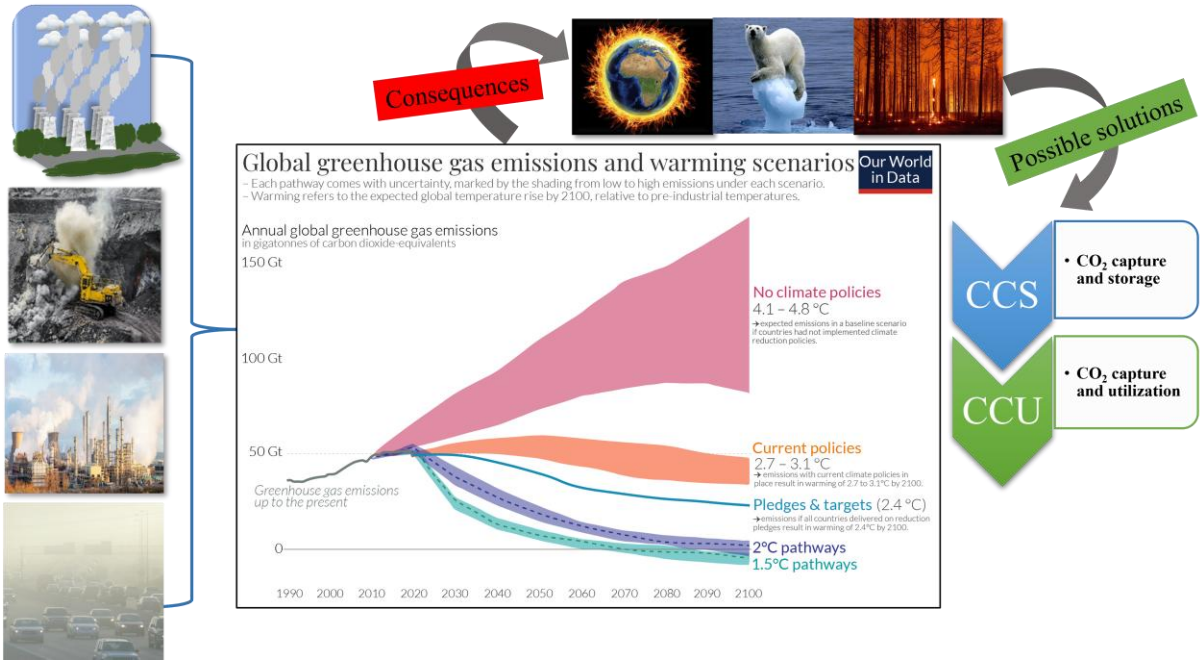


Figure 1.2. *Global greenhouse gas emission sources, warning scenarios, consequences, and possible solutions to mitigate the carbon footprint. (Adapted from source: www.methanol.org International Renewable Energy Agency Report* [36,39,48,50]*).*

Fossil fuel combustion accounts for approximately 89% of global CO_2 emissions**,** with contributions from coal (39%), oil (31%), and natural gas (18%), while clinker production in cement plants contributes nearly 4% [44]. Reduction of CO_2 emissions from non-renewable resources can only be achieved through accelerated deployment of renewable energy technologies such as wind, solar, hydropower, nuclear energy, and through sustainable biofuel production [9,38,52]. In parallel, CO_2 capture technologies from flue gases of thermal power plants and industrial sources remain indispensable mitigation tools [10,21,53]. Due to the rising atmospheric CO_2 concentration, not only capture but also CO_2 utilization technologies (CCU) are being actively pursued to reduce the overall carbon footprint [21,54].

1.3 History of methanol production

1.3.1 Early History (Pre-20th Century)

Methanol, historically called "wood alcohol," was initially produced by destructive distillation of wood until around 1600 [4]. The first successful synthesis of pure methanol was achieved by Robert Boyle in 1661 through the refinement of *Buxus* (boxwood), followed by further distillation. Later, in 1834, Jean B. Dumas and Eugene Peligot determined its elemental composition.

There are numerous similarities between the industrially produced methanol and ammonia. Developing high-pressure catalytic processes for ammonia synthesis by Haber and Bosch [55] inspired research into various organic compounds, including hydrocarbons and alcohols. While hydrogen and nitrogen react under high-pressure and high-temperature conditions to form ammonia, a similar process occurs when hydrogen is combined with carbon oxides. This reaction yields a diverse range of products, with most processes resulting in a mixture of compounds. By modifying process parameters, catalysts, equipment, and feedstocks, industries gained access to a broad spectrum of valuable chemical products, fuelling competition, innovation, and technological advancements [26].

1.3.2 CO Hydrogenation Era (1900s-1960s)

In 1905, Paul Sabatier proposed an artificial pathway for methanol production through CO hydrogenation [56]. Following the success of the Haber-Bosch process for ammonia synthesis in 1913, BASF developed the first industrial high-pressure technology for methanol synthesis

using syngas (CO and H_2) over a ZnO/chromia-based catalyst [57]. This process was commercialized in 1923, marking the transition to synthetic methanol. However, this early catalyst exhibited low activity, requiring high temperatures (300-400°C) and pressures (250-350 bar) to achieve acceptable conversion levels [58]. The primary catalyst for methanol synthesis until the mid-1960s was zinc oxide/chromia. This groundbreaking technology dominated the market for over fifty years, with DuPont and the Commercial Solvents Corporation in the United States pioneering its global licensing [26].

Meanwhile, advancements in optimizing operating conditions, such as temperature and pressure, have garnered significant attention from the global research community. In the 1940s, Switzerland's Lonza Company pioneered the synthesis of methanol using hydrogen produced through electrolysis and carbon dioxide. Building on this, Professor Natta in 1955 proposed a method for catalytically hydrogenating purified syngas over ZnO-based catalysts. Feedstocks (CO, CO_2, and H_2) were purified using calcium nitrate vapours to enhance methanol yield and selectivity, further refining the process [26,55,58].

However, in 1966, ZnO/Cr_2O_3 catalysts were replaced by $Cu/ZnO/Al_2O_3$ catalysts, which ICI first synthesized. Introducing low-pressure (40-80 bar) methanol synthesis technology by ICI reduced energy costs, improved efficiency, revolutionized the industry, and continues to dominate global methanol production today [8,26,59,60]. Synthesis gas (syngas), a mixture of CO, CO_2, and H_2 required for the methanol synthesis, can be derived from various carbon resources, including natural gas, coal, and biomass gasification [61]. One of the primary carbon sources for methanol production is natural gas, which provides a purified form of syngas, allowing methanol to be synthesized directly via oxidative transformation. However, the availability of feedstocks varies by region, influencing the preferred method of syngas generation and subsequent methanol synthesis. Due to the success of this process, the low-pressure ICI process was implemented for commercial methanol production. Later in the 1970s, plants such as Lurgi, Haldor Topsoe, and Linde were established for industrial-scale methanol production by sulfur-free syngas [8,26,58,62–64].

Beyond traditional syngas pathways, alternative methanol production routes are being explored to improve sustainability. Methanol is widely used as a raw material in numerous industrial applications and is gaining attention as a promising alternative fuel due to its liquid state at ambient temperature and high energy density, making it a viable option for automotive and

energy sectors [3]. Due to the rise in CO_2 emissions associated with global warming, there is a need to use CO_2 as a primary reactant for methanol synthesis over the same $Cu/ZnO/Al_2O_3$ catalyst, which sets the stage for CO_2 hydrogenation to methanol [26,54].

1.3.3 Emergence of CO_2 hydrogenation (1990s - Present)

1.3.3.1 Environmental Drivers: Climate Concerns and CO_2 Utilization

- **Problem:** Rising atmospheric CO_2 concentration (from fossil fuel combustion, deforestation, and flue gases released from thermal power plants) is the primary driver of global warming. Mitigating CO_2 emissions is critical to limiting temperature rise to 1.5-2°C (as per IPCC goals) [36,39].

- **Solution:** Instead of merely capturing and storing CO_2 (CCS), researchers and industries began exploring carbon capture and utilization (CCU). Converting CO_2 into valuable products, such as methanol, achieves two key objectives: reducing emissions and producing a sustainable fuel [8,22,54].

Extensive research has been dedicated to advancing processes that operate at progressively lower temperatures and pressures. Today, modern industrial plants utilizing Cu/ZnO-based catalysts achieve optimal performance at conditions of 240-300°C and 50 bar, reflecting decades of innovation in efficiency and sustainability [8,26,59].

1.4 Methanol Economy and World Methanol Demand

George A. Olah, a Nobel Prize-winning chemist for carbonation chemistry, proposed the "methanol economy" concept as a sustainable alternative to the fossil fuel-based economy. This process utilizes captured CO_2 (either industrial flue gases or direct air) and green H_2 (produced through water electrolysis using renewable electricity) to synthesize methanol via a hydrogenation reaction, ensuring the process is carbon neutral [3,4,65].

In 2011, Carbon Recycling International (CRI) launched the George Olah Renewable Methanol Plant in Iceland, utilizing geothermal energy to produce green hydrogen (H_2) and convert CO_2 (captured from a nearby geothermal plant) into methanol. Today, CO_2 hydrogenation to methanol is a cornerstone of the green chemistry movement, aligning with global net-zero

goals. At present, few other companies are synthesizing methanol on a commercial scale via CO_2 hydrogenation using the same process [3,4,65].

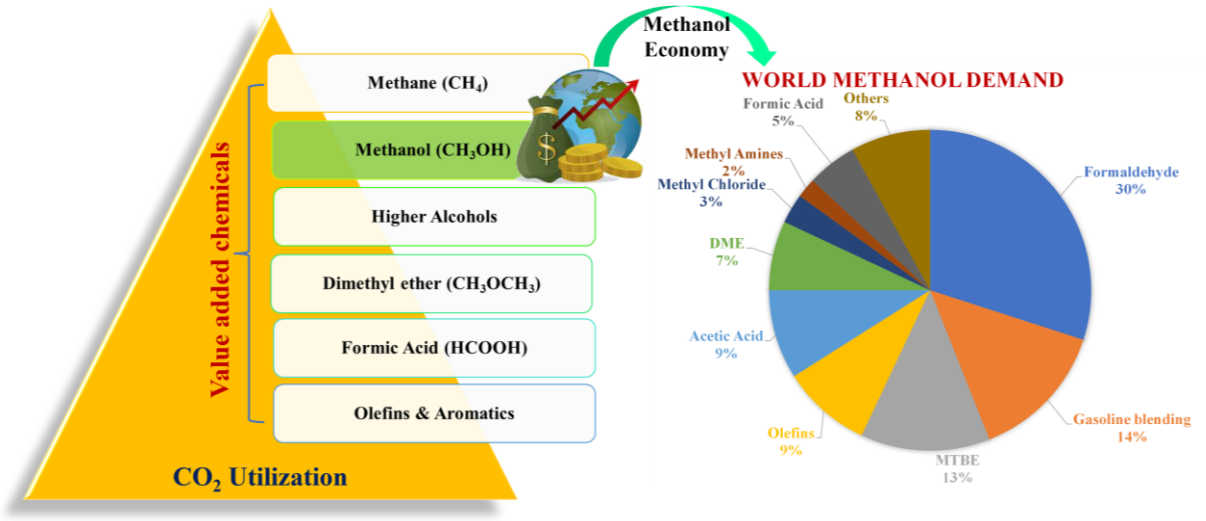


Figure 1.3. *Schematic representation of CO_2 utilization pathways for producing value-added chemicals and global methanol demand distribution across key industrial applications.*

The global methanol economy is experiencing significant growth and transformation, driven by its versatile applications and the push for cleaner energy alternatives. Currently, methanol ranks among the top five widely traded compounds globally on an annual basis. Over the past two decades, there has been a significant increase in the demand for methanol. This is primarily due to the emergence of the methanol economy and its derivatives, which have been crucial in driving global methanol demand **(Figure 1.3).** Due to its high hydrogen-to-carbon ratio, methanol is considered a cleaner energy source. Advancements in production technologies, particularly those that optimize energy efficiency and utilize cost-effective processes, are expected to enhance their economic viability compared to conventional methods. Additionally, it signifies a domain of focus in reducing carbon footprint [8]. This process has been well known for decades, but it still presents different challenges, including thermodynamic limitations, catalyst deactivation, low reactivity, and higher water production.

1.5 Thermodynamics and challenges in synthesizing methanol via CO_2 hydrogenation

The direct hydrogenation of CO_2 to produce methanol is both cost-effective and environmentally friendly. However, this process is subject to certain thermodynamic

constraints. The thermodynamic restrictions arise from the enhanced stability and kinetic inertness of CO_2, making it challenging to activate the CO_2 molecule. The CO_2 hydrogenation to methanol involves two reactions: methanol synthesis and the reverse water-gas shift process [8,22,59,66].

Reactions System

$$CO_2 + 3H_2 \rightleftharpoons CH_3OH + H_2O, \quad \Delta H_{25℃} = -49.5\ kJmol^{-1} \tag{1.1}$$

$$CO_2 + H_2 \rightleftharpoons CO + H_2O, \quad \Delta H_{25℃} = 41.2\ kJmol^{-1} \tag{1.2}$$

The CO formed by the reverse water-gas shift (RWGS) reaction can potentially be converted into methanol through hydrogenation. However, this conversion necessitates an additional energy input, as indicated by equation (3).

$$CO + 2H_2 \rightleftharpoons CH_3OH, \quad \Delta H_{25℃} = -90.6\ kJmol^{-1} \tag{1.3}$$

Equations (1.1) and (1.3) demonstrate that, in accordance with Le Chatelier's principle, the production of methanol is thermodynamically advantageous under conditions of low temperature and high pressure. Due to the chemical inertness and increased thermal stability of CO_2, a high temperature is necessary to initiate the methanol formation. The elevated reaction temperature facilitates the activation of CO_2 and the subsequent production of methanol. The RWGS reaction exhibits a greater propensity at elevated reaction temperatures than the methanol synthesis reaction. Additionally, the methanol produced undergoes decomposition, resulting in the formation of unwanted by-products, such as higher hydrocarbons and alcohols. These by-products have a negative impact on the selectivity and yield of methanol. Furthermore, the catalyst's deactivation occurs at elevated temperatures because of the sintering and agglomeration of the active site on the catalyst surface [67]. Therefore, the high-temperature process is strongly contrary to the thermodynamics of the reaction [8,22,59,66].

According to Le Chatelier's principle, high pressure is thermodynamically advantageous due to the molecular reduction reaction of CO_2 hydrogenation to methanol. Various catalysts have been suggested for achieving optimal CO_2 conversion in methanol synthesis by employing extended pressure ranges. The pressure range spans from 10 bar to 442 bar. However, the conversion of CO_2 was considerably lower at lower pressures due to the more favourable thermodynamics at higher pressures. Bansode et al. achieved the highest conversion and

methanol selectivity levels by using a co-precipitated $Cu/ZnO/Al_2O_3$ catalyst in a micro-reactor, operating under high-pressure conditions of up to 360 bar. The process surpasses the kinetic barrier at elevated operating conditions and transitions into a thermodynamically regulated zone [8,68].

Furthermore, the RWGS (**Equation 1.2**) and the methanol decomposition reaction involving molecular reactions would be hindered as pressure increases. Therefore, in both scenarios, the rate and selectivity of methanol synthesis will be increased due to thermodynamic factors [59]. The thermodynamic analysis of methanol synthesis was performed using Aspen Plus design software, utilizing the RGIBBS block to minimize the total Gibbs free energy of the reaction mixture. Graaf et al. implemented the SRK equation of state in Aspen Plus software to account for non-ideality corrections and accurately calculate Gibbs free energy values for ideal gas behaviour. The feasibility of a reaction is determined by the change in Gibbs free energy ($\Delta G_{25°C}$), whereas the change in enthalpy ($\Delta H_{25°C}$) defines whether the reaction is endothermic or exothermic [69].

The hydrogenation reaction of CO_2 results in the generation of methanol, which is accompanied by the formation of water molecules. Furthermore, the inevitable production of water is a significant component in deactivating the catalyst used in methanol synthesis. Additionally, when exposed to high temperatures, water acts as a potent oxidizing agent, causing the metal to undergo oxidation and form metal oxides. Therefore, catalyst deactivation occurs when the active sites for the reactant gas molecules are lost. Several studies have investigated this issue and found that eliminating water during the hydrogenation process is the most effective approach [59,67]. Nevertheless, a viable remedy has not yet been proposed. As previously mentioned, the thermodynamics of the methanol process involve operating at low temperature and high pressure. This condition is advantageous for achieving high conversion and yield, as illustrated in **Figure 1.4.** When the temperature is raised over a thermodynamically favourable range, both the conversion and yield of methanol synthesis from the direct hydrogenation of CO_2 drop. Furthermore, as clearly shown in the **Figure 1.4,** the temperature increase promotes the RWGS reaction, resulting in CO formation, which is attributed to its endothermic characteristics [16].

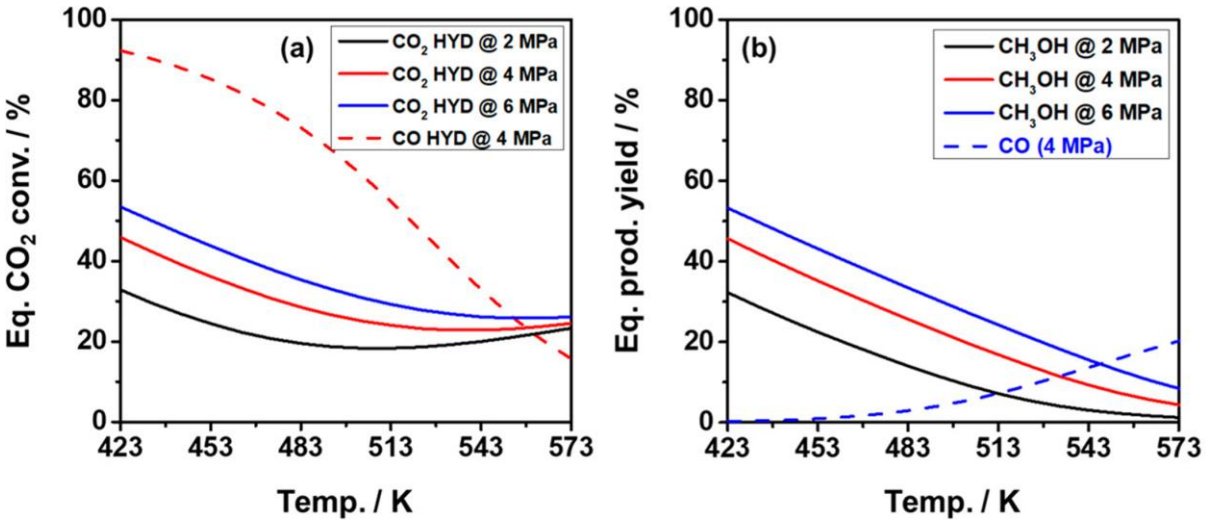


Figure 1.4. *Influence of thermodynamic conditions (T and P) on equilibrium conversion and product yield. Adapted from ref* [16].

1.6 Reaction kinetics of CO_2 hydrogenation to methanol

While the thermodynamics analysis defines the equilibrium limits and the feasibility of temperature and pressure for methanol synthesis, the actual conversion achieved under given conditions is predominantly governed by reaction kinetics [32,63,70]. Even under the thermodynamically favourable conditions, the sluggish activation of CO_2, owing to its strong C=O bonds and linear geometry, introduces substantial kinetic limitations [25]. As a result, the reaction often proceeds through multiple surface-mediated pathways involving the formation and transformation of reaction intermediates such as formate (HCOO*), formyl (HCO*), and methoxy (CH_3O*) [25,71,72]. These intermediates evolve through a series of adsorption, surface reaction, and desorption steps that collectively dictate the overall rate of methanol formation [25,71,72].

The kinetics of CO_2 hydrogenation to methanol are further complicated by the competing reverse water-gas shift (RWGS) reaction, which consumes both CO_2 and H_2 while generating CO and H_2O [25,71,73]. This side reaction becomes increasingly dominant at elevated temperatures, reducing methanol selectivity and introducing additional equilibrium constraints [32,73,74]. Therefore, understanding the interplay between thermodynamics and kinetics is essential for defining optimal operating windows where the methanol synthesis pathway is kinetically favoured without significant inhibition by side reactions [32].

The intrinsic rate of methanol formation is strongly influenced by catalyst composition and surface structure. In Cu-based catalysts, for instance, the metallic copper sites facilitate hydrogen dissociation, whereas the adjacent ZnO or ZrO_2 components promote CO_2 activation and stabilize reaction intermediates. The synergistic interaction among these components modulates the adsorption energies of reaction intermediates and alters the apparent activation energies of the elementary steps, thereby determining both activity and selectivity. To capture such complex behaviour, mechanistically derived rate expressions, typically of the Langmuir-Hinshelwood-Hougen-Watson (LHHW) form, provide a quantitative description of surface kinetics.

In this context, kinetic modeling is crucial for linking catalyst design with reactor performance. It enables the estimation of intrinsic rate parameters, the identification of rate-determining steps, and the prediction of methanol yields under varying reaction conditions. The insights drawn from kinetic studies thus complement the thermodynamic framework and guide both catalyst optimization and process intensification. Detailed mechanistic insights, kinetic modeling, and validation for CO_2 hydrogenation to methanol are extensively discussed in the subsequent chapters of this thesis.

1.7 Current possible approaches to overcome limitations

Building on the thermodynamic and kinetic perspectives, several methodologies have been proposed to mitigate the inherent limitations of CO_2 hydrogenation to methanol. Optimizing reaction conditions, such as temperature, pressure, and feed composition, is crucial to strike a balance between the competing demands of thermodynamic favourability and kinetic activity. Additionally, the use of thermally stable solvents and novel reactor configurations (e.g., slurry-phase or structured catalytic reactors) can aid in heat management and enhance mass transfer as both CO_2 absorption and hydrogenation reactions are exothermic in nature, thereby improving overall processing efficiency [57,59,75].

Modifying the catalyst is crucial for enhancing the conversion of CO_2 and the selectivity of methanol. It is essential to carefully adjust the catalyst's properties to achieve optimal catalytic efficiency. This adjustment depends on several factors, including: (i) the composition and structure of the metal and support; (ii) particle size uniformity; (iii) dispersion and distribution of active sites; (iv) surface area and porosity; (v) active and defect sites concentration; (vi)

metal-support interactions; (vii) incorporation of promoters or ternary oxides that modify surface basicity and reducibility. Such rational design strategies can simultaneously accelerate the rate-determining steps, suppress side reactions like RWGS, and enhance methanol selectivity even under mild operating conditions [59].

In this context, the present work focuses on developing advanced Cu-based catalytic systems with optimized composition, structure, and reaction environment to achieve superior CO_2 conversion and methanol productivity. By integrating experimental investigations with kinetic modeling and machine learning approaches, this study aims to establish a comprehensive framework for understanding and optimizing the CO_2-to-methanol process under industrially relevant conditions.

1.8 Data-driven and machine learning approaches in catalyst design

The growing complexity of catalytic systems and the vast parameter space associated with catalyst synthesis, structure, and performance have driven the adoption of data-driven and machine learning (ML) methodologies in modern catalyst design. Though fundamental, traditional experimental and mechanistic approaches often face limitations due to high experimental costs and the multidimensional nature of catalyst descriptors. Machine learning provides an efficient alternative by identifying hidden correlations between physicochemical features and catalytic performance, thereby accelerating the discovery and optimization of high-performance materials [13,76].

In CO_2 hydrogenation to methanol, ML techniques such as principal component analysis (PCA), random forest regression (RFR), support vector machines (SVM), gaussian process regression (GPR) and artificial neural networks (ANN) have been applied to predict CO_2 conversion, methanol selectivity, and space-time yield based on input descriptors like crystallite size, surface area, Cu dispersion, Cu^o/Cu^+ ratio, and metal-support interaction strength. Beyond prediction, interpretable ML tools such as SHapley Additive exPlanations (SHAP) or permutation importance analyses help identify the most influential parameters governing catalytic behavior, offering a mechanistic understanding complementary to kinetic modeling and experimental characterization [13,77,78].

The present thesis establishes an intelligent, data-driven framework for rational catalyst design by integrating these ML-derived insights with experimental synthesis and kinetic studies. The

approach leverages literature-based datasets for model training, validated experimentally using synthesized Cu/ZnO/ZrO_2 catalysts, to provide predictive guidance for optimizing catalyst composition and reaction conditions for CO_2 hydrogenation to methanol.

1.9 Summary and Future Outlook

This introductory chapter has provided an extensive framework for the current research, beginning with the motivation derived from the global CO_2 emission challenge and the role of methanol as a sustainable carbon carrier. The discussion is confined to the historical evolution of methanol production, the concept of a methanol economy, world methanol demand, and the industrial relevance of Cu-based catalysts. The debate on thermodynamic limitations and kinetic complexities established the foundational context for catalyst and process design. Subsequently, recent advancements and strategies to overcome these challenges were summarized, highlighting the critical role of catalyst composition, structure, and reaction engineering.

Introducing data-driven and machine learning strategies represents a paradigm shift in catalyst development, enabling predictive modeling and rational optimization that complement experimental and mechanistic approaches. Together, these elements provide a coherent foundation for the present work, which combines experimental synthesis, kinetic modeling, and ML-based predictive frameworks to advance the understanding of CO_2 hydrogenation to methanol. Chapter 2: Literature Review builds upon this foundation by providing an in-depth discussion of previous studies on hydrogen production, development of catalytic systems, data-driven methodologies in catalyst design, reaction mechanisms, and kinetic modeling approaches relevant to CO_2 hydrogenation to methanol.

1.10 Thesis Organisation

Chapter 1 This chapter introduces global scenario of CO_2, its impact on the environment, the possible solutions, the history of methanol production, the methanol economy, its demand, reaction thermodynamics, kinetics, possible approaches to overcome limitations, machine learning approaches in catalyst design.

Chapter 2 The recent advancements in the open literature are critically reviewed, and the drawbacks of the current system are highlighted. The aim and approaches of this research are introduced based on the literature gaps.

Chapter 3 The detailed description of different materials, catalyst preparation methods, analytical characterisation techniques, experimental and computational procedures is elucidated in more detail.

Chapter 4 This chapter integrates machine learning with experimental catalysis by developing a predictive model trained on literature data and validated with the experimental dataset. This approach bridges traditional kinetic modeling with data-driven tools to guide future catalyst development.

Chapter 5 This chapter presents the hydrothermal synthesis and characterization of a novel Cu/MgO catalyst with exceptionally high (up to 50% Mg) incorporation into the Cu lattice. It highlights the structural and catalytic behaviour of Cu/MgO for CO_2 hydrogenation, showcasing the impact of Mg promotion.

Chapter 6 This chapter is organized to explore the scalable synthesis of Cu-Zn hydroxy-carbonate precursors via mechano-chemical ball milling and investigate the synergistic role of ZnO-ZrO_2 in enhancing catalytic properties.

Chapter 7 This chapter investigates the kinetics of CO_2 hydrogenation over Cu/ZnO/ZrO_2, focusing on parameter-driven catalytic performance. A LHHW kinetic model is developed to uncover reaction mechanisms and rate-controlling steps.

Chapter 8 This chapter concludes the thesis and presents some future directions to be explored.

Chapter 2 Literature Review

This chapter contains excerpts from the following publications.

1. ***Aakash Bhardwaj†****, Akshdeep S. Ahluwalia†, K.K. Pant, Sreedevi Upadhyayula*, "A principal component analysis assisted machine learning modeling and validation of methanol formation over Cu-based catalysts in direct CO_2 hydrogenation", Separation and Purification Technology, Volume 324, 1 November 2023, 124576.*
2. ***Aakash Bhardwaj[a,1]****, Meenakshi Pokhriyal[a,1], Vaibhav Pandey[a], Kamal Kishore Pant[a], Sreedevi Upadhyayula[a,]*, "Enhanced Methanol Formation over Cu/MgO catalyst derived from Mg-Rich Active Hydroxycarbonate Precursor", ACS Appl. Energy Mater. 2024, 7, 12, 5163-5178.*

2.1 Overview

This chapter presents a comprehensive and critical review of CO_2 hydrogenation to methanol, intending to establish the scientific and technological foundation for the present thesis. Building on the broader context introduced in Chapter 1, this chapter systematically examines the hydrogen production routes, catalytic systems, mechanistic understanding, kinetic modeling strategies, and reactor considerations that govern the performance and scalability of CO_2-to-methanol processes.

The chapter begins with a discussion on green and sustainable routes for hydrogen production (Section 2.2), followed by a detailed review of heterogeneous catalytic systems for the direct hydrogenation of CO_2 to methanol (Section 2.3), with special emphasis on the evolution and development of Cu-based catalysts, which remain the industrial benchmark.

Subsequent sections focus on the precursor-guided catalyst synthesis, highlighting the critical role of malachite, zincian malachite, and rosasite-type hydroxycarbonate phases in controlling copper dispersion, oxygen vacancy formation, and metal-support interactions (Section 2.3.1.2). The chapter then provides a comparative evaluation of Cu-based binary and ternary catalysts to summarize activity-selectivity trends (Section 2.3.1.3). Emerging machine learning approaches in catalyst design and performance prediction (Section 2.3.2) are also reviewed, reflecting the growing role of data-driven strategies in accelerating catalyst discovery and optimization.

A major portion of the chapter is dedicated to the reaction pathways and mechanisms of CO_2 hydrogenation to methanol (Section 2.3.3), covering competing formate and CO-mediated pathways, the influence of the Cu surface and oxidation state, the role of interfacial water, support-driven and multi-component synergies. The transition from mechanistic understanding to kinetic modeling (Section 2.3.4) is then examined, with emphasis on LHHW kinetic frameworks used to quantify intrinsic reaction rates. Finally, reactor aspects (Section 2.3.5) relevant to heat transfer, mass transport, and process intensification are discussed to connect intrinsic kinetics with practical reactor performance. A brief chapter summary consolidates the key insights before identifying the remaining challenges (Section 2.4).

The chapter concludes with a clear identification of research gaps and motivation (Section 2.5) arising from limitations in precursor phase control, scalable catalyst synthesis, oxygen vacancy engineering, mechanistic ambiguity, and the lack of experimentally validated kinetic models. These gaps directly shape the research objectives (Section 2.6) and thereby establishing a direct intellectual link between the existing literature and the original contributions of this thesis.

2.2 Green routes to produce hydrogen

In the CO_2 hydrogenation to methanol process, hydrogen plays a significant role in the transformation by participating in the reaction, using three times the number of moles of CO_2. Therefore, various green routes to produce hydrogen have been investigated to meet the massive demand for hydrogen and are illustrated in **Figure 2.1.** At present, industrial hydrogen is mainly produced through fossil-based methods such as methane steam reforming, coal gasification, and partial oxidation of petroleum residues, thereby accelerating fossil fuel depletion and increasing CO_2 levels in the atmosphere [8,15,79,80]. To produce renewable methanol from CO_2 and H_2 as primary reactants, the amount of CO_2 consumed during synthesis must be greater than the CO_2 generated during hydrogen production. This requirement highlights the necessity of using green hydrogen sources [8,15,81–83]. Water electrolysis represents a promising alternative for large-scale green hydrogen generation; however, its widespread adoption is currently limited by high costs, primarily due to the use of noble-metal (Pt-based) electrodes and the high price of electricity [15,82].

Water electrolysis driven by electrical energy generated from green and renewable sources, such as photovoltaics, wind energy, ocean energy, and geothermal power is considered the

most appropriate routes for green hydrogen production. Among the available electrolysis technologies, alkaline water electrolysis is currently the most established and widely used. In this process, two electrodes are immersed in an alkaline electrolyte, where hydroxide ions (OH^-) migrate from the cathode to the anode, leading to hydrogen generation at the cathode. For the optimization of alkaline water electrolysis costs, novel Ni-based electrodes were used instead of the costly Pt electrodes. Ni-based electrodes show good corrosion resistance, making this technology cost-effective. These are the most advanced electrolysis technologies, characterized by lower capital costs. However, the low efficiency of this technology, in turn, leads to higher electrical energy costs, opening the door for other green water electrolysis methods [8,15,82,83].

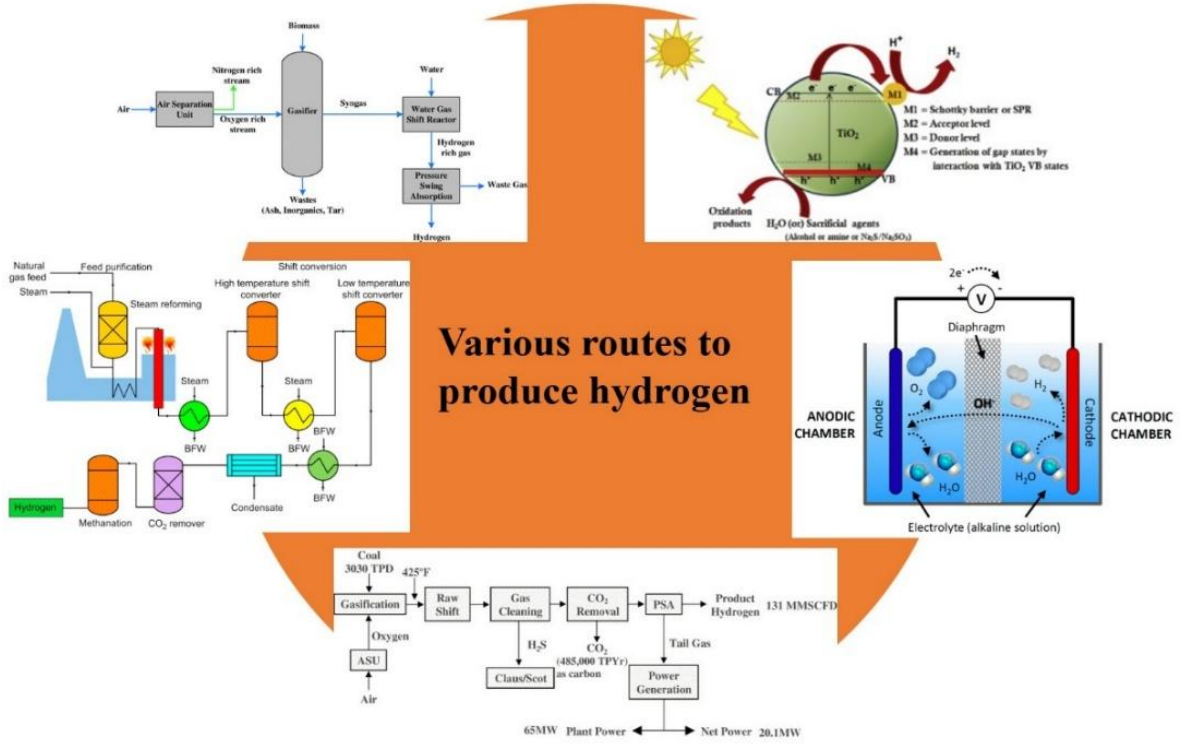


Figure 2.1. *Various routes for the production of hydrogen.*

Several emerging technologies are also being explored for green hydrogen production via water electrolysis, including polymer electrolyte membrane (PEM) electrolysis, solid oxide electrolysis cells (SOECs), and carbon-assisted water electrolysis (CAWE) [8,15]. PEM electrolysers offer advantages such as higher efficiency and the absence of corrosion and sealing issues commonly associated with alkaline systems; however, their widespread adoption is limited by high capital costs. In contrast, SOECs exhibit strong potential for large-scale industrial applications due to their ability to achieve nearly 100% Faradaic efficiency at

elevated operating temperatures. Nevertheless, challenges such as material degradation, sealing failures, thermal cycling instability, and chromium migration hinder their long-term durability. Beyond electrochemical approaches, photocatalytic water splitting has also attracted considerable attention as a promising clean and renewable pathway for sustainable hydrogen generation. This process has a significant advantage due to its negligible emissions of CO_2 and SO_2. Various investigations have been conducted on the direct splitting of water into hydrogen and oxygen using semiconductor-based photocatalysts under solar irradiation. Numerous efforts have been made to efficiently utilize solar radiation by developing photocatalysts that are active under both ultraviolet and visible light. Titanium dioxide (TiO_2) has been one of the most widely investigated photocatalysts for water splitting due to its chemical stability, environmental compatibility, abundance, and low cost. However, TiO_2-based systems suffer from major limitations, including rapid recombination of photogenerated electron-hole pairs, backward reactions, and limited absorption of the solar spectrum. Employing a composite is an excellent approach to increase photocatalytic performance [15,82,83]. Such composites are typically prepared by coupling oxide semiconductors with non-oxide materials to form heterojunction structures, including CdS-TiO_2, CdS-ZnO, CdS-MoS_2, and CdS-AgI. Among these heterojunctions, CdS-TiO_2 and CdS-MoS_2 have received particular attention due to their improved charge separation efficiency and expanded light absorption capability [15]. Overall, substantial progress has been made toward the development of environmentally benign hydrogen production routes through photocatalytic water splitting. Water electrolysis in combination with renewable sources should be the preferred option. The availability of low-cost electric technology produced by solar, wind, hydro, geothermal, and other sources in specific locations may justify its commercialization.

Despite significant progress, the large-scale deployment of green hydrogen technologies remains challenging, particularly in industrial regions that serve as major sources of CO_2 emissions. High capital investment and operating costs continue to be key barriers to widespread implementation. In the case of photocatalytic hydrogen production, further advances in material development are required to address persistent challenges related to photocatalyst stability and low energy conversion efficiencies. If these limitations can be mitigated to a reasonable extent, photocatalytic water splitting has the potential to play a more effective role in supporting the green hydrogen economy in the near future [82,83].

2.3 Heterogeneous catalytic system for the direct hydrogenation of CO_2 to methanol

The direct hydrogenation of CO_2 to methanol sustains a solid potential to convert a tremendous amount of CO_2 quickly due to its high reaction rate. George Olah et al. have proposed a closed carbon cycle for CO_2 hydrogenation to methanol and DME and vice versa [3,65]. The CO_2 emissions released into the open atmosphere have been captured and catalytically reduced using hydrogen produced from greener routes, such as photocatalytic water splitting and H_2O electrolysis powered by natural/renewable energy sources [82,83].

Over the last few decades, researchers have proposed several studies on the direct hydrogenation of CO_2 to methanol using various combinations of heterogeneous catalysts. Still, Cu-based commercial catalysts, such as $Cu/ZnO/Al_2O_3$, have been used for methanol synthesis on an industrial scale, utilizing syngas as the primary reactant species due to their high activity and product selectivity [8,16,22,26,59,66,84]. These heterogeneous conventional catalysts for CO_2 hydrogenation to CH_3OH require high temperature and pressure. Various reactor configurations have been employed for methanol synthesis at both laboratory and commercial scales, which can sustain very high reaction conditions. Among them, the fixed-bed reactor configuration has been widely used for CO_2 hydrogenation reactions, utilizing $Cu/ZnO/Al_2O_3$ as a commercial catalyst [8,26,59]. This methanol formation process has several shortcomings, including heat removal, hot spot formation, catalyst deactivation, and, last but not least, the energy-intensive steps involved in the CO_2 capture process. To overcome these shortcomings, liquid-phase reactions have been proposed using slurry and trickle-bed reactors. The benefit of using such reactors is the controlled reaction conditions, and the energy required for the capture and storage has been reduced [59]. In this context, the integrative CO_2 capture and utilization (CCU) approach has been implemented using metal-complex homogeneous catalysts. However, this has never been combined with laboratory and commercial-scale multiphase reactors.

The primary attention has been given to methanol synthesis via the CCU process and direct utilization. The direct hydrogenation of CO_2 to methanol has been researched in parallel with heterogeneous catalysts. Therefore, transitioning to an entirely new process (ICCU with homogeneous catalysts in three-phase reactors) will be challenging and will require multiple years of trial and optimization for commercialization. Hence, we should remain within a known

reaction system using the commercialized process and focus on addressing its shortcomings to further optimize the catalytic system and method.

2.3.1 Catalytic Systems

2.3.1.1 Evolution and Development of Cu-based Catalysts

Copper-based catalysts have remained the cornerstone of methanol synthesis for decades, particularly since the introduction of highly selective $Cu/ZnO/Al_2O_3$ systems by Imperial Chemical Industries (ICI) in the 1960s for use with naphtha and natural gas feedstocks. This innovation replaced the high-pressure ZnO/Cr_2O_3 catalytic system, initially pioneered by BASF, enabling the methanol process to operate under significantly milder conditions (typically 5-10 MPa and 200-300°C) while achieving higher methanol selectivity and efficiency [8,22,26,59,66].

This innovation marked a paradigm shift, enabling the production of methanol from naphtha- or natural gas-derived syngas with reduced energy consumption and improved process economics. The superior performance and the environmental and cost advantages of operating at lower pressures established Cu-based catalysts as the industrial benchmark. Since then, extensive research has focused on optimizing Cu-containing systems, with a particular emphasis on enhancing metal dispersion, tuning support interactions, and improving long-term stability [26].

These Cu-based catalysts were initially extensively evaluated using syngas (a mixture of CO, CO_2, and H_2) as the feedstock [8,22]. The majority of early investigations focused on enhancing performance under syngas conditions, resulting in a profound understanding of the $Cu/ZnO/Al_2O_3$ system and its structure-activity relationships [8,22]. However, with the growing urgency to mitigate CO_2 emissions and reduce carbon footprints, attention has increasingly shifted towards direct CO_2 hydrogenation as a sustainable alternative.

Interestingly, even as CO_2 replaced syngas as the feedstock, the $Cu/ZnO/Al_2O_3$ system remained a starting point for investigation, due to its well-documented performance and known active sites. Over time, however, researchers recognized that catalysts optimized for syngas conditions were not necessarily ideal for CO_2-rich feeds [26]. The thermodynamic and kinetic behaviour of CO_2 differs significantly from that of CO, necessitating the development of new catalyst formulations tailored specifically for CO_2 activation and hydrogenation [64,85,86].

Among various systems explored, Cu-based catalysts [8,14,16,22,25,26,64,66,85] continue to dominate due to several compelling reasons:

- The intrinsic activity of Cu for the hydrogenation of CO_2 to methanol is mainly due to its ability to stabilize key intermediates such as formate and methoxy species [26].
- Favourable electronic structure and moderate binding energy for reaction intermediates, enabling efficient conversion without excessive side reactions [26]a.
- The low cost, abundance, and non-toxic nature of copper make it an attractive option for large-scale deployment [8,26].

Despite a wide array of catalyst formulations, the Cu/ZnO system prepared by co-precipitation remains a foundational reference, often used as a baseline for further modification [85–87]. This system's well-characterized behaviour provides a valuable benchmark for understanding the effects of dopants, support morphology, and synthesis methods on activity and selectivity. Within this system, ZnO plays a multifaceted role, acting as a structural promoter, enhancing copper dispersion, and stabilizing the Cu^0/Cu^+ interface, which is widely considered the active site ensemble for methanol synthesis. Furthermore, ZnO contributes to the adsorption and activation of CO_2, thereby enhancing the intrinsic reaction rate. The well-established synergistic interaction between Cu and ZnO underscores the importance of intimate interfacial contact and optimized metal-support interactions for achieving high activity and selectivity [8,25,26,64,85,87].

To further enhance the catalytic performance and overcome the limitations of binary Cu/ZnO systems, researchers have explored the incorporation of secondary oxide supports, including Al_2O_3, ZrO_2, MgO, and CeO_2, into the catalyst matrix **(Figure 2.2).** These oxides introduce a range of functional benefits that can be tailored to meet specific catalytic requirements [8,22,26,59,66]. For instance, Al_2O_3 imparts thermal stability and mechanical strength, making it favourable for industrial applications, although it may weaken the metal-support interaction and reduce Cu-ZnO synergy [8,22,26,59,66]. In contrast, ZrO_2 enhances reducibility and oxygen mobility, which improves CO_2 adsorption and facilitates the formation of intermediates [8,66,88–92]. MgO, known for its basic character, helps suppress the reverse water-gas shift (RWGS) reaction, thereby increasing methanol selectivity by minimizing CO formation [14,66,93,94]. CeO_2 contributes to the formation of oxygen vacancies and redox buffering, both of which promote CO_2 activation and potentially enhance reaction kinetics [66,89,95–98].

Together, these modifications reflect a strategic evolution in catalyst design, where the classical Cu/ZnO system is no longer treated as a static solution but rather as a flexible platform for tailoring performance through multi-component engineering. This has led to the development of ternary and quaternary systems that capitalize on the combined effects of dispersion control, surface basicity, oxygen storage capacity, and structural stability-key factors in advancing Cu-based catalysts for low-temperature, low-pressure CO_2 hydrogenation to methanol [26].

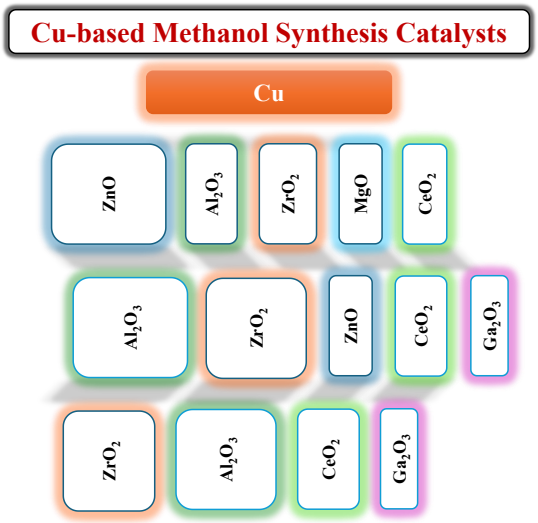


Figure 2.2. *Various catalyst combinations have been used in the methanol synthesis reaction via CO_2 hydrogenation in the last decade.*

2.3.1.2 Precursor-guided synthesis: the critical foundation for high-performance Cu-based methanol catalysts

As discussed in the previous section, Cu-based catalysts, particularly Cu/ZnO systems, have long served as the benchmark for methanol synthesis, owing to the intrinsic activity of copper, the promotional role of ZnO, and the positive contributions from secondary supports such as Al_2O_3, ZrO_2, MgO, and CeO_2 [16,22,26,66]. These oxides modulate surface basicity, oxygen mobility, and thermal stability, suppressing side reactions such as the RWGS reaction and stabilizing the active phases. However, despite numerous compositional optimizations, consistently high performance in CO_2 hydrogenation still relies heavily on the catalyst synthesis methodology and the precursor phase rather than on the elemental composition alone [14,64,85,93].

The compositional evolution of Cu-based catalysts has significantly advanced methanol synthesis performance, yet it is increasingly evident that the catalyst's synthesis method and,

more critically, the precursor phase it produces, play a decisive role in determining its final catalytic behaviour [64,85,93,95,99–102]. This structure-property-performance linkage, often underrepresented in earlier studies, is now recognized as a key parameter in the rational design of catalysts for CO_2 hydrogenation. Catalyst precursors act as a "chemical memory", determining essential characteristics such as metal dispersion, Cu-ZnO interfacial area, support morphology, and thermal stability. Upon calcination and reduction, these precursor phases decompose to form an active Cu^0 phase closely interfaced with ZnO and other oxide supports. The quality and homogeneity of this transformation depend on the phase purity, crystallinity, and distribution of metal ions in the precursor [25,85,87,88,93,103].

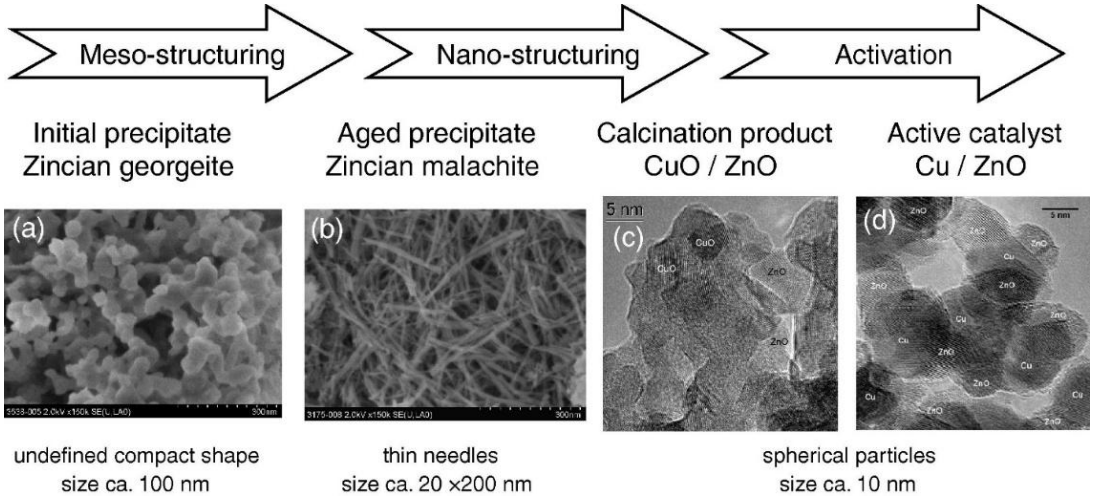


Figure 2.3. *Microstructural transformation of Cu/ZnO catalyst precursors during meso-structuring, nano-structuring, calcination, and activation steps. Adapted from Behrens et al.* [85,104]

Calcination and reduction steps significantly alter the catalyst's structure and morphology, transitioning from meso-structuring to nano-structuring **(Figure 2.3).** The high metal dispersion and stability of Cu-based catalysts arise from a unique microstructure obtained after reduction. The ZnO component in $Cu/ZnO/Al_2O_3$ catalyst acts as a geometrical spacer between the elemental Cu particles, prevents Cu sintering, enhances Cu dispersion, and helps facilitate CO_2 adsorption and activation on the catalyst surface to be subsequently hydrogenated to methanol. In contrast, the Al_2O_3 component improves the chemical and thermal stability of the catalyst [8,66,104]. Behrens et al. [85,104] described this phenomenon by forming defect sites and migrating ZnOx species onto the Cu nanoparticles, resulting in a strong metal-support interaction (SMSI) effect as illustrated in **Figure 2.3.** In addition to a high copper surface area (SA_{Cu}) and an optimized Cu^0/Cu^+ ratio, other structural factors such as metal-oxide interactions

(MO/SMSI) and defect engineering also play critical roles in determining catalytic efficiency, as illustrated in **Figure 2.4.**

Among the various synthesis methods, co-precipitation (CP) remains the most extensively used due to its simplicity and scalability [64,87,104]. However, conventional CP often yields mixed-phase precursors, including aurichalcite, zincian malachite, and hydrotalcite, whose formation strongly depends on critical parameters such as pH, temperature, metal salt concentration, and aging conditions. Despite their functional activity, mixed-phase precursors suffer from batch-to-batch variability, limited reproducibility, and poor phase purity, especially under the stringent controls of laboratory-scale synthesis. The importance of precursor chemistry in governing the final catalyst structure and performance has gained increasing recognition [26,85].

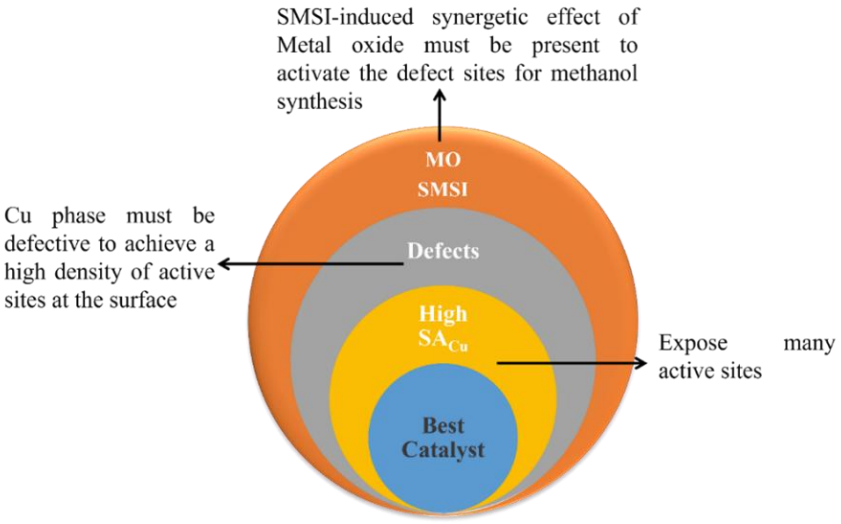


Figure 2.4. *Structure-performance correlation for Cu-based methanol synthesis catalysts, demonstrating how SMSI effects, defect density, and Cu surface area integrates to produce the highest catalytic activity. Modified from ref* [85].

Over the past decade, growing research has recognized that catalytic performance is not solely dictated by the final catalyst composition but is deeply rooted in the precursor phase and the synthesis strategy employed. The precursor effectively acts as a "chemical memory," governing the catalyst's metal dispersion evolution, support interaction, textural properties, and active site formation. Recent advances in Cu-based methanol synthesis catalysts have highlighted the crucial role of the precursor phase and the synthesis method employed [25,64,103,104]. Studies by Behrens et al. emphasized that forming phase-pure zincian malachite or rosasite-type hydroxycarbonates precursor yields catalysts with finely dispersed

metallic Cu and robust Cu-ZnO interfaces upon thermal decomposition. These interfacial sites stabilize key intermediates, such as formate and methoxy species, enabling selective CO_2 hydrogenation [25,85,105].

Additionally, increasing Zn^{2+} substitution within the malachite lattice enhances the synergistic effects between the metal and support, improves structural stability, and suppresses Cu sintering, thereby boosting methanol productivity. However, thermodynamic constraints limit Zn^{2+} substitution to about ~27 at.%, restricting complete phase purity [25,64,85,102,104]. The introduction of Mg^{2+}, desirable for increasing surface basicity and suppressing the RWGS reaction, further complicates precipitation, as it promotes undesired CuO formation and disrupts uniform crystallization. Hence, traditional co-preparation often fails to produce fully phase-pure precursors under controlled, reproducible conditions [93].

Alternative precursor structures, such as zincian georgeite, have emerged as promising options due to their superior microstructural uniformity and high surface area, yielding catalysts with ~20% higher activity than those from aurichalcite or zincian malachite [93]. Modified CP methods, including low-temperature precipitation or controlled carbonate addition, have also enabled higher Zn^{2+} incorporation (>30 at.%), improved surface area, and reduced activation energy for methanol synthesis [26,106,107].

Despite these advances, a persistent synthesis-performance disconnect remains, as illustrated in **Figure 2.5**, which classifies existing synthesis methods by their influence on:

- Catalyst structural properties (e.g., metal dispersion, particle size, surface area, textural morphology).
- Active site characteristics (e.g., Cu^0/Cu^+ ratio, oxygen vacancies, Cu-ZnO interface, surface basicity).
- And practical application metrics (e.g., scalability, mechanical strength, simplicity).

Many conventional precipitation or lab-scale methods (e.g., sol-gel, microwave-assisted synthesis, ammonia evaporation) address one of these domains but fail to meet all simultaneously. Only a few synthesis routes successfully integrate structural precision, active site optimization, and industrial scalability, such as hydrothermal, combustion & pyrolysis, ball milling (mechanochemical synthesis), and spray drying [16].

Building on these insights, our thesis focuses on two advanced synthesis methodologies that directly address these challenges:

1) Hydrothermal synthesis enables the controlled crystallization of mcguinnessite ($CuMgCO_3(OH)_2$), a rosasite-type hydroxycarbonate phase, facilitating well-defined Cu-MgO interfaces. This approach prevents unwanted CuO formation, enhances surface basicity, and yields a phase-pure, thermally stable precursor. The resulting catalyst exhibits improved methanol selectivity, structural stability, and active site exposure [14].
2) Mechano-chemical ball milling (MCBM) provides a scalable, solvent-free method for synthesizing phase-pure Cu-Zn hydroxycarbonate precursors, utilizing ZrO_2 as a ternary promoter. Atomic-level mixing achieved by milling ensures excellent metal dispersion, strong metal-support interaction, and efficient promoter incorporation. The final catalysts display superior space-time yields, lower CO formation, and improved durability under reaction conditions.

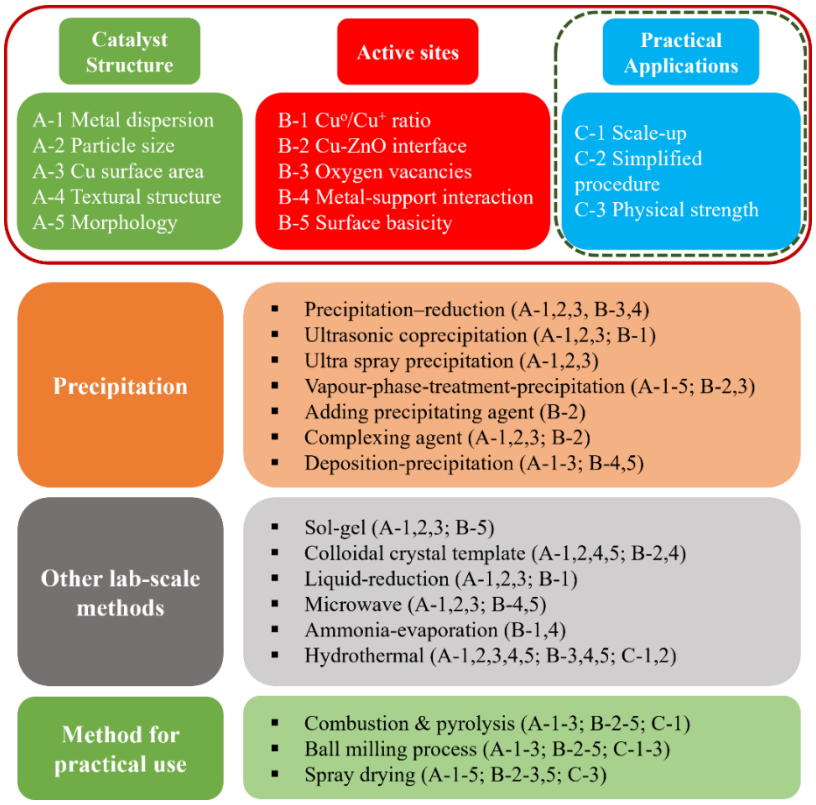


Figure 2.5. *Comprehensive summary of catalyst design parameters for Cu-based catalysts, illustrating the interrelation between catalyst structure, active site features, and catalytic activity, along with corresponding synthesis methodologies. Modified from ref* [16].

These findings highlight that catalytic performance cannot be attributed solely to composition but must be interpreted through a precursor-structure-property relationship. Parameters such as crystallographic identity, metal substitution behaviour, and interfacial stability govern:

- the dispersion and accessibility of metallic Cu;
- the stability and intimacy of Cu-support interfaces; and
- the electronic and acid-base properties that control intermediate binding and desorption.

Thus, integrating rational synthesis design with precursor phase engineering marks a paradigm shift from empirical catalyst development toward predictive and scalable synthesis strategies, bridging the gap between academic research and industrial applicability [16].

2.3.1.3 Comparative catalytic performance of Cu-based catalysts for CO_2 hydrogenation to methanol

The growing understanding that catalyst performance originates from precursor chemistry and synthesis strategy makes it essential to benchmark how these design parameters translate into actual catalytic behaviour across different Cu-based systems. Literature consistently demonstrates that the catalytic efficiency of Cu-based catalysts for CO_2 hydrogenation to methanol depends not only on chemical composition but also on the synthesis route, precursor structure, and the resulting metal-oxide interfaces. Beyond simple compositional effects, the transformation of precursors into active Cu^0-Cu^+ ensembles, the density of oxygen vacancies, and the degree of metal dispersion collectively determine CO_2 activation and methanol selectivity [26]. A comparative analysis of representative literature studies is summarized in **Table 2.1,** followed by a discussion of synthesis-dependent performance trends to contextualize these relationships.

Table 2.1. *Overview of literature-reported Cu-containing catalysts and their performance in CO_2 hydrogenation to methanol as a function of synthesis route, operating parameters, and productivity indicators.*

Catalyst	Preparation Methods	CO_2/H_2 Ratio	Operating Conditions	X_{CO2} (%)	S_{MeOH} (%)	MeOH STY ($mg_{MeOH}/g_{cat}.hr$)	Ref
CZA-LDH (Heng Zhang 2024)	Hydrotalcite-like precursor derivation	1:3	T = 523 K P = 30 bar	18	49	515	[108]

			W = 18000 ml g^{-1} h^{-1}				
1Cu/ZnO-Air (Chen 2024)	Hydrothermal	1:3	T = 553 K P = 30 bar W = 3600 ml g^{-1} h^{-1}	8.2	38.5	-	[109]
CuZnZr-flower (Hao Chen 2022)	Hydrothermal with urea hydrolysis	1:3	T = 503 K P = 30 bar W = 3600 ml g^{-1} h^{-1}	16.5	56.2	138	[110]
CuMgZn-20HT (Sharma 2021)	Hydrothermal	1:3	T = 523 K P = 30 bar W = 7200 ml g^{-1} h^{-1}	12.3	79.8	10	[6]
Cu-ZnO-ZrO_2-pH-8 (W. Gao 2019)	Co-precipitation	1:3	T = 523 K P = 30 bar G = 3000 h^{-1}	28.1	59.0	-	[92]
CuZnZr@SBA-15 (Mureddu 2019)	Impregnation-sol-gel auto-combustion	1:3	T = 523 K P = 30 bar G = 6600 h^{-1}	19.2	30.6	376	[111]
CuZnAlZr-FA-650 (Hou 2019)	Co-precipitation	1:3	T =523 K P = 30 bar G = 4000 h^{-1}	25.88	49.17	232	[112]
CuZnCe/TNTs (Shi 2019)	Deposition-precipitation	1:3	T = 533 K P = 30 bar W = 7500 ml g^{-1} h^{-1}	23.3	59.8	298	[113]
M-Cu-ZnO-ZrO_2 (Wang 2019)	Co-precipitation	1:3	T = 493 K P = 30 bar W = 6000 ml g^{-1} h^{-1}	18.9	80.2	297	[88]

Cu-ZnO-ZrO_2-WO_3 (Wang 2019)	Co-precipitation	1:3	T = 513 K P = 30 bar W = 2400 $ml.g^{-1}.h^{-1}$	19.4	47.8	74.6	[114]
Cu-ZnO-ZrO_2-TPABr (Shuyao Chen 2019)	Co-precipitation with VPT	1:3	T = 523 K P = 50 bar W = 3000 $ml.g^{-1}.h^{-1}$	26.7	55.2	-	[115]
CuZnAlZr-USP (Ramli 2018)	Ultrasonic Spray Precipitation	1:3	T = 503 K P = 30 bar G = 10,000 h^{-1}	22.5	22.6	-	[116]
Cu-ZnO-ZrO_2-5 (Dong 2016)	Precipitation-reduction	1:3	T = 543 K P = 50 bar G = 4600 h^{-1}	23.0	56.8	20	[117]
CuO-ZnO-ZrO2 (Angelo 2015)	Microfluidic continuous co-precipitation	1:3	T = 553 K P = 50 bar G = 10,000 h^{-1}	21.0	34.0	486	[118]
Cu/ZnO (Hong Lei 2015)	Hydrothermal	1:3	T = 513 K P = 30 bar W = 12000 $ml.g^{-1}.h^{-1}$	16.5	78.2	550	[119]
Cu-ZnO-ZrO_2 (Angelo 2015)	Co-precipitation	1:3	T = 553 K P = 50 bar G = 10,000 h^{-1}	23	33	331	[89]
Cu-ZrO_2(IV) (Samson 2014)	Citric Precursor method	1:3	T = 533 K P = 80 bar G = 3600 h^{-1}	8.6	92.0	-	[120]
CuZnZr-Ce	Co-precipitation	1:3	T = 503 K	22.8	53.0	102	[121]

(Fujimoto 2014)			P = 50 bar W = 2226 $ml.g^{-1}.h^{-1}$				
Cu-Zn-Zr-OX **(Frusteri 2014)**	Gel-oxalate co-precipitation	1:3	T = 513 K P = 30 bar G = 80,000 h^{-1}	9.0	51.5	1200	[122]
$Cu-Ga_2O_3-ZrO_2$ **(Liu 2006)**	Solid state reaction + deposition-coprecipitation	1:3	T = 523 K P = 20 bar G = 2,500 h^{-1}	13.7	75.6	61	[123]

Hydrothermal synthesis routes have enabled the controlled formation of nanostructured and defect-rich oxides. $Cu/ZnO/Al_2O_3$ catalysts derived from hydrotalcite-like precursors (CZA-LDH) exhibit a high Cu^0 surface area, uniform metal dispersion, and strong Cu-ZnO interactions, resulting in superior methanol productivity and stability (Heng Zhang, 2024 [108]). Likewise, the incorporation of Mg and Zn through hydrothermal co-precipitation promoted synergistic Cu/MgO/ZnO interfaces with abundant oxygen vacancies and basic sites, thereby facilitating CO_2 adsorption and selective hydrogenation to methanol with greater than 99% selectivity (Sharma, 2021[6]). Morphology-controlled hydrothermal synthesis of $Cu/ZnO/ZrO_2$ with flower-like ZnO produced catalysts with the highest oxygen vacancy concentration and enhanced CO_2 activation capability, confirming the role of lattice defects in lowering activation barriers (Hao Chen, 2022 [110]).

Co-precipitation-based methods remain the most versatile for tuning precursor phase chemistry and metal-support interactions. For instance, Cu/Zn/Zr catalysts prepared at optimized pH values (~8) produce hydroxycarbonate precursors such as zincian malachite, which transform into highly dispersed Cu-ZnO phases with intimate contact upon reduction (W. Gao, 2019 [92]). Promoters such as Zr or Ce enhance oxygen mobility and interfacial stability, as observed for Cu/Zn/Zr/Ce and Cu/Zn/Zr/Al systems, improving both methanol yield and long-term stability (Fujimoto, 2014 [121]; Hou, 2019 [112]). Moreover, chemical additives such as formaldehyde pre-activation partially reduce Cu^{2+} to Cu^+ during synthesis, yielding highly dispersed Cu^0 nanoparticles and crystalline ZnO phases that synergistically promote CO_2 conversion (Hou, 2019 [112]).

Advanced precipitation and post-treatment techniques such as ultrasonic spray precipitation (USP), vapor-phase treatment (VPT), and microfluidic co-precipitation offer better control over particle uniformity, scalability, and interfacial control. USP-generated Cu/Zn/Al/Zr catalysts offer enhanced Cu dispersion and surface area but require optimization to balance methanol productivity (Ramli, 2018 [116]). In contrast, vapor-phase-treated Cu/Zn/Zr catalysts (TPABr-assisted VPT) exhibit surface enrichment of Zn and Zr with abundant oxygen vacancies, achieving a methanol selectivity of over 90% and stability of more than 100 hours (Shuyao Chen, 2019 [115]). The microfluidic continuous co-precipitation route reported by Angelo (2015) [118] provides precise control over particle size and precursor formation kinetics, resulting in catalysts with homogeneous distribution, improved Cu surface exposure, and reproducible activity, which outperforms batch-synthesized counterparts.

Support engineering and promoter incorporation also play decisive roles in tailoring surface basicity, reducibility, and interface stability. CeO_2 and TiO_2 nanotubes support the enhancement of CO_2 adsorption and hydrogen spillover by introducing redox-active sites and additional basicity, leading to higher methanol selectivity (Shi, 2019 [113]). The introduction of MoO_3 or WO_3 as secondary promoters further strengthens surface basic sites and CO_2 binding energy, resulting in improved methanol productivity compared to Cr_2O_3-modified analogues in a ternary Cu/Zn/Zr catalyst (Wang, 2019 [114]). Similarly, ZrO_2 acts as a promoter, providing structural stability and oxygen vacancy sites, while Ga_2O_3 or MgO modifies electronic interactions and suppresses side reactions, thereby facilitating the activation and hydrogenation of CO_2 (Liu, 2006 [123]; Sharma, 2021 [6]).

Synthesis-dependent structure-activity relationships emerge across these studies: catalysts prepared via homogeneous or gel-oxalate precipitation routes show improved dispersion, balanced Cu^0/Cu^+ ratios, and superior methanol selectivity (Frusteri, 2014 [122]). The gel-oxalate-derived Cu/Zn/Zr catalyst maintained a stable STY of 1200 $mg_{MeOH}/g_{cat}.hr$ over 200 hr due to its well-defined metal-oxide interfaces and optimal particle size. Similarly, continuous-flow and hydrothermal synthesis consistently outperform batch precipitation and impregnation methods in terms of reproducibility, dispersion, and defect control.

In summary, the literature clearly demonstrates that synthesis routes play a crucial role in determining precursor structure, active site distribution, and, ultimately, catalytic performance. Methods that enable homogeneous precursor formation, control defect density, and optimize

the Cu^0-Cu^+ interfacial balance, such as hydrothermal treatment, vapor-phase treatment, and microfluidic co-precipitation, consistently yield superior catalysts. However, achieving a truly phase-pure precursor while maintaining scalability and reproducibility remains a persistent challenge, leaving significant scope for innovation in catalyst synthesis strategies.

To address this gap, the present thesis adopts hydrothermal and mechanochemical ball milling synthesis strategies. Both approaches yield pure precursors with superior Cu dispersion, interfacial synergy, and durability under reaction conditions. These studies aim to establish a predictive framework for designing high-performance Cu-based catalysts by linking precursor phase chemistry with catalytic performance. The following section introduces machine learning (ML) as a complementary data-driven approach that extends this framework, enabling quantitative prediction and optimization of catalyst behaviour based on fundamental physicochemical descriptors.

2.3.2 Machine learning approaches in catalyst design for CO_2 hydrogenation to methanol

Despite considerable progress in Cu-based catalyst design, achieving high metal dispersion, stable metal-support interfaces, and long-term structural integrity under industrial operating conditions remains a challenge. These challenges highlight the limitations of traditional empirical methods, which rely on iterative, resource-intensive experimentation. This evolving complexity in catalyst development necessitates rational design strategies that transcend trial-and-error approaches. In this context, machine learning (ML) has emerged as a transformative, data-driven tool capable of deciphering multidimensional relationships between catalyst properties, reaction conditions, and performance metrics.

The design and optimization of catalysts for CO_2 hydrogenation to methanol is a multifactorial problem. Catalytic performance depends not only on chemical composition but also on synthesis methods, precursor phases, surface structure, particle morphology, and reactor operating conditions. As the number of variables increases, the experimental search space expands exponentially. Thus, a purely experimental strategy becomes impractical due to time, cost, and scalability constraints. ML provides a data-driven alternative, offers predictive accuracy, pattern recognition, and the potential to accelerate catalyst discovery while significantly reducing experimental burden [13,77].

A reasonably large but heterogeneous dataset on CO_2-to-methanol conversion exists in the literature. However, these datasets often suffer from inconsistencies such as unsystematic variability, missing data, and limited coverage across important reaction variables and catalyst descriptors. Robust data interpretation frameworks are crucial for extracting meaningful correlations from diverse sources. Traditional computational tools, such as regression analysis or basic statistical models, fall short in handling the nonlinear, multi-variable interdependencies that govern catalytic systems. Moreover, these approaches frequently suffer from overfitting, computational complexity, or limited generalizability [13,76].

Several attempts have been made to apply ML techniques to catalytic systems in recent years. For example, Hossain et al. [124] and Ayodele et al. [125] applied artificial neural networks (ANNs) to model syngas production from methane reforming over Ni- and Co-based catalysts, respectively. Their work demonstrated the capability of an ANN to correlate operational variables with product distributions. Later, Smith et al. [76] proposed a generalized ML framework to predict catalytic performance by identifying descriptors correlating with experimental outcomes, highlighting ML's role in guiding experimental planning and formulation screening.

A more relevant study by Perez-Ramirez [126] and coworkers explored the prediction of methanol space-time yield (STY) using a comprehensive database of 1425 experimental data from the CO_2 hydrogenation literature. They used advanced ML models, such as Extreme Gradient Boosting (XGB), Random Forest (RF), and Gradient Boosting Decision Trees (GBDT), to train predictive algorithms. However, their model's applicability was limited to STY prediction and failed to maintain prediction accuracy when validated on new experimental data. This limitation underscores a key shortcoming of most data-driven models: they often require retraining on additional datasets and lack generalizability beyond their training scope.

Another work by Bahri et al. [127] presented a multi-level hypothesis-based model using only a limited set of catalyst characterization parameters and reaction conditions (temperature, pressure) [17]. Although the model attempted to improve yield predictions through linear regression, it overlooked key variables such as feed ratios, metal loadings, and surface properties, making the output incomplete and prone to statistical errors. While conceptually novel, this approach risks excluding high-performing catalysts that fall outside predefined statistical clusters, limiting its applicability for comprehensive catalyst screening.

To overcome these limitations, recent advances in ML-assisted catalyst design have emphasized the importance of thorough data preprocessing, dimensionality reduction, and robust model validation. Techniques like principal component analysis (PCA) often reduce redundancy and ensure that input features are orthogonal and informative. Cross-validation methods, such as k-fold validation, assess model generalizability and help prevent overfitting. Furthermore, integrating domain knowledge, such as mechanistic insights and structure-property relationships, into ML pipelines has significantly enhanced model interpretability and reliability [13].

These modern ML frameworks are increasingly capable of predicting multiple catalytic outputs, such as CO_2 conversion, methanol selectivity, CO selectivity, and methanol yield-using a single unified model. Such multi-output modeling offers a more realistic representation of catalytic behaviour under variable process conditions. Feature selection techniques are also applied to identify the most influential catalyst descriptors, allowing researchers to focus on tuning critical parameters during catalyst design [13].

In summary, machine learning offers a powerful complement to experimental methodologies in catalyst research. When appropriately designed and validated, ML models can accelerate the discovery of high-performance Cu-based catalysts for CO_2 hydrogenation, provide valuable insights into key structure-performance relationships, and enable more targeted, cost-effective experimental strategies. However, their predictive power is greatly enhanced with a clear mechanistic understanding of reaction pathways, active site structures, and surface chemistry. Integrating ML with mechanistic insights derived from spectroscopy, microscopy, and computational modeling ensures that predictions are statistically robust and chemically meaningful. The following section further discusses the fundamental reaction pathways and surface mechanisms governing CO_2 hydrogenation to methanol, thereby strengthening this understanding.

2.3.3 Reaction Pathways and Mechanisms in CO_2 Hydrogenation to Methanol

The catalytic hydrogenation of CO_2 to methanol is a complex reaction system involving multiple competitive and parallel pathways, diverse intermediate species, and intricate surface interactions. Investigating the fundamental reaction mechanism is essential for rational catalyst design and kinetic modeling, particularly for Cu-based systems, where both metallic Cu^0 and partially oxidized Cu^+ species contribute to activity.

2.3.3.1 Nature of Active Sites

Despite more than a century of research, the precise nature of the active sites responsible for catalysis remains debatable [128,129]. Several studies have proposed that Cu^+ species serve as the primary active centers for methanol formation, while others correlated catalytic activity more directly with surface metallic (Cu^0) [130]. Investigations on single-crystal surfaces, such as Cu (100), Cu (110), and polycrystalline films predominantly exposing the Cu (111) facet, have provided compelling evidence that metallic Cu plays a crucial role in facilitating hydrogen activation and hydrogenation reactions [71].

Accordingly, most kinetic models assume Cu (111) as the representative reactive surface, owing to its thermodynamic stability and preferential exposure under reducing conditions. Moreover, experimental kinetic rates obtained on polycrystalline copper, primarily characterized by the Cu (111) surface, also show close agreement with those of industrial Cu/ZnO catalysts [71].

However, this view has been challenged by reports describing the coexistence of Cu^0 and Cu^+. Chinchen et al. [130] revealed that optimal catalytic performance arises from synergistic Cu^0/Cu^+ interfacial sites, which enable CO_2 adsorption and activation on Cu^+ while promoting hydrogen dissociation and hydrogenation on Cu^0. This synergistic redox behaviour enhances the formation of formate and methoxy intermediates, which are central to methanol synthesis. To clarify the role of these intermediates and their site-specific formation pathways, the key surface intermediates and their associated active sites are listed in **Table 2.2**.

Table 2.2. *Key surface intermediates and their associated active sites in the CO_2 hydrogenation to methanol process.*

Intermediate Species	Role in Mechanism	Associated Active Site/Catalyst Feature
CO_2 (adsorbed)	Initial adsorption and activation	Cu^+ sites, Cu-ZnO interface, oxygen vacancies
HCOO (Formate)*	Key intermediate in the formate pathway	Stabilized on Cu^+ and Cu-ZnO interface
H_2COO/HCOOH	Hydrogenated intermediates (route-dependent)	Cu^+/basic oxide supports (e.g., ZrO_2, MgO)
CH_2O (Formaldehyde)*	Common intermediate in multiple pathways	Cu^0 surfaces (e.g., Cu(111))
CH_3O (Methoxy)*	Precursor to methanol	Cu^0, Cu^0-ZnO interface

CH_3OH	Final product	Desorbs from Cu^0 or Cu^+ sites
CO*	Formed via RWGS; may re-enter the methanol route	Cu^0 surface; competitive pathway
H_2O*	Co-product; influences surface coverage	Desorbs or interacts with support (e.g., Al_2O_3, ZrO_2)

In addition to the oxidation state, the metal-support interface, particularly Cu-ZnO, has also been identified as a key structural motif for methanol synthesis. Studies by Behrens et al. using operando spectroscopy and high-resolution microscopy revealed that a strong Cu-ZnO interaction, especially in catalysts derived from zincian malachite precursors, generates highly dispersed Cu sites and stabilizes reaction intermediates through oxygen vacancies and dynamic ZnO species [25,131].

Furthermore, modern in-situ and operando techniques, such as X-ray absorption spectroscopy (XAS), ambient-pressure XPS, DRIFTS, and HAADF-STEM, have provided deeper insights into the dynamic nature of active sites. These studies demonstrate that the surface structure of Cu undergoes changes under reaction conditions, and the active phase may not correspond to a static oxidation state, but rather to a dynamic ensemble of species maintained by the chemical potential of the gas-phase reactants [26,131–133].

Recent computational studies, particularly DFT simulations, support this evolving perspective, showing that formate binding is generally more favourable on partially oxidized Cu^+ sites, whereas methoxy desorption is energetically favoured on the metallic Cu^0 surface. This dual-site functionality underpins the high activity of industrial Cu-ZnO-based catalysts [25,71,73,74,88,105].

In summary, while the exact nature of the active site is still debatable, the current agreement points toward a multifunctional active environment involving:

- Metallic Cu^0 surfaces (primarily Cu (111)),
- Cu^0/Cu^+ redox pairs, and
- Cu-ZnO or Cu-oxide interfaces enriched with oxygen vacancies and basic sites.

This ensemble collectively governs CO_2 adsorption, activation, and subsequent hydrogenation steps, stabilizing key intermediates such as formate (HCOO*) and methoxy (CH_3O*) [29,73,74,105,134–136].

Various investigations have sought to decode the mechanism of CO_2 hydrogenation on heterogeneous Cu-based catalysts; however, a universally accepted pathway remains elusive due to the complexity of parallel and competing reactions. The overall reaction for methanol formation:

$$CO_2 + 3H_2 \rightleftharpoons CH_3OH + H_2O, \quad \Delta H_{25^\circ C} = -49.5\ kJmol^{-1} \tag{2.1}$$

is exothermic and is accompanied by competing reactions such as the reverse water-gas shift (RWGS) and CO hydrogenation, which introduce mechanistic complexity. Consequently, methanol synthesis may proceed via three interconnected mechanistic routes:

1. Direct CO_2 hydrogenation to methanol (via surface-bound intermediates),
2. RWGS followed by CO hydrogenation, and
3. Direct CO hydrogenation (especially when CO is formed in situ).

The formate route is most widely accepted among proposed pathways for CO_2 hydrogenation to methanol. In this mechanism, CO_2 is first activated (often at Cu^+ or interfacial sites) to form a surface formate (HCOO*), which then hydrogenates through intermediates such as formaldehyde (CH_2O*) and methoxy (CH_3O*), ultimately yielding methanol. Experimental studies, such as DRIFTS and TPD, have consistently confirmed the presence of formate and methoxy species, underscoring their mechanistic relevance [110,133,135,137].

2.3.3.2 Mechanistic Overview: Competing Pathways in CO_2 Hydrogenation

Complementing this general understanding, Yang et al. (2010) [138] combined experimental and theoretical studies over Cu (111), Cu nanoclusters, and Cu/ZnO (0001) surfaces, demonstrating that Cu_{29} nanoclusters supported on ZnO (0001) exhibited higher activity than the planar Cu (111) surface. DFT calculations revealed that the reaction proceeds via a formate pathway (HCOO* → H_2COO* → H_2CO* → H_3CO*), with the hydrogenation of formate (HCOO*) and dioxymethylene (H_2COO*) identified as the rate-determining step. They also observed that CO formation occurs via RWGS, noting that on metallic Cu, CO hydrogenation to methanol is kinetically unfavourable due to unstable formyl (HCO*) species, suggesting that suitable promoters are required to stabilize this intermediate.

Grabow and Mavrikakis (2011) [71] extended this understanding through a comprehensive microkinetic model coupled with DFT calculations over the Cu (111) surface. They confirmed

that formate forms directly from CO_2 without the involvement of carbonate (CO_3*) intermediates, and that methanol proceeds through HCOO*, HCOOH*, CH_3O_2*, CH_2O*, and CH_3O* species. CO generated from RWGS was shown to further hydrogenate to methanol through the formyl (HCO*) intermediate and CH_2O*, CH_3O*, and CH_3OH* species. The rate-limiting step for both formate and CO pathways is methoxy (CH_3O*) formation or hydrogenation, depending on the COR ratios in the feed.

- **Role of Cu Surface, Oxidation State, and the Influence of Water**

Zhao et al. (2011) [73] investigated the methanol synthesis pathway using periodic DFT calculations on Cu (111) to identify key elementary steps via the dimer method. Their study revealed that direct hydrogenation of formate species is kinetically unfavourable due to high activation barriers. However, in the presence of water, CO_2 hydrogenation proceeds more favourably through a distinct water-assisted pathway involving intermediates such as COOH*, COH*, COHOH*, HCOH*, H_2COH*, and H_3COH*, facilitated by a unique hydrogen transfer mechanism. Water thus acts as a co-catalyst, lowering the activation barrier and providing new insights into reaction mechanisms beyond those observed spectroscopically in surface species.

Behrens et al. (2012) [25] laid foundational insights by employing advanced operando characterization techniques and DFT calculations to investigate the active sites on industrial $Cu/ZnO/Al_2O_3$ catalysts. They established that methanol formation occurs at the Cu-ZnO interface, where metallic Cu facilitates H_2 dissociation and ZnO stabilizes key intermediates such as formate and methoxy species. They highlighted the dynamic redox interplay between Cu^o/Cu^+ as central to CO_2 activation and selective methanol production.

- **Interface Engineering and Support-Driven Pathways**

Studt et al. (2015) [64] further advanced the mechanistic understanding by combining DFT calculations and microkinetic modeling to investigate both CO_2 and CO hydrogenation pathways over various Cu surfaces. They concluded that CO_2 hydrogenation predominantly proceeds via the formate pathway, involving intermediates such as HCOO*, H_2COO*, CH_2O*, and CH_3O*, while the CO route follows an efficient path through the formyl (HCO*) intermediate, previously described by Grabow et al. (2011) [71]. Methoxy (CH_3O*) was confirmed as the common intermediate in both routes, with its hydrogenation being rate-limiting under typical industrial conditions. The Cu-ZnO interface was reaffirmed as the active

center for CO_2 activation, and their model demonstrated that direct CO hydrogenation (originating from CO formed via RWGS) becomes significant at high CO partial pressures, effectively bridging both carbon-source pathways.

Kattel et al. (2016) [105] investigated how oxide supports, such as ZrO_2 and TiO_2, influence the reaction pathway. Using a combination of density functional theory (DFT), kinetic Monte Carlo (KMC) simulations, in-situ DRIFTS, and steady-state reactor studies, they found that these oxide supports favour a RWGS + CO hydrogenation mechanism over the direct formate route. CO_2 adsorption occurs at the Cu-ZrO_2 interface, forming bent CO_2 and carboxyl (HOCO*) intermediates, yielding CO that hydrogenates to methoxy and methanol. Although formate species are spectroscopically abundant, KMC simulations indicate that they act mainly as spectators due to their thermodynamic stability. ZrO_2 exhibited superior activity compared to TiO_2, as reduced Zr^{3+} centers optimized the binding of CO_2*, CO*, and HCO* species. This work highlights how combining theory and experiments helps clarify reaction mechanisms and guide better catalyst design.

Building on this, Wang and Kattel (2019) [88] extended these insights to ternary Cu-ZnO-ZrO_2 (CZZ) catalytic systems. In-situ DRIFTS and DFT calculations confirmed that the reaction proceeds via the formate pathway, with ZnO-ZrO_2 interfaces acting as key active sites for CO_2 adsorption and intermediate stabilization. Compared to binary systems, ZnO-ZrO_2 showed superior ability for activating CO_2, while Cu facilitated H_2 dissociation. This study highlights the importance of optimizing the interactions between ZnO and ZrO_2 for enhancing catalytic activity.

Studt et al. (2019) [139] conducted a DFT study using a Cu nanowire model supported on tetragonal ZrO_2(101), representing the Cu-Zr interface. Adsorption-energy calculations indicated a stronger binding of key intermediates (HCOO*, H_2COO*, H_2COOH*, and H_3CO*) at Zr-supported Cu sites compared to unsupported Cu (111) and Cu (211) surfaces, underscoring the beneficial role of metal-oxide contact. The adsorption energies were found to scale linearly with those of O and OH species, consistent with general trends observed for transition-metal catalysts.

- **Multi-Component and Synergistic Catalysts**

The mechanistic complexity increases for multi-component systems that integrate multiple oxides. Dharmalingam et al. (2023) [29] investigated Cu/ZnO/ZrO_2/Al_2O_3 catalysts using DFT-based microkinetic modeling and in-situ DRIFTS. Their reaction pathway analysis revealed that methanol formation proceeds mainly via the formate pathway near the reactor inlet, whereas the CO hydrogenation via the carboxyl route becomes more significant in downstream regions. Although DFT results suggested CO_2 adsorption at the Cu-ZrO_2 interface, the validated microkinetic model identified the Cu-ZnO interface as the primary reaction center in driving methanol synthesis. This cooperative interplay between interfaces enhances intermediate stabilization and hydrogenation kinetics, explaining the superior performance of these multi-component systems for future catalyst design and process optimization.

Fernandez-Villanueva et al. (2024) [136] investigated Cu-MgO-Al_2O_3 catalysts, highlighting the synergistic effect between Cu^+ species and water. The combined experimental and theoretical approaches revealed that the coexistence of Cu^+/Cu^0, in conjunction with water, facilitated the formation of surface formate and methoxy intermediates, thereby enhancing methanol selectivity. This work reiterated the importance of dynamic redox behaviour and surface hydroxyl groups in modulating CO_2 activation, reaction intermediates, and kinetics.

Liu et al. (2025) [135] provided further mechanistic insights into Zr-modified Cu/ZnO/Al_2O_3 catalysts. Both experimental and DFT calculations confirmed that Zr incorporation enhances Cu dispersion, strengthens CO_2 adsorption, and lowers the activation barrier for methanol synthesis. The improved performance arises from a greater abundance of oxygen vacancies and stabilized formate and methoxy intermediates, showcasing the benefits of multi-component systems in tailoring reaction energetics and interfacial chemistry.

- **Mechanistic synthesis and transition to kinetic modeling**

Cumulative evidence from both early and recent studies consistently identifies the formate (HCOO*) pathway as the dominant route for methanol synthesis over Cu-based catalysts, with methoxy (CH_3O*) hydrogenation often serving as a key rate-limiting step. However, complementary roles of CO-assisted hydrogenation, water-mediated pathways, and multi-component synergistic effects demonstrate that the reaction mechanism is susceptible to catalyst composition, structure, and operating conditions [71,140,141].

The reaction mechanism and the active-site chemistry are intrinsically coupled [25,64,142], requiring a holistic approach that integrates the electronic structure of the catalyst surface, the nature of the metal-support interface, and the dynamic behaviour of intermediates under reaction conditions. Such an integrated perspective is crucial for rational catalyst design, with an optimized Cu^0/Cu^+ ratio, tunable oxygen vacancies, and tailored surface properties, to maximize methanol selectivity and yield [140,141].

Building on this reaction mechanism foundation, kinetic modeling provides a quantitative framework to link active-site chemistry and reaction pathways to measurable reaction rates. In methanol synthesis, identifying the dominant carbon source (CO_2 vs. CO) and accounting for competing pathways such as RWGS are essential for accurate rate expressions. However, despite these mechanistic insights, significant uncertainty still surrounds the true origin of the carbon atom in methanol. Determining whether methanol primarily forms via direct CO_2 hydrogenation, through CO formed by the RWGS reaction, or by a combination of both, remains a central question that kinetic modeling seeks to resolve [143–147].

The following section discusses the evolution of kinetic models, including the Langmuir-Hinshelwood-Hougen-Watson (LHHW) and power-law formulations, examines their underlying assumptions, and explores their applicability to various catalyst systems and operating conditions.

2.3.4 Kinetic Modeling

Many early kinetic models considered CO hydrogenation as the primary pathway to methanol, while CO_2 was considered kinetically inert or only indirectly involved via RWGS (e.g., Klier et al., 1982 [148]). These models are generally designed based on experimental data obtained at CO-rich feed compositions, where CO_2 hydrogenation was found to be negligible. However, isotopic labeling experiments and studies using high-purity CO_2 feeds revealed that, under typical industrial feed gas ratios, methanol formation mainly occurs via CO_2 hydrogenation (Graaf et al., 1988 [149]; Van den Bussche & Froment, 1996 [70]; Behrens et al., 2012 [25]).

The roles of CO and CO_2 in methanol formation are strongly dependent on the feed composition, catalyst formulation, and operating conditions. Kunkes et al. (2014) [64] reported that ZnO and ZrO_2 promoted Cu catalysts favor CO_2 hydrogenation even in the presence of CO. In contrast, Villa et al. (1995) [150] found measurable CO hydrogenation rates under CO-

rich conditions. Similarly, the inevitable formation of CO (via RWGS reaction) has been identified as a significantly competitive reaction in CO_2-rich feeds, influencing both CO selectivity and methanol formation rates (Askgaard et al., 1995 [151]; Grabow & Mavrikakis, 2011 [71]).

Due to this ongoing uncertainty, numerous kinetic models have been developed based on different assumptions regarding the origin of carbon, mechanistic pathways, and the inclusion/exclusion of competitive reversible reactions, such as RWGS. These models can be broadly classified into four categories [143] **(Figure 2.6)**: Category I considers both CO_2 and CO as carbon sources and explicitly includes RWGS (Graaf et al., 1988 [149]; Seidel et al., 2018 [152]); Category II models include both hydrogenation routes but neglect RWGS (Klier et al., 1982 [148]); Category III focuses solely on CO_2 hydrogenation (Askgaard et al., 1995 [151]; Skrzypek et al., 1991 [153]; Van den Bussche & Froment, 1996 [70]); whereas Category IV synthesize methanol exclusively from CO hydrogenation (Villa et al., 1985 [150]).

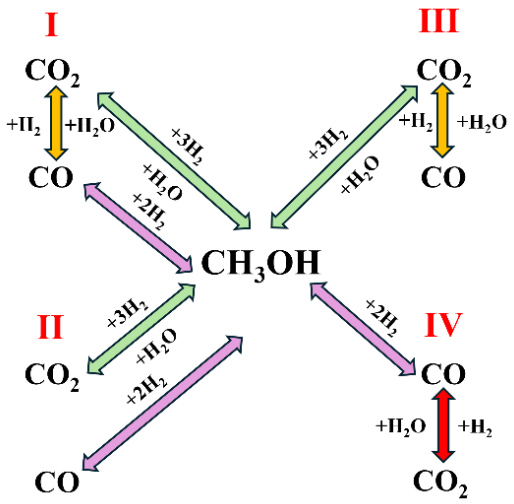


Figure 2.6. *Illustration of the four elementary methanol synthesis pathways (I-IV), showing the hydrogenation of CO_2 and CO and the reverse transformations among these species.*

Kinetic modeling of CO_2 hydrogenation to methanol has evolved through nearly four decades of research, reflecting both advances in mechanistic understanding and the growing complexity of catalytic systems. Despite differences in mathematical treatment, most studies converge on the Langmuir-Hinshelwood-Hougen-Watson (LHHW) framework, which provides a physically meaningful description of surface adsorption, surface reaction, and desorption steps over Cu-based catalysts. The gradual progression from early single-site to multi-site and

microkinetic models illustrates an apparent effort to reconcile laboratory-scale observations with industrially relevant conditions.

Table 2.3 provides an outline of key kinetic studies reported in the literature for CO_2 hydrogenation to methanol over Cu-based catalysts, summarizing their modeling approaches, underlying assumptions, and mechanistic treatment. The following section systematically evaluates these model categories, discusses their theoretical foundations, and assesses their applicability to modern Cu-based catalytic systems.

Table 2.3. Overview of literature-reported kinetic models describing CO_2 hydrogenation to methanol on Cu-based catalytic systems.

Reference	Principal Catalyst and Mechanism	Kinetic Expression ($CO_2 \rightarrow CH_3OH$)	Carbon Source
Graaf et al. [149]	$Cu/ZnO/Al_2O_3$ (Dual Site)	$\frac{kK_{CO_2}\left(p_{CO_2}p_{H_2}^{3/2}-\frac{p_{CH_3OH}p_{H_2O}}{p_{H_2}^{3/2}K_{eq1}}\right)}{(1+K_{CO}p_{CO}+K_{CO_2}p_{CO_2})\left[p_{H_2}^{1/2}+\frac{K_{H_2O}}{K_{H_2}^{1/2}}p_{H_2O}\right]}$	CO_2 dominant
Bussche & Froment [70]	$Cu/ZnO/Al_2O_3$ (Single Site)	$\frac{kK_{H_2}p_{CO_2}p_{H_2}\left[1-\left(\frac{1}{K_{eq1}}\right)\left(\frac{p_{CH_3OH}p_{H_2O}}{p_{CO_2}p_{H_2}^3}\right)\right]}{\left[\left(1+\left(\frac{K_{H_2O}}{K_8K_9K_{H_2}}\right)\left(\frac{p_{H_2O}}{p_{H_2}}\right)+\sqrt{K_{H_2}p_{H_2}}+K_{H_2O}p_{H_2O}\right)^3\right]}$	CO_2 dominant
Kubota et al. [154]	$Cu/ZnO/Al_2O_3/ZrO_2$	LHHW with CO & CO_2 on distinct Cu sites; ~48 RDS	CO & CO_2 mixed
Park et al. [155]	$Cu/ZnO/Al_2O_3$ (Triple Site)	$\frac{kK_{CO_2}\left(f_{CO_2}f_{H_2}^{3/2}-\frac{f_{CH_3OH}f_{H_2O}}{f_{H_2}^{3/2}K_{P,C}}\right)}{(1+K_{CO_2}f_{CO_2})\left[1+K_{H_2}^{1/2}f_{H_2}^{1/2}+K_{H_2O}f_{H_2O}\right]}$	CO & CO_2 mixed
Slotboom et al. [143]	$Cu/ZnO/Al_2O_3$ (Triple Site)	$\frac{k_{CO_2}f_{CO_2}f_{H_2}^{3/2}\left[1-\left(\frac{1}{K_{p_{CO_2}}^{\circ}(T)}\right)\left(\frac{f_{CH_3OH}f_{H_2O}}{f_{CO_2}f_{H_2}^3}\right)\right]}{\left[\left(k_{H_2}f_{H_2}^{1/2}+k_{H_2O/9}f_{H_2O}+f_{CH_3OH}\right)^2\right]}$	CO & CO_2 mixed

Assaf et al. [137]	$Cu/ZnO/ZrO_2$ (Dual Site)	$\frac{k_1\left(pCO_2 p_{H_2}^{3/2} - \frac{p_{CH_3OH} p_{H_2O}}{p_{H_2}^{3/2} K_{eq1}}\right)}{(1 + K_{CO} p_{CO} + K_{CO_2} p_{CO_2})\left[p_{H_2}^{1/2} + \frac{K_{H_2O}}{K_{H_2}^{1/2}} p_{H_2O}\right]}$	CO_2 dominant
Portha et al. [145]	$Cu/ZnO/Al_2O_3$ (Dual Site)	$\frac{k_3 b_{CO_2}\left(P_{CO_2} P_{H_2}^{3/2} - \frac{P_{CH_3OH} P_{H_2O}}{P_{H_2}^{3/2} K_3}\right)}{(1 + b_{CO} P_{CO} + b_{CO_2} P_{CO_2})\left[P_{H_2}^{1/2} + \frac{b_{H_2O}}{b_{H_2}^{1/2}} P_{H_2O}\right]}$	CO_2 dominant
Bisotti et al. [146]	$Cu/ZnO/Al_2O_3$ (Dual Site)	$\frac{k_1 K_{CO_2}\left(f_{CO_2} f_{H_2}^{3/2} - \frac{f_{CH_3OH} f_{H_2O}}{f_{H_2}^{3/2} K_{eqCO_2}}\right)}{(1 + K_{CO} f_{CO} + K_{CO_2} f_{CO_2})\left[f_{H_2}^{1/2} + \frac{K_{H_2O}}{K_{H_2}^{1/2}} f_{H_2O}\right]}$	CO & CO_2 mixed
Angelo et al. [144]	$Cu/CeO_2/ZrO_2$ (Dual Site)	$\frac{k_1 b_{CO_2}\left(pCO_2 p_{H_2}^{1.5} - \frac{p_{CH_3OH} p_{H_2O}}{p_{H_2}^{1.5} K_{eq1}}\right)}{(1 + b_{CO} p_{CO} + b_{CO_2} p_{CO_2})\left[p_{H_2}^{0.5} + \frac{b_{H_2O}}{\sqrt{b_{H_2}}} p_{H_2O}\right]}$	CO & CO_2 mixed
Varghese et al. [29]	$Cu/ZnO/ZrO_2/Al_2O_3$	DFT-based microkinetic model; no single closed-form	CO_2 dominant
Kouzehli et al. [156]	$Cu/ZnO/Al_2O_3$ (Dual Site)	$\frac{k_{CH_3OH} b_{CO_2}\left(P_{CO_2} P_{H_2} - \frac{P_{CH_3OH} P_{H_2O}}{P_{H_2}^2 K_{eqCH_3OH}}\right)}{\left(1 + b_{CO_2} P_{CO_2} + \sqrt{b_{H_2} P_{H_2}} + b_{CO} P_{CO} + b_{H_2O} P_{H_2O}\right)^2}$	CO & CO_2 mixed
Varghese et al. [28]	Cu/ZnO_x	Facet-dependent LHHW with parameters varying by facet	CO & CO_2 mixed

The foundational models by Graaf et al. (1988) [149] and Vanden Bussche and Froment (1996) [70] form the cornerstone of modern kinetic descriptions. Graaf et al. proposed a dual-site LHHW model in which CO_2 and CO competitively adsorb on one type of site while H_2 and H_2O compete on another. The model assumes dissociative adsorption of hydrogen and neglects methanol adsorption, successfully describing both CO_2 and CO hydrogenation routes as well

as their inhibition by products. It captured the thermodynamic coupling between methanol synthesis and the reverse water-gas shift (RWGS) reaction and has since served as a benchmark for numerous later studies. In contrast, Vanden Bussche and Froment (1996) developed a single-site LHHW model assuming CO_2 as the only carbon source, with methanol formed exclusively via CO_2 hydrogenation and RWGS treated as a side reaction. This simplification provided excellent predictive stability and thermodynamic consistency, making it highly applicable for process-scale reactor design, particularly when CO_2-rich feeds are predominant.

Following these seminal contributions, later researchers sought to refine the mechanistic picture and expand model applicability to wider operating windows, promoting catalyst systems. Kubota et al. (2001) [154] derived kinetic equations for Cu/ZnO-based catalysts by integrating mechanistic hypotheses with extensive plant-scale data, demonstrating that such rate laws could reliably guide reactor design and scale-up. These efforts reinforced the practical utility of LHHW-type kinetics when parameterized correctly in industrial conditions.

Building upon the dual-site foundation, Park et al. (2014) [155] introduced a three-site adsorption mechanism, distinguishing between sites for CO_2, CO, and hydrogen species. This formulation allowed a more detailed representation of parallel reaction channels and better captured product selectivity trends. Seidel et al. [152] later expanded this mechanistic framework, but the increased complexity prompted Slotboom et al. (2020) [143] to simplify it substantially, reducing parameter redundancy while maintaining fidelity to the experimental data. Their streamlined model reverted to a CO_2-dominant pathway but retained flexibility to describe the RWGS reaction. This refinement marked an important balance between mechanistic realism and practical regression capability.

Complementary studies have explored how promoters and support influence apparent kinetics and mechanistic routes. Assaf et al. (2021) [137] proposed a dual-site LHHW model for $Cu/ZnO/ZrO_2$ catalysts, emphasizing how ZrO_2 polymorphism alters adsorption and activation behaviour. Their model incorporated both CO_2 and CO routes and quantitatively linked structural promotion to methanol selectivity. Similarly, Portha et al. (2017) [145] applied the Graaf framework to $Cu/ZnO/Al_2O_3$ and $Cu/ZnO/ZrO_2$ catalysts under high-pressure CO_2 hydrogenation. They confirmed that ZrO_2-enhanced catalysts yield improved methanol selectivity due to stronger CO_2 adsorption and higher interfacial stability, demonstrating that support composition must be explicitly considered in kinetic parameterization.

At the industrial scale, Bisotti et al. (2021) [146] extended LHHW-type models into empirical reactor-level correlations, using plant data to predict conversion and selectivity under complex recycle conditions. Although largely phenomenological, such correlations emphasize predictive control and process optimization rather than microkinetic interpretation. In a similar effort toward thermodynamic consistency, Kouzehli et al. (2024) [156] developed a robust LHHW expression that incorporates the competitive adsorption of CO_2, H_2, and H_2O. Their model reproduced experimental data with high accuracy and identified surface formate species as inhibitory intermediates, in line with spectroscopic evidence.

The role of promoter oxides and active interfaces has become increasingly central in recent kinetic analyses. Angelo et al. (2022) [144] systematically compared single-, dual-, and three-site LHHW models for $CuO/CeO_2/ZrO_2$ mixed oxide catalysts, revealing that oxygen vacancies and Ce/Zr synergy significantly modify adsorption energetics and the rate-determining steps. Their work demonstrated that kinetic constants extracted from classical models must be reinterpreted when redox-active supports participate in the activation of CO_2. Similarly, Assaf's and Portha's findings corroborate that the inclusion of promoter-dependent terms or additional active-site types is necessary to represent the kinetics of these multifunctional systems accurately.

With the increasing use of computational insights, hybrid models have begun to bridge macroscopic kinetics with atomic-scale mechanisms. Varghese et al. (2023) [29] integrated DFT-based microkinetic modeling with reactor data for $Cu/ZnO/ZrO_2/Al_2O_3$ catalysts, explicitly accounting for the interfacial contributions of Cu-ZnO and Cu-ZrO_2. Their results showed that methanol primarily forms via the formate pathway near the reactor inlet, while CO-assisted hydrogenation gains significance downstream, explaining the composition-dependent switching between routes. A subsequent study by the same group introduced facet-dependent LHHW formulations, which map surface-specific energetics (Cu (111), steps, and nanoclusters) into kinetic parameters, thereby connecting catalyst morphology to macroscopic rates and selectivity.

The collective progression of kinetic models, from the dual-site formulation of Graaf to modern hybrid microkinetic and DFT-assisted approaches, reveals a consistent trend: methanol formation cannot be universally described by a single mechanistic route or carbon-source assumption. Under CO_2-rich feeds, methanol synthesis proceeds primarily through CO_2

hydrogenation via formate and methoxy intermediates. In contrast, at higher temperatures or CO-rich conditions, the RWGS reaction, followed by CO hydrogenation, becomes increasingly significant. The apparent kinetics are thus strongly governed by feed composition, catalyst morphology, active-site distribution, and promoter chemistry, all of which reshape adsorption equilibria and reaction energetics.

Over time, kinetic modeling of CO_2 hydrogenation to methanol has evolved from empirical rate equations toward mechanistically informed, thermodynamically consistent frameworks that bridge surface chemistry and reactor-scale behaviour. Modern LHHW-based schemes now capture the interplay between Cu^0/Cu^+ redox sites, metal-oxide interfaces, and key reaction intermediates, offering a more unified understanding of the process. Yet, despite these advances, no single kinetic model can fully represent all catalyst systems or operating regimes, highlighting the necessity for system-specific parameterization that reflects both structural characteristics and process conditions.

Ultimately, mechanistic and kinetic insights achieve practical value only when coupled with reactor engineering strategies that can translate molecular-scale understanding into process-scale performance. The design of suitable reactor systems, capable of managing the strong exothermicity, equilibrium constraints, and catalyst stability issues inherent to CO_2 hydrogenation, is therefore pivotal to realizing efficient and scalable methanol synthesis. These reactor considerations are discussed in the following section.

2.3.5 Reactor Aspects

The translation of molecular-level insights into process-scale performance is ultimately governed by the choice and design of reactors [32,70]. Methanol synthesis from CO_2/H_2 mixtures poses distinct challenges due to the strongly exothermic nature of the reaction ($\Delta H_{25°C} \approx$ -90.7 kJ/mol) coupled with thermodynamic equilibrium constraints [3]. Unlike combustion reactions, which benefit from high temperatures, methanol synthesis requires moderate temperatures (220-280 ^oC) and elevated pressures (50-100 bar) to achieve appreciable yields [4,32,68,157]. This necessitates reactor concepts that can simultaneously (i) remove the substantial heat of reaction, (ii) prevent catalyst deactivation by sintering or carbon deposition, (iii) recycle unreacted gases, and (iv) maintain high per-pass and overall conversions [8,32,68].

Historically, methanol was produced from syngas with a high CO content; however, the increasing emphasis on CO_2 utilization has led to feedstocks with higher CO_2/H_2 ratios [4]. This shift accentuates equilibrium limitations and increases the importance of reactor engineering. Industrially, three main reactor concepts have been commercialized: tubular boiling-water reactors, quench reactors, and multi-bed adiabatic reactors with interstage cooling [8,22].

1. **Tubular boiling-water reactors (BWRs)**

One of the earliest and most widely deployed designs, the Lurgi process employs tubular reactors containing catalyst-filled tubes immersed in a boiling water jacket. Heat released from methanol synthesis is absorbed by water at saturation conditions, providing nearly isothermal operation. The boiling water also serves as a utility to generate medium-pressure steam, enhancing process integration. By adjusting the pressure of the boiling water, stable operating temperatures are maintained across long campaigns, minimizing the risk of catalyst overheating and sintering.

The BWR offers excellent thermal control and high productivity; however, its complexity lies in the large number of tubes (often exceeding 10,000) and the substantial investment required for pressure-resistant shells and heat exchange infrastructure. Mechanical stresses resulting from differential thermal expansion, fouling, and pressure drop issues further increase capital and maintenance costs. Despite these challenges, BWRs remain the benchmark for large-scale methanol synthesis owing to their robustness and proven lifetime of 4-6 years for $Cu/ZnO/Al_2O_3$ catalysts [8,22,63,158].

2. **Quench reactors**

ICI (now Johnson Matthey) developed a quench reactor design to simplify construction, where the reaction proceeds in a series of adiabatic catalyst beds separated by cold gas injection. Each bed operates adiabatically, with the hot effluent cooled by mixing with fresh or recycled cold feed before entering the next bed. This avoids the need for complex tube bundles and jackets.

While easier to construct and operate, quench reactors have inherent disadvantages. The injection of quench gas dilutes the reactant mixture, lowering the driving force for reaction and reducing per-pass conversion. Additionally, incomplete utilization of the catalyst bed may occur due to localized hot spots. Such drawbacks reduce overall efficiency for CO_2

hydrogenation, where equilibrium conversion is already limited. Consequently, quench reactors are less common today in new installations but remain in operation in older plants [8,22,63].

3. Multi-bed adiabatic reactors with interstage cooling

The Kellogg and Haldor-Topsoe processes adopted an intermediate approach: multi-bed adiabatic reactors with external heat exchangers between catalyst beds. Here, the reaction mixture is passed through one adiabatic bed, cooled in an intercooler, and then fed to the next bed. This design reduces gas dilution compared to quench reactors while maintaining better temperature control than a single adiabatic unit.

Mechanical innovations, such as spherical reactor vessels, have been employed to minimize stress at high pressures and reduce pressure drop across beds. These reactors strike a balance between heat removal, catalyst utilization, and operating simplicity, making them widely adopted in modern methanol plants [8,22,63].

4. Recycle strategies and equilibrium control

Regardless of reactor type, per-pass CO_2 conversion is typically limited (<20% under standard conditions) due to equilibrium. Industrial practice, therefore, relies on high recycle ratios, with unconverted CO_2, H_2, and CO separated from the crude methanol product and returned to the reactor inlet. This recycle loop boosts overall yield and stabilizes reactor operation by diluting the reactant mixture and moderating temperature rise. Advanced gas separation units, often based on cryogenic or pressure-swing adsorption, are employed to optimize the recycle composition [8,22,63,159,160].

5. Emerging reactor concepts for CO_2 hydrogenation

In the context of CO_2-based methanol synthesis, conventional syngas reactors face limitations. To overcome these, several advanced designs have been investigated:

- Membrane reactors: The integration of Pd- or zeolite-based membranes enables the selective removal of products (e.g., methanol or water) during the reaction, thereby shifting the equilibrium and increasing the per-pass conversion. Studies by Gallucci et al. and others have demonstrated significant improvements in CO_2 conversion, but

challenges include membrane stability under high pressures, cost, and scalability [8,22,63,161].

- Structured reactors: Monoliths, microchannel reactors, and coated foams provide enhanced heat and mass transfer, enabling better temperature control and reduced hot spots. These designs are attractive for small-scale or modular methanol plants powered by renewable H_2. Coating uniformity, long-term adhesion, and scalability remain active areas of research [162–164].
- Slurry-phase reactors: Gas-liquid-solid systems, where finely dispersed Cu-based catalysts are suspended in an inert oil, offer highly effective heat management due to excellent liquid-phase heat transfer. However, challenges with catalyst separation, attrition, and oil stability have limited their industrial adoption [8,59,75,165–168].
- Process intensification strategies: Coupling methanol synthesis with in-situ CO_2 capture (sorption-enhanced synthesis) or RWGS integration has been proposed to improve yields further, although these approaches are primarily at the lab or pilot scale [22].

Overall, reactor engineering in methanol synthesis involves striking a balance among heat management, equilibrium control, and long-term catalyst stability. While boiling-water reactors remain the industrial standard for large-scale operation, multi-bed adiabatic designs provide simpler and cost-effective alternatives. For CO_2 hydrogenation, equilibrium limitations and more substantial heat effects make conventional designs less efficient, driving interest in membrane-assisted, structured, and slurry-phase concepts [22].

Future reactor development is expected to focus on (i) integration with renewable hydrogen production, (ii) modular and flexible reactor concepts for distributed methanol plants, and (iii) hybrid configurations that combine conventional designs with process intensification strategies. Thus, while catalyst innovation defines intrinsic activity and selectivity, reactor design ultimately determines whether CO_2 hydrogenation to methanol can be implemented at a commercial scale in a sustainable and economically viable manner.

2.4 Summary

This chapter critically reviewed the scientific foundations of CO_2 hydrogenation to methanol, covering sustainable hydrogen production, Cu-based catalytic systems, precursor-guided

synthesis, reaction mechanisms, kinetic modeling, and reactor aspects. The evolution of Cu-based binary and ternary catalysts was discussed with emphasis on the decisive role of hydroxycarbonate precursors, oxide promoters, metal dispersion, oxygen vacancies, and metal-support interactions in governing catalytic performance, selectivity, and stability.

Recent advances in machine learning-assisted catalyst design further demonstrated the growing role of data-driven strategies in accelerating catalyst development and performance prediction. Mechanistic studies revealed the dominance of formate- and CO-mediated pathways, which are strongly influenced by the Cu surface state, water, and the effects of support-driven and multi-component synergistic interactions. Kinetic and reactor studies further demonstrated the importance of linking intrinsic reaction behaviour with practical process conditions**.**

Overall, this literature review establishes that precursor chemistry, promoter engineering, defect modulation, and metal-support synergy are the key determinants of high-performance CO_2-to-methanol catalysis, while also revealing the need for fully integrated studies that link precursor structure, reaction mechanism, intrinsic kinetics, and reactor performance. These insights directly motivate the research gaps and objectives defined in the subsequent sections of this chapter and form the scientific basis for the machine learning, experimental, and kinetic studies presented in this thesis.

2.5 Research gaps and motivation

1. Lack of standardized catalyst data and experimental validation limits reliable ML-based catalyst design for methanol synthesis.
2. There is a limited understanding of how high Mg incorporation in Cu-based catalysts influences catalytic performance in CO_2 hydrogenation to methanol.
3. The role of ZnO-ZrO_2 synergy in tuning active sites and enhancing methanol productivity over ball-milled Cu-based catalysts is not well established.
4. Validated kinetic models integrating mechanistic and experimental insights for CO_2 hydrogenation over Cu/ZnO/ZrO_2 remain scarce.

2.6 Research Objectives

This work integrates machine learning-guided catalyst design with experimental studies on Cu-based precursor development and promoter incorporation, advancing to mechanistic

understanding through reaction intermediate analysis and kinetic modeling of CO_2 hydrogenation to methanol. The specific chapter-wise objectives are as follows-

1. To develop and validate an ML model for methanol synthesis catalysts using curated literature data and experimental results from in-house synthesized catalysts.
2. To evaluate Cu/MgO catalysts with high Mg content for CO_2 hydrogenation and correlate their performance with key physicochemical properties.
3. To evaluate mechano-chemically synthesized Cu/ZnO/ZrO_2 catalysts and investigate how ZnO-ZrO_2 synergy influences activity in CO_2 hydrogenation to methanol.
4. To construct and validate a comprehensive Langmuir-Hinshelwood-Hougen-Watson kinetic model incorporating experimental data and intermediate species behaviour for methanol synthesis.

Chapter 3 Material and Methods

This chapter contains excerpts from the following publications.

1. ***Aakash Bhardwaj†**, Akshdeep S. Ahluwalia†, K.K. Pant, Sreedevi Upadhyayula*, "A principal component analysis assisted machine learning modeling and validation of methanol formation over Cu-based catalysts in direct CO_2 hydrogenation", Separation and Purification Technology, Volume 324, 1 November 2023, 124576.*
2. ***Aakash Bhardwaj[a,1]**, Meenakshi Pokhriyal[a,1], Vaibhav Pandey[a], Kamal Kishore Pant[a], Sreedevi Upadhyayula[a,]*, "Enhanced Methanol Formation over Cu/MgO catalyst derived from Mg-Rich Active Hydroxycarbonate Precursor", ACS Appl. Energy Mater. 2024, 7, 12, 5163-5178.*

3.1 Overview

This chapter outlines the integrated methodology employed in this study, which combines machine learning, experimental synthesis, computational modeling, and kinetic analysis to develop and evaluate Cu-based catalysts for CO_2 hydrogenation to methanol. Machine learning models were employed to construct data-driven predictive frameworks using both literature and experimental datasets. Complementing the computational approach, a range of catalyst materials was synthesized through hydrothermal, co-precipitation, impregnation, and ultrasonication-assisted methods, followed by extensive physicochemical characterization and catalytic performance testing. Density functional theory calculations provided molecular-level insights into adsorption behaviour. The kinetic modeling component established mechanistic rate expressions, incorporated reactor and transport considerations, and used parameter estimation and validation procedures to ensure consistency between predicted and experimental behaviour. Together, these methodologies form a cohesive framework that links catalyst design, mechanistic understanding, and performance optimization in the CO_2-to-methanol process.

3.2 Methodology for machine learning

The dataset comprises 227 points, capturing over 30 different kinds of unique formulations for Cu-based catalysts, with 12 sets of binary and 18 sets of tertiary formulations. The input parameters that were taken for building the non-linear regression models using machine

learning algorithms are temperature, pressure, space velocity, BET area, metal dispersion, and copper grain size. Although the other variables characterizing the physical conditions, like CO_2/H_2 ratio and other catalyst properties such as metal surface area, catalyst weight, and copper weight percent, were collected, these turned out to be either not fit enough to be used in a linearly independent capacity or were not exhaustively present for all the points. This work evaluates the use of three algorithms, namely, Artificial Neural Networks (ANN), Support Vector Regression (SVR), and Gaussian Process Regression (GPR). All the algorithms were evaluated based on 10-fold cross-validation and then further tested on a dataset curated from the laboratory for a ternary CZZ-C catalyst used in a fixed-bed reactor. The catalytic activity tests of the laboratory-synthesized catalyst were evaluated with pure CO_2 using a high-pressure fixed-bed tubular reactor with a temperature range of (200-250 °C), a pressure range of (20-40 bar), at constant space velocity (2600 ml/g_{cat}.hr). Overall, the final model validation was performed using 30 datasets derived from a ternary CZZ-C laboratory catalyst under varying operating conditions, including temperature and pressure, at a constant space velocity [13].

The physical conditions, such as temperature and pressure, are essential for proceeding with any reaction; their range depends on the reaction's thermodynamics; therefore, they are the two primary input parameters. Furthermore, the third parameter is space velocity, which quantifies the incoming volumetric flow rate and directly impacts both catalytic activity and output. These fairly accurately characterize the physical conditions [169]. To accurately capture the catalyst's fundamental insights, the three metrics being used are Brunauer-Emmett-Teller (BET) Surface Area (m^2/g), Metal Dispersion (%), and Copper Grain Size (nm). The BET area is determined by the total surface area of a solid, which is measured by suspending a powdered analyte in an inert gaseous bath and measuring the adsorption of gas molecules to the surface and its porous structures. This explains the physical adsorption of gas molecules on a solid surface. Moreover, Dispersion (D_{Cu}) is an important concept in heterogeneous catalysis, as only atoms exposed to the surface can participate in catalytic surface reactions. Finally, Copper grain size (d_{Cu}) has been shown to have a positive effect on MeOH selectivity and yield, which is attributed to the improved hydrolysis of methoxy to methanol (in the mechanism) by enhancing the desorption and diffusion of water vapor [170]. The catalyst insights will significantly depend on the support material used in combination with Cu-based catalysts. The proper selection and implementation of the best-suited support are essential for enhancing catalytic

properties and all those directly related to catalytic performance. The main reactions involved during the catalysis process are given in **Table 3.1.**

Table 3.1. *Reactions involved during the hydrogenation reaction of CO_2 to methanol.*

Primary Reaction		
$\mathbf{CO_2 + 3H_2 \rightleftharpoons CH_3OH + H_2O}$	$\Delta H_{25℃} = -49.5\ kJmol^{-1}$	Methanol Synthesis
Side Reactions		
$\mathbf{CO_2 + H_2 \rightleftharpoons CO + H_2O}$	$\Delta H_{25℃} = 41.2\ kJmol^{-1}$	(Reverse Water-gas Shift Reaction)
$\mathbf{CO + 2H_2 \rightleftharpoons CH_3OH}$	$\Delta H_{25℃} = -90.6\ kJmol^{-1}$	Methanol Synthesis
$\mathbf{CO_2 + 4H_2 \rightleftharpoons CH_4 + 2H_2O}$	$\Delta H_{25℃} = -165.0\ kJmol^{-1}$	Methanation
$\mathbf{CO + 3H_2 \rightleftharpoons CH_4 + H_2O}$	$\Delta H_{25℃} = -201.1\ kJmol^{-1}$	Methanation

Although another important parameter is the metal surface area (S_{Cu}), as its increase allows more reactants to reach the catalyst atoms/molecules, thus increasing the number of "collisions" and resulting in a faster rate. Nevertheless, it is intercoupled with dispersion. Metal surface area is more widely characterized than dispersion; however, dispersion better serves the purpose of being used as the input. The two are mathematically derived from **Equations (3.1)** and **(3.2),** respectively [171], wherever the dispersion value was not reported during dataset collection, it was estimated by interlinking the two.

$$S_{Cu} = \frac{2n_{H_2} \text{x N}}{1.4 \text{ x } 10^{19} \text{ x W}} (m^2 g^{-1}) \quad (3.1)$$

$$D_{Cu} = \frac{2n_{H_2} \text{x } M_{Cu}}{\text{W x X}} \text{ x } 100\% \quad (3.2)$$

where N is Avogadro's constant ($6.02*10^{23}$ atoms mol^{-1}), and M_{Cu} is the relative atomic mass (63.546 g mol^{-1}). n_{H_2} is the molar number of consumed H_2. W is the weight of the catalyst and X is the composition of Cu (wt.%), and $1.4*10^{19}$ is the number of copper atoms per square meter.

Furthermore, at times, the average pore diameter (d_{Cu}) was also evaluated in conjunction with pore volume and BET surface area [172], as per **Equation (3.3)**.

$$d_{Cu} = \frac{4 \text{ PV}}{S_{BET}} \quad (3.3)$$

Regarding the dataset's outlook, several statistical metrics are reported in **Table 3.2** and **Table 3.3.** Additionally, for visualization, Principal Component Analysis (PCA) is employed to generate 2-dimensional score plots for the dataset; the testing data is also projected onto the same space to assess where the points fall [76].

For any given dataset, PCA attempts to transform the original space of the variables to the space characterized by the maximum possible variance that can be captured. The algorithm for a standardized dataset usually first evaluates the covariance matrix for the data and subsequently derives the eigenvectors ($v_i's$) and corresponding eigenvalues ($\lambda_i's$) such that $||v_i||^2=1$. Sorting and clubbing the eigenvectors based on the maximum eigenvalues yields a matrix P, called the projection matrix. The transformation of the data into the new space is represented using a scores matrix S and input dataset D, calculated as;

$$S = D*P \tag{3.4}$$

The projection matrix, also sometimes referred to as the loadings, when plotted, helps evaluate the contribution of variables in creating the principal components that comprise the new space. With the projection matrix P known, it can help project any new dataset onto the same space; for example, for dataset T, the scores Y for its transformation could be evaluated as;

$$Y = T*P \tag{3.5}$$

The methodology was used to project the laboratory data into the space of the collected dataset from the literature survey. Four outputs were chosen to characterize the reaction output appropriately and, therefore, to be regressed: CO_2 Conversion (%), Methanol Selectivity (%), CO selectivity (%), and Methanol space-time yield (STY) ($mmol_{MeOH}/g_{cat}.hr$) were collected, each being an essential and independent output for the reaction.

3.2.1 Machine Learning Models

3.2.1.1 Neural Network Model

A feedforward artificial neural network (ANN) was employed to develop a nonlinear regression model that simultaneously predicts multiple catalytic performance indicators. The model consisted of six input parameters and four output parameters, representing the key physicochemical and operational variables influencing methanol synthesis. A representative 3-layer ANN architecture with one hidden layer is illustrated in **Figure 3.1.** The ANN model was

trained using a standard supervised learning approach, in which network weights and biases were iteratively updated to minimize the prediction error between the measured and predicted outputs. Instead of using specialized learning algorithms such as Levenberg-Marquardt, Bayesian regularization, or scaled conjugate gradient, the network was trained using a conventional backpropagation optimization framework with typical gradient-based weight updates. This choice aligns with establishing a generalizable and easy-to-implement ANN model without introducing algorithm-specific complexity [124,125].

The development of a single multi-output ANN model was preferred over constructing separate individual networks for each output. A combined model captures the interdependence among outputs, such as the interplay between CO_2 conversion, methanol selectivity, and by-product formation, and therefore better reflects the real catalytic system, where these properties are not independent of each other. In contrast, individual-output models may overlook these intrinsic correlations and can diverge substantially from real reactor behaviour. To ensure robust performance evaluation, the ANN was assessed using a 10-fold cross-validation procedure. The model's predictive capability was quantified using the average mean squared error (MSE), and corresponding R^2 values for each output were computed for every fold and subsequently averaged. These statistical indicators collectively confirmed that the joint multi-output ANN provided superior predictive reliability compared to individually trained models.

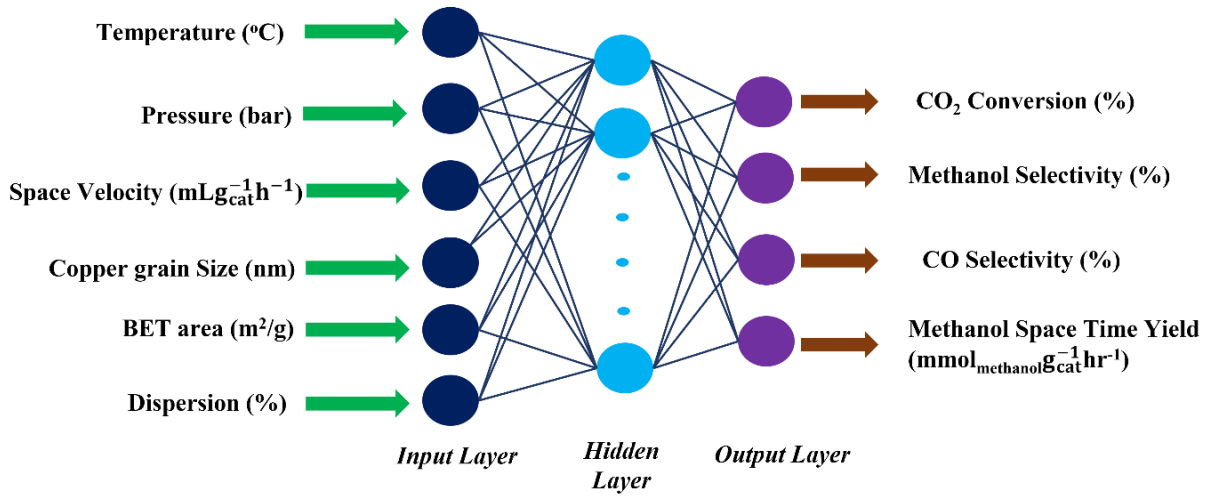


Figure 3.1. *Illustrative ANN regression model.*

The interesting feature of our model assessment is that the number of neurons in the hidden layer is not fixed and is evaluated for the optimal number between 1 and 20 for each fold. Then, based on the average number of optimum neurons of each fold, an estimate for that algorithm

was obtained, as depicted in **Figure 3.2.** While evaluating the optimum for a particular fold, MSE values on the corresponding test set were used.

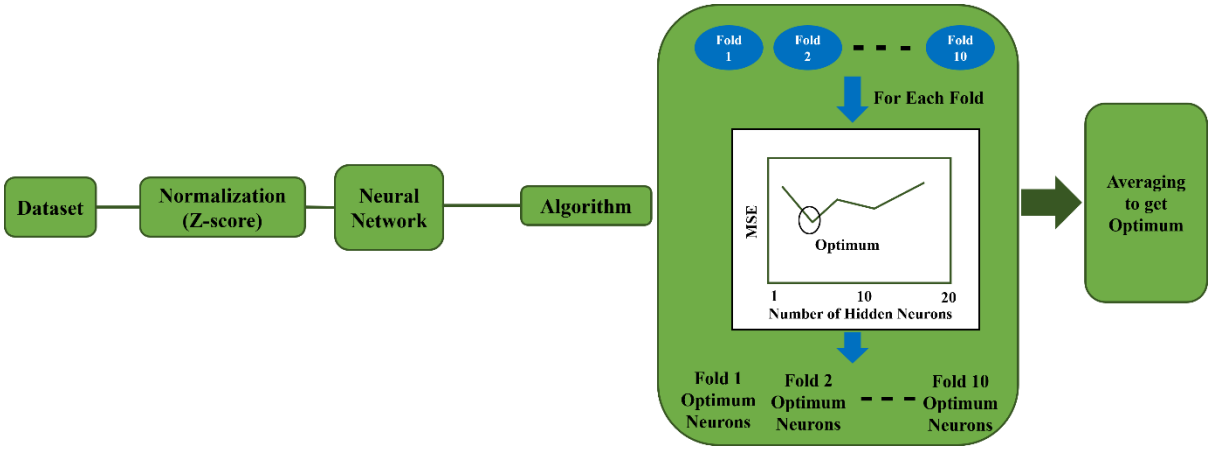


Figure 3.2. *General scheme to calculate the optimum number of neurons in the hidden layer.*

The activation function used when passing from the input to the hidden layer was a sigmoid function, resulting in an output response in the range [0, 1]. The activation function used to get output from the hidden layer is the Linear activation (ReLU) function. The ANN and subsequent modeling were performed in MATLAB R2021a using the appropriate packages. There are four kinds of network weights in the model:

1. The input-to-hidden layer weights: w^1 (No. of hidden units x 6; matrix)
2. The hidden-to-output layer weights: w^2 (No. of hidden units x 4; matrix)
3. The input-to-hidden layer bias: b^1 (No. of hidden units x 1)
4. The hidden-to-output layer bias: b^2 (4x1)

Hence, the total associated weights in the final model can be evaluated by adding the above, leading to (number of hidden units × 11 + 4) total weights. For the sensitivity analysis for the ANN, Garson's method [173] has been used to measure the influence of variables on the response. This method utilizes the connection weights of the neural network, as specified in **Equation (3.6).**

$$I_j = \frac{\sum_{m=1}^{m=N_h}\left(\left(\frac{|w_{jm}^{ih}|}{\sum_{k=1}^{k=N_i}|w_{km}^{ih}|}\right)x\,|w_{mn}^{ho}|\right)}{\sum_{k=1}^{k=N_i}\left\{\sum_{m=1}^{m=N_h}\left(\left(\frac{|w_{km}^{ih}|}{\sum_{k=1}^{k=N_i}|w_{km}^{ih}|}\right)x\,|w_{mn}^{ho}|\right)\right\}} \quad (3.6)$$

where I_j refers to the relative importance of the j^{th} input variable on the response, 'w' represents the neural network weights, and N_i and N_h refer to the numbers of input and hidden neurons, respectively. The superscripts 'i', 'h', and 'o' denote input, hidden, and output layers, and the subscripts 'k', 'm', and 'n' are related to input, hidden, and output neurons, respectively.

3.2.1.2 Support Vector Machine Regression

The Support Vector Machine (SVM) utilizes kernels to expand the feature space in a specific manner. Unlike other generic regression methods, it provides us the flexibility to define how much error is acceptable in our model and identifies an appropriate line (or hyperplane in higher dimensions) to fit the data. Here, we highlight the mathematics for a linear regression SVM problem and then extend it to non-linear [174].

For a multivariate training data set, x_n of N observations and observed response values y_n. Our objective is to find the linear function:

$$f(x) = x'\beta + b \tag{3.7}$$

For f(x) to be formulated, the convex optimization problem that is to be minimized is:

$$J(\beta) = \frac{1}{2}\beta'\beta \tag{3.8}$$

Subject to the residuals having a value less than ε, called the error margin. In mathematical terms, it'd be written as:

$$\forall n: |y_n - f(x)| \leq \varepsilon \tag{3.9}$$

The epsilon (ε) can be tuned to get the desired accuracy for the model. But as a matter of fact, no such function might exist to satisfy the constraints for all points. In that case, a necessity arises to introduce so-called slack variables ξ_i, for each point in our objective function. That denotes the deviation from the margin for the values that fall outside the error margin.

Thus, the objective function is modified as follows:

$$J(\beta) = \frac{1}{2}\beta'\beta + C\sum_{i=1}^{n}|\xi_i| \tag{3.10}$$

Subject to,

$$\forall n: |y_n - f(x)| \leq \varepsilon + |\xi_i| \tag{3.11}$$

The non-linear form is written with the help of the non-linear kernel function, $G(x_i, x)$. The kernel, in general, involves the use of inner products. The inner product of two r-vectors is defined as $\langle a, b\rangle = \sum_{i=1}^{r} a_i b_i$. Thus, the inner product of two observations x_i and $x_{i'}$, is given by $\langle x_i, x_{i'}\rangle = \sum_{j=1}^{p} x_{ij} x_{i'j}$.

The function, in this case, is written as:

$$f(x) = \sum_{i=1}^{n} \beta_i G(x_i, x) + b \tag{3.12}$$

Thus, it is a powerful algorithm that allows us to adjust our tolerance for errors by defining an acceptable error margin (ε) and also tweaking our tolerance for exceeding that acceptable error rate. In this study, we have employed both Gaussian and polynomial functions of order up to 3 to test their performance and select the best one for model assessment. Higher-order polynomials were not used, as their inclusion would have significantly increased the computational expense without yielding a substantial improvement in the model's performance. The dataset was randomly split into an 80% training set and a 20% testing set while selecting the optimum kernel function. After this, complete regression was evaluated based on average metrics of 10-fold cross-validation. The general scheme used for SVM regression is shown in **Figure 3.3.**

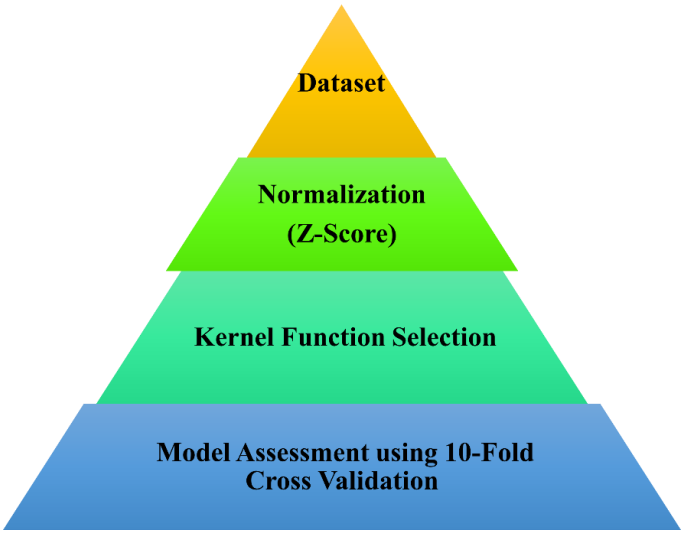


Figure 3.3. *Scheme for Support Vector Regression Evaluation.*

3.2.1.3 Gaussian Process Regression

This regression model is based on nonparametric kernel-based probabilistic models. These models have found widespread usage in machine learning applications due to the flexibility of their representations and built-in uncertainty metrics for predictions. Multivariate normal distribution, kernels, nonparametric models, and joint and conditional probability are the fundamental ideas on which a Gaussian process is based. Considering the training set $\{(x_i,y_i);i=1,2,...,n\}$, where $x_i \in \mathbb{R}^d$ and $y_i \in \mathbb{R}$, drawn from an unknown distribution. A GPR model addresses the question of predicting the value of a response variable y_{new}. The regression function modelled by a multi-variate gaussian is as- $P(f \mid X) = N(f \mid \mu, K)$, where $X = [x_1, \ldots, x_n]$, $f = [f(x_1), \ldots, f(x_n)]$, $\mu = [m(x_1), \ldots, m(x_n)]$ and $K_{ij} = k(x_i, x_j)$. The two variables, m and k, stand for the mean function and a positive definite kernel function, respectively. When there are no observations, the mean function is set to $m(X) = 0$, given that the data is often normalized to a zero mean [175]. A distribution over functions with a shape (smoothness) determined by K is the Gaussian process model. The trained model can also calculate prediction intervals, as a GPR model is probabilistic. The regression is of the form,

$$y = x^T\beta + \varepsilon \tag{3.13}$$

where $\varepsilon \sim N(0,\sigma^2)$. The error variance, σ^2, and the coefficients, β, are estimated from the data. In this work, the 'fitrgp' function was used in MATLAB to estimate the basis function coefficients, β, the noise variance, σ^2, and the hyperparameters with the help of the 'Optimize Hyperparameters' argument. The general scheme used is illustrated in **Figure 3.4.**

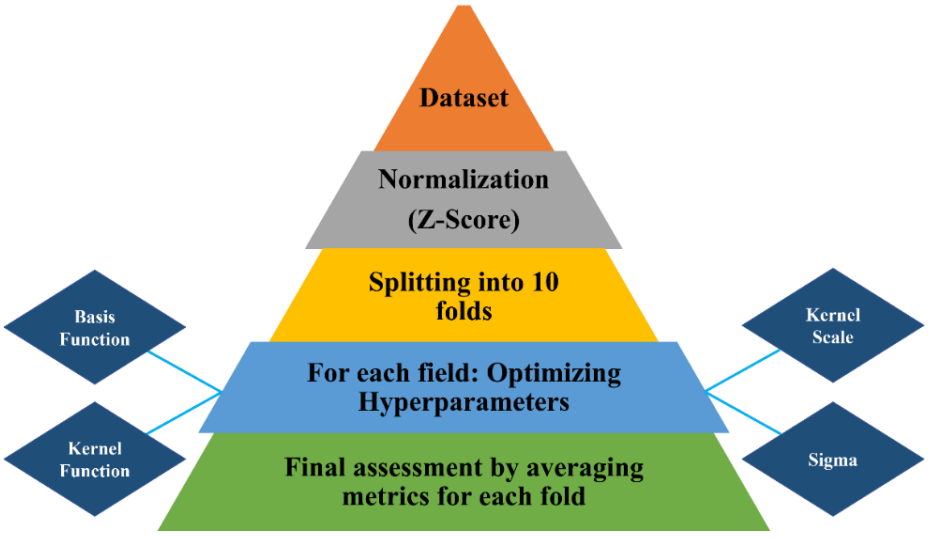


Figure 3.4. *The general scheme used for model assessment for Gaussian Process Regression (GPR).*

3.3 Experimental Methods

The experimental work performed for this research is represented in three separate sections. These sections contain: catalyst synthesis, characterization techniques, and catalyst activity in a high-pressure fixed-bed reactor system **(Figure 3.5).**

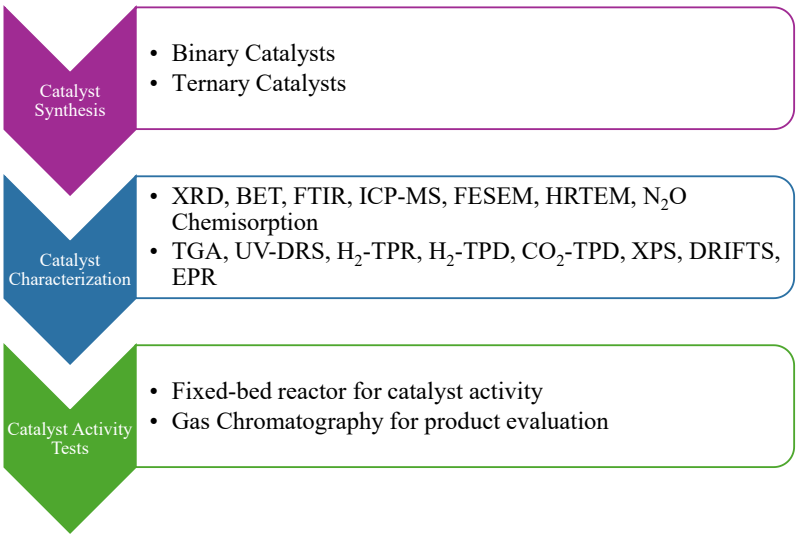


Figure 3.5. *Discrete sections of experimental work.*

3.3.1 Catalyst Synthesis

The carbon conversion and methanol selectivity over the Cu-Zn-based catalyst remain low, facing significant challenges such as difficulties in obtaining a single-phase pure precursor, weak SMSI, low creation of oxygen vacancies, and catalyst stability issues. Keeping the challenges in mind and aiming to capture all the possible properties of the best catalyst, the ultimate goal is to synthesize a catalyst that achieves the highest catalytic performance with enhanced catalytic stability. This is achieved by introducing novel catalyst precursor methods which enhance active and defect sites in the binary and ternary catalysts such as Cu/MgO, Cu/ZnO, Cu/ZnO/ZrO_2, Based on literature and preliminary experiments, Cu is chosen as an active metal for all the catalyst synthesized and partially reducible oxide (MgO, ZnO, ZrO_2) are chosen as support materials for the final catalysts to be selected for study. Several strategies of catalyst synthesis have been employed in the dissertation for CO_2 hydrogenation reaction i.e. (1) synthesis of ($(Cu,Mg)_2(OH)_2CO_3$) precursors using hydrothermal method, (2) synthesis of Cu/MgO catalysts using conventional co-precipitation and impregnation method, (3) synthesis of Cu-Zn hydroxycarbonate precursor with zirconium oxide support, (4) synthesis of CuO-ZnO-ZrO_2 catalyst by simultaneous co-precipitation followed by ultrasonication, (5)

synthesis of CuO-ZnO-ZrO_2 catalyst by conventional co-precipitation followed by ultrasonication.

Elaborated catalyst synthesis materials and methodologies are described in subsequent sections.

3.3.1.1 Materials used to synthesize all Cu/MgO-based catalysts used in Chapter 5

$Cu(NO_3)_2.3H_2O$ (Merck≥ 99%), $Mg(NO_3)_2.6H_2O$ (Thomas baker, 99%), ammonium carbonate solution (Merck, 99 %), and deionized water (resistivity ≥ 18.2 MΩ).

3.3.1.2 Methodologies adopted to synthesize all Cu/MgO-based catalysts used in Chapter 5

- **Synthesis of ($(Cu,Mg)_2(OH)_2CO_3$) precursors using hydrothermal method**

All the reactants and reagents employed in this study were of analytical grade and were used as purchased. For the synthesis of the Cu/MgO catalyst, the first step is to synthesize a hydroxy carbonate precursor equivalent to mcguinnessite using a hydrothermal route for the synthesis of 50 at.% Mg (i.e., nominal Cu: Mg =1:1) substituted precursor, 0.5194 g (2.15 mmol) of $Cu(NO_3)_2.3H_2O$ was dissolved in a minimum amount of deionized water, and to this solution, 0.5518 g (2.15 mmol) of $Mg(NO_3)_2.6H_2O$ was added under stirring. After the complete dissolution of the salts, 60 ml of 0.1 M ammonium carbonate solution was added slowly to the metal solution (pH 7.0). The resulting precursor suspension, exhibiting a dense cyan color, was then transferred to a 100 ml Teflon-lined stainless-steel autoclave and maintained at 150°C for 16 hours. The solid product was collected using vacuum separation, washed with copious amounts of deionized water, and dried overnight at 60°C. The precursor obtained (CM50) was subjected to various characterization techniques and then calcined at 350°C and 400°C for 3 hr individually in static air. Other samples with different Mg substitutions (0%, 12.5%, 25.0%, and 37.5%) were also prepared using the above recipe by adjusting the molar concentrations of Cu and Mg salts. The samples are labeled as CM0, CM12.5, CM25, and CM37.5, representing 0%, 12.5%, 25%, and 37.5% atomic percent (at. %) of Mg-substituted precursor samples, respectively [14].

- **Catalyst preparation by co-precipitation and wet impregnation**

For the co-precipitation route to synthesize the Cu-Mg hydroxycarbonate precursor, the procedure was adapted directly from the literature [93,176]. Cu/Mg (1.0 M) nitrate solutions

and a Na_2CO_3 solution (1.6 M) were used as the precipitating agent, and the mixture was precipitated at a constant pH of 9.0. The variation in the Cu to Mg ratio was done by altering the weight of the individuals. The final catalyst obtained was calcined at 400°C (2°C /min) for 3 hr (CM-CP).

The Cu/MgO catalyst with equimolar Cu and Mg was prepared via the wet impregnation method, as adapted from the preparation by Kleiber et al [177]. Firstly, the $4MgCO_3.Mg(OH)_2.4H_2O$ (BDH, 98%) was taken and calcined at 550°C for 2 h. The calcined MgO (1 g) was then impregnated with 100 ml aqueous solution of 0.25 M $Cu(NO_3)_2.3H_2O$ with continuous stirring for two hours. The blue precipitate was filtered and washed with copious amounts of water, then dried overnight at 60°C in an oven. The dried powder was further calcined in the muffle furnace at 400°C for 3 h to obtain the final catalyst (CM-IMP).

3.3.1.3 Materials used to synthesize all Cu/ZnO-based catalysts used in Chapter 6

Copper hydroxycarbonate (CDH, 99%), zinc carbonate (CDH, 99%), $Cu(NO_3)_2.3H_2O$ (Merck, 99%), $Zn(NO_3)_2.6H_2O$ (CDH, 99%), $ZrO(NO_3)_2.xH_2O$ (CDH, 99%), Na_2CO_3 (Merck, 99%), acetone (SRL, 99%), and deionized water (resistivity ≥ 18.2 MΩ).

3.3.1.4 Methodologies adopted to synthesize CZ and CZZ catalysts used in Chapter 6

- **Synthesis of Cu-Zn hydroxycarbonate precursor with zirconium oxide support**

The copper hydroxycarbonate and zinc carbonate precursors were used in a specific ratio on a metal basis (2.33:1) in powder form as the starting material for synthesis. A high-energy planetary ball mill (Retsch, PM 100) was used for the mechanochemical wet ball milling and ion-exchange of metal precursors in an acetone medium under ambient atmospheric conditions at a constant rotational speed of 500 rpm. The size reduction and ion-exchange of metal precursors were done with zirconia balls (2mm and 3mm) in a zirconia-lined stainless steel vessel with a feed-to-ball ratio of 1:15. The precursors with a time variation of 3-12 hr were synthesized, dried at 80°C for 12 hr, and simultaneously checked with X-Ray diffraction technique for phase purity. No significant change in precursor phases was noticed after 9 hr of milling. The as-prepared Cu-Zn phase pure precursor (zincian malachite) was then thermally treated at 350°C for 4 hours under a static atmosphere, and the obtained catalyst sample was denoted as CZ-MCBM-C. To study the effect of a weakly hydrophilic material, zirconium, a similar synthesis procedure was adopted by mixing the previously prepared CZ-MCBM

precursor with the nitrate salt of zirconia (Zirconyl oxynitrate) and milling for an additional 3 hours to attain the zirconia-supported Cu-Zn precursor. The prepared catalyst precursor was then recovered with solvent, and the mill was cleaned. It was then subjected to drying in a hot air oven at 80°C for 12 hours prior to thermal treatment (calcination) in static air at 350°C for 4 hours. The final catalyst obtained after calcination was termed CZZ-MCBM-C.

- **Synthesis of Cu-ZnO-ZrO_2 catalyst by simultaneous co-precipitation followed by ultrasonication.**

The Cu-ZnO-ZrO_2 catalyst was synthesized via simultaneous precipitation, followed by ultrasonication, to enhance metal dispersion on the support surface. $Cu(NO_3)_2$. $3H_2O$, $Zn(NO_3)_2$. $6H_2O$, and $ZrO(NO_3)_2$. xH_2O was taken in a molar composition of (56/24/20) and by maintaining the molar ratio of (2.33:1) for Cu/Zn. The metal nitrate salts stated above were dissolved in 250 ml of deionized water. The metal nitrate salt solution and 1.0 M Na_2CO_3 basic solution were simultaneously added to a 500 ml beaker under vigorous stirring at a bath temperature of 60°C, while maintaining a pH of around 8-8.5. The mixture was then subjected to ultrasonication for 30 min in an ultrasonication bath (machine specifications). The precipitant was then left to age for 6-8 hours to attain the desired phase-pure precursor. The solid product was then collected after multiple washings and vacuum filtration with a sufficient amount of deionized water, and dried overnight at 80°C. The product obtained (CZZ-SPUSI-P) was subjected to a phase purity check by X-ray diffraction technique. The precursor obtained was then calcined at 350°C for 4 hr in a static atmosphere and denoted as CZZ-SPUSI-C.

- **Synthesis of Cu-ZnO-ZrO_2 catalyst by conventional co-precipitation followed by ultrasonication.**

The Cu-ZnO-ZrO_2 catalyst was synthesized via conventional co-precipitation, followed by ultrasonication to enhance metal dispersion on the support surface. $Cu(NO_3)_2$. $3H_2O$, $Zn(NO_3)_2$. $6H_2O$, and $ZrO(NO_3)_2$. xH_2O was taken in a molar composition of (56/24/20) and by maintaining the molar ratio of (2.33:1) for Cu/Zn. The metal nitrate salts stated above were dissolved in 250 ml of deionized water. After the complete mixing of nitrate salts, a 1.0 M Na_2CO_3 solution was slowly added under vigorous stirring at a bath temperature of 60°C, while maintaining the pH at around 8-8.5. The mixture was then subjected to ultrasonication for 30 min in an ultrasonication bath (machine specifications). The precipitant was then left to age for

6-8 hours to attain the desired phase-pure precursor. The solid product was then collected after multiple washings and vacuum filtration with a sufficient amount of deionized water, and dried overnight at 80°C. The product obtained (CZZ-CPUSI-P) was subjected to a phase purity check by X-ray diffraction technique. The precursor obtained was then calcined at 350°C for 4 hours in a static atmosphere and denoted as CZZ-CPUSI-C.

3.3.2 Catalyst Characterization Techniques

Extensive catalyst characterizations were executed for a complete series of in-house synthesized catalyst matrices (Cu, Mg, Zn, and Zr) using several cutting-edge characterization techniques **(Figure 3.6).** The detailed procedure for each analysis is provided below.

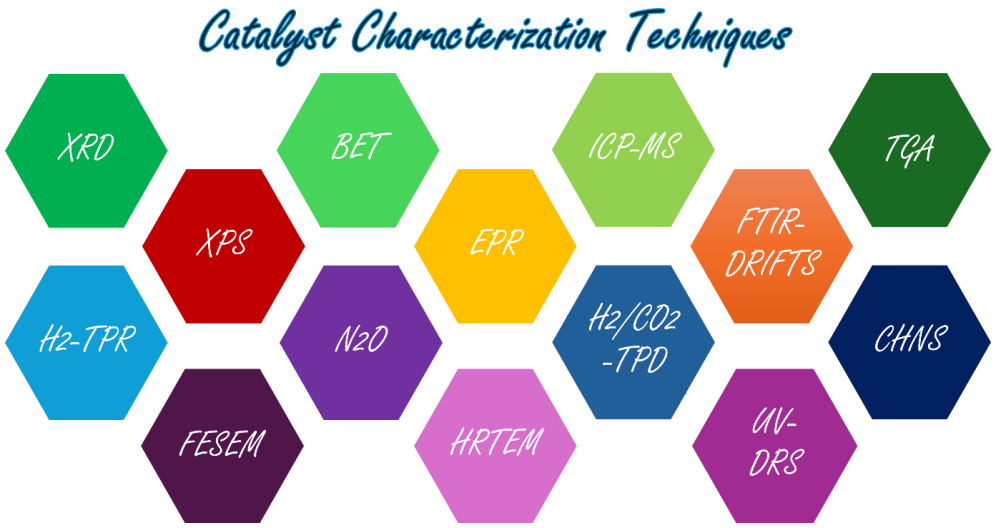


Figure 3.6. *Schematic diagram of catalyst characterization techniques during this work.*

The powder X-ray diffraction (PXRD) data of the Cu/MgO catalyst samples were collected using a Rigaku Miniflex 600 equipped with a CuKα (λ= 0.15418 nm) source generated at 40 kV/15 mA. Each catalyst sample was scanned over a 2θ range of 10° to 80° at a speed of 4°/min and a step size of 0.02°. The crystallite sizes of CuO and Cu phases were estimated from the reflections of CuO (*111*) and Cu (*111*) planes by Scherrer's Equation [6,13,14,94,98,178].

The Fourier Transform Infrared (FTIR) analysis was performed using a Thermo Fisher Nicolet IS-50 spectrometer in transmittance mode, with a wavenumber range of 400-4000 cm^{-1}. The pellet was prepared with a dried, finely ground catalyst and potassium bromide (KBr) powder [13,14].

The model SDT650 simultaneous DSC-TGA instrument was used to test the thermal stability of the catalyst sample using Thermal Gravimetric Analysis (TGA), with a temperature range from ambient to 1000°C under zero air flow at a rate of 100 ml/min [13,14].

An Agilent (Cary-4000) spectrometer equipped with an integrating sphere attachment was used to record the ultraviolet diffuse reflectance spectrum (UV-DRS) with a step-size of 0.2 nm in the range of 200-800 nm with $BaSO_4$ as the reference sample [14].

A Microtrac BELSORB MAX II surface area analyzer was used to study the textural properties of the catalyst samples, i.e., BET Surface area from the Multipoint BET method, pore volume, pore size distribution, and mean pore diameter from the Barrett-Joyner-Halenda (BJH) method. Before characterization, the catalyst samples were heated and degassed under vacuum at 200°C for 12-16 hours [13,14,94,98,178].

An Agilent 7900 ICP-MS with UHMI technology instrument was used to determine the chemical composition of the catalyst sample. An aqua regia mixture of HCl and HNO_3 (3:1 by volume) was used to digest 100 mg of the catalyst sample, which was then diluted with Milli-Q water for analysis [6,13,14,94,98,178].

Field-emission scanning electron microscopy (FESEM) and energy-dispersive spectroscopy (EDS) analysis were used to gather surface topographical information and surface elemental data using a JEOL JSM-7800F Prime microscope with an accelerating voltage of 10 kV. Elemental distribution can be determined by mapping using the exact spectrophotometer. The finely ground powdered catalyst sample was charged on aluminium pin flat stubs, and then gold sputtering was done to prepare the sample for analysis [6,13,14,94,98,178].

High-resolution transmission electron microscopy (HRTEM) techniques were used to characterize surface morphological changes, including shape, pore size, average particle size, and particle size distribution. The HRTEM images were recorded on the FEI Tecnai TF20 microscope, with a maximum accelerating voltage of 200 kV and an FEG source. For the HRTEM analysis, the catalyst samples were dispersed in 99.99% pure ethanol and then mounted onto a carbon-containing copper grid, which was allowed to dry under a lamp [6,13,14,94,98,178].

The Electron Paramagnetic Resonance (EPR) data of the samples were recorded on an Electron Paramagnetic Resonance spectrometer (Bruker A300-9.5/12/S/W), with a working frequency of 9.78 GHz at room temperature [14].

A temperature-programmed reduction (H_2-TPR) chemisorption technique was employed to investigate the reduction behaviour using the Chem BET Pulsar instrument. A calcined catalyst sample (50 mg) was used to create a catalyst bed in a quartz reactor, and the temperature was raised to 300°C at a rate of 10°C/min under a He gas flow for the physical and chemical removal of adsorbed water. The furnace was cooled to room temperature under an inert He gas flow. The furnace temperature was again raised to 600°C using a ramp of 10°C/min under a 5 vol.% H_2/Ar mixture flow of 50 ml/min, and the total H_2 was quantitatively monitored by a thermal conductivity detector (TCD). To determine the active surface area (SA_{Cu}) and metal dispersion (D_{Cu}), the N_2O chemisorption technique was used. The first step reduction profile was recorded during an earlier TPR run to reduce CuO and obtain metallic Cu, which was then exposed to a N_2O gas flow for 30-45 minutes to completely oxidize the exposed surface Cu atoms to Cu_2O. The sample was then cooled to room temperature under an inert He atmosphere. The second step reduction profile was then recorded with a similar H_2/Ar composition to reduce the Cu_2O again, thereby obtaining Cu metal by raising the temperature to 600°C at a rate of 10°C/min. Based on the amount of H_2 consumed during the reduction steps, SA_{Cu} and D_{Cu} were calculated, assuming that Cu crystallites are spherical [6,13,14,94,98,178].

The active copper surface area (SA_{Cu}), copper metal dispersion (D_{Cu}), and Cu particle size were calculated based on the formula given in **Equations (3.14-3.16).**

$$SA_{Cu}\left(\frac{m^2}{gm}\right) = [10^2(\text{Mol } H_2)(SF)(N_A)]/[(SD_{Cu})(W_{Cu})] \quad (3.14)$$

$$D_{Cu}(\%) = [10^4(\text{Mol } H_2)(SF)(\text{At. wt. Cu})]/(W_{Cu}) \quad (3.15)$$

$$d_p = 6M/D\rho\sigma N_A \quad (3.16)$$

where SA_{Cu} = active copper surface area, D = D_{Cu} = copper metal dispersion, d_p= copper particle size, Mol H_2 = amount of H_2 consumed per gm catalyst (mol H_2/g_{cat}), Stoichiometric factor (SF) = 2, Avogadro's number (N_A) = $6.022*10^{23}$, Copper surface density (SD_{Cu}) = $1.46*10^{19}$ atoms/m^2, Catalyst Cu content (W_{Cu}) determined from ICP-MS analysis (wt%), Atomic weight of Cu = molecular weight (M) of Cu = 63.546 g/mol, Cu metal density (ρ) = 8.94 g/cm^3, area occupied by a surface Cu atom (σ) = 6.85 A^2/atom.

Temperature-programmed desorption (CO_2-TPD) was used to determine the surface basicity of the calcined catalyst sample with the same apparatus as for other chemisorption characterization techniques. For the CO_2-TPD analysis, a similar procedure was applied as in other chemisorption techniques: helium gas flow, catalyst degassing at approximately 300°C, followed by reduction of the H_2 gas flow, flushing, and cooling with inert helium gas to room temperature. The surface of the catalyst sample was then completely saturated with pure CO_2 flow rate (50 ml/min) at 50°C for 30-45 min and flushed with the He gas flow (50 ml/min) to remove all the physically adsorbed molecules. The CO_2 Desorption profiles were recorded from 50 to 700°C at a ramp rate of 10°C/min under continuous He gas flow [6,13,14,94,98,178].

An AXIS SUPRA instrument equipped with an Al Kα X-ray emissive source, operating at 1488.6 eV, 12 kV, and 6 mA, was used to perform X-ray photoelectron spectroscopy (XPS). The scans were performed over an energy range of 0-1200 eV, with a step size of 1 eV. The C 1*s* peak was used to correct the XPS spectra at 284.8 eV, and then the electronic properties of Cu 2*p*, Mg 2*p*, and O 1*s* were determined [14,94,98,178].

An Elementar Vario MACRO Cube was used to measure the elemental analysis of C in the spent catalyst samples using a CHNS analyzer. The CHNS analyzer determined the carbon percentage of the coke deposited on the catalyst surface during the CO_2 reduction reaction [14,179].

In-situ DRIFTS (Diffuse reflectance infrared Fourier transform spectroscopy) experiments were conducted to identify the reaction intermediates involved in the CO_2 hydrogenation to methanol reaction. It is performed on a Nicolet-6700 FTIR spectrometer equipped with a liquid nitrogen-cooled MCT detector (accumulates 64 scans at a resolution of 4 cm^{-1}) to draw the reaction mechanism. The FTIR instrument, equipped with an additional DRIFTS cell fitted with ZnSe windows, was used as the chamber for performing the experiments. Initially, the catalyst samples were pretreated with N_2 gas at 300°C for 60 min to remove moisture and physically adsorbed species, which were then reduced with a 10% H_2/Ar (30 ml/min) mixture for 60 min. The temperature was then lowered to 50°C under a N_2 atmosphere, and 5% CO_2/N_2 (30 ml/min) was introduced into the cell and flowed for 30 min to saturate the catalyst surface. The adsorbed CO_2 spectra were then recorded at different intervals. The gases then changed to CO_2/H_2 with a feed gas ratio of 1:3 and maintained an overall flow (50 ml/min) with N_2 as

balanced with temperature increased to 300ºC at a ramp rate of 10ºC/min. The *in-situ* DRIFTS spectra were recorded at an interval of 50°C during temperature-programmed processes from 50 to 300°C [14].

3.3.3 Catalytic Activity Tests Setup

The catalytic activity tests were performed in a continuous high-pressure fixed-bed reactor **(Figure 3.7)** over a temperature range of 200-260°C, a pressure range of 20-40 bar, and a WHSV range of 2600-10400 ml/g_{cat}.hr to study the effect of process parameters. The calcined catalyst sample was fine ground, pelletized, crushed, and sieved to obtain the desired 40-60 mesh size. The catalyst sample of 3.0 g diluted with SiC beads in a 1:3 weight ratio was loaded into a reactor of 12.7 mm ID and length 400 mm with a thermocouple in the middle of the catalyst bed to sense the actual bed temperature. The *in-situ* reduction of the catalyst samples was performed at 300°C for 2 hours in a pure H_2 stream at 100 ml/min under atmospheric pressure prior to the catalytic activity test. The reactor was flushed with N_2 and cooled to the desired operating temperature. The gas mixture with the feed composition (H_2:CO_2 = 3:1) was then introduced into the reactor to achieve the desired operating pressure [13,14].

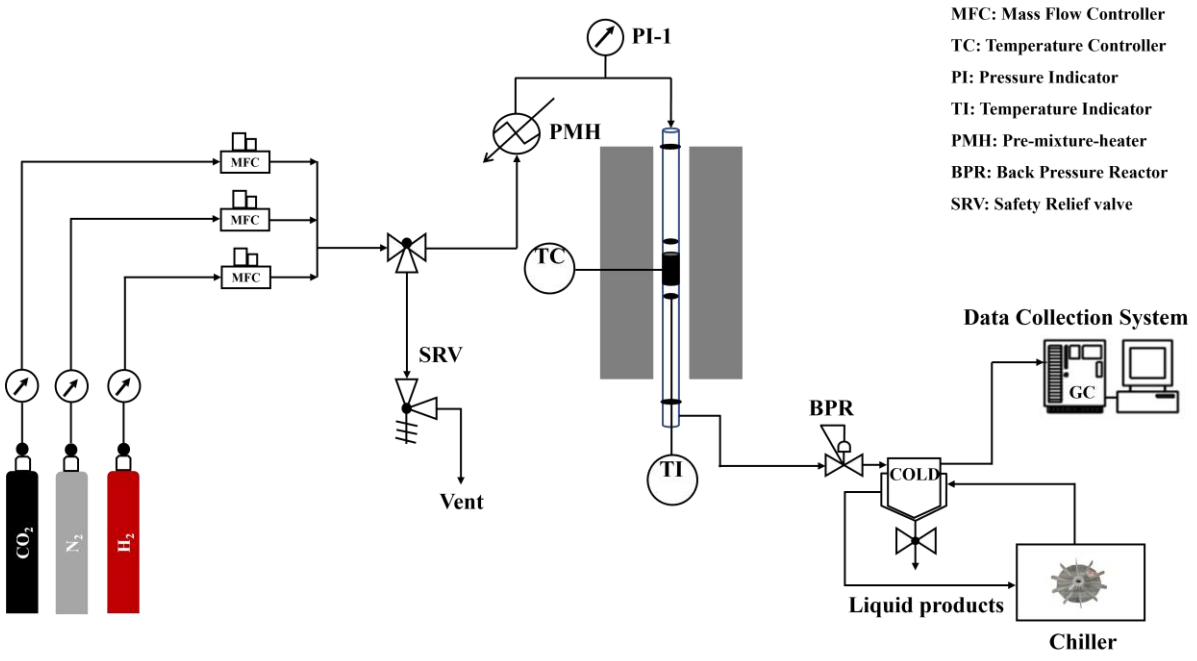


Figure 3.7. *Schematic diagram of the high-pressure fixed-bed tubular reactor setup with an inline gas analyzer.*

After attaining a steady state, the products were analyzed using an online Gas Chromatography (GC 5800, Centurion) equipped with molecular sieves and Porapak-Q packed

columns. To introduce a consistent gas sample flow into the GC, a 0.5 mL stainless steel loop was installed. TCD responds explicitly based on the difference in thermal conductivity between the gas sample and the carrier gas passing through the detector. Herein, the inorganic gas products (CO_2, H_2, N_2, CO) were analyzed by TCD. FID works on the principle of ionization of organic compounds that burn in a hydrogen-oxygen flame. In this work, organic gas products (CH_3OH and CH_4) were analyzed using an FID [13,14]. Detailed, analytical, and optimized conditions for both detectors are given in **Table 3.2.**

Table 3.2. *Optimized analytical conditions for the GC-5800 model.*

Apparatus	GC-TCD	GC-FID
Loop Volume	0.5 mL	0.5 mL
Column	Molecular Sieve	Porapak-Q
Gas carrier & Flow rate	Argon, 56 psi (30 mL/min)	Argon, 56 psi (30 mL/min)
Oven Temperature	60°C (5 min), 15°C/min to 220°C, 220°C (3 min)	60°C (5 min), 15°C/min to 220°C, 220°C (3 min)
Detector Temp	220°C	220°C
H_2 flow rate	--	30 ml/min
Air flow rate	--	60 ml/min

Based on the obtained GC data, the overall carbon balance was performed to calculate the CO_2 conversion, CH_3OH selectivity, CO selectivity, and CH_3OH space-time yield for the CO_2 hydrogenation to methanol.

The **Equations (3.17-3.19)** applied for the calculation were as follows:

$$CO_2\ Conversion, \left(X_{CO_2}, \%\right) = \frac{(Moles\ of\ CO_2)in - (Moles\ of\ CO_2)out}{(Moles\ of\ CO_2)in} \times 100 \quad (3.17)$$

$$Selectivity\ (\%) = \frac{Desired\ Product\ Moles}{Total\ Products\ Moles\ Formed} \times 100 \quad (3.18)$$

$$Methanol\ STY = \frac{CO_2\ Conversion \times MeOH\ Selectivity \times F_{CO_{2,in}} . M_{MeOH}}{W_{cat} \times Molar\ Volume} \quad (3.19)$$

where $(\text{moles of } CO_2)_{in}$ and $(\text{moles of } CO_2)_{out}$ are the number of moles at the inlet and outlet of the reactor, MeOH Selectivity- Methanol Selectivity, $F_{CO_{2,in}}$- volumetric feed flow rate of CO_2 at STP in (ml/min), M_{MeOH}- Molecular weight of methanol (32.04 g/mol), W_{cat} is the weight of catalyst (g), Molar volume-22400 ml/mol. After unit conversion and calculation, the final unit of Methanol STY is expressed as (mg_{MeOH}/g_{cat}.hr) [14].

3.4 DFT Computational details

The first principles DFT calculations of the catalyst precursor were performed using the well-tested CASTEP code [180–183]. The geometry optimization of malachite ($(Cu_2(OH)_2CO_3)$) structure having monoclinic space group $P2_1/a$ with lattice parameters, a = 3.240 Å, b = 11.974 Å, c = 9.502 Å, and β = 98.75° was performed using the ultrasoft pseudopotentials [181,182,184], periodic boundary conditions, k-point sampling techniques, and BFGS scheme [181,182]. The exchange-correlation potential function was described by the Local Density Approximation (LDA) [181,182,185]. The computational parameters were given a maximum energy cutoff set to 380 eV, SCF tolerance was 10^{-6} eV/atom, and the k-point Brillouin zone was set to 3×2×8. The convergence thresholds for the total energy change, maximum force, stress, and displacement were 1×10^{-6} eV/atom, 0.05 eV/Å, 0.05 GPa, and 0.001 Å, respectively [181,182]. Following the same computational method and model, the optimized cell models with different substitution of Mg at total of eight Cu positions were investigated: four Cu_1 positions (labeled as 1,2,3,4) and four Cu_2 positions (labeled as 5,6,7,8) [181,182], as listed in **Figure 3.8.** The total energy and relative formation energies of Mg-substituted malachite were investigated.

DFT calculations for magnesium were performed using malachite as the initial structure; the crystal belongs to a monoclinic symmetry (S.G. P 121/a1) with the following lattice parameters: a = 9.502 Å, b = 11.974 Å, c = 3.240 Å, and β = 98.75° [182]. The malachite structure suggests two different crystallographic copper atoms, i.e., Cu_1 (labeled as 1, 2, 3, 4) and Cu_2 (labeled as 5, 6, 7, 8) in the unit cell **(Figure 3.8).** Previous studies suggest that the Cu2 site is more favourable for Zn and Mg substitution, providing stable structures [181,182]. Similar observations have been obtained here with various levels of Mg substitution (12.5%, 25%, 37.5%, and 50%) performed at the Cu1 and Cu2 sites of the malachite precursor.

The optimized relative formation energies (E_f) for pure and magnesium-substituted malachite structures were determined using the following **Equation 3.20**.

$$E_f = (E_{Tot,\ substituted} + nE_{Cu} - E_{Tot,\ pure} - nE_{Mg})/\ n \qquad (3.20)$$

where $E_{Tot,\ pure}$, and $E_{Tot,\ substituted}$ denote the total energies of pure malachite and Mg-substituted malachite systems, respectively. E_{Cu} and E_{Mg} are the energies of optimized single Cu and Mg

atoms, respectively, and ‘n’ denotes the number of Mg substituted for Cu atoms in the malachite lattice.

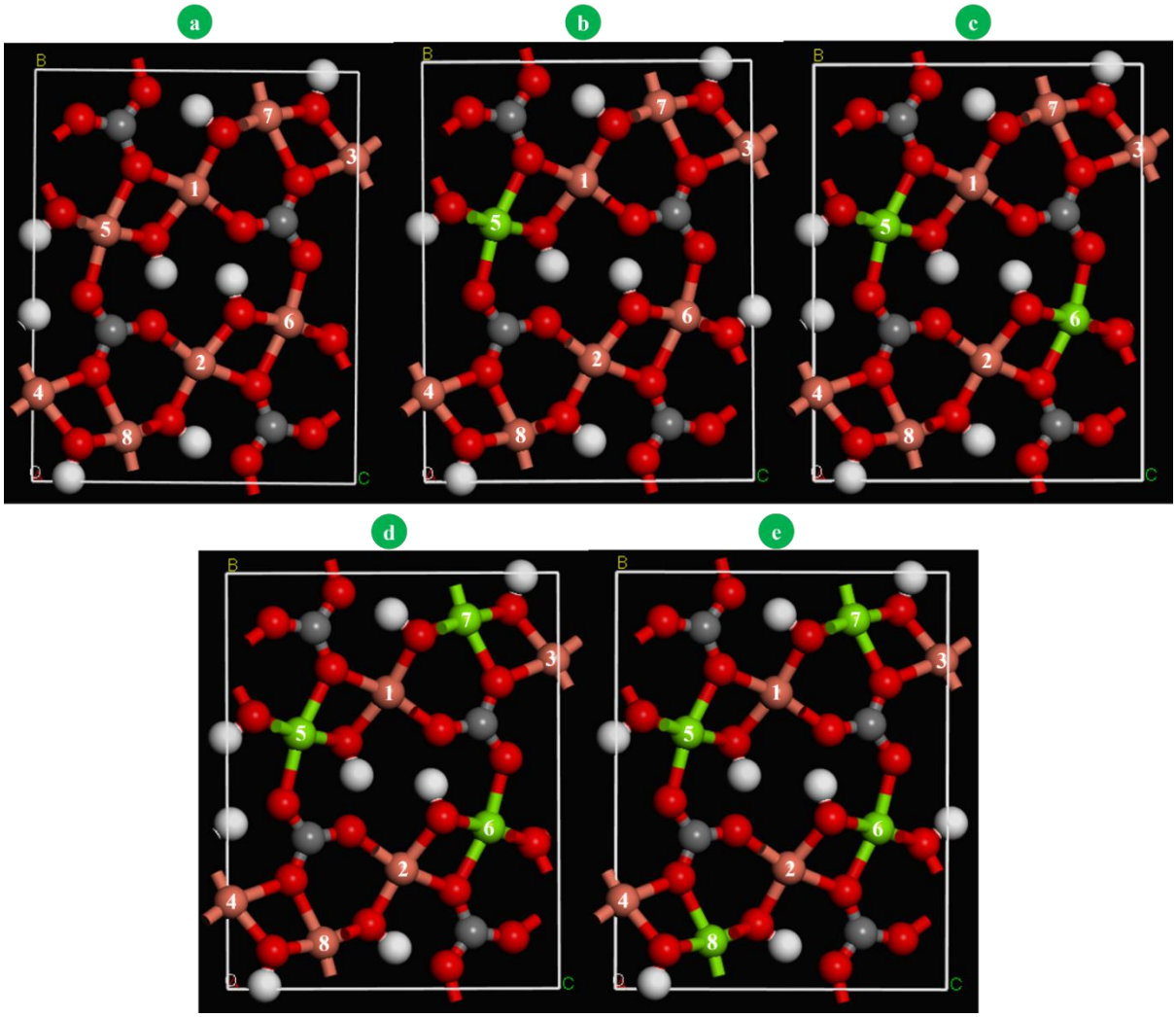


Figure 3.8. *Most stable configurations of* $(Cu_{1-x}Mg_x)_2(OH)_2CO_3$ *systems, (a) x = 0, (b) x = 0.125, (c) x = 0.25, (d) x = 0.375, and (e) x = 0.50. The orange, green, red, grey, and white colours represent Cu, Mg, O, C, and H atoms, respectively.*

3.5 Kinetic modelling and parameter fitting

3.5.1 Selection of a kinetic model framework

The intrinsic kinetics of CO_2 hydrogenation to methanol were modeled using Langmuir-Hinshelwood-Hougen-Watson (LHHW) rate expressions, which explicitly represent adsorption-desorption equilibria and surface reaction steps. Three model families from the literature were implemented to identify the formulation that best describes the behaviour of the CZZ-MCBM catalyst:

Model A- Single-site two-reaction model

Vanden Bussche & Froment (1996) [70] - ($CO_2 \rightarrow CH_3OH$ and RWGS)

Model B - Dual-site two-reaction model

(Graaf et al., 1988) [149] - ($CO_2 \rightarrow CH_3OH$ and RWGS)

Model C - Dual-site three-reaction model

(Graaf et al., 1988) [149] - ($CO_2 \rightarrow CH_3OH$, RWGS, and $CO \rightarrow CH_3OH$)

The single-site LHHW model treats all species as adsorbing on a single type of active site and contains 10 kinetic parameters. The dual-site LHHW models introduce two distinct surface sites- CO_2/CO adsorbs on one site (S_1) while H_2/H_2O adsorbs on another site (S_2). The two-reaction model determines 10 kinetic parameters, while the three-reaction model determines 12 kinetic parameters. These models were initially discriminated based on their accuracy in fitting the random experimental data collected in a laboratory-scaled plug flow reactor. Realistic kinetic parameters were then estimated using a genetic algorithm [70,144,149].

3.5.2 Model assumptions and elementary reaction mechanisms

For completeness and mechanistic clarity, the elementary steps and assumptions used for each model are provided below.

(A) Single-site two-reaction model - Vanden Bussche & Froment (1996) [70]

Assumptions

- CO_2 and H_2 dissociatively adsorb on the same site.
- Formate hydrogenation is the RDS.
- CO_2 adsorption participates in RDS.

Reaction Mechanism

- $H_2(g) + 2s \rightleftharpoons 2H{\cdot}s$
- $H_2O + s \rightleftharpoons H_2O{\cdot}s$
- $CO_2 + s \rightleftharpoons CO_2{\cdot}s$
- $CO_2\ (g) + s \rightleftharpoons O{\cdot}s + CO(g)$ (RDS)

- $CO_2 + O{\cdot}s + s \rightleftharpoons CO_3{\cdot}2s$
- $CO_3{\cdot}2s + H{\cdot}s \rightleftharpoons HCO_3{\cdot}2s + s$
- $HCO_3{\cdot}2s + s \rightleftharpoons HCO_2{\cdot}2s + O{\cdot}s$
- $HCO_2{\cdot}2s + H{\cdot}s \rightleftharpoons H_2CO_2{\cdot}2s + s$ (RDS)
- $H_2CO_2{\cdot}2s \rightleftharpoons H_2CO{\cdot}s + O{\cdot}s$
- $H_2CO{\cdot}s + H{\cdot}s \rightleftharpoons H_3CO{\cdot}s + s$
- $H_3CO{\cdot}s + H{\cdot}s \rightleftharpoons CH_3OH(g) + 2s$
- $O{\cdot}s + H{\cdot}s \rightleftharpoons OH{\cdot}s + s$
- $OH{\cdot}s + H{\cdot}s \rightleftharpoons H_2O{\cdot}s + s$
- $H_2O{\cdot}s \rightleftharpoons H_2O(g) + s$

(B) Dual-site two-reaction Graaf model (1988) [149]

Assumptions

- CO_2/CO adsorb on site S_1
- H_2/H_2O adsorb on site S_2
- RDS = hydrogenation of formate species

Reaction Mechanism

Adsorption

- $CO_2 + s_1 \rightleftharpoons CO_2{\cdot}s_1$
- $H_2 + 2s_2 \rightleftharpoons 2H{\cdot}s_2$
- $H_2O + s_2 \rightleftharpoons H_2O{\cdot}s_2$

CO_2 hydrogenation

- $CO_2{\cdot}s_1 + H{\cdot}s_2 \rightleftharpoons HCO_2{\cdot}s_1 + s_2$
- $HCO_2{\cdot}s_1 + H{\cdot}s_2 \rightleftharpoons H_2CO_2{\cdot}s_1 + s_2$ (RDS)
- $H_2CO_2{\cdot}s_1 + H{\cdot}s_2 \rightleftharpoons H_3CO_2{\cdot}s_1 + s_2$
- $H_3CO_2{\cdot}s_1 + H{\cdot}s_2 \rightleftharpoons H_2CO{\cdot}s_1 + H_2O{\cdot}s_2$
- $H_2CO{\cdot}s_1 + H{\cdot}s_2 \rightleftharpoons H_3CO{\cdot}s_1 + s_2$
- $H_3CO{\cdot}s_1 + H{\cdot}s_2 \rightleftharpoons CH_3OH + s_1 + s_2$

RWGS

- $CO_2 \cdot s_1 + H \cdot s_2 \rightleftharpoons HCO_2 \cdot s_1 + s_2$
- $HCO_2 \cdot s_1 + H \cdot s_2 \rightleftharpoons CO \cdot s_1 + H_2O \cdot s_2$ (RDS)

(C) Dual-site three-reaction Graaf model (1988) [149]

Assumptions

- CO_2/CO adsorb on site S_1 and H_2/H_2O adsorb on site S_2
- RDS = hydrogenation of formate species
- Additional RDS possibility: formate → dioxymethylene → methoxy

Reaction Mechanism

Adsorption

- $CO_2 + s_1 \rightleftharpoons CO_2 \cdot s_1$
- $H_2 + 2s_2 \rightleftharpoons 2H \cdot s_2$
- $H_2O + s_2 \rightleftharpoons H_2O \cdot s_2$

CO_2 hydrogenation

- $CO_2 \cdot s_1 + H \cdot s_2 \rightleftharpoons HCO_2 \cdot s_1 + s_2$
- $HCO_2 \cdot s_1 + H \cdot s_2 \rightleftharpoons H_2CO_2 \cdot s_1 + s_2$ (RDS)
- $H_2CO_2 \cdot s_1 + H \cdot s_2 \rightleftharpoons H_3CO_2 \cdot s_1 + s_2$
- $H_3CO_2 \cdot s_1 + H \cdot s_2 \rightleftharpoons H_2CO \cdot s_1 + H_2O \cdot s_2$
- $H_2CO \cdot s_1 + H \cdot s_2 \rightleftharpoons H_3CO \cdot s_1 + s_2$
- $H_3CO \cdot s_1 + H \cdot s_2 \rightleftharpoons CH_3OH + s_1 + s_2$

RWGS

- $CO_2 \cdot s_1 + H \cdot s_2 \rightleftharpoons HCO_2 \cdot s_1 + s_2$
- $HCO_2 \cdot s_1 + H \cdot s_2 \rightleftharpoons CO \cdot s_1 + H_2O \cdot s_2$ (RDS)

CO hydrogenation

- $CO \cdot s_1 + H \cdot s_2 \rightleftharpoons HCO \cdot s_1 + s_2$

- $HCO{\cdot}s_1 + H{\cdot}s_2 \rightleftharpoons H_2CO{\cdot}s_1 + s_2$
- $H_2CO{\cdot}s_1 + H{\cdot}s_2 \rightleftharpoons H_3CO{\cdot}s_1 + s_2$ (RDS)
- $H_3CO{\cdot}s_1 + H{\cdot}s_2 \rightleftharpoons CH_3OH + s_1 + s_2$

3.5.3 Reactor Model and Assumptions

A one-dimensional plug flow reactor (PFR) model was employed to simulate the fixed-bed catalytic reactor under differential conditions [70,149]. The following assumptions were applied:

- Isothermal and isobaric operation.
- Negligible axial and radial dispersion.
- No catalyst deactivation during the experimental runs.
- Intrinsic kinetics free of transport limitations.
- Adsorption sites are uniform and independent.

3.5.4 Assessment of Transport Limitations

Intrinsic kinetic data must be free from diffusional artifacts. To ensure this, external and internal mass transfer resistances were evaluated [70,95,144,146,147,149]:

- **Mears Criterion (External mass transfer limitation)**

$$(C_m) = \frac{r_{obs}.R_P}{k_c.C_{A,b}} \tag{3.21}$$

where r_{obs} is the observed reaction rate (mol/g/s), R_P is the catalyst particle radius (m), k_c is the external mass transfer coefficient (m/s), and $C_{A,b}$ is the bulk concentration of reactant A (mol/m^3).

- **Weisz-Prater Criterion (Internal mass transfer limitation)**

$$(C_{WP}) = \frac{r_{obs}.R_P^2}{C_s D_{eff}} \tag{3.22}$$

where r_{obs} is the observed reaction rate (mol/g/s), R_P is the catalyst particle radius (m), D_{eff} is the effective diffusivity inside catalyst pores (m^2/s), and C_s is the reactant concentration at the external surface of the catalyst (mol/m^3).

3.5.5 General Rate Law Formulation

- **Arrhenius form for rate constants**

$$k_j = A_j exp\left(\frac{B_j}{RT}\right) = k_{j,o} exp\left(-\frac{E_{a,j}}{RT}\right) \quad (3.23)$$

where k_j is the rate constant, $k_{j,o}$ is the pre-exponential factor, $E_{a,j}$ is the activation energy, R is the universal gas constant, and T is the temperature (K).

- **Van't Hoff form for adsorption constants**

$$K_j = A_j exp\left(\frac{B_j}{RT}\right) = exp\left(\frac{\Delta S^o_{ads,j}}{R}\right) exp\left(-\frac{\Delta H^o_{ads,j}}{RT}\right) \quad (3.24)$$

where K_j is the adsorption constant, $\Delta S^o_{ads,j}$ is the standard entropy, $\Delta H^o_{ads,j}$ is the enthalpy of adsorption, R is the universal gas constant, and T is the temperature (K).

Adsorption constants were estimated for CO_2, CO, and H_2O, as these species strongly influence surface coverage.

- **Thermodynamic equilibrium constants**

$$K_P^o = exp\left(-\frac{\Delta G^o}{RT}\right) \quad (3.25)$$

where $\Delta G^o = \Delta H^o - T\Delta S^o$

$$\ln K_P^o = \frac{1}{RT}\left(a_1 + a_2 T + a_3 T^2 + a_4 T^3 + a_5 T^4 + a_6 T \ln T\right)$$

A simplified version of the Equation for the temperature range 200-300°C is:

$$\log_{10} K^o_{P_j} = \frac{B_1}{T} + B_2 \quad (3.26)$$

where $K^o_{P_j}$ is the equilibrium constant, B_1 and B_2 are the constants for that component, T is the temperature (K).

Table 3.3. *Thermodynamic equilibrium constant of all the reactions as a function of temperature (Adapted from Graaf et al. 1988* [149]*).*

Equilibrium constant	Expression	Units
K_{eq1}	$\log_{10} K_{eq1} = \frac{3066}{T} - 10.592$	bar^{-2} with T in K

K_{eq2}	$\log_{10}K_{eq2} = -\frac{2073}{T} + 2.029$	Dimensionless with T in K
K_{eq3}	$\log_{10}K_{eq3} = \frac{5139}{T} - 12.629$	bar^{-2} with T in K

3.5.6 Model-Specific Rate Expressions

Single-site two-reaction model - Vanden Bussche & Froment (1996)

- **CO_2 hydrogenation to methanol**

$$r_{CO_2-CH_3OH} = \frac{k'_{CH3OH}K'_2K_3K_4K_{H_2}p_{CO_2}p_{H_2}\left[1-\left(1/K_{eq1}\right)\left(p_{CH_3OH}p_{H_2O}/p_{CO_2}p_{H2}^3\right)\right]}{\left(1+\left(K_{H_2O}/K_8K_9K_{H_2}\right)\left(p_{H_2O}/p_{H_2}\right)+\sqrt{K_{H_2}p_{H_2}}+K_{H_2O}p_{H_2O}\right)^3} \quad (3.27)$$

- **RWGS reaction**

$$r_{CO_2-CO} = \frac{k'_1p_{CO_2}\left(1-\frac{p_{H_2O}p_{CO}}{K_{eq2}p_{CO_2}p_{H_2}}\right)}{\left(1+\left(K_{H_2O}/K_8K_9K_{H_2}\right)\left(p_{H_2O}/p_{H_2}\right)+\sqrt{K_{H_2}p_{H_2}}+K_{H_2O}p_{H_2O}\right)} \quad (3.28)$$

Dual-site two-reaction Graaf model (1988)

- **CO_2 hydrogenation to methanol**

$$r_{CO_2-CH_3OH} = k_1K_{CO_2}\left\{\frac{p_{CO_2}p_{H_2}^{3/2}-\frac{p_{CH_3OH}\,p_{H_2O}}{p_{H_2}^{3/2}K_{eq1}}}{\left(1+K_{CO}p_{CO}+K_{CO_2}p_{CO_2}\right)\left[p_{H_2}^{1/2}+\frac{K_{H_2O}}{K_{H_2}^{1/2}}p_{H_2O}\right]}\right\} \quad (3.29)$$

- **RWGS**

$$r_{CO_2-CO} = k_2K_{CO_2}\left\{\frac{p_{CO_2}p_{H_2}-\frac{p_{CO}p_{H_2O}}{K_{eq2}}}{\left(1+K_{CO}p_{CO}+K_{CO_2}p_{CO_2}\right)\left[p_{H_2}^{1/2}+\frac{K_{H_2O}}{K_{H_2}^{1/2}}p_{H_2O}\right]}\right\} \quad (3.30)$$

Dual-site three-reaction Graaf model (1988)

- **CO_2 hydrogenation to methanol**

$$r_{CO_2-CH_3OH} = k_1 K_{CO_2} \left\{ \frac{p_{CO_2} p_{H_2}^{3/2} - \frac{p_{CH_3OH}\, p_{H_2O}}{p_{H_2}^{3/2} K_{eq1}}}{(1+K_{CO} p_{CO} + K_{CO_2} p_{CO_2}) \left[p_{H_2}^{1/2} + \frac{K_{H_2O}}{K_{H_2}^{1/2}} p_{H_2O} \right]} \right\} \quad (3.31)$$

- **RWGS reaction**

$$r_{CO_2-CO} = k_2 K_{CO_2} \left\{ \frac{p_{CO_2} p_{H_2} - \frac{p_{CO} p_{H_2O}}{K_{eq2}}}{(1+K_{CO} p_{CO} + K_{CO_2} p_{CO_2}) \left[p_{H_2}^{1/2} + \frac{K_{H_2O}}{K_{H_2}^{1/2}} p_{H_2O} \right]} \right\} \quad (3.32)$$

- **CO hydrogenation to methanol**

$$r_{CO-CH_3OH} = k_3 K_{CO} \left\{ \frac{p_{CO} p_{H_2}^{3/2} - \frac{p_{CH_3OH}}{p_{H_2}^{1/2} K_{eq3}}}{(1+K_{CO} p_{CO} + K_{CO_2} p_{CO_2}) \left[p_{H_2}^{1/2} + \frac{K_{H_2O}}{K_{H_2}^{1/2}} p_{H_2O} \right]} \right\} \quad (3.33)$$

3.5.7 Parameter Estimation and Optimization

Kinetic parameters were estimated by performing a nonlinear regression between the experimental outlet compositions and the model-predicted values [145].

- **A two-step optimization strategy was employed:**

1. Global optimization using a Genetic Algorithm (GA) to explore the parameter space broadly and avoid local minima.
2. Local refinement using the Sequential Quadratic Programming (SQP) algorithm (via *fmincon*) to achieve precise convergence near the global optimum.

- **Objective Function (minimization):**

$$OF = \sum_{k=1}^{n_{exp}} \sum_{j=1}^{m} (F_{k,j}^{model} - F_{k,j}^{exp})^2 \quad (3.34)$$

where $F_{k,j}^{exp}$ represents the experimental value of the molar flow rate of species j in experiment k. The experimental data are incorporated with corresponding inlet flow rates, inlet compositions, temperatures, and total pressures. On the contrary, $F_{k,j}^{model}$ represents the one

calculated by the numerical model based on the design equation of a fixed-bed reactor. The solver ode15s of MATLAB R2024a software is used to solve the differential equation system.

$$\frac{dF_i}{dw_{cat}} = \sum_{j=1}^{N_r}(r_j v_{ji}) \tag{3.35}$$

where, F_i = Molar flow rate of the component i, w_{cat} = Catalyst weight, N_r = Total number of reactions involved, v_{ji} = Stoichiometric number of the component i in reaction j, r_j = Reaction rate expression.

3.5.8 Model Validation

Model adequacy was evaluated using multiple, complementary approaches:

- **Parity Plots** - experimental vs modeled outlet molar flows (1:1 line) for CH_3OH and CO, ±10% bounds are shown for visual inspection, and ±95% parameter confidence bands are superimposed where possible.
- **Error metrics** - root-mean-square error (RMSE), and the coefficient of determination (R^2).
- **Thermodynamic consistency** - check predicted compositions against thermodynamic equilibrium and ensure no violation of conservation laws.
- **Parameter physicochemical checks**

Table 3.4. *Physicochemical constraints of the kinetic parameters* [144,145,149].

Parameter	Physicochemical constraints
Pre-exponential factor, $\boldsymbol{k_{j,o}}$	$k_{j,o} > 0$
Activation energy, $\boldsymbol{E_{a,j}}$	$E_{a,j} > 0$
Enthalpy of adsorption, $\boldsymbol{\Delta H^o_{ads,j}}$	$\Delta H^o_{ads,j} < 0$
Entropy of adsorption, $\boldsymbol{\Delta S^o_{ads,j}}$	$0 < -\Delta S^o_{ads,j} < S^o_{g,j}$

Chapter 4 Catalyst design using principal component analysis machine learning approach in methanol formation from direct CO_2 hydrogenation

This chapter contains excerpts from the following publication.

1. ***Aakash Bhardwaj†**, Akshdeep S. Ahluwalia†, K.K. Pant, Sreedevi Upadhyayula*, "A principal component analysis assisted machine learning modeling and validation of methanol formation over Cu-based catalysts in direct CO_2 hydrogenation", Separation and Purification Technology, Volume 324, 1 November 2023, 124576.*

4.1 Overview

The catalytic hydrogenation of CO_2 to methanol is a promising strategy to mitigate rising CO_2 emissions while producing a versatile fuel, hydrogen carrier, and chemical feedstock. Copper-based binary and ternary catalysts, especially with promoters such as Zn, Zr, and Al, remain the benchmark systems due to their activity and affordability. However, their performance is strongly influenced by multiple catalyst features (synthesis method, promoter type/loading, dispersion, metal-support interaction) and operating parameters (temperature, pressure, space velocity). Optimizing such a multidimensional system through conventional experimentation alone is both resource-intensive and time-consuming.

Machine learning (ML) provides a powerful approach for analyzing complex catalytic datasets, capturing nonlinear correlations, and guiding both catalyst design and process optimization. Various existing ML models have been reported for methanol synthesis, yet overfitting, redundant descriptors, single-output prediction, or poor generalization on new datasets limit many.

In this chapter, a Principal Component Analysis (PCA)-assisted ML framework is developed for Cu-based binary and ternary catalysts in CO_2 hydrogenation to methanol. A curated dataset of 227 literature points was first analyzed using PCA to assess descriptor relationships and reduce dimensionality. Three algorithms-Artificial Neural Networks (ANN), Support Vector Machine Regression (SVR), and Gaussian Process Regression (GPR) were then trained to

predict four key outputs: CO_2 conversion, methanol selectivity, CO selectivity, and methanol space-time yield (STY).

Model validation was performed using 30 experimental data points obtained from a laboratory-synthesized Cu/ZnO/ZrO_2 catalyst prepared via ultrasonic-assisted reverse coprecipitation and tested in a fixed-bed, plug-flow reactor. Among all algorithms, the ANN demonstrated the best performance ($R^2 > 0.9$ for multiple outputs), while PCA facilitated the identification of data-rich regions, thereby enhancing prediction confidence.

Overall, this PCA-assisted ML framework provides a robust and experimentally validated predictive tool for methanol synthesis, providing a practical pathway to accelerate catalyst development, reduce trial-and-error experimentation, and guide process optimization [13].

4.2 Results and Discussion

4.2.1 Final Evaluation

Having conducted preliminary model evaluations using the collected literature data set and 10-fold cross-validation, we proceed with the best-identified regression method. The final evaluation is assessed on the data derived from the laboratory experiment. The first step is to appropriately normalize the datasets, which is achieved by first estimating the population mean and standard deviation using the training data (the literature dataset) and then applying these derived metrics to normalize both the training and testing data using a Z-score. Furthermore, training with the most promising algorithm (in our case, ANN) is followed by evaluation on the test set. The standard practice of iterating the procedure several times is followed to remove the initialization bias, and the best model based on the lowest MSE is saved [186]. The general scheme followed is given in **Figure 4.1.**

This section first presents the dataset evaluation and then discusses the results of each algorithm, highlighting the most promising one. Finally, the performance of the promising algorithm on the laboratory dataset is presented.

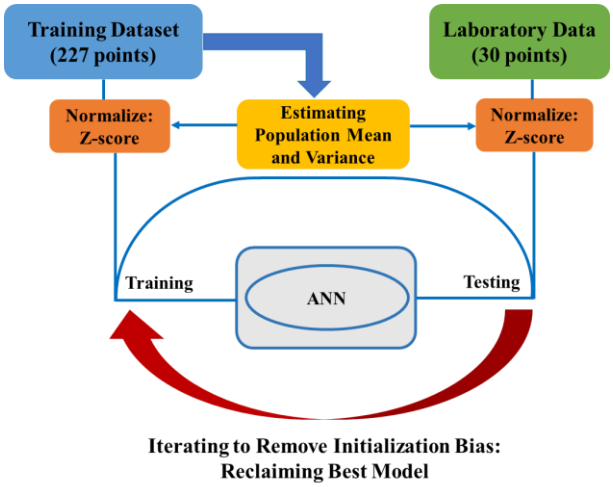


Figure 4.1. *Scheme for model evaluation on testing data.*

4.2.1.1 Dataset assessment

For all input and output parameters, **Table 4.1** and **Table 4.2** present the various statistical metrics for the collected dataset. We can see that the minima and maxima are reasonably separated, with the corresponding variance for each parameter, thereby suggesting that our training set is robust. **Table 4.3** shows the catalytic and physical metrics for the laboratory catalyst.

Table 4.1. *Statistics for Input parameters.*

Input Parameters	Range	Minimum	Maximum	Std. Error	Std. Deviation	Variance
Temperature (°C)	130	170	300	2.15	32.96	1086.66
Pressure (bar)	356	4	360	5.29	81.29	6608.12
BET area (m^2/g)	462.3	8	470.3	5.94	91.28	8331.33
Copper Grain Size (nm)	20.6	3.5	24.1	0.32	4.83	23.33
Dispersion (%)	46.56	0.64	47.2	0.57	8.83	78.03
Space Velocity ($ml/g_{cat}.hr$)	200345	716	201061	2816.97	43275.05	1872730078

Table 4.2. *Statistics for Output parameters.*

Output Parameters	Range	Minimum	Maximum	Std. Error	Std. Deviation	Variance
CO_2 Conversion (%)	33.6	0.1	33.7	0.45	6.94	48.18
MeOH Selectivity (%)	99.1	0.9	100	1.73	26.63	709.2
CO Selectivity (%)	99.1	0	99.1	1.84	27.65	765
MeOH STY ($mmol_{MeOH}/g_{cat}.hr$)	17.43	0.031	17.461	0.21	3.27	10.7

Table 4.3. *Laboratory evaluation of catalytic performance and physicochemical properties of the CZZ-UARCP catalyst.*

Parameters	Values
BET area (m^2/g)	36.9
Cu Loading (wt%)	36
Crystallite size (d_{Cu}, nm)	13
Metal Surface Area (S_{Cu}, m^2/g)	13.1
Dispersion (%)	5.378
WHSV (Space Velocity, $ml/g_{cat}.hr$)	2600
Temperature (°C)	200-250
Pressure (bar)	20-40

4.2.2 Dimensionality reduction using Principal Component Analysis (PCA)

To visualize the collected literature data, Principal Component Analysis was performed to project the data into a lower-dimensional 2D space for visualization. The PCA or the scores plot is shown in **Figure 4.2.** Additionally, the catalysts were color-coded according to the number of other primary metals besides Cu, i.e., binary or ternary, to identify any possible clustering or trends. The scores plot has no clear trend, and the binary catalysts clearly overlap with the space exploited by the ternary ones. The percentage number beside the principal component number represents the percentage of variance explained by that principal component. In total, six principal components were obtained, and a bar plot showing the trend is illustrated in **Figure 4.3.** It can be noted that the first two principal components capture approximately 50% of the total variance, thus, are reasonable for depictional purposes.

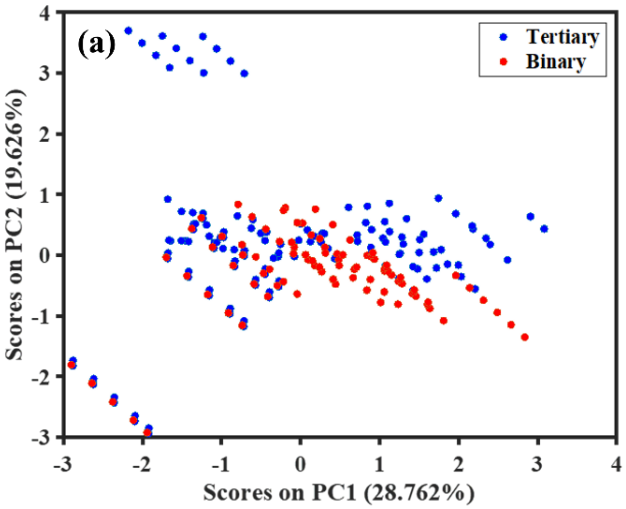


Figure 4.2. *Scores plot for the input parameters onto the first two principal components.*

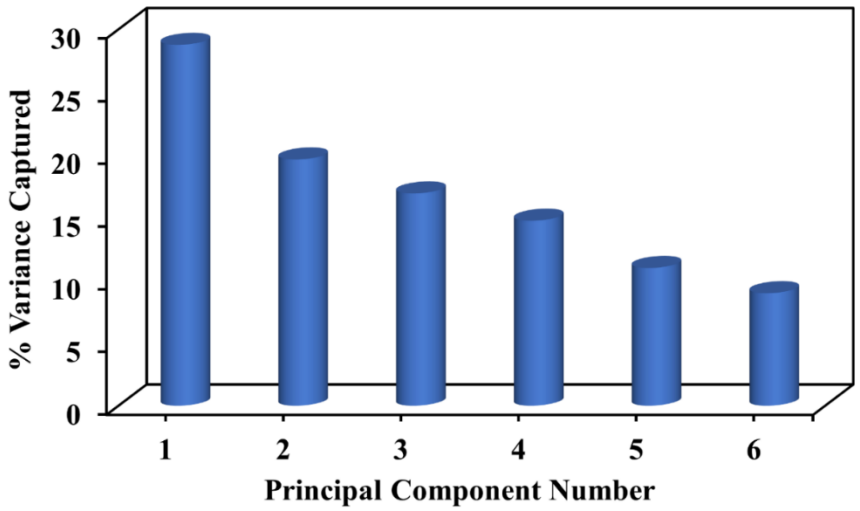


Figure 4.3. *Bar plot for variance explained for each principal component for input variables.*

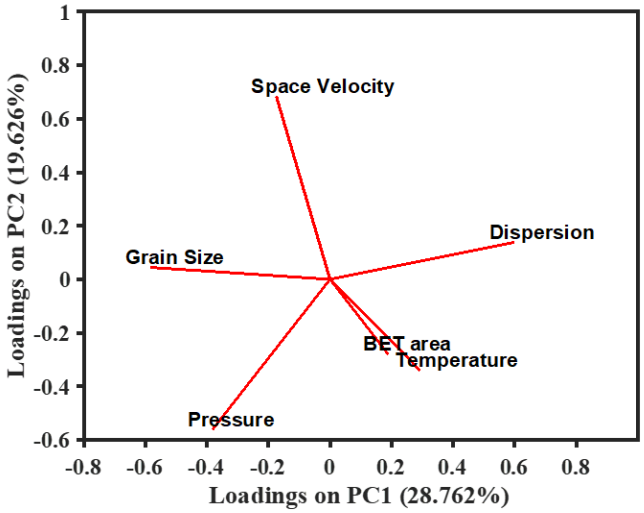


Figure 4.4. *Loadings for the first two Principal Components for input variables.*

Also, an essential feature of the PCA plot is the corresponding loadings, which help identify how much each variable contributes to building any particular PC and its effect. **Figure 4.4** depicts the loadings plot for the first two principal components. From **Figure 4.4,** we can infer that the variable with the most contribution is pressure, followed by space velocity and dispersion. Grain Size, BET area, and temperature are the least contributing ones.

To evaluate the laboratory dataset in terms of any outliers or the extent to which it differs from the collected dataset, it was projected onto the same previous score space, using loadings. The combined plot is as in **Figure 4.5.** We observe that the laboratory ternary catalyst falls close to the space already explored by the previous dataset, so, for now, it is consistent according to a preliminary inspection. Finally, we observed the presence of a promoter in the PCA landscape,

as depicted in **Figure 4.6,** which is an essential parameter that affects catalytic efficiency. In the plot, we observe that almost the entire landscape has been explored without a promoter. However, some essential promoters that primarily help navigate the PCA space are potassium and barium, as well as the use of methanol as a catalytic promoter.

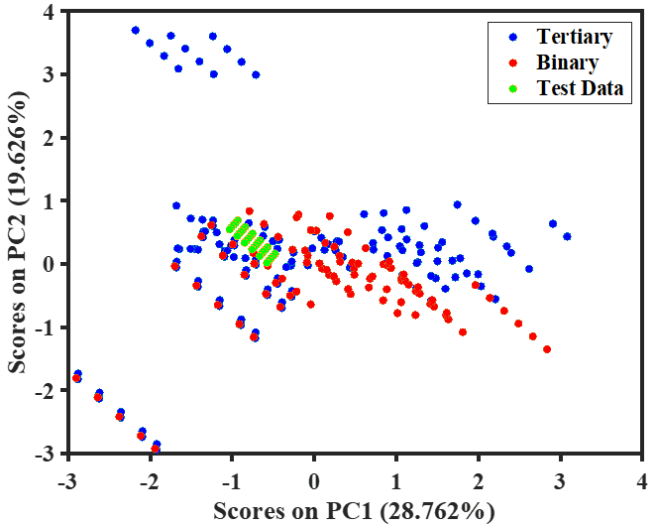


Figure 4.5. *Projection of test data onto the previous scores plot of the training dataset.*

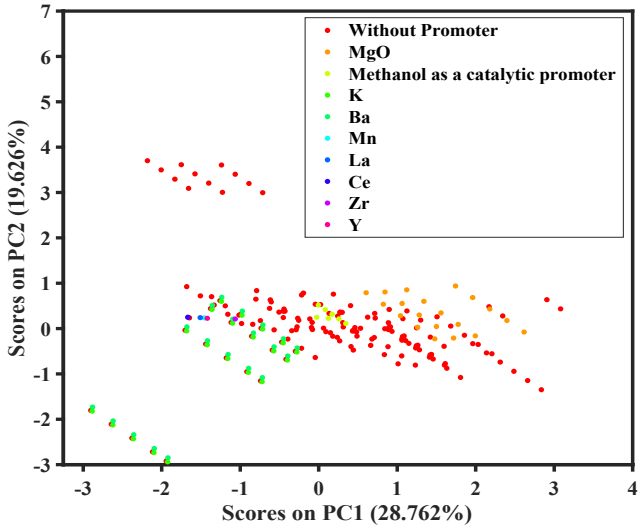


Figure 4.6. *PCA plot for input descriptors of the training dataset characterized by the presence of promoters.*

After verifying the consistency of the input parameters, a similar analysis is conducted for the outputs, serving the same purpose. Four principal components were obtained based on the four variables; the first two components explain more than 85% of the total variance. Thus, a two-dimensional representation, using the scores plot in **Figure 4.7 (a),** is very appropriate for physical visualization. From the loadings plot given in **Figure 4.7 (b),** we understand that for the most important axes, i.e., PC1, the contribution of CO_2 is negligible, in contrast to having

the highest for PC2 as marked by the projection of its vector on the corresponding axes**.** Further, for building PC1, methanol yield and selectivity are opposed to CO selectivity. In PC2, the least contribution is from MeOH selectivity, which has the opposite effect compared to the rest. **Figure 4.8** depicts the overall trend of captured variance by each principal component. The first two being the dominant ones.

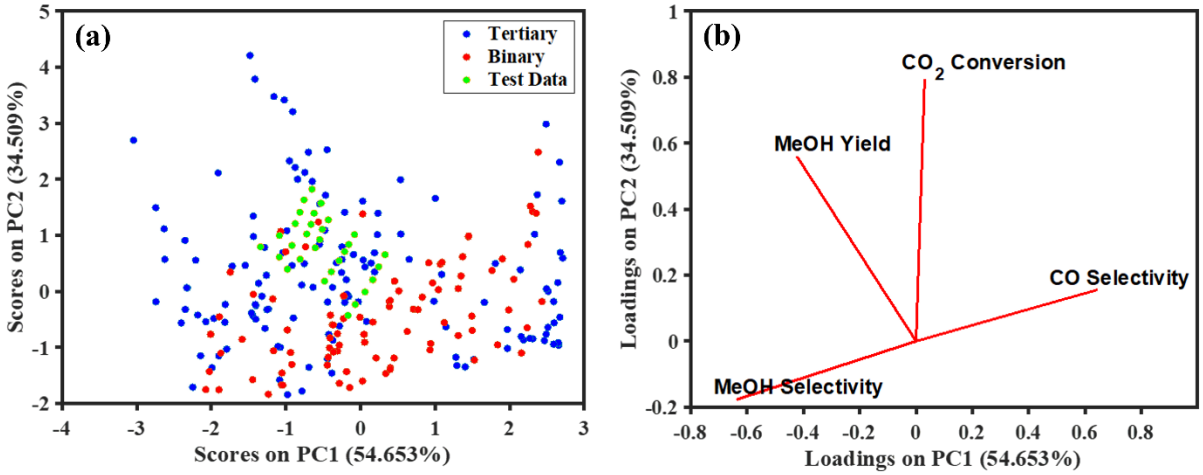


Figure 4.7. (a) *Scores plot for the output parameters onto the first two principal components,* ***(b)*** *Loadings plot for the first two principal components for output variables.*

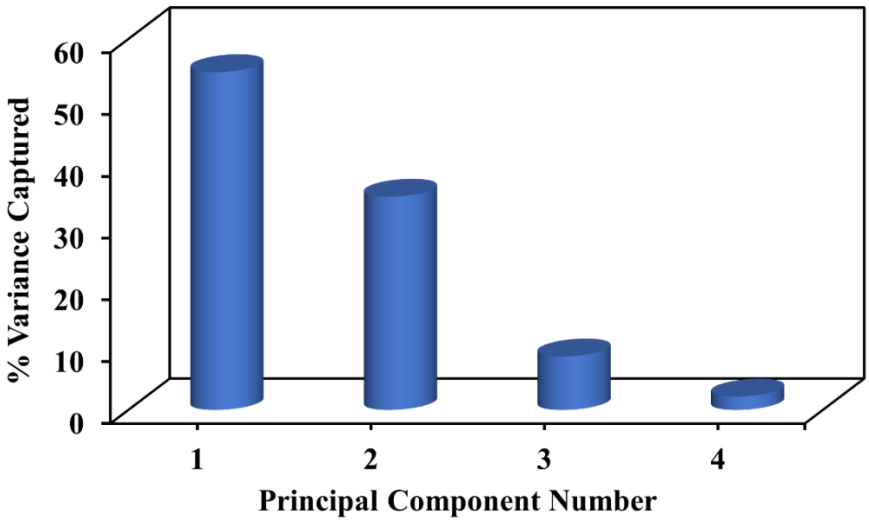


Figure 4.8. *Bar plot for variance explained for each principal component.*

4.2.3 Performance Comparison of the Applied Algorithms

4.2.3.1 Performance of the ANN Model

The ANN was the first algorithm among three (ANN, SVM, GPR) for which the assessed data were used to train the model to determine its accuracy. The scheme followed for each algorithm is discussed in the methods section. **Table 4.4** has the 10-fold results for this particular

algorithm. Here, MeOH selectivity and CO selectivity are modeled with more than 90% accuracy, and the remaining two are also modeled with an R^2 score of more than 0.75. The optimized number of average units is 15.

Table 4.4. *10-Fold results for ANN Algorithm.*

	Optimized Hidden Units	**R^2-CO_2 Conversion**	**R^2-MeOH Selectivity**	**R^2-CO Selectivity**	**R^2-MeOH STY**
Fold-1	13	0.687	0.971	0.929	0.671
Fold-2	12	0.824	0.874	0.868	0.775
Fold-3	19	0.753	0.857	0.881	0.703
Fold-4	14	0.696	0.883	0.936	0.716
Fold-5	20	0.818	0.892	0.953	0.781
Fold-6	17	0.745	0.925	0.895	0.688
Fold-7	18	0.678	0.882	0.912	0.713
Fold-8	16	0.752	0.917	0.894	0.738
Fold-9	17	0.827	0.908	0.939	0.775
Fold-10	7	0.912	0.934	0.958	0.857
Averaged	15.3	0.769	0.904	0.916	0.751

Here, in fact, for CO_2 conversion and MeOH STY, we observe an accuracy greater than 75% for a 5-fold increase. Artificial Neural Networks (ANNs) are flexible and robust modeling tools that can approximate nonlinear relationships provided their transfer, weight, and net input functions are differentiable. Training is carried out by iteratively adjusting weights to minimize error, enabling the network to capture complex input-output dependencies and obtain an MSE value of 20.71 [187,188].

Sensitivity Analysis

Sensitivity analysis of the neural network was performed using Garson's method, based on the model weights. The plots for the sensitivity analysis are illustrated in **Figure 4.9.** The results highlight that copper dispersion is the most influential parameter, emerging as the primary catalyst property governing CO_2 conversion, methanol selectivity, and space-time yield. Pressure is identified as the most critical operating condition, exerting a direct impact on methanol productivity and overall process performance. Together, dispersion and pressure dominate the catalytic outcome.

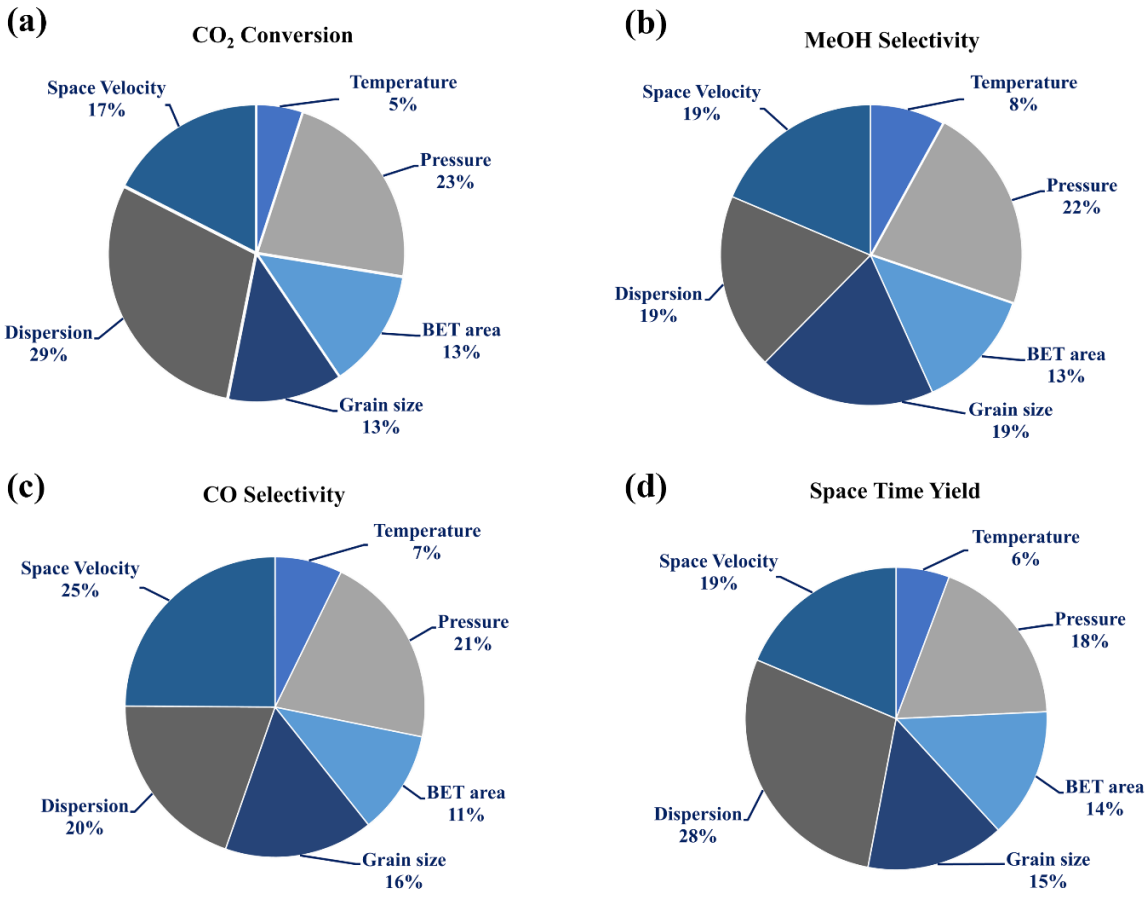


Figure 4.9. (a) *Contribution pie chart for CO_2 Conversion* ***(b)*** *Contribution pie chart for MeOH Selectivity* ***(c)*** *Contribution pie chart for CO Selectivity* ***(d)*** *Contribution pie chart for MeOH STY.*

Among the other variables, space velocity plays a notable role by modulating product distribution, suppressing CO formation while favouring methanol selectivity. In contrast, grain size and BET surface area exert only a moderate influence, acting as secondary parameters that are useful for process fine-tuning but lack decisive control. Interestingly, temperature appeared as the least sensitive parameter in the ANN-derived analysis. This outcome may be attributed to the fact that the experimental dataset was collected within a relatively narrow and optimized temperature window, where the system already operates close to the thermodynamic and kinetic optimum for methanol synthesis. Within such a constrained range, slight temperature variations produce limited incremental changes compared to dispersion or pressure.

However, from a thermodynamic standpoint, temperature remains one of the most sensitive levers for the CO_2-to-methanol equilibrium, with even slight deviations capable of altering methanol selectivity and, consequently, space-time yield. The apparent discrepancy, therefore,

reflects the context-dependent nature of sensitivity: while temperature is a critical variable globally, under the studied operating conditions, the dominant effects of dispersion and pressure overshadow its relative influence.

In summary, effective process optimization should prioritize dispersion and pressure, with space velocity as a secondary lever. Grain size, surface area, and temperature act as supporting variables, although the fundamental thermodynamic role of temperature must still be acknowledged in broader process design.

4.2.3.2 Performance of the SVM Model

For SVM regression, we begin by selecting the kernel function to be used. We have tried Gaussian and polynomial kernels of orders one, two, and three to evaluate the MSE and R values. The lowest MSE is achieved with the second-order kernel, which has a value of 179.56 and a corresponding R-value of 0.893, as depicted in **Figure 4.10;** therefore, it is selected for further regression. We note an interesting observation wherein the third-degree polynomial results in an MSE value (~800) approximately 4 times that observed using other algorithms in the preliminary evaluation. Several reasons could cause this observation, including overfitting, noise sensitivity, parameter tuning, and the curse of dimensionality itself. Out of the previously mentioned possible factors, our results are exempt from noise sensitivity and parameter tuning, as there were no extreme outliers, as observed in **Figure 4.2 (a),** for which the higher-degree kernels are sensitive, explaining the marginal role of noise. Furthermore, our evaluation scheme, as represented in Chapter 3, Material and Methods, in **Figure 3.3,** optimizes the hypermeter comprehensively, thereby mitigating the effects of inappropriate parameter tuning. Thus, the drastic increase occurs due to overfitting and the innate requirement for a higher number of data points to achieve effective generalization, which demands an exponential growth.

The 10-fold modeling results for SVM regression are shown in **Table 4.5.** All variables are modeled with approximately 60% accuracy, except for MeOH selectivity, which is modeled with 75% accuracy. In the 10-fold evaluation, we observe that the performance, as indicated by the MSE values, has not been consistently characterized by abrupt fluctuations (standard deviation of 21.500), in contrast to the ANN, which exhibited consistent fluctuations (standard deviation of 11.342). This highlights the trait of inconsistency in this methodology. The comparison of performance with the ANN is in the next section.

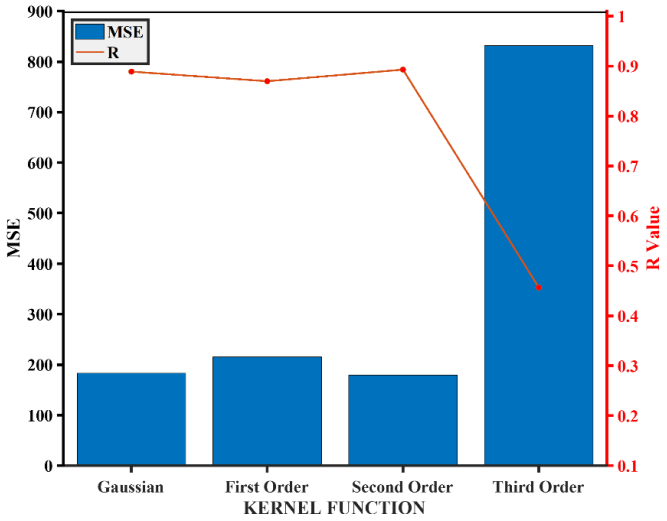


Figure 4.10. *Optimal kernel function selection based on MSE and R values.*

Table 4.5. *10-fold results for SVM regression.*

	R^2-CO_2 Conversion	R^2-MeOH Selectivity	R^2-CO Selectivity	R^2-MeOH STY
Fold-1	0.735	0.843	0.79	0.353
Fold-2	0.747	0.772	0.672	0.81
Fold-3	0.44	0.836	0.76	0.754
Fold-4	0.456	0.782	0.625	0.727
Fold-5	0.238	0.783	0.602	0.393
Fold-6	0.77	0.583	0.491	0.271
Fold-7	0.544	0.515	0.405	0.479
Fold-8	0.628	0.774	0.631	0.829
Fold-9	0.84	0.709	0.597	0.505
Fold-10	0.624	0.863	0.648	0.357
Averaged	0.602	0.746	0.622	0.548

4.2.3.3 Performance of the GPR Model

In Gaussian process regression, two hyperparameters need to be optimized. In **Error! Not a valid bookmark self-reference.,** while assessing each fold, hypermeters were optimized correspondingly, as establishing them uniquely could bias the results towards a particular fold due to its specific innate data distribution.

We observe that three output variables are modeled with more than 90% accuracy, except for CO_2 conversion, which achieves an accuracy of approximately 78%. The corresponding average value for MSE is 33.5. Here again, we note that the performance, as measured by MSE

values across the folds, is consistent with SVM regression (standard deviation of 16.537), but still lower than that of the ANN model.

Table 4.6. *10-fold results for GPR.*

	R^2-CO_2 Conversion	R^2-MeOH Selectivity	R^2-CO Selectivity	R^2-MeOH STY
Fold-1	0.901	0.942	0.954	0.952
Fold-2	0.621	0.921	0.853	0.788
Fold-3	0.754	0.901	0.881	0.949
Fold-4	0.783	0.895	0.932	0.969
Fold-5	0.714	0.911	0.961	0.967
Fold-6	0.899	0.935	0.938	0.963
Fold-7	0.595	0.75	0.753	0.753
Fold-8	0.721	0.969	0.973	0.971
Fold-9	0.886	0.947	0.934	0.926
Fold-10	0.869	0.949	0.942	0.968
Averaged	0.774	0.912	0.912	0.921

4.2.3.4 Comparison Evaluation of ANN, SVM, and GPR

This section draws the final comparison to establish the most promising algorithm for the methanol output modeling statement. The results of both mean squared error (MSE) and R^2 scores for the output variables are summarized in **Table 4.7** and **Table 4.8.** From the perspective of overall model error, ANN clearly outperforms the other two approaches, achieving the lowest MSE value of 20.71, compared to 113.36 for SVM and 33.5 for GPR. Since MSE directly reflects prediction accuracy by penalizing deviations, it provides the most robust indication of model performance. On this basis, ANN is the most reliable algorithm for minimizing predictive error.

Table 4.7. *Evaluation of ANN and GPR performance based on MSE values.*

	ANN algorithm	**SVM algorithm**	**GPR algorithm**
MSE	20.71	113.36	33.5

The R^2 score, however, provide additional nuance. Both ANN and GPR deliver high predictive accuracy for methanol selectivity and CO selectivity (above 0.90), while SVM consistently lags with significantly lower scores across all variables. Notably, GPR achieves the highest R^2

score (0.921) for methanol space-time yield, outperforming ANN (0.751). This highlights the ability of GPR to capture the trend of a numerically smaller but critical performance parameter. However, the advantage in STY prediction does not translate into a lower MSE because STY values are numerically smaller in magnitude and therefore contribute less to the global error metric.

***Table 4.8**. Comparison of the R^2 score for ANN, SVM, and GPR algorithms.*

	R^2-CO_2 Conversion	**R^2-MeOH Selectivity**	**R^2-CO Selectivity**	**R^2-MeOH STY**
ANN	0.769	0.904	0.916	0.751
SVM	0.602	0.746	0.622	0.548
GPR	0.774	0.912	0.912	0.921

An additional benefit of ANN is its ability to backtrack input contributions via sensitivity analysis, something SVM cannot provide, and which is central to this study for guiding experimental optimization. Although GPR also provides strong accuracy, ANN combines competitive R^2 scores with the lowest overall MSE and interpretability, making it the most balanced and practically useful approach.

In summary, SVM shows the weakest performance and is unsuitable for accurate modeling in this context. Both ANN and GPR are competitive, but ANN emerges as the most promising regression method due to its lowest mean squared error (MSE), strong R^2 scores across key outputs, and the added advantage of enabling sensitivity analysis. GPR, however, remains valuable as a complementary approach, particularly for improving the accuracy of methanol space-time yield predictions. This gives weight to MSE as the primary metric, explains the nuances of the R^2 score, and concludes that ANN > GPR > SVM, while acknowledging the specific strengths of GPR in terms of STY.

4.2.4 Experimental validation on the best optimized model

Having established the ANN as the most promising algorithm for modeling methanol synthesis performance. The optimized model was further validated using an independent laboratory dataset comprising 30 experimental points generated over the $Cu/ZnO/ZrO_2$ catalyst. This step not only serves to evaluate the true predictive capability of the model but also demonstrates the impact of expanding the training pool, as the complete literature database (227 points) was employed for final model training. As described in the methodology, the ANN was iteratively

trained to remove the initialization bias, and the best-performing model was identified and saved. Upon testing with the laboratory dataset, the optimized ANN model achieved a lowest MSE of 9.08, which is significantly lower than the 10-fold cross-validated average MSE of 20.71 obtained during preliminary model assessment. This improvement is attributed to the increased number of training points, from 204 (representing 90% of the previously used literature dataset for 10-fold training purposes) to the entire dataset of 227 points, which strengthened the network's ability to learn nonlinear relationships more robustly.

Figure 4.11 (a-d) display the parity plots for the four modeled output variables: CO_2 Conversion, MeOH Selectivity, CO Selectivity, and MeOH STY, comparing predicted values against experimental measurements. These plots provide a direct visual assessment of prediction accuracy, complementing the statistical metrics. The corresponding R^2 scores, summarized in **Table 4.9,** indicate excellent predictive performance for MeOH Selectivity ($R^2 \approx 0.94$) and CO Selectivity ($R^2 \approx 0.95$), in strong agreement with the 10-fold cross-validation estimates. Notably, the CO_2 conversion ($R^2 \approx 0.91$) is substantially higher than that obtained from fold-averaged estimation, indicating that the expanded training dataset significantly enhanced the model's generalization capability for this variable. In contrast, the MeOH STY prediction ($R^2 \approx 0.79$) exhibits only a marginal improvement over its 10-fold estimate, reflecting the inherent difficulty in modeling STY due to its numerical scale, compounded error propagation from conversion and selectivity, and relatively narrower data distribution.

During preliminary dataset assessment using PCA, the influence of low STY values could not be distinctly captured in the score space. This behaviour can be rationalized by the fact that STY ranked as the third most influential descriptor within PC1, and with each variable contributing approximately 25% to the total variance, its statistical weight remained relatively subdued. Furthermore, the limited number of extreme STY values in the experimental dataset restricted the model's exposure to boundary conditions. Given the strongly nonlinear coupling between outputs in multi-target regression, further enrichment of the training dataset, particularly with very low and very high STY regimes, is expected to improve not only STY prediction but also the mutual consistency among all output variables.

A useful comparison can be drawn with the work of Perez-Ramirez et al.[126], who reported an R^2 of ~0.85 for MeOH STY using a much larger dataset of 1425 points, spanning a wide spectrum of active phases, including Cu-, In_2O_3-, Pd-, and ZnO-ZrO_2-based catalysts.

However, their model relied on 12 input descriptors, which, while statistically robust, limit its practicality for rapid experimental screening and preliminary optimization. In contrast, the present work deliberately restricts itself to a compact set of six physically meaningful descriptors, ensuring both model robustness and experimental applicability.

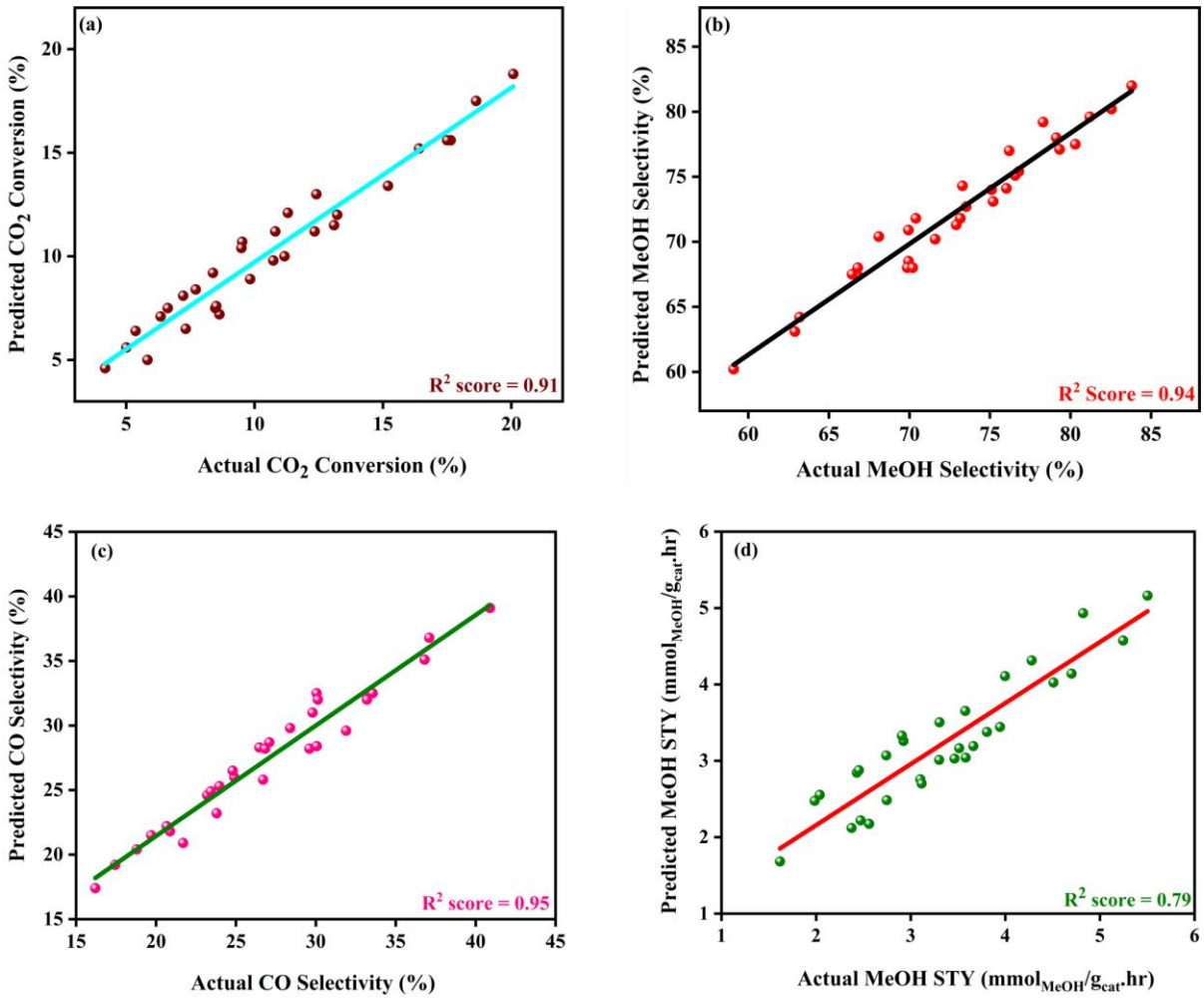


Figure 4.11. *Parity plots comparing experimental and ANN-predicted values for* ***(a)*** *CO_2 conversion,* ***(b)*** *MeOH selectivity,* ***(c)*** *CO selectivity, and* ***(d)*** *MeOH STY using the independent laboratory validation dataset. The solid lines represent ideal parity (y = x), and the corresponding R^2 values indicate the predictive accuracy of the optimized ANN model.*

Table 4.9. *Comparative R^2 scores of output variables for the training and validation datasets obtained using 10-fold cross-validation with the optimized ANN model.*

	CO_2 Conversion	**MeOH Selectivity**	**CO Selectivity**	**MeOH STY**
R^2-value (10-folds)	0.769	0.904	0.916	0.751
R^2-value	0.91	0.94	0.95	0.79

Moreover, in contrast to broad multi-catalyst datasets, the present ANN model is exclusively trained on Cu-based binary and ternary catalysts, which retain direct industrial relevance. Copper-based catalysts have dominated commercial methanol synthesis for the past six to seven decades, initially for syngas conversion and, more recently, for CO_2-based methanol synthesis using $Cu/ZnO/Al_2O_3$ systems. By confining the modeling space to Cu-based systems, the present framework achieves higher mechanistic specificity, improved predictive reliability, and stronger relevance for industrial catalyst optimization.

4.3 Summary and Future Outlook

This chapter establishes a PCA-assisted machine learning framework for the predictive design and performance evaluation of Cu-based binary and ternary catalysts for CO_2 hydrogenation to methanol. A curated dataset of 227 literature data points was systematically analyzed to capture the complex nonlinear relationships between catalyst properties, operating parameters, and reaction outputs. Three algorithms-Artificial Neural Networks (ANN), Support Vector Machine Regression (SVM), and Gaussian Process Regression (GPR) were developed for the simultaneous prediction of CO_2 conversion, methanol selectivity, CO selectivity, and methanol space-time yield (STY). Based on a comprehensive evaluation using R^2 scores and mean squared error (MSE), the ANN emerged as the most reliable and experimentally relevant model due to its lower overall prediction error and the ability to perform sensitivity backtracking of input parameters. Although GPR exhibited competitive R^2 values for multiple outputs, its higher MSE and lack of interpretability limited its practical utility.

The optimized ANN model was experimentally validated using 30 independent laboratory data points generated over a $Cu/ZnO/ZrO_2$ catalyst. The model demonstrated excellent predictive accuracy for methanol and CO selectivity, significantly improved prediction of CO_2 conversion, and moderate accuracy for MeOH STY, the latter being constrained by the limited representation of low-STY regimes in the training dataset. PCA further confirmed that STY contributes relatively weakly to the dominant variance space, explaining its comparatively lower predictability.

Sensitivity analysis revealed that Cu dispersion and operating pressure are the most influential parameters governing catalytic performance, followed by space velocity, while grain size, BET surface area, and temperature play secondary roles within the investigated operating window.

These findings highlight that structural attributes and metal-support interactions significantly influence catalytic behaviour, extending beyond purely thermodynamic effects**.**

Overall, this chapter demonstrates that a PCA-guided ANN framework offers a robust, experimentally validated, and practically applicable tool for catalyst screening and process optimization in CO_2-to-methanol conversion. By focusing exclusively on industrially relevant Cu-based catalysts, the developed model provides high predictive reliability, mechanistic specificity, and direct experimental relevance, thereby enabling accelerated catalyst development with reduced trial-and-error experimentation.

The insights gained from this ML-based screening, particularly the dominant role of metal dispersion, support interaction, and pressure, provide a strong rational basis for the experimental precursor engineering of alternative Cu-based catalyst systems. Accordingly, the next chapter extends this data-guided design philosophy toward the development of Mg-promoted Cu/MgO and Zr-promoted Cu/ZnO/ZrO_2 catalysts, focusing on precursor chemistry, defect modulation, and structure-activity relationships for enhanced methanol synthesis from CO_2.

Chapter 5 Enhanced methanol formation over Cu/MgO catalyst derived from Mg-rich hydroxycarbonate precursor

This chapter contains excerpts from the following publication.

1. ***Aakash Bhardwaj***[a,1]*, Meenakshi Pokhriyal*[a,1]*, Vaibhav Pandey*[a]*, Kamal Kishore Pant*[a]*, Sreedevi Upadhyayula*[a,]**, "Enhanced Methanol Formation over Cu/MgO catalyst derived from Mg-Rich Active Hydroxycarbonate Precursor", ACS Appl. Energy Mater. 2024, 7, 12, 5163-5178.*

5.1 Overview

The hydrogenation of CO_2 to methanol is a promising pathway for carbon capture and utilization, but it requires highly efficient and stable catalysts to overcome the significant energy barrier of reducing CO_2. While Cu/ZnO-based systems remain the industrial benchmark, the role of alternative promoters such as MgO has attracted increasing interest. MgO enhances catalyst performance by boosting surface basicity, increasing defect sites, stabilizing Cu dispersion, and inhibiting side reactions such as the reverse water-gas shift. Recent experimental and computational studies also highlight the Cu-MgO interface as an active site for methanol synthesis.

A critical aspect of Cu-based catalyst preparation is the choice of precursor, as the "chemical memory" effect strongly links precursor phases with the final catalyst structure and activity. For Cu/ZnO systems, precursor phases such as zincian malachite are well established; however, the incorporation of Mg^{2+} into crystalline Cu hydroxycarbonates has been far less explored. Conventional co-precipitation methods limit Mg incorporation to ~18 at.% due to solid-state restrictions, typically leading to amorphous phases or mixed precursors. In contrast, the naturally occurring mcguinnessite, $(CuMg)_2(OH)_2CO_3$, represents a stable Mg-rich rosasite analogue, but synthesizing this phase in a controlled laboratory setting has remained a challenge.

This chapter addresses this gap by employing a one-pot hydrothermal synthesis route to stabilize mcguinnessite-like $(CuMg)_2(OH)_2CO_3$ precursors with substantially higher Mg incorporation. First-principles formation-energy calculations for compositions spanning x = 0.0-0.5 in $(Cu_{1-x}Mg_x)_2(OH)_2CO_3$ were used to predict stability trends, which were then

experimentally validated. Catalysts derived from the hydrothermal precursor were benchmarked against those prepared via conventional co-precipitation and wet impregnation to assess the influence of synthesis method on structure and performance.

The hydrothermally prepared Cu/MgO catalyst exhibited superior catalytic performance, achieving 15.17% CO_2 conversion, 68.49% methanol selectivity, and a methanol STY of 98.11 $mg_{MeOH}/g_{cat}.hr$ at T = 240°C, P = 40 bar, and WHSV = 2600 $ml/g_{cat}.hr$. It also exhibited excellent durability, maintaining remarkable activity over a 100 hr stability test. *In-situ* DRIFTS measurements further revealed the formation of key surface intermediates and demonstrated a favourable mechanistic pathway for methanol synthesis.

Overall, this chapter establishes, for the first time, the successful stabilization of mcguinnessite-based precursors for Cu/MgO catalysts and demonstrates how tailored precursor chemistry can drive desirable structure-activity relationships. The integration of hydrothermal synthesis, detailed characterization, catalytic testing, and computational insights provides a comprehensive framework for advancing Mg-promoted Cu catalysts for CO_2 hydrogenation to methanol.

5.2 RESULTS AND DISCUSSION

5.2.1 Structural identification of precursor phase

The structures of malachite precursors with magnesium substitution, denoted as $(Cu_{1-x}Mg_x)_2(OH)_2CO_3$ (x = 0, 0.125 (1/8), 0.25 (2/8), 0.375 (3/8), and 0.50 (4/8)), have been investigated through a combination of first-principles calculations employing DFT followed by experimental trials. The experimental evidence for zinc substitution has already been validated by first principles studies by Li et al [181]. The calculation results obtained from the geometry optimization of a structure show that $(Cu_{6/8}Mg_{2/8})_2(OH)_2CO_3$, in which 25% Mg is substituted for Cu at the Cu_2 site, is the most thermodynamically stable structure, owing to its lowest formation energy (-1.863 eV) with the weakest Jahn-Teller distortion. The formation energy calculated for different configurations follows the stability order as $(Cu_{6/8}Mg_{2/8})_2(OH)_2CO_3$ > $(Cu_{7/8}Mg_{1/8})_2(OH)_2CO_3$ > $(Cu_{4/8}Mg_{4/8})_2(OH)_2CO_3$ > $(Cu_{5/8}Mg_{3/8})_2(OH)_2CO_3$. The lower stabilities observed in compositions with higher Mg substitutions might indicate the malachite structure's limited flexibility in forming magnesian malachite due to structural constraints. These findings align well with the common occurrence

of the mineral mcguinnessite in the Earth's crust, demonstrating notable flexibility in allowing higher magnesium levels [189]. On the other hand, the first-principles calculations investigating zinc substitution in malachite suggested that $(Cu_{6/8}Zn_{2/8})_2(OH)_2CO_3$ precursor presents the most stable arrangement, also consistent with experimental observations [181,182] and does not coincide with the naturally occurring composition of rosasite (Zn≥50 %). Following these observations, the experiments for the Mg-incorporated precursor formation were performed for $(Cu_{1-x}Mg_x)_2(OH)_2CO_3$ (x = 0, 0.125 (1/8), 0.25 (2/8), 0.375 (3/8), and 0.50 (4/8)) compositions using a simple one-step hydrothermal method. The progress of the precursor phase formation under different conditions has been followed by recording the powder X-ray diffraction (PXRD) patterns. It has been found that with the right choice of carbonate source and with the correct set of reaction conditions, the desired phase can be achieved under hydrothermal treatments. Initial experiments conducted at various temperatures (120°C to 180°C) for durations of 6-20 h showed a single crystalline phase formation only at 150°C for 16 h; a detailed description is provided in **(Figure 5A1 (a)).** After optimizing the reaction conditions and selecting the right carbonate source, experiments were conducted to explore different levels of Mg substitutions.

Figure 5.1 (a) and **Figure 5A1 (b)** illustrate the PXRD patterns for precursor compositions ($(Cu_{1-x}Mg_x)_2(OH)_2CO_3$) with x = 0, 0.125, 0.25, 0.375, and 0.50. Notably, as Mg substitution increased, an intensity reversal of (*020*) and (*120*) occurred, supporting the Mg substitution. More prominent changes were observed in the (*20T*) reflection with increasing Mg content, manifesting as a shift to higher 2θ angles attributed to structural alterations due to the substitution of the Jahn-Teller ion Cu^{2+} with non-Jahn-Teller Mg^{2+} ions **(Figure 5A2).** In this instance, the intensity of the (*20T*) reflection in each composition was nearly suppressed, while a simultaneous significant increase in the intensity of reflections near 34.5° was observed. As the substitution level reaches 50%, the intensities in the 34-37° region become more prominent, matching well with the relative intensities observed in naturally occurring mineral data **(Figure 5.1 (a)).** These observations contrast with a previous study where Mg ion substitution beyond 18% resulted in a mixture of magnesian malachite and mcguinnessite [190]. The PXRD patterns of the single-phase products could readily be indexed in monoclinic symmetry (S.G. $P12_1/a1$) with the refined lattice parameters of a = 12.15157(5); b = 9.20767(3); c = 3.19374(8) Å; β = 94.999 (5)°. Moreover, the broad peaks in the PXRD pattern of CM50 indicated a small average crystallite size of 32 nm calculated using Scherrer's formula. In

contrast, similar experiments conducted using the conventional co-precipitation method resulted in the formation of an amorphous phase for a Cu/Mg ratio of 70/30 identified as magnesian georgeite, as reported earlier [93]. Increased magnesium concentrations did not result in crystalline formation; instead, the precipitate transitioned to a deep brown hue before crystallization occurred. This colour change was attributed to the exceedingly high pH necessary for magnesium precipitation, suggesting the conversion to CuO through oxolation.

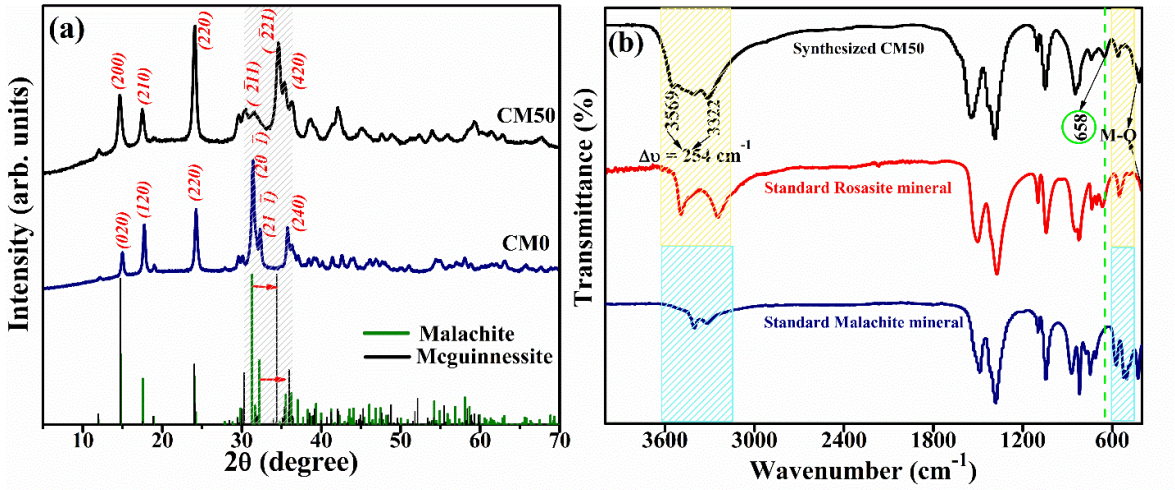


Figure 5.1. (a) *PXRD patterns of Cu-Mg hydroxycarbonate precursor with nominal substitution of Mg to be 50% (CM50) and no substitution (CM0), in comparison to the line diagrams of standard Malachite (PDF No. (PDF No.-41-1390) and McGuinnessite (AMCSD-0011133) structures, and* ***(b)*** *FTIR of Cu-Mg hydroxycarbonate precursor in comparison with the standard data (Extracted from RRUFF database No. R050508 (malachite), R050294 (rosasite)).*

The FTIR spectrum of CM50 samples, compared to the data extracted from the database of standard minerals (rosasite and malachite), is presented in **Figure 5.1 (b).** The bands at higher wave numbers at 3569 and 3322 cm^{-1} are ascribed to the hydroxyl stretching modes of two distinct crystallographic sites of OH^- in the lattice. The spectrum of CM50 closely resembles that of standard rosasite, indicating a higher substitution of Mg^{2+} ions, in agreement with the PXRD results. It is worth noting that a significant disparity between the spectra of malachite and rosasite occurs within the 600-700 cm^{-1} range. A band at 658 cm^{-1} in the CM50 and standard rosasite spectra suggests structural alterations caused by M^{2+} substitution, serving as a distinctive feature for forming a rosasite-like structure [191].

5.2.2 Physical and Chemical Properties of the final catalyst

Figure 5.2 (a) shows the PXRD pattern of the calcined CM50 (CM-HT) compared with the other two calcined samples for assessment purposes. All three samples showed the formation

of CuO, i.e., tenorite phase (PDF No. 80-0076), along with the slight presence of cubic MgO phase (PDF No. 87-0653) in CM-HT and CM-IMP samples. The broad nature of the reflections of the CM-HT sample indicates a smaller crystallite size compared to the other two samples. The BET surface area of all three samples belonged to type-IV isotherm (**Figure 5.2 (b)),** and the particle size varied in the order HT < CP < IMP. The surface area, along with other physicochemical details of the samples, is summarized in **Table 5.1**. It could be observed that the graph shows that the CM-HT catalyst formed by the hydrothermal method has a smaller crystallite size than the other two catalysts.

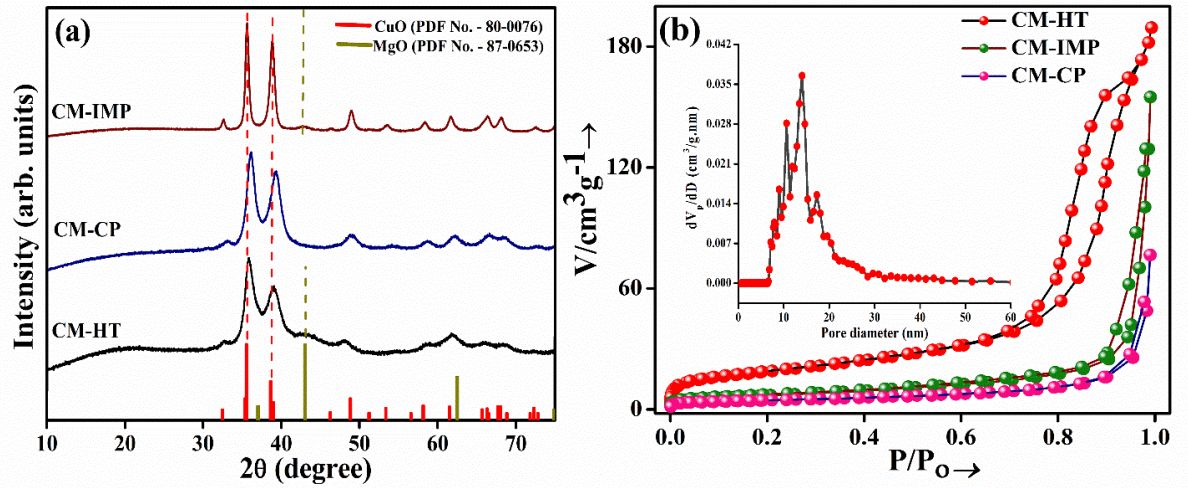


Figure 5.2. (a) *PXRD patterns, and* ***(b)*** *N_2-adsorption-desorption isotherms of calcined samples prepared via different methods. Inset in (b) shows the pore size distribution curve for the CM-HT sample.*

Table 5.1. *Structural and textural properties of the catalysts.*

Catalyst	S_{BET}[a] (Calcined) (m^2/g)	V_p[a] (cc/g)	d_{CuO}[b] (calcined) (nm)	d_{Cu}[b] (reduced) (nm)	SA_{Cu}[c] (m^2/g)	D_{Cu}[c] dispersion (%)	Surface atomic Metal (at.%)[d]	
							Cu	Mg
CM-HT	66.84	0.287	8.5	7.1	20.62	5.78	55.20	
CM-CP	16.46	0.117	9.9	8.3	5.36	1.34	72.12	
CM-IMP	23.7	0.233	17.0	13.1	7.01	2.04	50.43	

[a]From N_2 Physisorption (multipoint BET method), [b]Calculated using Scherrer Formula, [c]Measured using N_2O chemisorption method, and [d]atomic percent obtained from ICP-MS.

The chemical state and elemental surface composition of all the CM samples are confirmed using the XPS technique. The deconvoluted curves at binding energies indexed in the range of 933.4-933.8 eV and 953.5-953.9 eV are attributed to the states of Cu $2p_{3/2}$ and Cu $2p_{1/2}$, respectively, in **Figure 5.3 (a)** in all three samples. These bands are coupled with corresponding

satellite peaks at 942.8 eV and 962.6 eV, respectively [91]. These characteristics are typical of Cu in the +2-oxidation state as CuO. **Figure 5.3 (b)** spectra revealed that the single band in the range of 48-54 eV in all three calcined samples is assigned to Mg 2*p*, clearly demonstrating that magnesium species were present as MgO [192]. **Figure 5.3 (c)** displays the XPS spectrum of O 1*s*; the asymmetric shape of the peak was deconvoluted into two peaks at 531.2 and 529.2 eV, assigned to the chemisorbed oxygen (O_{ads}), and the oxygen belonging to the lattice (O_L) respectively [91,193]. In general, an adsorbed peak is a result of surface vacancies in the catalyst, which is closely related to the presence of MgO in the sample and is in total agreement with the literature [91]. The $O_{ads}/(O_{ads}+O_L)$ ratio can be used to determine the relative oxygen vacancy concentration (C_{OV}) [110,193], in the present case, which was found to be maximum for CM-HT (91.46 %), followed by CM-IMP (80.10 %) and CM-CP (79.02 %). These results revealed that more Mg in the sample is beneficial for inducing defects in the crystal structure, which would ultimately be favourable to modulate electronic properties at the metal-oxide interface, i.e., Cu-MgO [194].

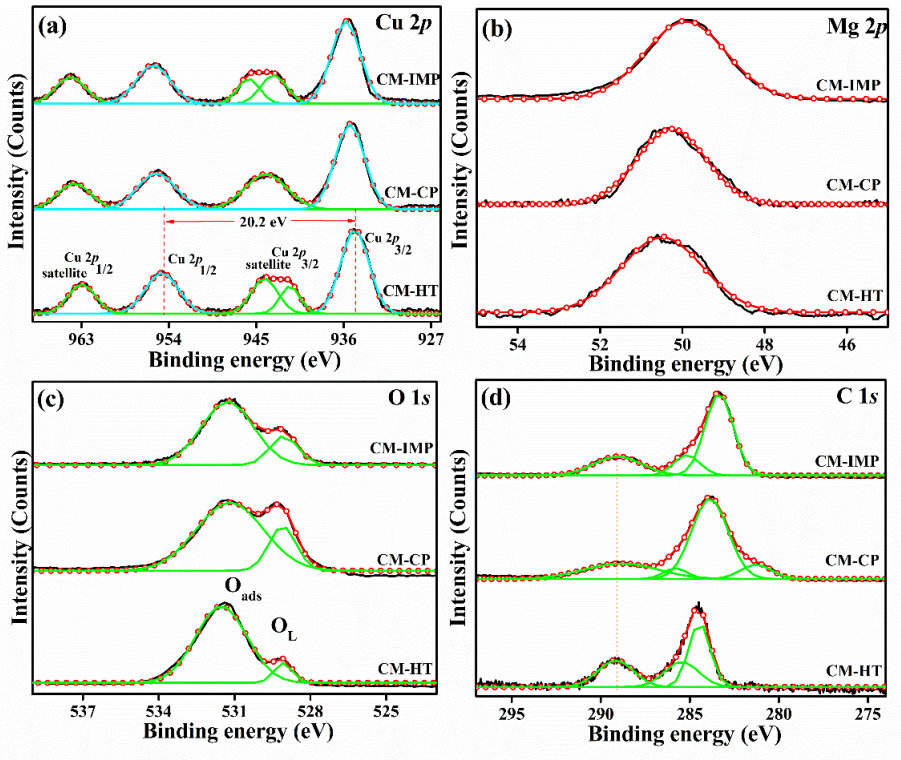


Figure 5.3. *High-resolution XPS spectrum of* ***(a)*** *Cu 2p,* ***(b)*** *Mg 2p,* ***(c)*** *O 1s, and* ***(d)*** *C 1s of the calcined catalyst samples.*

Interestingly, the introduction of such defects also boosts the reduction behaviour of CuO particles, consequently lowering the reduction temperature; these observations are in good

agreement with the existing reports and temperature-programmed reduction (TPR) results discussed in the next section [94,98]. C1*s* spectrum in **Figure 5.3 (d)** showed that there are mainly two peaks near binding energies of 284.6 eV and 289 eV. The lower binding energy peak is assigned to the C1*s* peak of the reference, and the peak at high binding energy in all samples indicates -C=O formed during the annealing of the samples. Furthermore, the sub-peak in the CM-CP catalyst at 281.5 eV corresponds to carbides formed in the sample during calcination, likely due to the amorphous nature of the precursor [192]. No other peaks were observed in the CM-HT sample, indicating the absence of other carbon moieties.

H_2-TPR of the samples provided insight into the promotional effect of the Mg^{2+} dopant on the reducibility of the copper species. The profiles of calcined Cu/MgO catalysts in the temperature range of 90-400°C are depicted in **Figure 5.4**, and the corresponding H_2 consumption data are shown in **Table 5.2**. Each TPR profile was analyzed to identify characteristic peaks associated with distinct reduction processes and interactions with the support. The reduction peaks of CM-HT, CM-CP, and CM-IMP mainly consisted of two peaks with asymmetries in the profiles arising from the interaction between CuO and MgO. They were found to be the maximum for the CM-HT sample. To gain deeper insights into the CuO-MgO interactions, the reduction profile in the range of 50-200°C was further deconvoluted into two subsequent peaks (α and β). This represents a two-stage reduction of Cu^{2+} to Cu^{+} and Cu^{+} to Cu^{o}. The peaks in the lower-temperature range indicate a weak interaction between CuO and the MgO support, corresponding to the reduction of highly isolated, smaller, and more dispersed CuO species [94,195]. The third peak (γ) at higher temperatures signifies strong metal-support interaction, representing the reduction of either interface CuO or bulk CuO, requiring elevated temperatures for reduction [195]. It is worth mentioning that throughout the temperature range, the reduction peaks of copper oxide exhibit asymmetry and broadness, indicative of a broader particle size distribution [94]. These findings provide insights into the intricate CuO-MgO interactions within the catalysts synthesized through different methods.

The variation in H_2 consumption (peaks α and β) is intriguing, considering they share similar constituents. CM-HT exhibits the highest consumption (69.39%), followed by CM-IMP (66.98%) and CM-CP (53.45%). Notably, CM-HT exhibits lower reduction temperatures and a higher maximal H_2 consumption (in α and β), indicating potentially smaller and more uniformly dispersed CuO crystallites with fewer CuO aggregates, a conclusion in good agreement with the XRD results. Further, the total H_2 consumed by all synthesized catalysts

exceeds the theoretically expected H_2 consumption for complete CuO reduction, with CM-HT showing the highest (7.23 mmol/g). This excess H_2 consumption beyond theoretical values may be attributed to hydrogen spillage over the reduced Cu surface [94,196]. Such spillage potentially aids in MgO support reduction, creating oxygen vacancy defect sites, a phenomenon reported on metal oxide support reduction due to a similar effect [196].

Table 5.2. *Quantitative data of H_2-TPR analysis of Cu/MgO catalysts.*

Catalyst	T (°C) (α)	Area (%)	T (°C) (β)	Area (%)	T (°C) (γ)	Area (%)	Total H_2 consumed (mmol/g)[a]	H_2/Cu
CM-HT	122.7	50.47	144.6	18.92	301.6	30.59	7.23	1.05
CM-CP	129.7	39.5	148.5	13.95	294.3	46.5	7.07	1.02
CM-IMP	136.8	25.75	151.7	41.23	342.7	33.0	7.16	1.04

[a]*Theoretical H_2 consumed = 6.91 mmol/g*

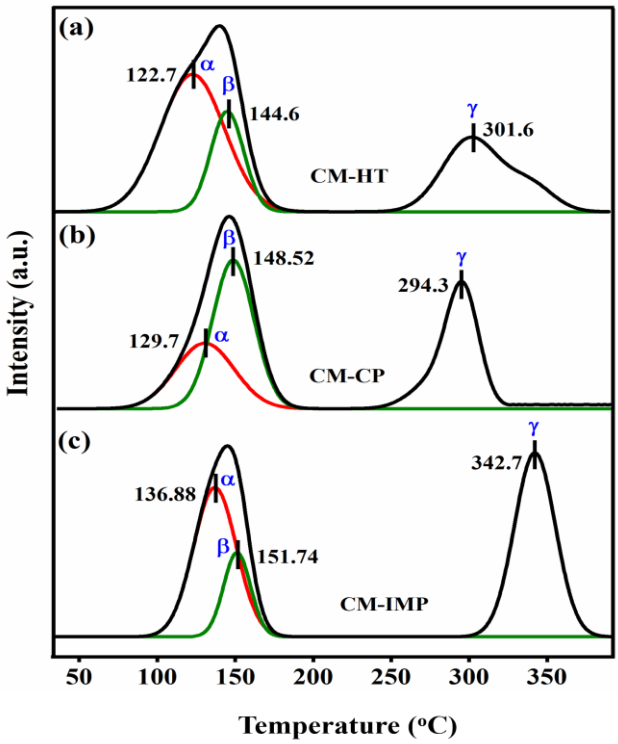


Figure 5.4. *H_2 -TPR profiles of calcined catalyst samples **(a)** CM-HT, **(b)** CM-CP, **(c)** CM-IMP.*

The surface basicity of Cu/MgO catalysts was examined through CO_2-TPD analysis. **Figure 5.5 (a)** illustrates CO_2-TPD profiles of CM-HT, CM-CP, and CM-IMP catalysts in the temperature range of 80-550°C. Commercial MgO's TPD analysis was also recorded, and the profiles showed three temperature ranges: 80-200°C for weak sites (α), 200-400°C for medium sites (β), and > 400°C for strong sites (γ). CM-HT and CM-IMP contain weak (100-150°C)

and strong basic (>400°C) sites, while CM-CP contains weak, medium, and strong sites. These weak, medium, and strong basic sites confirm the formation of bicarbonate, bidentate, and monodentate carbonate, respectively. Bicarbonate formation proceeds from hydroxyl group interactions, while bidentate and monodentate carbonate formation resulted from CO_2 bonding with Mg^{2+}-O^{2-} pairs and low coordination oxygen atoms (O^{2-}) ions, respectively **Figure 5.5 (b)** [197]**.** Interestingly, CM-HT and CM-IMP lack moderately basic sites (β) compared to commercial MgO, as interaction of copper metal with MgO creates a well-dispersed catalyst surface. Additionally, bidentate carbonate species on medium-basic sites, coupled with H_2 adsorption on Cu surfaces, generate CO and H_2O via the reverse Water-Gas Shift (RWGS) reaction[198]. The hydrogenation of unidentate carbonate (i.e., strong basic sites) leads to methanol production through formate pathways, and consequently, their presence proves advantageous in methanol synthesis through CO_2 hydrogenation [90]. Hence, the absence of medium basic sites and the presence of strong basic sites not only inhibit the RWGS reaction but also increase the efficiency of methanol formation by preventing the catalyst deactivation [90,198]. Notably, the strong basic sites (γ) in CM-HT and CM-IMP align with the XPS measurements, showing maximal low coordination O^{2-} anions (or defects/unsaturated ions). Additionally, the total CO_2 desorption followed the order: CM-HT (1647 μmol/g) > CM-IMP (603 μmol/g) > CM-CP (505 μmol/g). CM-HT, with maximum total basic sites, correlates with the BET data, where a higher surface area offers more basic sites [90,98]. To confirm this, strong basic site densities were calculated and found to be 23.11, 21.94, and 19.26 μmol/m^2 for CM-HT, CM-IMP, and CM-CP, respectively. CM-HT showed enhanced, strong basic sites and density, indicating superior metal-support interaction. The amount of desorbed CO_2 for all samples is listed in **Table 5.3**.

Table 5.3. *Quantitative data of CO_2-TPD analysis of Cu-MgO catalysts.*

Catalyst	T (°C) (α)	CO_2 desorbed (μmol/g)	T (°C) (β)	CO_2 desorbed (μmol/g)	T (°C) (γ)	CO_2 desorbed (μmol/g)	Total CO_2 desorbed (μmol/g)	Density of strong basic sites (μmol/m^2)
MgO	147	130 (4.4%)	382	1193 (40%)	465	1656 (55.6%)	2979	-
CM-HT	135	102 (6%)	-	-	479	1545 (94%)	1647	23.11

CM-CP	146	31 (6%)	379	158 (31%)	429	316 (63%)	505	19.26
CM-IMP	143	83 (14%)	-	-	468	520 (86%)	603	21.94

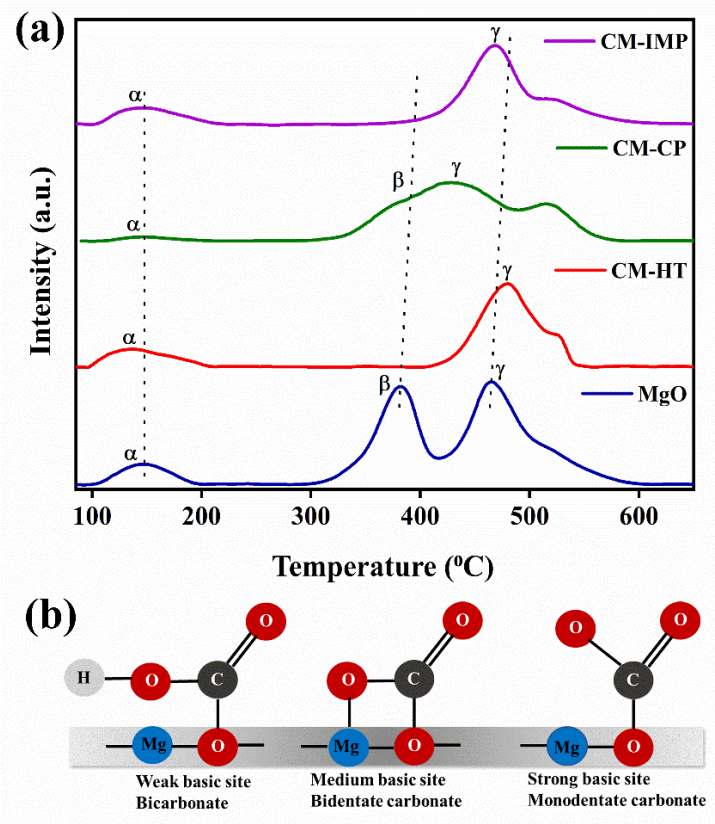


Figure 5.5. (a) *CO_2-TPD profiles of the reduced catalyst samples compared to commercial MgO,* ***(b)*** *mode of CO_2 adsorption over weak, medium, and strong basic sites.*

The differences and similarities in the morphological features of all three catalysts were analyzed using microscopic imaging. **Figure 5.6** shows the FESEM images of the CM-HT catalyst with the other two catalysts (CM-CP and CM-IMP). The spherical ball-like morphology of the calcined catalyst is intact, as observed in the precursor sample, indicating that the CM-HT sample is both morphologically sound and thermally stable (Figure 5A3). This effect is induced by the incorporation of Mg^{2+} ions in the pure phase, transforming it into a rosasite-like structure through the HT route of synthesis, which tends to result from preserved shapes and chemical memory in the calcined catalyst. These results indicate that the precursor synthesized by the HT route yields a catalyst with an improved constructive interaction of compactness and controlled shape, a metal oxide, which is favourable for the methanol formation reaction [119,199]. Conversely, the other two samples showed spheres with chunks of particles sticking together, forming agglomerates.

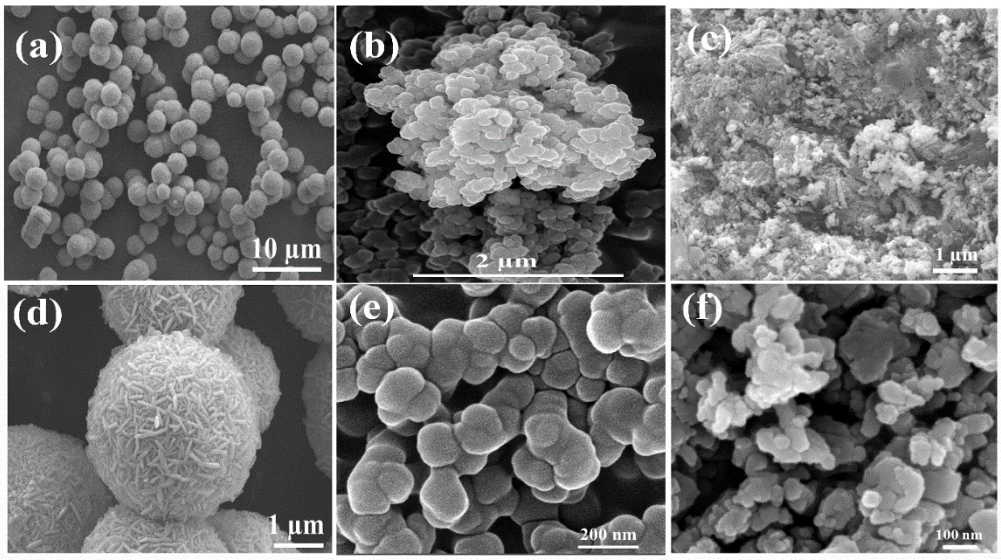


Figure 5.6. *FESEM images of* ***(a, d)*** *CM-HT,* ***(b, e)*** *CM-CP, and* ***(c, f)*** *CM-IMP calcined catalyst samples.*

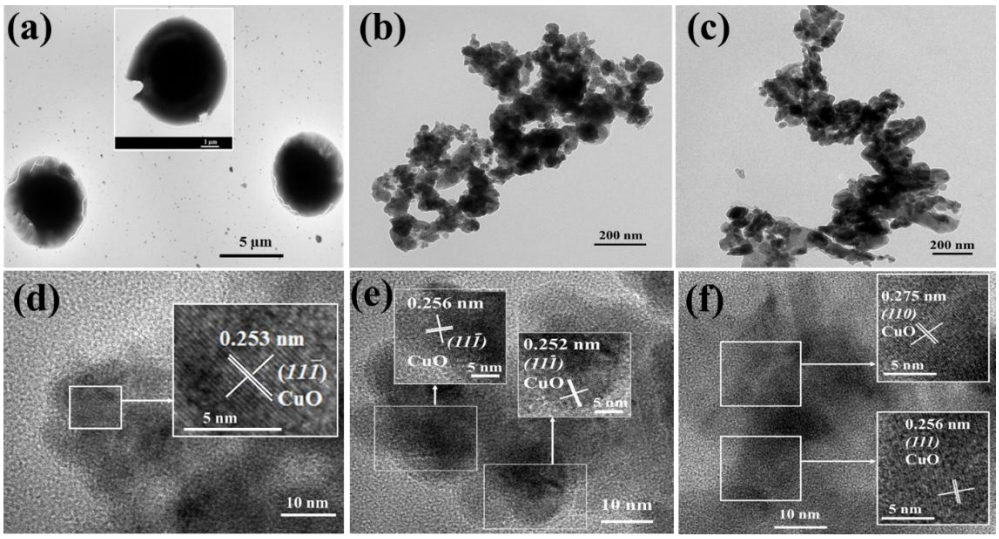


Figure 5.7. (a, b, c) *TEM and* ***(d, e, f)*** *HRTEM images of CM-HT, CM-CP, and CM-IMP, respectively.*

To capture the dispersion in all three samples, the samples were scrutinized by HRTEM **Figure 5.7.** The presence of agglomerated particles in CP and IMP clearly indicates the superiority of the HT method used for catalyst synthesis in the initial stage of preparation. The HRTEM image of the CM-HT and CM-CP catalyst showed a fringe width of 0.253 nm compatible with the *d*-spacing corresponding to the *(1$\bar{1}$1) hkl* plane of CuO. In contrast, the CM-IMP sample displayed an additional fringe width of 0.275 nm assigned to the *(110)* plane of CuO. The absence of *hkl* planes in the presence of MgO in all catalysts is apparent due to its amorphous nature, as also evident in the PXRD data.

5.2.3 Catalytic activity results

5.2.3.1 Effect of operating conditions

The catalytic performance of the CM-HT catalyst was assessed by varying temperature, pressure, and space-time velocity (WHSV) while maintaining a feed gas ratio of 3:1. Methanol synthesis is an exothermic reaction favoured at low temperatures and high pressures. The impact of these operating conditions on the catalytic performance is illustrated in **Figure 5.8 (a-d).** It was observed from **Figure 5.8 (a-c)** that increasing temperature leads to higher CO_2 conversion and methanol STY. In contrast, increasing pressure resulted in an upward trend in CO_2 conversion, methanol STY, and selectivity. The reactions of 260°C, 40 bar, and 2600 WHSV showed a CO_2 conversion, methanol selectivity, and methanol STY of 17%, 65%, and 104 $mg_{MeOH}/g_{cat}.hr$, respectively, aligning closely with thermodynamic predictions [22,71,207]. Despite the higher CO_2 conversion and STY at 260°C, methanol selectivity was lower than at 240°C due to the increased formation of CO and CH_4.

The decrease in methanol selectivity is attributed to increased CO selectivity at higher temperatures, promoting the RWGS reaction [6,177,200]. The final optimized conditions for CO_2 hydrogenation to methanol over this lab-synthesized catalyst were established at 240°C and 40 bar. Increasing the WHSV decreased CO_2 conversion by approximately fourfold, while methanol selectivity and MeOH STY increased, as shown in **Figure 5.8 (d).** This trend was attributed to reduced residence time in the packed bed reactor as WHSV increased [98,201,202].

In the CO_2 hydrogenation to methanol, various reactions occur besides methanol formation as the primary product, including the formation of CH_4 and CO, as well as carbon formation. The equations of CH_3OH, CO, and CH_4 formation via CO_2 and CO hydrogenation and carbon formation through the Boudouard reaction are written in **Equations (5.1) to (5.6)**.

$$CO_2 + 3H_2 \rightleftharpoons CH_3OH + H_2O, \quad \Delta H_{25°C} = -49.5\ kJmol^{-1} \tag{5.1}$$

$$CO_2 + H_2 \rightleftharpoons CO + H_2O, \quad \Delta H_{25°C} = 41.2\ kJmol^{-1} \tag{5.2}$$

$$CO + 2H_2 \rightleftharpoons CH_3OH, \quad \Delta H_{25°C} = -90.6\ kJmol^{-1} \tag{5.3}$$

$$CO_2 + 4H_2 \rightleftharpoons CH_4 + 2H_2O, \quad \Delta H_{25°C} = -165.0\ kJmol^{-1} \tag{5.4}$$

$$CO + 3H_2 \rightleftharpoons CH_4 + H_2O, \quad \Delta H_{25°C} = -206.5\ kJmol^{-1} \tag{5.5}$$

$$2CO \rightleftharpoons CO_2 + C \quad \Delta H_{25°C} = -172.0\ kJmol^{-1} \tag{5.6}$$

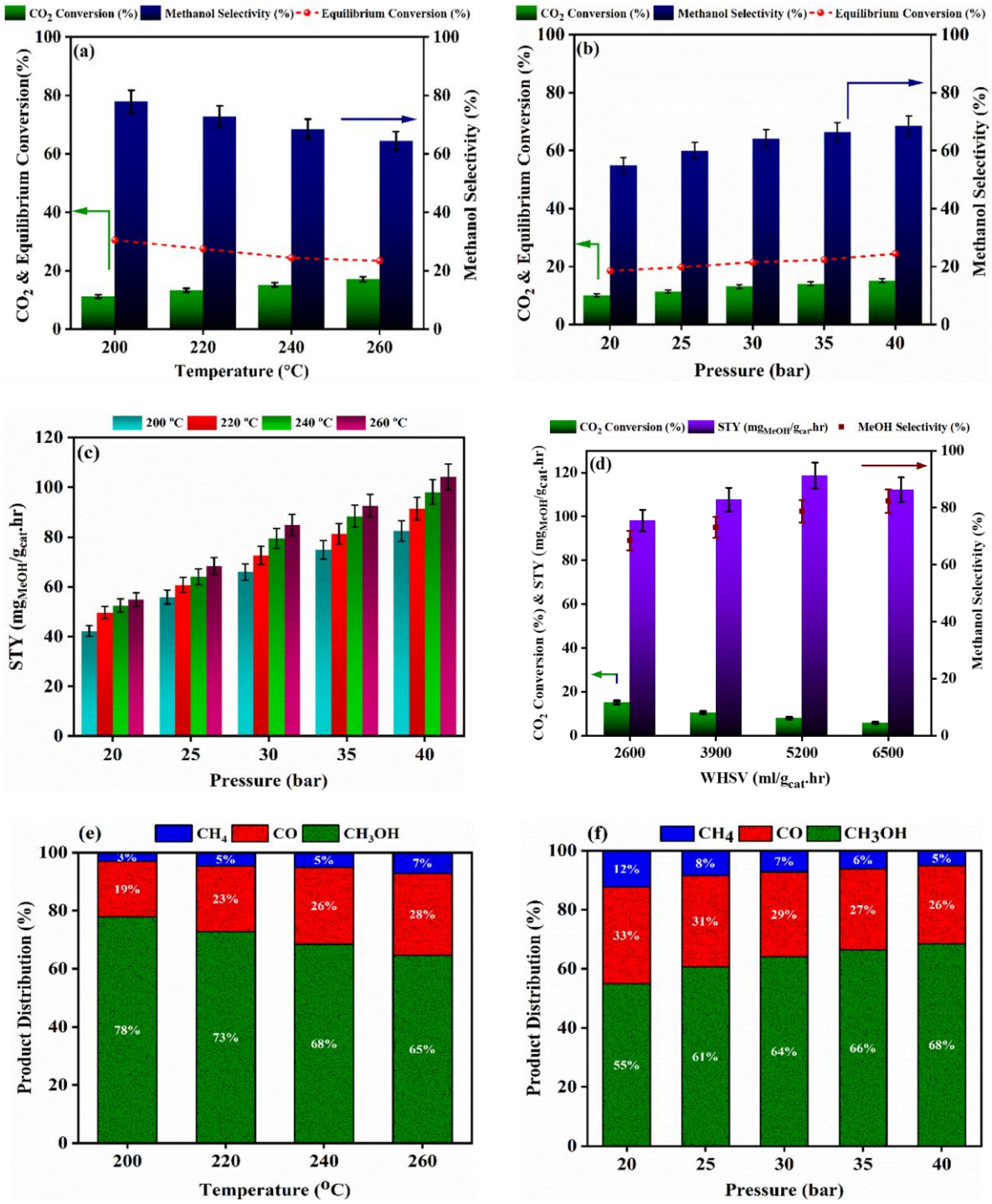


Figure 5.8. (a) *Effect of reactor temperature (at P = 40 bar, WHSV = 2600 ml/g_{cat}.hr, and H_2:CO_2 = 3:1),* ***(b)*** *Effect of pressure (at T = 240°C, WHSV = 2600 ml/g_{cat}.hr, and H_2:CO_2 = 3:1) on the CO_2 conversion and methanol selectivity of CM-HT sample,* ***(c)*** *Effect of pressure with the varying temperature range on the MeOH STY (at WHSV = 2600 ml/g_{cat}.hr, and H_2:CO_2 = 3:1),* ***(d)*** *Effect of WHSV on the catalytic performance (at T = 240°C, P = 40 bar, and H_2:CO_2 = 3:1),* ***(e)*** *Effect of temperature on the product distribution (at P = 40 bar, WHSV= 2600 ml/g_{cat}.hr, and H_2:CO_2 = 3:1),* ***(f)*** *Effect of pressure on the product distribution (at T = 240°C, WHSV = 2600 ml/g_{cat}.hr, and H_2:CO_2 = 3:1).*

Higher pressures and temperatures facilitated CO_2 activation, notably increasing CO formation through the reverse water-gas Shift (RWGS) reaction [6,177]. Product distribution, illustrated in **Figure 5.8 (e) and (f),** highlighted that lower temperatures (e.g., 200°C) corresponded to reduced CO formation (~19%), favouring increased methanol production. However, at such lower temperatures, overall catalytic performance (CO_2 conversion and MeOH STY) resulted in markedly low values [13,98]. Figure 5.9(a) reveals the comparative catalytic performance of all three catalysts at 240°C, 40 bar pressure, and a WHSV of 2600 ml/g_{cat}.hr, at which a CO_2 conversion of 15%, a methanol selectivity of 68.5%, and a methanol STY of 98 mg_{MeOH}/g_{cat}.hr is achieved. Under similar conditions, the CM-IMP catalyst showed a CO_2 conversion of 10.5%, methanol selectivity of 61%, and a methanol STY of 60.5 mg_{MeOH}/g_{cat}.hr, while the CM-CP catalyst exhibited a CO_2 conversion of 8%, methanol selectivity of 55.4%, and a methanol STY of 43 mg_{MeOH}/g_{cat}.hr **(Figure 5.9 (a)** and **(b))**.

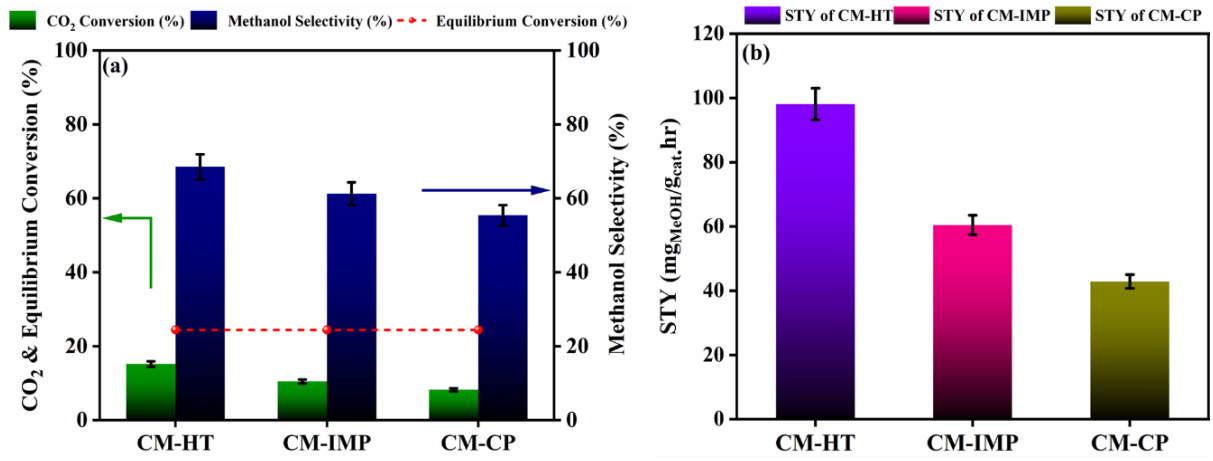


Figure 5.9. (a) *Bar chart illustrating the comparative catalytic performance (CO_2 conversion and methanol selectivity) of Cu/MgO catalysts at optimized reaction conditions (T = 240°C, P = 40 bar, WHSV = 2600 ml/g_{cat}.hr, and H_2:CO_2 = 3:1),* ***(b)*** *Overall comparison of methanol STY at optimized reaction conditions.*

The subsequent analysis aimed to understand the changes in spent catalyst properties after the catalytic experiments. It could be noticed that the PXRD pattern **(Figure 5.10 (a))** of all the spent samples (CM-HT-S, CM-CP-S, and CM-IMP-S) showed typical diffraction peaks of Cu (PDF No. 04-836); these significant reflections are accompanied by a minimal diffraction from CuO (PDF No. 48-1548) also. Due to the closeness in the diffraction pattern of Cu_2O and Cu, the identification was challenging. The average crystallite size, calculated from the Cu (111) metal diffraction peaks, followed the order CM-HT-S < CM-CP-S < CM-IMP-S **(Table 5.1).** As is evident, the lowest crystallite size and highest BET surface area were observed for CM-

HT-S, which potentially explains its superior performance compared to the others **(Figure 5.10 (b)).**

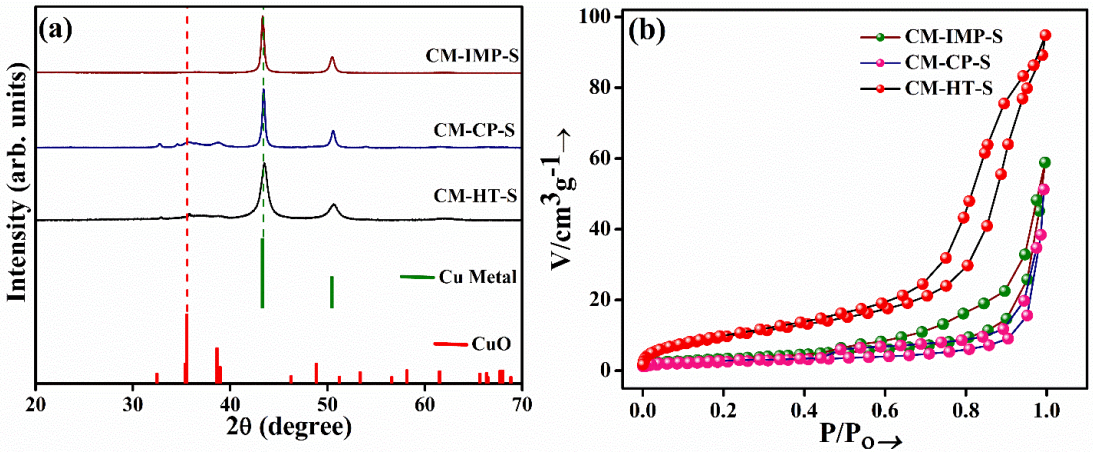


Figure 5.10. (a) *PXRD patterns, and* ***(b)*** *N_2-adsorption desorption isotherm of the spent samples.*

The stability of the promising catalyst (CM-HT) was also tested in a long-term on-stream (TOS) run under the optimized conditions of 240°C and 40 bar for 100 hours at a flow rate of 2600 ml/g_{cat}.hr. The TOS run does not exhibit significant deactivation over the 100-hour test period, as shown in **Figure 5.11**.

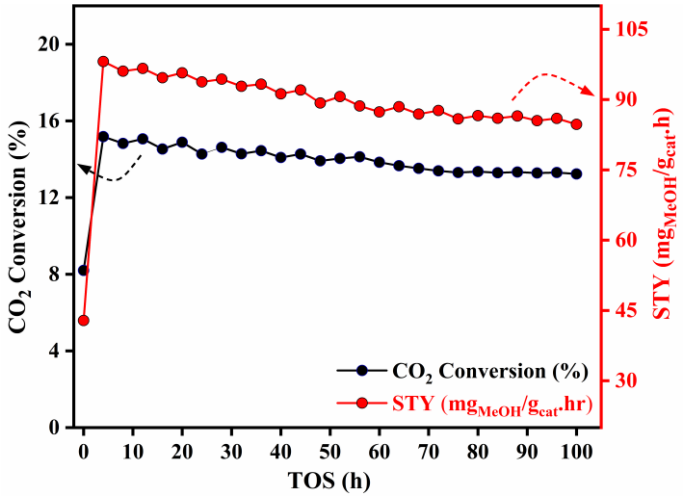


Figure 5.11. *Catalyst stability test (TOS) for CM-HT catalyst at optimized reaction conditions (T = 240°C, P = 40 bar, WHSV = 2600 ml/gcat.hr, and H_2:CO_2 = 3:1).*

Additionally, post-catalysis elemental analysis revealed approximately 2% carbon deposition, as determined by CHNS analysis, a result of the Boudouard reaction, which was almost negligible after such a prolonged on-stream period. CM-HT catalyst exhibited reasonably good stability during the 100 hr test, demonstrating some resistance to deactivation caused by coke formation or major agglomeration and sintering.

5.2.4 Structure-activity relationship

The structure-activity relationship of Cu/MgO catalysts synthesized via different preparation routes was systematically evaluated by correlating their physicochemical properties with catalytic performance. Clear distinctions were observed among the CM-HT, CM-CP, and CM-IMP catalysts. As summarized in **Table 5.1** and visualized in the spider plot **(Figure 5.12),** CM-HT exhibits the smallest crystallite size, along with the highest BET surface area, Cu surface area (SA_{Cu}), and Cu dispersion (D_{Cu}) compared to CM-CP and CM-IMP. The reduction in crystallite size in CM-HT enhances the number of exposed active Cu sites, strengthens Cu-Mg interfacial contact, and minimizes particle agglomeration, thereby directly contributing to superior catalytic activity.

Quantitatively, the BET surface area, SA_{Cu}, and D_{Cu} follow the order- CM-HT (66.84 m^2/g, 20.62 m^2/g, 5.78%) > CM-IMP (23.7 m^2/g, 7.01 m^2/g, 2.04%) > CM-CP (16.46 m^2/g, 5.36 m^2/g, 1.34%), which is in excellent agreement with the observed methanol STY trend: CM-HT (98 $mg_{MeOH}/g_{cat}.hr$) > CM-IMP (64.5 $mg_{MeOH}/g_{cat}.hr$) > CM-CP (43 $mg_{MeOH}/g_{cat}.hr$). This strong parallelism between dispersion-related properties and methanol productivity confirms that Cu dispersion and accessible active surface area are the dominant descriptors governing catalytic performance.

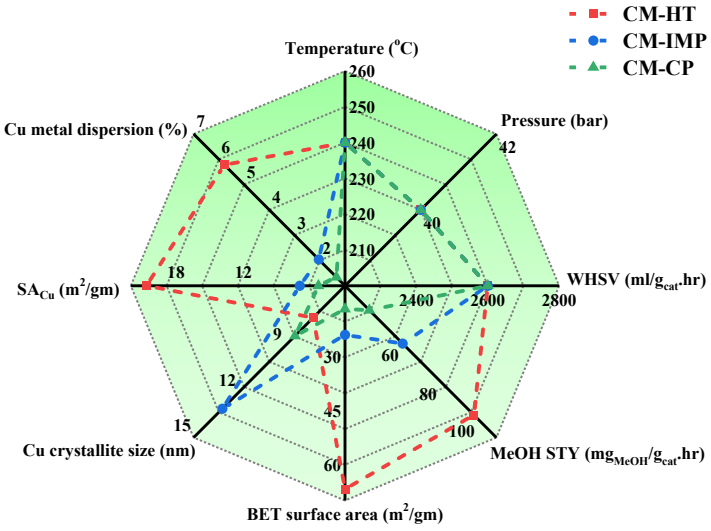


Figure 5.12. *Radar plot illustrating the structure-activity relationship of Cu/MgO catalysts.*

Furthermore, CO_2-TPD analysis **(Figure 5.5)** reveals that CM-HT possesses a more favourable distribution of basic sites, characterized by suppression of excessive medium basic sites (β) compared to pristine MgO. This modification in surface basicity, induced by strong Cu-Mg

interaction, effectively suppresses the reverse water-gas shift (RWGS) reaction, thereby enhancing methanol selectivity. The spider plot **(Figure 5.12)** clearly integrates these structure-property-performance correlations, illustrating how the synergistic effects of smaller crystallite size, higher surface area, superior Cu dispersion, and optimized surface basicity collectively drive the exceptional methanol synthesis performance of the CM-HT catalyst [90,198].

These findings align closely with the existing literature on similar CO_2 reduction catalysts, suggesting that both the BET surface area and the concentration of basic sites have a critical impact on refining methanol selectivity [90,199]. Furthermore, high experimental H_2 consumption values over the theoretical showed enhanced reduction of MgO in CM-HT with subsequent increase in strong basic sites (γ) [203]. The CO_2 molecules adsorbed on both sites (i.e., β and γ) undergo sequential hydrogenation steps, ultimately yielding HCOO*, H_2COO*, H_2COOH*, and H_2CO* with atomic hydrogen (H) being transferred via H spillover from Cu. Moreover, the adsorption of the C=O bond of H_2CO on the most robust basic sites (γ) causes reaction with surface hydrogen, resulting in methanol formation. In contrast, adsorption of the same species on medium basic sites (β) leads to the formation of CO [90]. The results of CO_2-TPD and H_2-TPR indicate the absence of medium basic sites and plenty of strong basic sites with the highest H_2-spillover as the driving force for high selective conversion to methanol. The superior physicochemical properties and catalytic performance result from incorporating the maximum amount of Mg^{2+} in the phase-pure precursor during the early stage of synthesis in CM-HT, which cannot be achieved by the CP route. Interestingly, the enhanced physical properties and catalytic performance of CM-IMP over CM-CP resulted from utilizing magnesium carbonate hydroxide ($4MgCO_3.Mg(OH)_2.4H_2O$) as a precursor for MgO. This choice creates an active porous surface conducive to the dispersion of active metal species [204]. In other words, the characterization results unveiled that the physicochemical attributes and the catalytic performance of the catalysts synthesized were significantly influenced by the morphology of the catalyst in the case of CM-HT, creating a more defective MgO interface for the reaction to proceed. Similar observations were earlier reported by Tsang's group for differently shaped Cu/ZnO catalysts, wherein the presence of (*002*) facets of the plate-like ZnO support showed a more vital interaction than the other crystal facets, resulting in a superior catalytic performance for CO_2 hydrogenation to methanol [198]. In another study by Lei et al. [119], the filament-structured morphology of the Cu sample supported by ZnO created more oxygen vacancies, which thereby improved the activation/adsorption of CO_2 [90]. These

findings underscore the significance of synthesis methodology in tailoring catalyst properties and thus offering insights into the structure-activity relationship of the catalyst in methanol formation from CO/CO_2 reduction.

5.2.5 Mechanistic insights into CO_2 hydrogenation to methanol over the CM-HT catalyst

To unveil the possible molecular intermediates formed during CO_2 activation and further hydrogenation, the *in-situ* DRIFTS experiments were conducted over the best Cu/MgO catalyst (CM-HT). Three distinct types of adsorbed species were detected: bicarbonate (HCO_3*), carbonate (CO_3^{2-}), and formate ($HCOO^*$) species in the CO_2 adsorbed sample **(Figure 5.13).** The presence of HCO_3^- and CO_3^{2-} is linked to CO_2 adsorption on surface hydroxyls (OH) and surface oxygen sites of the catalyst, respectively. The generation of $HCOO^-$ is attributed to the reaction between adsorbed HCO_3* and CO_3^{2-} with interstitial H atoms produced during the catalyst's pre-reduction treatment with H_2 [205]. The peak at 1668 cm^{-1} is assigned to ionic bicarbonate (i-HCO_3*) species. Two bands at 1588 cm^{-1} and 1360 cm^{-1} are associated with HCOO* species, while the band at 1470 cm^{-1} corresponds to monodentate carbonate (m-CO_3^{2-}) species [133,205,206]. Additionally, the band at 1407 cm^{-1} is attributed to polydentate carbonate (p-CO_3^{2-}) species. The intensity variation and presence of various carbonate forms are linked to different surface phenomena. For instance, the higher intensity of i-HCO_3* band results from an excess of surface hydroxyls, whereas the formation of p-CO_3^{2-} or b-CO_3^{2-} is attributed to coordinatively unsaturated bonds on the surface of defect-containing catalysts [205].

In-situ DRIFTS experiments were also conducted using CO_2 + H_2 (1:3) reactant gases under reaction conditions (H_2:CO_2 = 3:1, 1 bar) to explore the potential mechanism during CO_2 hydrogenation over the CM-HT catalyst. **Figure 5.13** illustrates the transient changes in major surface species during CO_2 hydrogenation from 50 to 300°C over these catalysts. As the reaction temperature increased, the peaks associated with i-HCO_3* species gradually diminished and nearly vanished at 150°C, while new bands corresponding to HCOO* species appeared at 2940, 2876, 1555, and 1365 cm^{-1}. The intensity of the p-CO_3^{2-} species peaks decreased notably with an increase in temperature, attributed to its reaction with H to generate HCOO* species. Additionally, bands corresponding to the methoxy group (H_3CO*) were detected at 2825 and 1060 cm^{-1}, indicating the formation of CH_3OH through the hydrogenation of HCOO* species [133]. Surprisingly, the absence of peaks at 2175 and 2115 cm^{-1},

characteristic of gaseous CO, suggests inhibition of the reverse water-gas shift (RWGS) reaction, a conclusion supported by CO_2-TPD analysis [205].

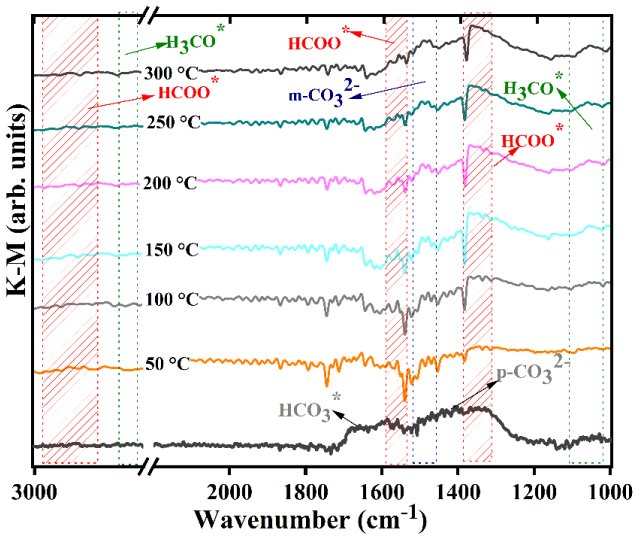


***Figure 5.13**. Characterization of the surface species on the Cu-MgO (CM-HT) sample. In-situ DRIFT spectra of Cu-MgO (CM-HT) with feed gas CO_2:H_2 (1:3) with a flow rate of 50 ml/min under atmospheric pressure and different temperatures. The bottom last spectra show the spectra with CO_2 activation over the catalyst surface before switching the feed gas to H_2.*

5.3 Summary and Future Outlook

In this study, a binary catalyst, Cu/MgO, was synthesized through a simple single-step procedure using a tailored precursor for CO_2 hydrogenation to methanol. The results clearly demonstrate that the methodology for precursor synthesis plays a critical role in governing the physicochemical properties and catalytic performance of Cu/MgO catalysts. The hydrothermally synthesized Mg-rich hydroxycarbonate precursor (mcguinnessite), analogous to the rosasite mineral, was found to be the most promising among the investigated preparation methods, outperforming co-precipitation and wet impregnation pathways by enabling enhanced CO_2 activation and H_2 adsorption.

Through comprehensive characterizations, the following insights were gathered: (1) the hydrothermal method facilitates the stabilization of a monophasic crystalline mcguinnessite (rosasite analogous) precursor across a wide range of Mg substitutions for the first time; (2) the precursor itself exhibited a high specific surface area and mesoporosity, favourable for the development of an active final catalyst; (3) the resulting Cu/MgO catalyst exhibited strong metal-support interactions and modulates the concentration and distribution of surface basic

sites, thereby enhancing H_2 adsorption and CO_2 activation, while suppressing the RWGS reaction; (4) an increased concentration of oxygen vacancies was observed for the hydrothermally synthesized catalyst, effectively strengthening the density and stability of active sites under reaction conditions.

Among all catalysts tested with different preparation histories, the CM-HT catalyst exhibited the highest catalytic activity, achieving a CO_2 conversion of 15%, a methanol selectivity of 68.5%, and a methanol STY of 98 mg_{MeOH}/g_{cat}.hr at 240°C, 40 bar, and WHSV = 2600 ml/g_{cat}.hr. The catalyst also demonstrated reasonably impressive long-term stability, as evidenced by a 100 hr time-on-stream test, attributed to the stabilization of active metal species, restricted metal particle agglomeration and sintering, and minimal coke formation. *In-situ* DRIFTS confirmed the formation of formates and methoxy intermediates during the CO_2 hydrogenation to methanol process.

The findings of this chapter establish that precursor chemistry is the central design handle governing the dispersion of active metal species, oxygen defect density, metal-support interaction, and ultimately the activity and durability of Cu-based catalysts for CO_2 hydrogenation to methanol. The successful stabilization of a phase-pure Mg-rich mcguinnessite precursor demonstrates that precise control over hydroxycarbonate chemistry is a powerful route to improve catalytic performance and stability in binary Cu/MgO systems.

Building on this fundamental understanding, the overall research objective is extended without deviating from precursor engineering by transferring this design philosophy from Cu/MgO to the industrially relevant Cu/ZnO system and subsequently upgrading it into a ternary $Cu/ZnO/ZrO_2$ catalyst through engineered oxide promotion. This progression preserves the core principles of phase-pure precursor formation, defect and dispersion control, and strong metal-support interactions, while enabling simplified and scalable mechanochemical synthesis strategies. Accordingly, the next chapter focuses on the mechano-chemical synthesis of Cu/ZnO-based catalysts and their transformation into high-performance $Cu/ZnO/ZrO_2$ systems for enhanced methanol productivity and stability.

Chapter 6 CO_2 hydrogenation to methanol over mechano-chemically synthesized phase-pure Cu-based catalysts

6.1 Overview

Following the insights gained from Mg-rich precursor engineering in the previous chapter, this chapter advances the catalyst design strategy toward the industrially relevant Cu-ZnO-based system. The focus now shifts to achieving phase-pure zincian malachite precursors and enhanced metal-support synergy through a mechanochemical synthesis route, enabling the development of high-performance $Cu/ZnO/ZrO_2$ catalysts.

Designing efficient catalysts for CO_2 hydrogenation requires more than just high activity; it demands a precise control over precursor phases, metal dispersion, and metal-support interactions to ensure both selectivity and long-term stability. For Cu-ZnO-based catalysts, the formation of a phase-pure zincian malachite precursor is critical, as it directly governs the generation of catalytically active Cu-ZnO interfaces after reduction [85]. However, conventional preparation methods such as co-precipitation often suffer from multiphase formation, poor dispersion, and structural inhomogeneity, which not only reduce methanol selectivity but also accelerate deactivation through sintering and the reverse water-gas shift reaction [26,106,107].

To overcome these limitations, the present study employs a mechanochemical ball milling (MCBM) strategy for the synthesis of $Cu/ZnO/ZrO_2$ catalysts [207–210]. This approach enables direct formation of zincian malachite with controlled incorporation of Zr, resulting in uniform metal distribution, enhanced oxygen vacancy concentration, and stronger metal-support interactions. These structural advantages are expected to translate into improved catalytic performance compared to catalysts prepared by conventional and ultrasonic co-precipitation methods. Extensive physicochemical characterization confirmed that the MCBM-derived $CuO/ZnO/ZrO_2$ (CZZ-MCBM) catalyst exhibits superior textural and structural properties, including higher Cu dispersion, stabilized surface area, and robust Zn-Zr synergy. These features establish a clear structure-property relationship, linking the synthetic method to the catalyst's performance. Catalytic evaluation under optimized conditions demonstrated methanol selectivity exceeding 75% with a methanol space-time yield of ~200 $mg_{MeOH}/g_{cat}.hr$, significantly outperforming conventionally synthesized

counterparts. Moreover, stability tests revealed minimal deactivation over extended operation, and post-catalytic characterization confirmed retention of active sites and structural integrity.

Overall, this chapter establishes mechanochemical ball milling as an effective and scalable route for producing high-performance Cu/ZnO/ZrO_2 catalysts. By correlating synthesis, structure, and activity, this approach highlights the robustness and durability of MCBM, laying the foundation for mechanistic and kinetic investigations explored in the subsequent chapter.

6.2 Results and Discussion

6.2.1 From hydroxycarbonate precursors to active Cu/ZnO phases: A structural and nanoscale investigation

Figure 6.1 (a) shows the PXRD plot of the catalyst precursor synthesis using commercial Cu and Zn precursors in a specific ratio, followed by a mechanochemical operation. The diffraction pattern of Cu, Zn precursors in comparison with the standard malachite (JCPDS no. 41-1390) and zincite (JCPDS no. 19-1458) was plotted. The exchange of ions occurs during the milling operation, which also involves size reduction. Different milling cycles (3, 6, and 9 hours) were employed during the entire ion-exchange operation, and the corresponding diffraction patterns are presented in **Figure 6.1 (a).** Plots of different cycles show the quantity of ions exchanged during that particular cycle and how many cycles are still needed for phase-pure precursor formation. It is observed that after the 3rd cycle (9 hours of run), the desired phase was obtained with some amorphous nature, which is due to the reduction in crystallite size by ball milling [207,209]. Moreover, due to surface etching by the solvent (acetone), peak broadening (resulting from a reduction in crystallite size) was observed. The mechanochemical operation involved in this catalyst synthesis results in the formation of a pure zincian malachite precursor. The phase-pure precursor was then subjected to calcination, whose XRD pattern is illustrated in **Figure 6.1 (b),** along with the standard patterns of CuO (JCPDS 48-1548) and ZnO (JCPDS 36-1451). The major diffraction peaks of CuO (111), (002), and ZnO (001) were observed.

Figure 6.2 shows an N_2 adsorption-desorption isotherm and the pore size distribution for the CZ-MCBM catalyst, which was synthesized using the MCBM method. This specific isotherm exhibits a Type IV hysteresis curve, characteristic of mesoporous materials. The sharp increase in adsorption at higher relative pressures ($P/P_o > 0.8$) suggests capillary condensation within

mesopores. The inset shows the pore size distribution (PSD) obtained from the desorption branch using the BJH method. The peaks in the PSD plot correspond to the presence of pores with varying diameters, primarily concentrated between 2 nm and 35 nm. The catalytic efficiency of Cu-based catalysts is often linked to the surface area and pore structure, which facilitate the dispersion of active metal sites and improve reactant accessibility. As earlier studies suggest, the high surface area and well-distributed mesopores enhance the catalyst's ability to adsorb CO_2 and H_2, increasing the methanol formation rate [14,98,178]. Therefore, we determine the CZ-MCBM catalyst's physicochemical properties **(Table 6.1)** here to gain a better understanding of it.

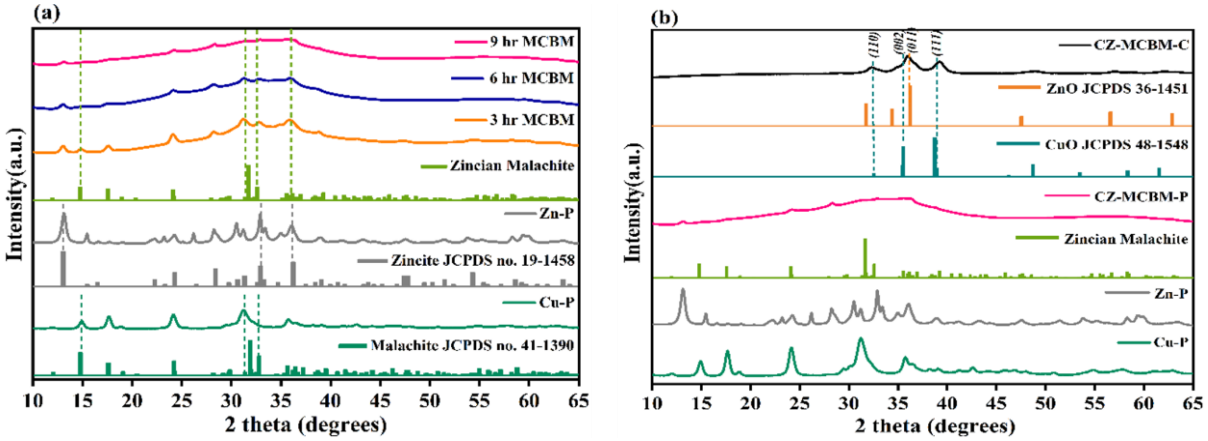


Figure 6.1. (a) *PXRD patterns illustrating the stepwise formation of hydroxycarbonate precursor via the MCBM method,* ***(b)*** *PXRD plot of calcined CZ-MCBM catalyst.*

Accordingly, the physicochemical properties of the CZ-MCBM catalyst were evaluated (**Table 6.1**) to gain deeper insight into its characteristics. Despite consisting of only two components (Cu and Zn), the catalyst exhibits satisfactory physicochemical parameters, clearly indicating the successful synthesis of a high-quality material derived from a phase-pure precursor. ICP-MS analysis **(Table 6.1)** further confirms that the experimentally measured metal composition closely matches the nominal Cu/Zn ratio (2.33/1), demonstrating that the MCBM synthesis route does not lead to metal leaching and effectively preserves the desired catalyst composition and properties. Other characterization techniques for the CZ-MCBM-C catalyst are presented in subsequent sections to facilitate a better correlation of properties with activity and comparison with the ZrO_2-incorporated CZ-MCBM catalyst.

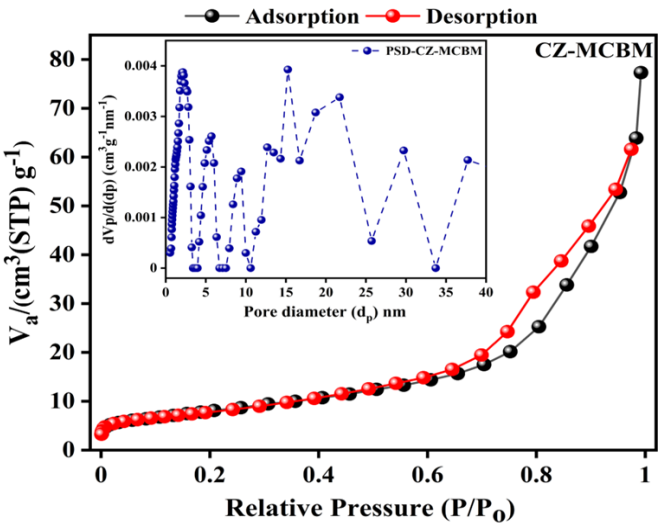


Figure 6.2. *N_2-adsorption-desorption isotherms of Cu-ZnO calcined catalyst prepared via the MCBM method. The inset shows the pore size distribution curve for the CZ-MCBM sample.*

Table 6.1*. Physicochemical properties of CZ-MCBM catalyst.*

Catalyst	S^a_{BET} (m^2/gm)	V^a_p (cc/gm)	d_{CuO}[b] (nm) calcined	d_{Cu}[b] (nm) reduced	SA^c_{Cu} (m^2/gm)	D^c_{Cu} (%)	[d]Metal Composition (%)		
							Cu (%)	Zn (%)	Zr (%)
CZ-MCBM	27.1	0.114	10.13	8.22	9.8	3.17	69.97	30.03	-

[a]From N_2 Physisorption (multipoint BET method), [b]Calculated using Scherrer Formula, [c]Measured using N_2O chemisorption method, [d]atomic percent obtained from ICP-MS.

To understand its catalytic performance, the catalyst was initially tested at varying temperatures (220-260°C), a constant pressure of 40 bar, and a WHSV of 2600-5200 ml/g_{cat}.hr. The radar plot indicates that as the temperature increases, the CO_2 conversion also increases and accelerates the hydrogenation reactions, resulting in enhanced methanol production. As illustrated in **Figure 6.3,** the selectivity towards methanol decreases at increasing temperatures due to side reactions, such as the reverse water gas shift (RWGS) reaction, which favours CO formation over methanol [14,98]. However, methanol STY increases significantly as the reaction temperature increases. The STY data in the given **Figure 6.3** demonstrates that the CZ-MCBM catalyst exhibits enhanced productivity as the temperature rises, with the highest STY at 260°C, around 110 mg_{MeOH}/g_{cat}.hr, with the highest value of CO_2 conversion and methanol selectivity at this point is 15.4% and 65%, respectively at 260°C, 40 bar, and 2600 ml/g_{cat}.hr. From the given Figure, we also observed the relationship between WHSV and catalytic performance. It stated that when the WHSV is increased from 2600 to 5200 ml/g_{cat}.hr

at constant temperature and pressure, the catalytic performance suddenly changes. Specifically, CO_2 conversion drops significantly as the contact time between the reactant molecules and the catalyst's active sites decreases. However, methanol selectivity increases, which in turn increases the STY up to a certain value. This confirms the catalyst's efficiency in methanol production at elevated temperatures and WHSV, which is consistent with established behaviours for Cu/ZnO-based catalysts [110,137,211,212]. However, the balance between the reaction parameters must be carefully optimized to ensure the best catalytic performance.

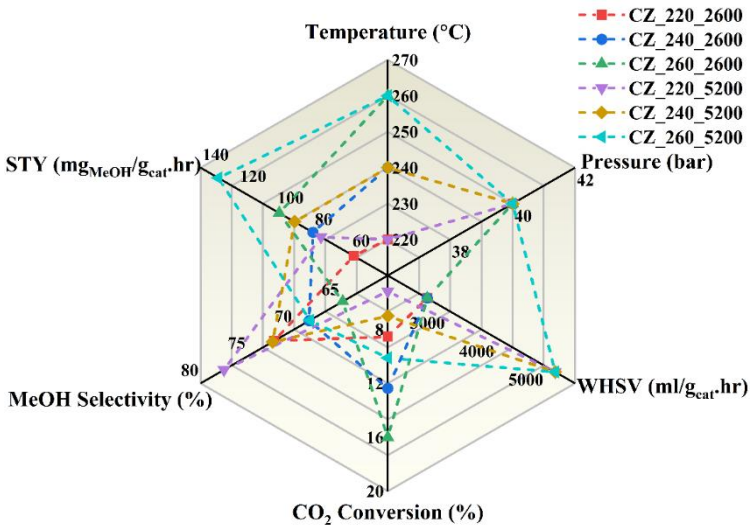


Figure 6.3. *Radar representation of the catalytic performance of the CZ-MCBM catalyst under varying temperature and WHSV at 40 bar.*

The CZ-MCBM exhibits optimal performance at 260°C, 40 bar, and 5200 ml/g_{cat}.hr, balancing both high CO_2 conversion and high methanol selectivity. Though conversion continues to rise at higher temperatures, methanol selectivity decreases, likely due to competing side reactions; therefore, it is important to include the optimized value of WHSV during the reaction. This performance profile is consistent with earlier findings on Cu-based catalysts used for CO_2 hydrogenation [110,211–214]. However, the catalytic system still has scope for improvement.

6.2.2 Engineering Cu/ZnO/ZrO_2 catalysts: Synthesis route comparison and structural insights

To further enhance the catalytic efficiency of the Cu/ZnO system for CO_2 hydrogenation to methanol, several interrelated catalyst parameters must be carefully optimized, including phase-pure precursor formation, high BET surface area and active Cu surface area, uniform metal dispersion, small crystallite size, strong metal-support interaction (SMSI), and optimized

reaction parameters such as temperature, pressure, and WHSV. The CZ-MCBM catalyst developed in this study satisfies most of these criteria and therefore exhibits commendable catalytic performance. However, insights from prior studies suggest that further improvements are feasible through strategic modifications to the support environment [88,97,122,215–217].

Therefore, to achieve this, ZrO_2 was incorporated as a highly basic, hydrophobic, and structurally stabilizing support, owing to its proven ability to enhance Cu dispersion, suppress sintering, promote oxygen vacancy formation, and strengthen metal-support interactions [66]. The previously synthesized phase-pure zincian malachite precursor (CZ-MCBM-P) was subjected to additional ball milling for three hours with ZrO_2 to obtain the ternary precursor, denoted as CZZ-MCBM-P. This precursor was subsequently calcined to yield the corresponding mixed-oxide CZZ-MCBM-C catalyst.

To systematically evaluate the influence of ZrO_2 and the role of synthesis strategy, two additional $Cu/ZnO/ZrO_2$ catalysts were synthesized by co-precipitation under ultrasonic irradiation (CPUSI) and simultaneous precipitation under ultrasonic irradiation (SPUSI)**.** The structural properties of all three CZZ catalysts, both in their precursor and calcined forms, were examined using powder X-ray diffraction (PXRD) to identify crystalline phases and assess phase purity. The corresponding diffraction patterns are presented in **Figure 6.4 (a) and (b).**

The XRD patterns presented in **Figure 6.4 (a)** compare the three CuZnZr-containing precursors synthesized via the MCBM, CPUSI, and SPUSI methods, namely CZZ-MCBM-P (mechano-chemical ball milling method), CZZ-CPUSI-P (ultrasonic irradiation-assisted coprecipitation), and CZZ-SPUSI-P (ultrasonic irradiation-assisted simultaneous coprecipitation). Standard diffraction patterns of aurichalcite (RRUFF ID: R060426), zincian malachite, and ZrO_2 (JCPDS 37-1484) are also included for phase identification. The diffractogram of the CZZ-MCBM-P diffraction peaks closely matches that of zincian malachite, indicating the formation of a dominant and phase-pure precursor, with ZrO_2 present only as a minor phase. In contrast, both CZZ-CPUSI-P and CZZ-SPUSI-P exhibit diffraction features corresponding to zincian malachite as the major phases, along with minor contributions from aurichalcite and ZrO_2, suggesting the coexistence of multiple precursor phases. The presence of these additional phases is known to influence active surface area, metal dispersion, and ultimately catalytic performance. Although the ZrO_2 phase appears less prominent in all precursor samples, its

presence is expected due to intentional incorporation to enhance catalyst stability and dispersion of active sites.

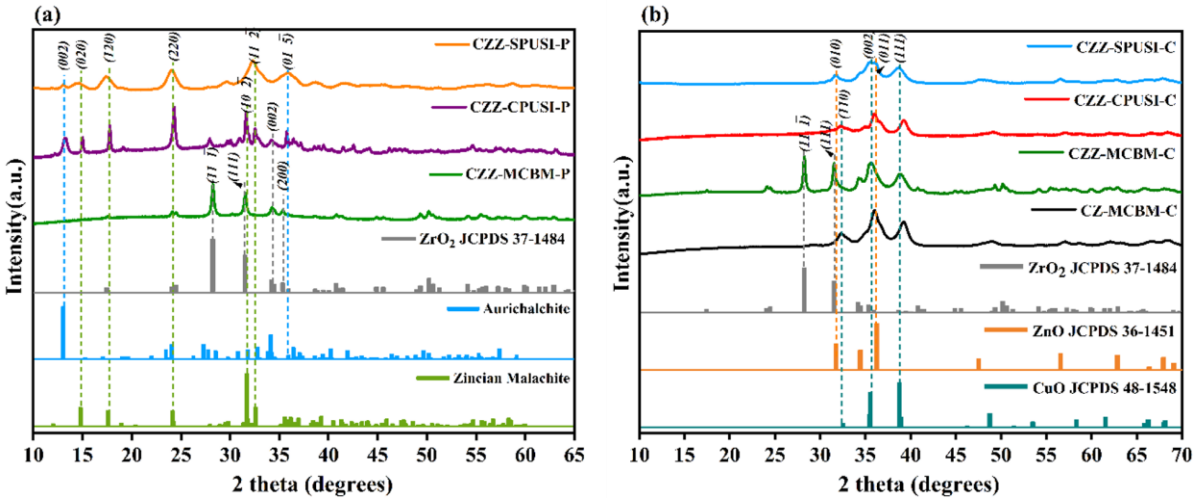


Figure 6.4. (a) *PXRD patterns of CuZnZr containing precursors synthesized via the MCBM, CPUSI, and SPUSI methods, illustrating phase evolution and precursor crystallinity after ZrO_2 incorporation,* ***(b)*** *PXRD patterns of the corresponding calcined CuO/ZnO/ZrO_2 (CZZ) catalysts prepared by MCBM, CPUSI, and SPUSI methods, showing the formation of mixed metal oxide phases.*

Similarly, **Figure 6.4 (b)** shows the PXRD patterns of the corresponding calcined Cu-based oxide catalysts. All samples exhibit the characteristic diffraction peaks of CuO (111), (002), and ZnO (001), with an additional ZrO_2 (111) and (11-1) being clearly observed in the CZZ-MCBM-C catalyst, confirming the successful ex-situ incorporation of ZrO_2 during the mechanochemical synthesis. The standard diffraction patterns of CuO (JCPDS 48-1548), ZnO (JCPDS 36-1451), and ZrO_2 (JCPDS 37-1484) were used for reliable phase verification.

Overall, these results demonstrate that precursor phase formation is strongly dependent on the synthesis route, with zincian malachite being the dominant phase in the MCBM-derived precursor, whereas a mixed precursor system of zincian malachite and aurichalcite is obtained via the CPUSI and SPUSI methods. Since zincian malachite is widely recognized as the most desirable precursor for Cu-based methanol synthesis catalysts, its preferential formation in the MCBM route is expected to promote higher Cu dispersion over the ZnO and ZrO_2 surfaces after calcination, ultimately leading to superior catalytic performance [85,102,218].

Consistent with the phase evolution observed in the PXRD analysis, the peak broadening exhibited by the CZZ-MCBM sample indicates a significantly smaller crystallite size compared to the CPUSI- and SPUSI-derived catalysts, as summarized in **Table 6.2.** This reduction in

crystallite size originates from the high mechanical energy imparted during the ball milling process, which causes lattice distortion, crystal fracture, and defect generation [207–210]. Multiple milling cycles and surface etching progressively disrupt long-range crystallinity due to mechanical deformation, an effect that is clearly evident from the diffraction patterns of both CZ-MCBM-P and CZZ-MCBM-P catalyst precursors. Upon calcination, these structural modifications are retained in the oxide phase. The resulting reduction in crystallite size is beneficial for catalysis, as it enhances the active surface area, increases the concentration of surface defects (including oxygen vacancies), and improves the dispersion of active Cu species, all of which directly contribute to improved catalytic performance [219] **(Table 6.2).** The crystallite size follows the trend: CZZ-MCBM < CZZ-CPUSI < CZZ-SPUSI.

Table 6.2. *Physicochemical properties of the calcined CZZ catalysts.*

Catalyst	S^a_{BET} (m^2/gm)	V^a_p (cc/gm)	d_{CuO}[b] (nm) calcined	d_{Cu}[b] (nm) reduced	SA^c_{Cu} (m^2/gm)	D^c_{Cu} (%)	[d]Metal Composition (%)		
							Cu (%)	Zn (%)	Zr (%)
CZZ-MCBM	32.10	0.148	7.39	6.12	15.64	5.56	62.87	26.95	10.18
CZZ-CPUSI	36.75	0.267	11.7	8.41	13.52	3.42	62.9	26.88	10.22
CZZ-SPUSI	28.92	0.089	13.2	10.33	11.80	2.98	63.07	26.85	10.08

[a]From N_2 Physisorption (multipoint BET method), [b]Calculated using Scherrer Formula, [c]Measured using N_2O chemisorption method, [d]atomic percent obtained from ICP-MS.

To further correlate these structural features with textural properties, **Figure 6.5** presents the N_2 adsorption-desorption isotherm with pore size distribution (PSD) profiles of the calcined CZZ catalysts. All catalyst samples exhibit a Type-IV isotherm with a well-defined hysteresis curve, confirming their mesoporous nature. The corresponding PSD curves, obtained from the desorption branch using the BJH method, reveal a broad distribution of pore diameters, predominantly in the 2-35 nm range. The extracted BET surface area and pore volume data are compiled in **Table 6.2.** Such mesoporous architectures are highly favourable for Cu-based catalysts, as they facilitate the dispersion of active metal sites and improve reactant diffusion and accessibility [14,98]. Additionally, N_2O chemisorption experiments were conducted to quantify the active Cu surface area and metal dispersion, with the results summarized in **Table 6.2.** Finally, the metal composition was determined using the ICP-MS analysis, confirming the

successful incorporation of all components and validating the compositional integrity of the synthesized catalysts.

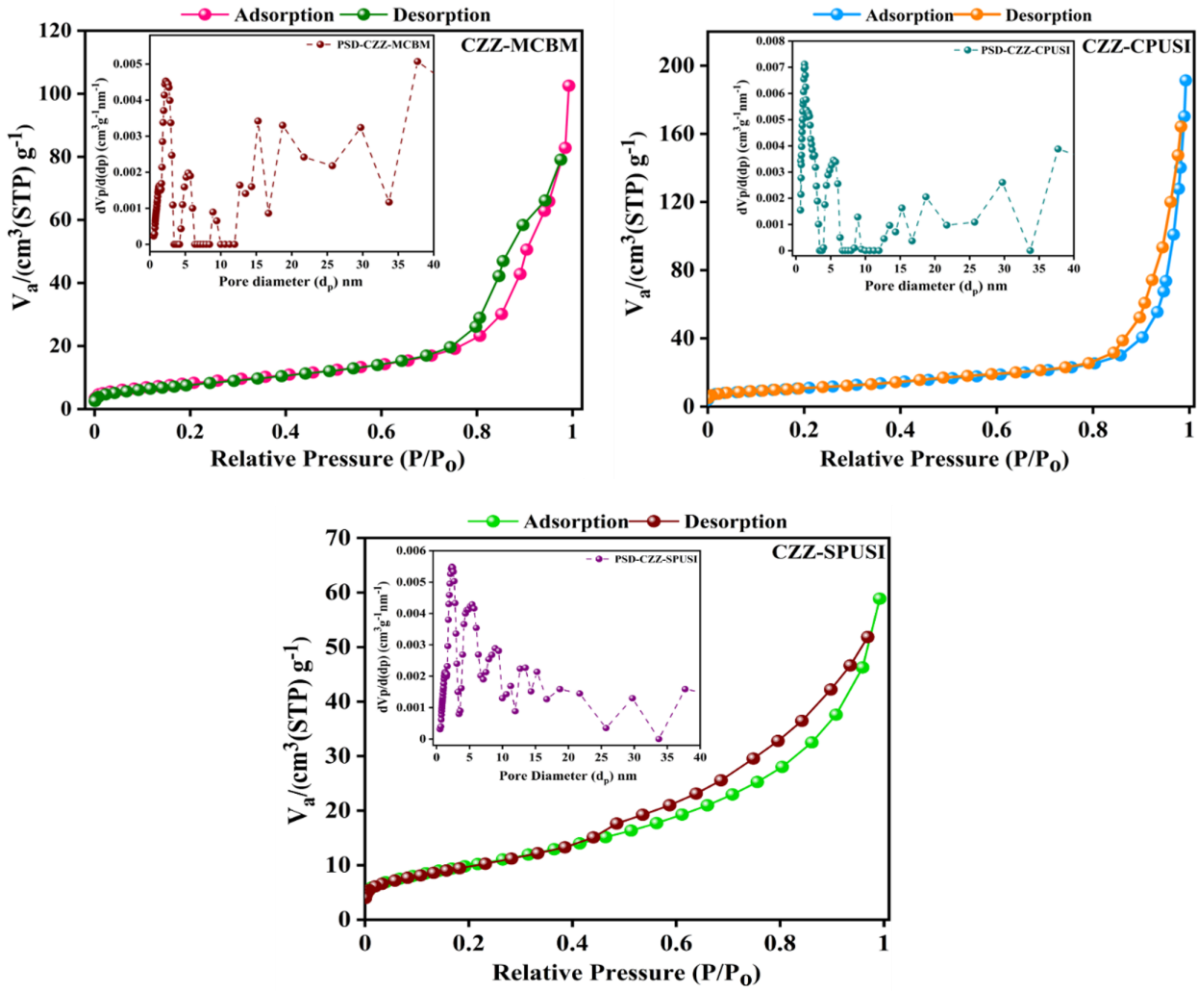


Figure 6.5. *N_2-adsorption-desorption isotherms of $CuO/ZnO/ZrO_2$ calcined catalyst prepared via the MCBM, CPUSI, and SPUSI preparation methods. The inset shows the corresponding pore size distribution curve for the $CuO/ZnO/ZrO_2$ sample.*

The HRTEM images presented in **Figure 6.6** provide detailed structural and morphological insights into the four catalyst samples, namely CZ-MCBM (a), CZZ-MCBM (b), CZZ-CPUSI (c), and CZZ-SPUSI (d). All samples exhibit well-defined lattice fringes, confirming their high crystallinity and the presence of multiple oxide phases. The measured interplanar (d-spacings) correspond well with the characteristic lattice planes of CuO, ZnO, and ZrO_2, and are in good agreement with the PXRD results, corresponding to the same facets; thereby validating the phase assignments.

Among all the catalysts synthesized, the CZZ-MCBM sample clearly displays the smallest particle size, the highest metal dispersion, and enhanced SMSI, suggesting that it will

outperform other catalysts and exhibit improved catalytic performance. The uniform distribution of CuO and ZnO domains over the ZrO_2 support, along with the intimate interfacial contact observed at the nanoscale, is expected to facilitate enhanced charge transfer, improved stabilization of active Cu species, and higher resistance to sintering under reaction conditions. In contrast, the CPUSI- and SPUSI-derived catalysts exhibit comparatively larger particle aggregates and less uniform dispersion.

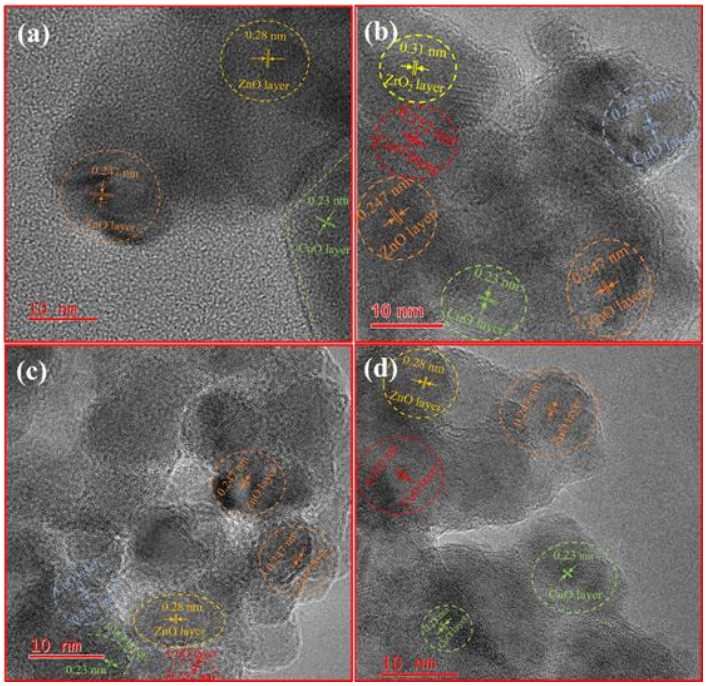


Figure 6.6. *HRTEM images of calcined* ***(a)*** *CZ-MCBM,* ***(b)*** *CZZ-MCBM,* ***(c)*** *CZZ-CPUSI, and* ***(d)*** *CZZ-SPUSI catalysts showing lattice fringes of CuO, ZnO, and ZrO_2 phases, highlighting the effect of synthesis route on crystallinity and metal dispersion.*

These HRTEM observations are fully consistent with the conclusions drawn from PXRD, BET surface area, and N_2O chemisorption analyses, further confirming that the mechanochemical ball milling route enables superior control over microstructure. Overall, the HRTEM study highlights the direct correlation between synthesis strategy, nanostructure, and catalytic performance, reinforcing the structure-activity relationships established for the CZZ-MCBM catalyst.

The H_2-TPR profiles of CZ-MCBM and the three CZZ catalysts **(Figure 6.7)** reveal the influence of ZrO_2 incorporation and synthesis route on the reduction behaviour. All reduction features appear within the 150-300°C range, with corresponding H_2 consumption values listed in **Table 6.3.** A clear distinction emerges between CZ-BM and the Zr-containing systems.

While CZ-MCBM exhibits a single α-peak, the CZZ catalysts (CZZ-MCBM, CZZ-CPUSI, and CZZ-SPUSI) display two well-resolved peaks, α and β, corresponding to sequential $Cu^{2+} \rightarrow Cu^{+}$ and $Cu^{+} \rightarrow Cu^{0}$ reduction steps. The α peak, at lower temperatures, is typically assigned to weakly interacting, highly dispersed CuO species, whereas the β peak at higher temperatures arises from bulk-like CuO or CuO strongly bound to the supports [114,178,214,220].

The incorporation of ZrO_2 significantly shifts the α peak to lower temperatures prominently for CZZ-MCBM, where the shift relative to CZ-MCBM is ~50°C, indicating enhanced reducibility and smaller CuO crystallites. Among the ternary catalysts, CZZ-MCBM exhibits the lowest reduction temperature, suggesting the presence of more labile oxygen species and stronger Cu-support synergy compared to CZZ-CPUSI and CZZ-SPUSI. This low-temperature reduction behaviour implies the generation of highly active metallic sites and partially reduced support species under reaction conditions, both of which are favourable for methanol synthesis [117]. Therefore, it was observed that CZZ-MCBM has slightly less H_2 consumption than CZ-MCBM due to Zr incorporation (Table 6.3), which enhances the reducibility due to uniform dispersion of active components. Hydrogen uptake follows the order: CZ-MCBM > CZZ-MCBM > CZZ-CPUSI > CZZ-SPUSI, and it is noticed that the total H_2 consumed by all the catalysts for the complete CuO reduction exceeds the theoretically consumed H_2 (7.38 mmol/g), with CZ-MCBM having the highest value, as illustrated in **Table 6.3.** The additional consumption of H_2 confirms the synergistic effect of the active metal and support material, reflecting H_2 spillover from reduced Cu sites to ZnO and ZrO_2 domains, which leads to partial reduction of the support while simultaneously creating oxygen-vacant sites. These vacancies are known to promote the CO_2 activation and enhance catalytic performance [97,217,221,222].

Table 6.3. *Quantitative data of H_2-TPR analysis of CZ and CZZ catalysts synthesized via the MCBM, CPUSI, and SPUSI preparation methods.*

Catalyst	T (°C) (α)	H_2 consumed (mmol/g)	T (°C) (β)	H_2 consumed (mmol/g)	Total H_2 consumed (mmol/g)[a]	H_2/Cu
CZ-MCBM	232	8.32 (100%)	-	-	8.32	1.13
CZZ-MCBM	182	2.35 (28.7%)	212	5.84 (71.3%)	8.19	1.11
CZZ-CPUSI	205	2.55 (32.5%)	221	5.29 (67.5%)	7.84	1.06
CZZ-SPUSI	209	2.67 (34.8%)	227	5.0 (65.2%)	7.67	1.04

[a]*Theoretical H_2 consumed = 7.38 mmol/g*

Overall, comparison with CZ-BM highlights that the ternary CuO/ZnO/ZrO_2 interface not only lowers the reduction temperature and improves Cu dispersion but also facilitates support reduction via spillover. Among them, CZZ-MCBM demonstrates the most favourable redox characteristics, combining high reducibility, strong metal-support interactions, and an abundance of active sites.

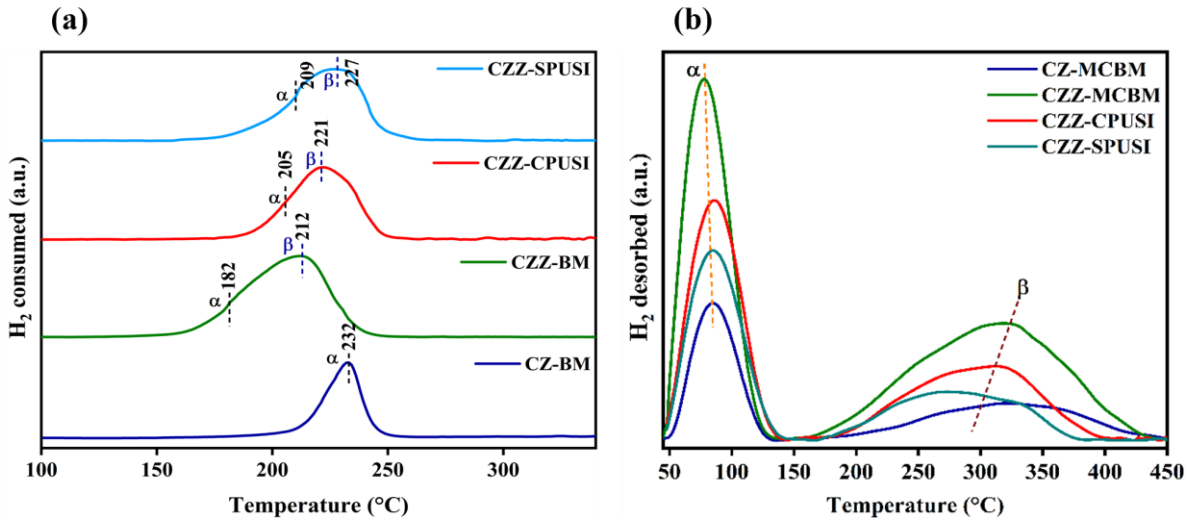


Figure 6.7. *(a) H_2-TPR profiles of CZ and CZZ calcined catalysts, (b) H_2-TPD profiles of CZ and CZZ calcined catalysts.*

The combined H_2-TPD profiles **(Figure 6.7)** of CZ-MCBM and the three CZZ catalysts provide clear insight into the effects of ZrO_2 incorporation and synthesis method on hydrogen adsorption-desorption behaviour. The desorption features divide into two regions: Region I (48-150°C, α sites), associated with weakly adsorbed hydrogen on metallic Cu sites, and Region II (150-450°C, β sites), corresponding to strongly bound hydrogen species, including spillover hydrogen at Cu-ZnO and Cu-ZrO_2 interfaces. Among all samples, CZZ-MCBM exhibits the most intense α and β peaks, indicating both a higher density of exposed metallic Cu sites (α) and a greater number of strong adsorption/spillover sites (β). This reflects improved Cu dispersion and stronger metal-support interactions, both of which are essential for efficient hydrogen activation, a critical step in CO_2 hydrogenation. The incorporation of ZrO_2 further enhances hydrogen uptake and spillover, as evident from the more pronounced β peaks in the CZZ catalysts, particularly CZZ-MCBM [89,92,110,118,214,221,223].

Peak intensity and position also reveal the impact of synthesis route: the mechano-chemical ball milling-derived CZZ-MCBM outperforms CZZ-CPUSI and CZZ-SPUSI in generating accessible active sites and promoting hydrogen spillover. This trend is consistent with H_2-TPR

results, where CZZ-MCBM showed enhanced Cu reducibility, higher hydrogen consumption, and better dispersion [115].

Collectively, these findings underscore the synergy between ZrO_2 incorporation and advanced synthesis. CZZ-MCBM achieves the most favourable surface characteristics, including superior Cu dispersion, stronger hydrogen adsorption, and enhanced spillover capacity, which explains its expected highest catalytic activity for CO_2 hydrogenation. Moreover, the excess hydrogen consumption observed in H_2-TPR is corroborated by the strong adsorption and spillover behaviour revealed by H_2-TPD, highlighting the crucial role of metal-support synergy and hydrogen mobility in these catalysts.

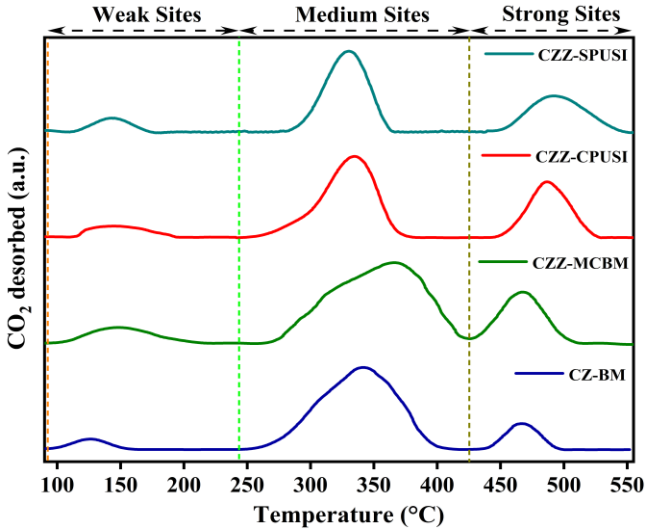


Figure 6.8. *CO_2-TPD profiles of CZ and CZZ calcined catalysts.*

The CO_2-TPD profiles **(Figure 6.8)** of CZ-BM and the CZZ catalysts (CZZ-MCBM, CZZ-CPUSI, and CZZ-SPUSI) clearly illustrate how the incorporation of ZrO_2 and the catalyst synthesis route strongly influence the distribution and strength of basic sites, which play a vital role in CO_2 adsorption and activation during methanol synthesis. The desorption peaks can be classified into weak basic sites (90-220°C) associated with hydroxyl groups, medium basic sites (220-425°C) related to CO_2 adsorption over metal-oxygen pairs such as Zn-O and Zr-O, and strong basic sites (<560°C) corresponding to CO_2 adsorption over lattice oxygen ions, typically linked to oxygen vacancies [110,117,178,214,224,225].

Compared to CZ-BM, all ZrO_2-containing catalysts exhibit significantly higher CO_2 desorption, with enhanced contributions from medium and strong basic sites. This confirms

that ZrO_2 not only increases the density of active basic sites but also promotes the creation of oxygen vacancies, which are crucial for stabilizing CO_2-derived intermediates. At the same time, differences among the CZZ catalysts highlight the effect of the synthesis method on tailoring surface basicity. In particular, CZZ-MCBM exhibits the highest intensity of medium and strong basic sites, indicating a greater proportion of bidentate and unidentate carbonate species, which reflects superior Cu dispersion, stronger metal-support interactions, and a higher concentration of oxygen vacancies [110,226,227]. This trend is quantitatively confirmed by the total CO_2 desorption capacities, which follow the order: CZZ-MCBM (3081 μmol/g) > CZZ-CPUSI (2449 μmol/g) > CZ-MCBM (2241 μmol/g) > CZZ-SPUSI (2211 μmol/g), with CZZ-MCBM exhibiting the highest density of total basic sites **(Table 6.4)**.

Table 6.4. *Quantitative data of CO_2-TPD analysis of CZ and CZZ catalysts synthesized via the MCBM, CPUSI, and SPUSI preparation methods.*

Catalyst	Weak sites, T (°C)	CO_2 desorbed (μmol/g)	Medium sites, T (°C)	CO_2 desorbed (μmol/g)	Strong sites, T (°C)	CO_2 desorbed (μmol/g)	Total CO_2 desorbed (μmol/g)
CZ-MCBM	(90-153°C)	100.8 (4.5%)	(250-410°C)	1882 (84%)	(440-500°C)	258.2 (11.5%)	2241
CZZ-MCBM	(90-218°C)	215.7 (7%)	(260-430°C)	2280 (74%)	(428-515°C)	585.3 (19%)	3081
CZZ-CPUSI	(110-190°C)	122.45 (5%)	(250-385°C)	1665.32 (68%)	(445-530°C)	661.23 (27%)	2449
CZZ-SPUSI	(115-180°C)	154.77 (7%)	(275-365°C)	1591.92 (72%)	(437-553°C)	464.31 (21%)	2211

Overall, the CO_2-TPD results clearly demonstrate that both ZrO_2 incorporation and the synthesis route dictate the quantity and nature of basic sites [110,117,227]. Medium- and strong-basic sites, which are most effective for CO_2 adsorption and activation, are maximized in CZZ-MCBM, thereby establishing its superior basic characteristics. When supported by complementary evidence from H_2-TPR and H_2-TPD findings, these results strongly suggest that CZZ-MCBM possesses the highest density of oxygen vacancies and the most favourable surface environment for CO_2 hydrogenation. This interpretation is further corroborated by O 1*s* XPS analysis.

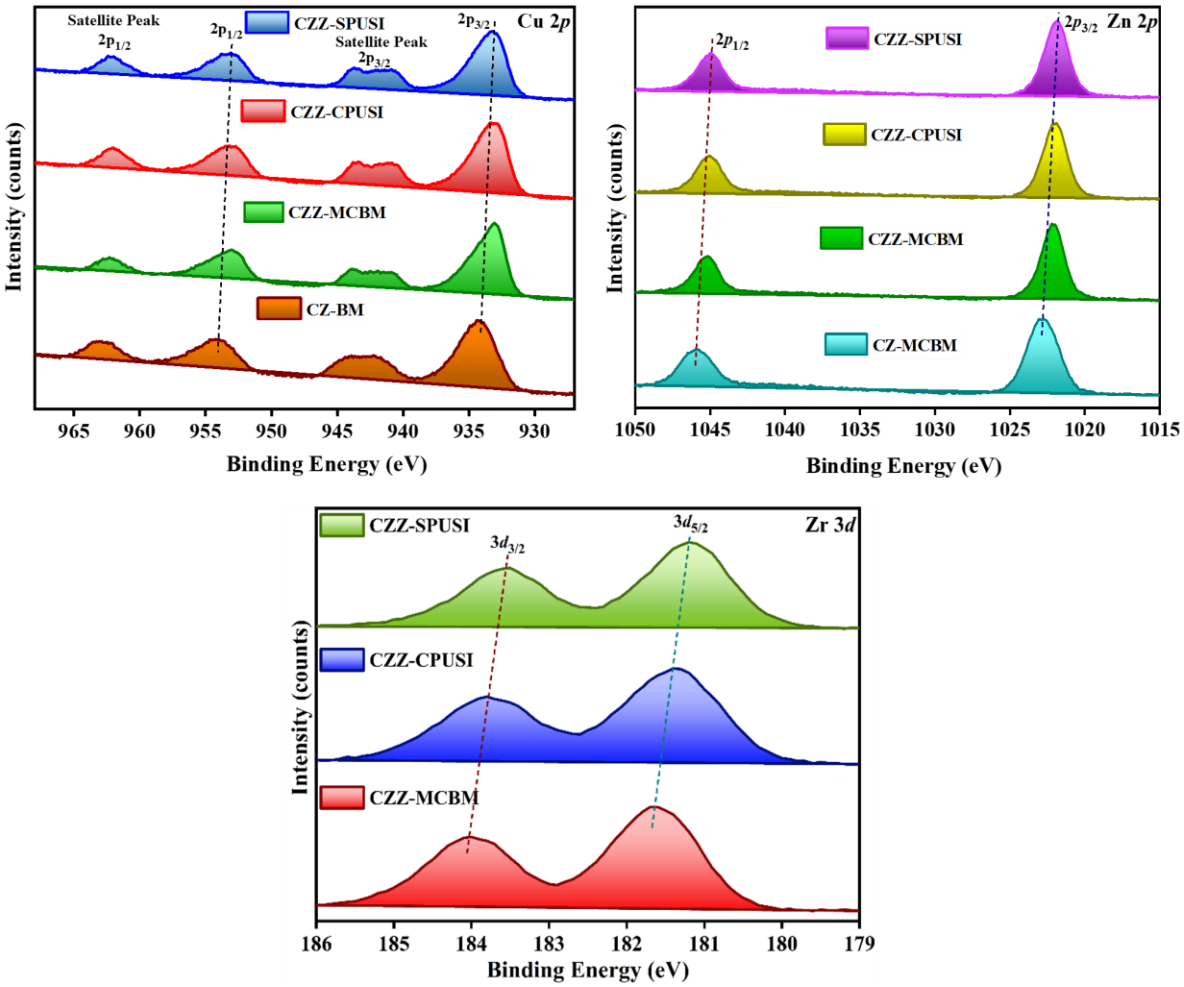


Figure 6.9. *Comparative high-resolution XPS spectra of Cu 2p, Zn 2p, and Zr 3d core levels for calcined CZ and CZZ catalysts.*

The chemical state and surface composition of Cu, Zn, Zr, and O in the catalysts were investigated by XPS and illustrated in **Figure 6.9 and Figure 6.10 (a),** providing comparative insight into the effects of ZrO_2 incorporation and synthesis method on surface chemistry and oxygen vacancy formation. For all catalysts, the Cu 2p spectra exhibit four distinct peaks- two main peaks corresponding to Cu $2p_{3/2}$ and Cu $2p_{1/2}$ recorded at (933.11-934.16 eV) and (953-954 eV), and two satellite peaks recorded at (942.2-942.9 eV) and (962.2-962.8 eV), ascribed to electron transfer between orbitals of O 2*p* and Cu 3*d*. These features are characteristic of Cu^{2+} species in the form of CuO. The Zn 2*p* spectra ascribed to Zn $2p_{1/2}$ and Zn $2p_{3/2}$ peaks recorded at (1044.9-1045.9 eV) and (1021.8-1022.8 eV), confirming Zn^{2+} as ZnO. For the CZZ catalysts, Zr 3*d* spectra display two characteristic peaks ascribed to Zr $3d_{3/2}$ and Zr $3d_{5/2}$ recorded at (183.53-184.03 eV) and (181.17-181.62 eV), implying the presence of Zr^{4+} in the form of ZrO_2 species. These results confirm the coexistence of Cu^{2+}, Zn^{2+}, and Zr^{4+} species in

the calcined catalysts, underscoring the strong metal-support interactions within the ternary systems [110,117,178,227].

The O 1*s* spectra **(Figure 6.10 (a))** were deconvoluted into two subsequent peaks, ascribed to O_{ads} (A_{ads}) and O_L (A_L), recorded at binding energies of 531.35-532.13 eV and 529.25-530.40 eV, implying the presence of both adsorbed oxygen and lattice oxygen species. The O_{ads}/O_L ratio, used to estimate relative oxygen vacancy concentration (OVC) [14,110,224], revealed significant differences among the catalysts. CZ-MCBM exhibited the lowest OVC (70%), and the ZrO_2 incorporated CZ-MCBM catalyst shows a substantial increase in oxygen vacancies. The order of OVCs is as follows: CZZ-MCBM (85%) > CZZ-CPUSI (79%) > CZZ-SPUSI (75%) > CZ-MCBM (70%). These findings align well with CO_2-TPD results, which indicate enhanced basicity in Zr-containing systems resulting from the formation of vacancies.

Among the ternary catalysts, CZZ-MCBM exhibited the highest OVC, indicating a greater defect density and stronger metal-support interactions compared to CZZ-CPUSI and CZZ-SPUSI. This enhancement can be attributed to the mechano-chemical ball milling route, which promotes improved dispersion of active species and robust CuO-ZnO-ZrO_2 interfacial interactions. Literature also supports that partial Zn^{2+} substitution into the ZrO_2 lattice promotes oxygen vacancy formation, thereby providing strong basic sites essential for CO_2 adsorption and activation [110].

Overall, the XPS findings are consistent with those of XRD, H_2-TPR, H_2-TPD, and CO_2-TPD analyses, establishing oxygen vacancy concentration as a key descriptor that links ZrO_2 incorporation and synthesis methodology to catalytic performance. The exceptionally high vacancy density in CZZ-MCBM is significant, as oxygen defects directly facilitate CO_2 activation and stabilize reaction intermediates, thereby enhancing methanol synthesis activity, as discussed in the subsequent sections.

The quantitative analysis of oxygen vacancies was conducted through XPS analysis, as discussed earlier, and EPR measurements further confirmed their presence. The EPR spectra **(Figure 6.10 (b))** show that all synthesized catalysts exhibit signals with g values close to ~2.0, consistent with reported standards, thereby confirming the presence of oxygen vacancy sites. The oxygen vacancies play a crucial role in the CO_2 activation, as they provide unsaturated coordination sites that act as strong electron donors. Such sites facilitate the

adsorption and polarization of CO_2, inducing bending of its linear structure, which enhances reactivity and enables the formation of intermediates such as carbonates and formates [228–231].

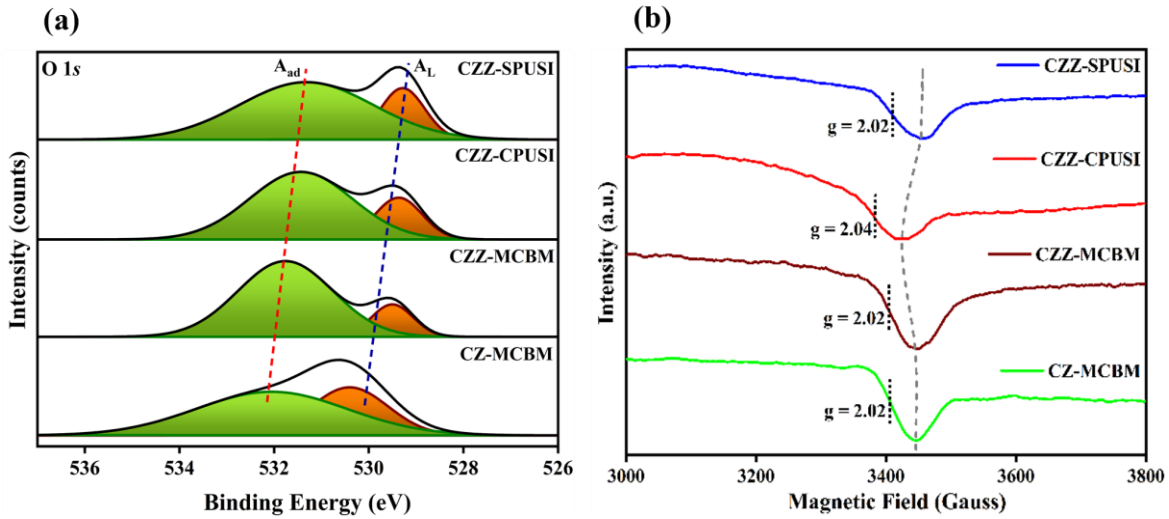


Figure 6.10 (a) *O 1s XPS spectra of calcined CZ and CZZ catalysts prepared via different synthesis routes, highlighting variations in lattice oxygen, surface oxygen species, and oxygen vacancy-related components* ***(b)*** *EPR spectra of calcined CZ and CZZ catalysts prepared via different synthesis routes, illustrating the variation in paramagnetic species and oxygen vacancy concentration.*

The interaction of oxygen vacancies with these intermediates preferentially stabilizes formate species, steering the pathway toward methanol synthesis while suppressing side reactions such as the RWGS process by lowering the energy barrier for intermediate conversion. Additionally, oxygen vacancies work synergistically with metal sites to promote H_2 dissociation, thereby supplying the reactive hydrogen species required for subsequent hydrogenation steps. Overall, oxygen vacancies are thus established as indispensable in CO_2 hydrogenation to methanol, as they enhance adsorption, activation, and stabilization of intermediates. By carefully tuning the density and nature of these vacancies, catalytic performance can be significantly improved, making them a central design parameter in the development of efficient catalysts.

6.2.3 Comparative catalytic performance studies of Cu-based catalysts

6.2.3.1 Impact of ZrO_2 Promotion

The radar plot **(Figure 6.11)** compares the catalytic performance of CZ-MCBM and CZZ-MCBM catalysts under optimized reaction conditions (T = 260°C, P = 40 bar, WHSV = 5200 ml/g_{cat}.hr), as identified in an earlier section. The data clearly illustrate the beneficial role of

ZrO_2 incorporation into the Cu/ZnO catalyst matrix. CZZ-MCBM demonstrates markedly higher CO_2 conversion, methanol selectivity, and methanol space-time yield (MeOH STY) compared to CZ-MCBM. This improvement stems from the multifunctional promotional effects of ZrO_2, including enhanced metal dispersion, increased active surface area, stronger metal-support interactions, and a higher density of oxygen vacancies. These vacancies facilitate CO_2 activation and promote hydrogen spillover, thereby accelerating methanol formation while suppressing side reactions such as the reverse water-gas shift (RWGS). Notably, even at high WHSV, where catalyst performance usually declines, CZZ-MCBM sustains its superior activity, underscoring its robustness and more effective utilization of active sites.

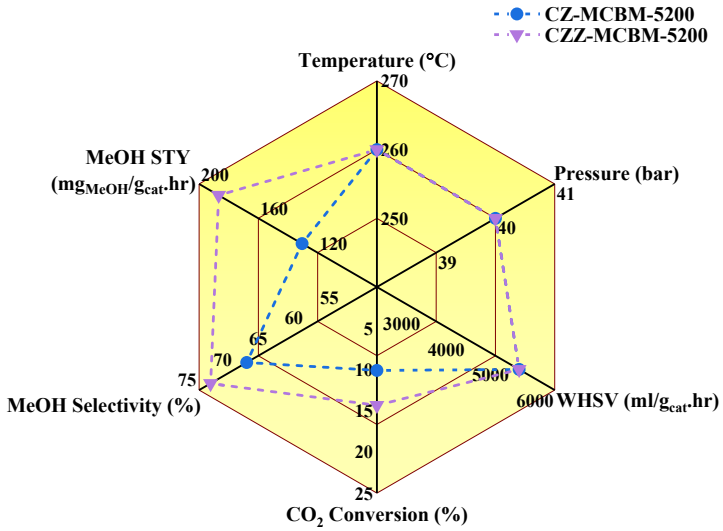


Figure 6.11. *Radar plot illustrating the comparative catalytic performance of CZ-MCBM and CZZ-MCBM catalysts at optimized reaction conditions (T = 260°C, P = 40 bar, WHSV = 5200 ml/g_{cat}·hr).*

In summary, the radar plot clearly demonstrates that ZrO_2 incorporation transforms both the structural and electronic properties of the catalyst, resulting in substantial gains in CO_2 conversion, methanol selectivity, and MeOH STY. The strong synergistic effect of ZrO_2 makes CZZ-MCBM a highly efficient and resilient catalyst for methanol synthesis, particularly under demanding high-throughput conditions.

6.2.3.2 Effect of Synthesis Route

The radar plot in **Figure 6.12** highlights the strong influence of synthesis methodology on catalytic performance under the optimized conditions (T = 260°C, P = 40 bar, WHSV = 5200 ml/g_{cat}.hr). Among the three catalysts, CZZ-MCBM delivered the highest activity and selectivity, achieving a CO_2 conversion of 14.4%, methanol selectivity of 73%, and a methanol STY of 187 mg_{MeOH}/g_{cat}.hr. In contrast, CZZ-CPUSI achieved a 11.3% conversion, 67%

selectivity, and 142 mg_{MeOH}/g_{cat}.hr STY, while CZZ-SPUSI showed the lowest performance with 9.2% conversion, 64% selectivity, and 110 mg_{MeOH}/g_{cat}.hr STY.

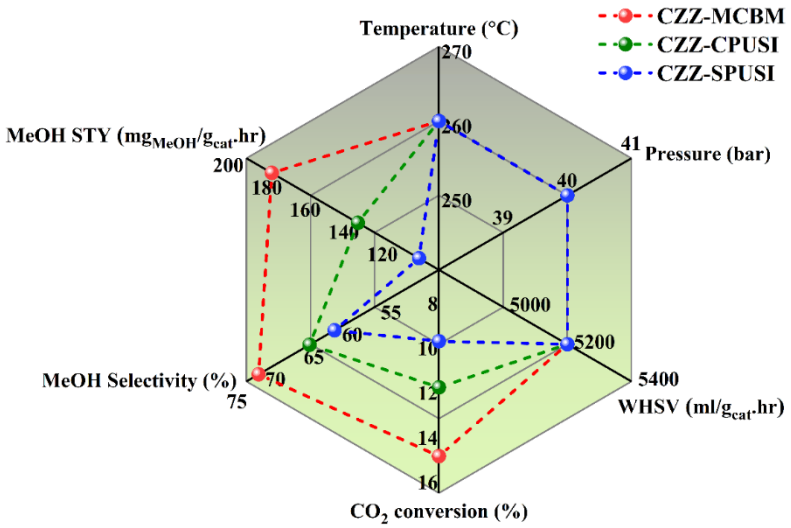


Figure 6.12. *Radar plot illustrating the comparative catalytic performance of CZZ catalysts at optimized reaction conditions (T = 260°C, P = 40 bar, WHSV = 5200 ml/g_{cat}·hr).*

These differences underscore that the synthesis route critically determines the structural and electronic features of the catalyst, which in turn dictate CO_2 activation and methanol formation pathways. Ball milling (MCBM) appears particularly effective in promoting intimate metal-support interactions, enhanced Cu dispersion, and abundant oxygen vacancies-features already identified in the earlier comparison of CZ-MCBM and CZZ-MCBM as decisive for boosting methanol synthesis. By contrast, CPUSI and SPUSI methods lead to comparatively weaker metal-support interactions and lower defect densities, which limit their catalytic efficiency. In summary, while ZrO_2 incorporation establishes the intrinsic promotional advantage, the synthesis route strongly governs how effectively these features are realized in practice. The MCBM route clearly outperforms conventional synthesis approaches by creating catalysts with optimized structure-property relationships, leading to superior CO_2 conversion, methanol selectivity, and STY.

6.2.3.3 Benchmarking of the CZZ-MCBM catalyst against state-of-the-art Cu-based catalysts

Figure 6.13 (a) compares the catalytic performance of all in-house synthesized catalysts under identical reaction conditions (T = 240°C, P = 40 bar, WHSV = 5200 ml/g_{cat}.hr). Among all the in-house catalysts synthesized via different preparation methods, considering the precursor chemistry, the CZZ-MCBM catalyst clearly outperforms the others, exhibiting the highest

methanol space-time yield, along with superior CO_2 conversion and methanol selectivity. This confirms the beneficial effect of ZrO_2 promotion combined with the mechano-chemical synthesis route, which enhances metal dispersion, oxygen vacancy concentration, and metal-support interactions.

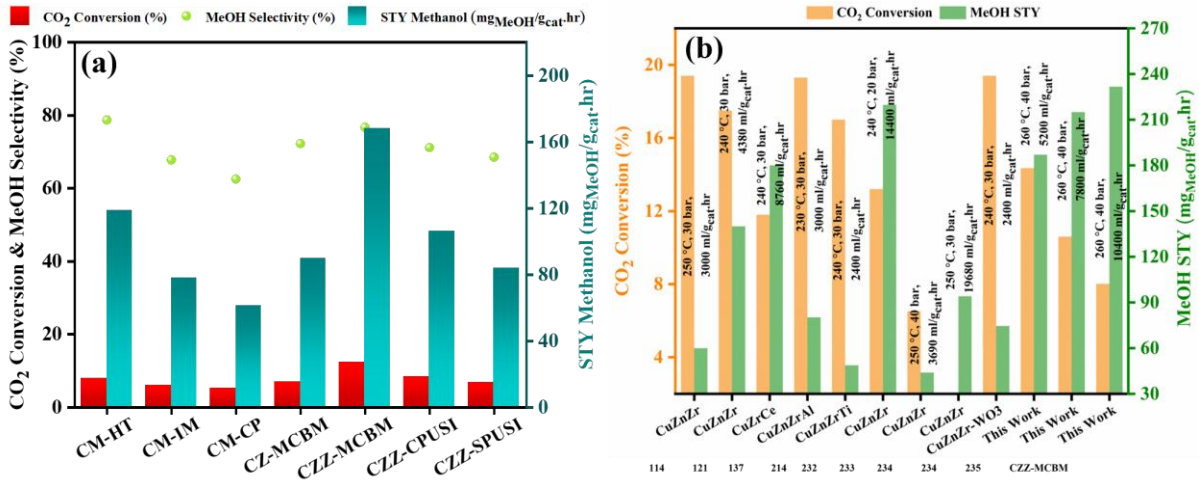


Figure 6.13. (a) *Comparative catalytic performance of all in-house synthesized Cu-based catalysts evaluated at T = 240°C, P = 40 bar, and WHSV = 5200 ml/g_{cat}.hr,* ***(b)*** *Benchmark comparison of the CZZ-MCBM catalyst with representative state-of-the-art Cu-Zn-based catalysts reported in the literature under comparable operating conditions* [114,121,137,214,232–235].

Figure 6.13 (b) further benchmarks the best-performing CZZ-MCBM catalyst against representative Cu-based catalysts reported in the literature, which primarily contain Cu and Zn as active components. Under comparable operating conditions, the CZZ-MCBM catalyst demonstrates competitive to superior methanol productivity and selectivity, confirming the effectiveness of the present precursor-engineering and synthesis strategy. This direct comparison establishes that the performance achieved in this work is not only superior internally but also comparable to state-of-the-art Cu-based catalytic systems reported for CO_2 hydrogenation to methanol.

Overall, these benchmarking results firmly validate the technological relevance and industrial potential of the CZZ-MCBM catalyst developed in this study.

6.2.4 Property-activity relationship

The spider plot **(Figure 6.14)** highlights the strong connection between the physicochemical properties of the catalysts and their catalytic performance. Higher Cu dispersion, larger active Cu surface area, and smaller crystallite size all coincide with enhanced CO_2 conversion and

methanol STY. These features reflect the quality and density of Cu-oxide interfacial sites, which are critical for stabilizing intermediates and facilitating hydrogenation. Among all samples, the mechanochemically prepared CZZ-MCBM occupies the outer envelope of this plot, with the smallest crystallite size and highest dispersion and surface area, directly translating into superior catalytic activity and productivity under identical reaction conditions (260°C, 40 bar, WHSV = 5200 ml/g_{cat}.hr).

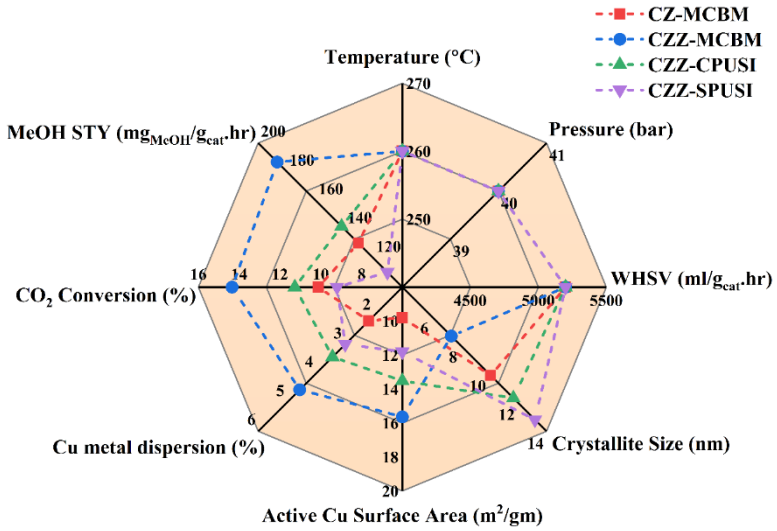


Figure 6.14. *Spider plot illustrating the structure-property-activity relationship of CZ-MCBM and CZZ catalysts synthesized via different preparation routes.*

While such physicochemical properties already explain much of the performance trend, the bar plots **(Figure 6.15** and **Figure 6.16)** further reveal the decisive role of oxygen vacancy concentration (OVC). Beyond dispersion and crystallite size, vacancies act as electronic and structural promoters that modulate CO_2 adsorption, H_2 activation, and intermediate stabilization. In the case of CZ-MCBM catalyst, the relative OVC is 70%, yielding a methanol STY of 131 mg_{MeOH}/g_{cat}.hr, whereas ZrO_2 incorporated Cu/ZnO raises OVC to 85 % in CZZ-MCBM, accompanied by a productivity jump to 187 mg_{MeOH}/g_{cat}.hr and higher CO_2 conversion. Similarly, across ternary catalysts, OVC increases in the order CZZ-SPUSI (75%) < CZZ-CPUSI (79%) < CZZ-MCBM (85%), exactly paralleling their CO_2 conversion (9.2% < 11.3% < 14.3%) and STY (110 < 142 < 187 mg_{MeOH}/g_{cat}.hr).

These correlations establish OVC as a unifying descriptor that links structural defects to catalytic function. A higher vacancy density not only provides additional CO_2 binding/basic sites but also strengthens Cu oxide interactions that improve reducibility (as confirmed by lower-temperature reduction peaks in H_2-TPR), enhance H_2 dissociation and spillover to

interface sites (evident from α and β peaks in H_2-TPD), and enrich medium/strong basic sites for CO_2 activation (shown by CO_2-TPD). In this way, vacancies serve as the connecting channel among the redox, hydrogen activation, and CO_2 adsorption characteristics of the catalyst, all of which converge to dictate overall methanol productivity [14,110].

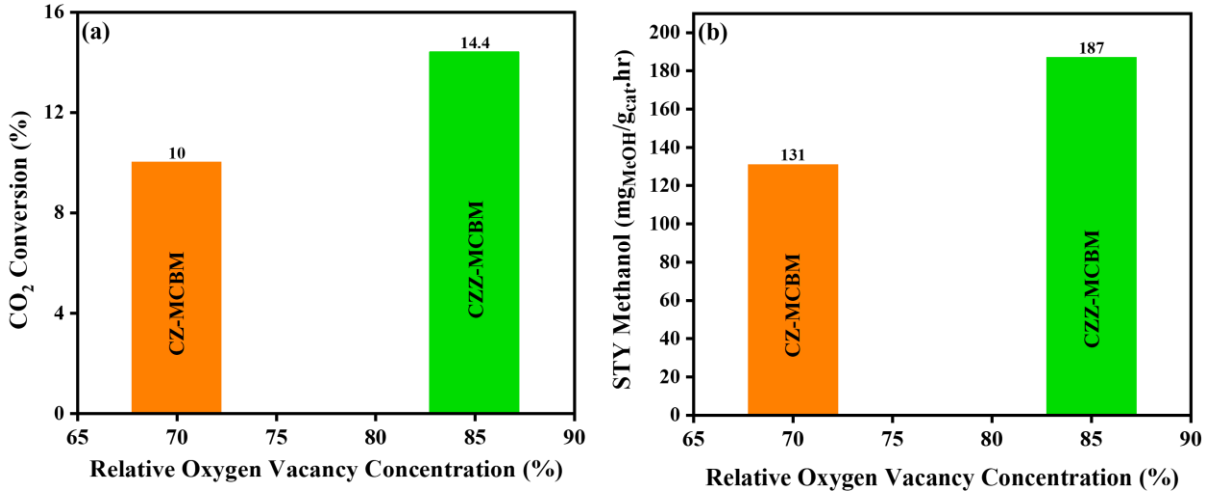


Figure 6.15. (a) *Comparative bar plot between relative oxygen vacancy concentration and CO_2 conversion for CZ-MCBM and CZZ-MCBM calcined catalysts,* ***(b)*** *Comparative bar plot between relative oxygen vacancy concentration and STY methanol for CZ-MCBM and CZZ-MCBM calcined catalysts.*

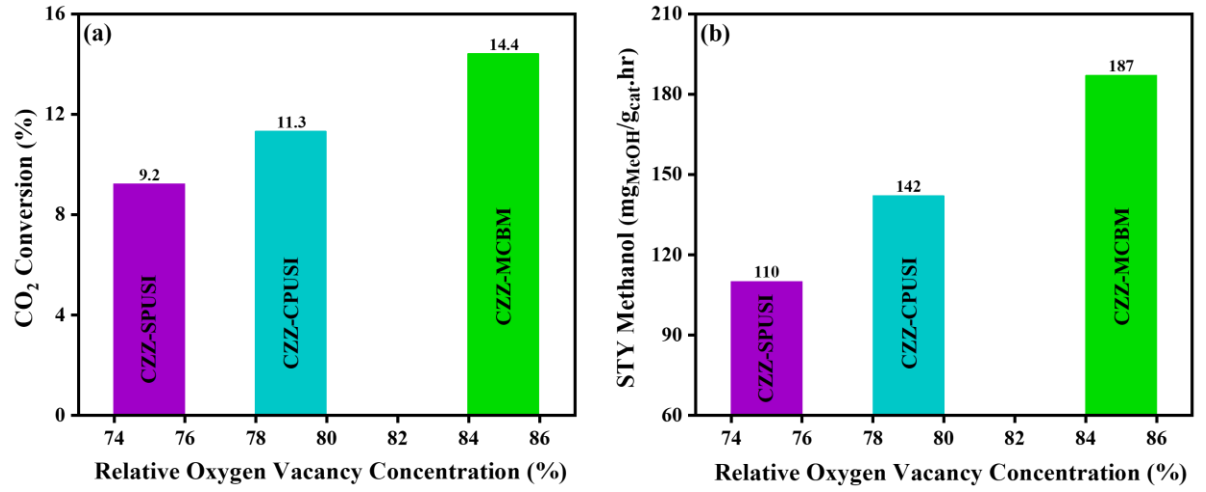


Figure 6.16. (a) *Comparative bar plot between relative oxygen vacancy concentration and CO_2 conversion for CZZ calcined catalysts,* ***(b)*** *Comparative bar plot between relative oxygen vacancy concentration and STY methanol for CZZ calcined catalysts.*

The synthesis route plays a crucial role in determining how effectively these properties are realized. Mechano-chemical ball milling (MCBM) maximizes both dispersion and OVC by producing finer crystallites and richer Cu-ZnO-ZrO_2 interfacial networks. In contrast, CPUSI and SPUSI yield relatively lower vacancy densities, larger crystallites, and weaker interfacial coupling, resulting in reduced activity.

In summary, the radar plot illustrates how intrinsic textural and dispersion-related factors drive activity, while the bar plots demonstrate that oxygen vacancies act as an equally critical lever, integrating structural, redox, and adsorption characteristics. Together, they point to a unified design principle: maximize both Cu dispersion and vacancy density, particularly through ZrO_2 promotion and optimized synthesis (MCBM), to achieve superior CO_2-to-methanol performance.

6.2.5 Catalyst Stability Studies

This stability plot **(Figure 6.17 (a))** evaluates the CZZ-MCBM catalyst under a sequence of variable operating conditions over 176 hours. CO_2 conversion (%) and methanol space-time yield (STY, $mg_{MeOH}/g_{cat}\cdot hr$) are plotted against TOS, with distinct background colours demarking transitions between different tested conditions (e.g., changes in temperature, pressure, or WHSV). After 76 hours, the system is returned to a reference set of conditions, and then performance is monitored for the next 100 hours.

The minimal change in performance across this extended period is quantified by the deviations: d_{XCO2} = 4.5% and d_{STY} = 4.57%, representing the difference in CO_2 conversion and STY between 76 and 176 hours. This slight deviation demonstrates the catalyst's high structural and chemical stability, maintaining both conversion and productivity despite repeated changes in operating parameters. The catalyst effectively recovers and sustains its initial activity throughout multiple cycles and variation windows.

The second plot **(Figure 6.17 (b))** shows the long-term TOS stability of CZZ-MCBM at the optimized reaction conditions: T = 260°C, P = 40 bar, WHSV = 5200 $ml/g_{cat}\cdot hr$, and H_2/CO_2 = 3:1. Over 184 hours, both CO_2 conversion and methanol STY remain highly consistent, exhibiting only minimal declines of d_{XCO2} = 4.22% and d_{STY} = 4.11% over the whole duration. The near-horizontal trends of both parameters confirm excellent resistance to deactivation, sintering, or loss of active sites, validating CZZ-MCBM as not only highly active but also exceptionally stable under continuous operation.

Together, these plots demonstrate that the CZZ-MCBM catalyst maintains outstanding stability in both dynamic and steady-state operation. Under highly variable and optimized fixed conditions, the catalyst exhibits minimal performance loss in both CO_2 conversion and

methanol productivity, confirming its suitability for prolonged industrial methanol synthesis applications.

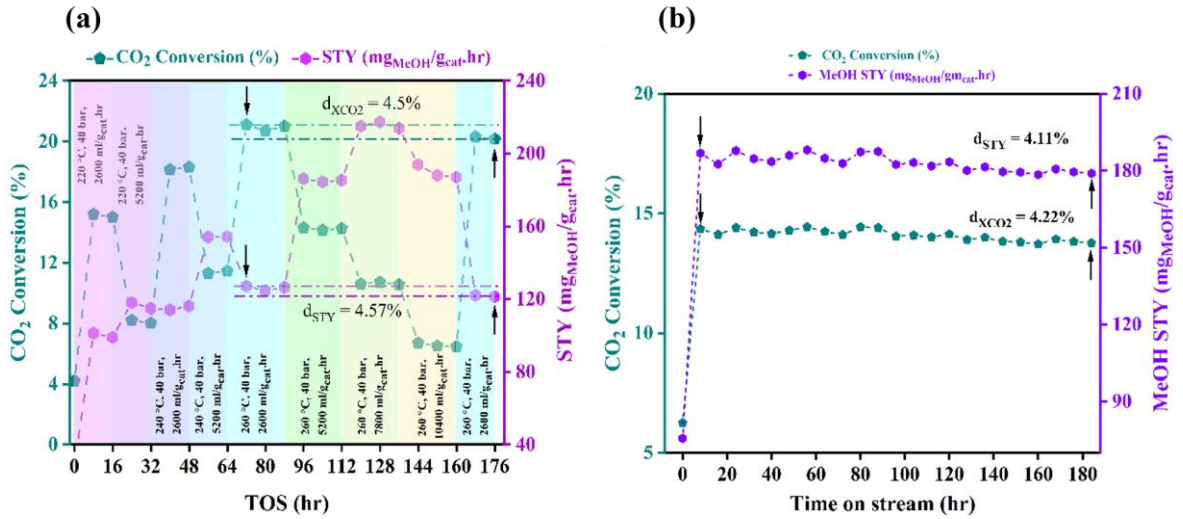


Figure 6.17. (a) *Catalyst stability test (TOS) of CZZ-MCBM catalyst on varying reaction conditions,* ***(b)*** *Catalyst stability test (TOS) of CZZ-MCBM catalyst at optimized reaction conditions (T = 260°C, P = 40 bar, WHSV = 5200 ml/g_{cat}·hr).*

6.2.6 Post-catalytic characterization studies

The post-catalysis characterization was conducted to evaluate the structural and surface changes in the spent catalyst following prolonged time-on-stream (TOS) experiments. Elemental CHNS analysis revealed a carbon deposition of only 2.66%, attributable to the Boudouard reaction **(Table 6.5).** This relatively low level of carbon accumulation, even after extended operation, highlights the catalyst's excellent resistance to coking.

Table 6.5. *Physicochemical properties of CZZ-MCBM spent catalyst.*

Catalyst	S^a_{BET} (m²/gm)	V^a_p (cc/gm)	$d_{Cu}{}^b$ (nm)	SA^c_{Cu} (m²/gm)	D^c_{Cu} (%)	[d]Carbon Content CHNS (%)
CZZ-MCBM-S	24.10	0.1019	9.54	10.68	3.06	2.66

The CZZ-MCBM catalyst exhibited remarkable stability during both dynamic and steady-state phases, showing minimal signs of deactivation due to coke formation, particle sintering, or agglomeration. Powder X-ray diffraction (PXRD) analysis of the spent catalyst **(Figure 6.18 (a))** confirmed the retention of the Cu^0 phase as the dominant crystalline component,

accompanied by minor peaks corresponding to ZnO (JCPDS 36-1451) and ZrO_2 (JCPDS 37-1484).

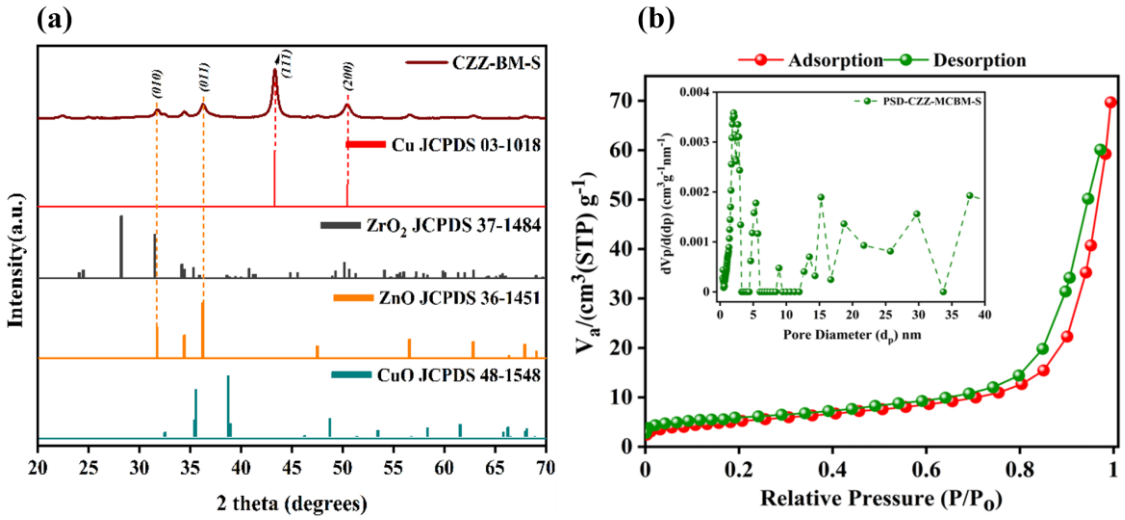


Figure 6.18. (a) *PXRD pattern of CZZ-MCBM-S spent catalyst,* ***(b)*** *N_2 adsorption-desorption isotherm and PSD plot of CZZ-MCBM spent catalyst.*

The crystallite size of metallic Cu, calculated from the Cu(111) reflection, was determined to be 9.54 nm **(Table 6.5),** which is only slightly increased compared to the fresh catalyst, indicating negligible sintering. Furthermore, the BET surface area (24.10 m^2/g), active Cu surface area (10.68 m^2/g), and Cu dispersion (3.06%) remained essentially unchanged relative to the pristine catalyst. This consistency in physicochemical properties before and after reaction underscores the structural integrity and robustness of the CZZ-MCBM catalyst under harsh reaction conditions. Overall, the post-catalytic analysis demonstrates that the CZZ-MCBM catalyst maintains its structural and surface properties exceptionally well, directly correlating with its superior catalytic performance and long-term operational stability compared to other formulations.

6.3 Summary and Future Outlook

In this chapter, a scalable mechano-chemical ball milling (MCBM) strategy was successfully employed for the synthesis of phase-pure zincian malachite precursors, enabling the rational design of highly efficient Cu-based catalysts for CO_2 hydrogenation to methanol. The method demonstrated excellent control over precursor phase formation, which is critical for achieving favourable structure-activity relationships in the final calcined catalysts.

Comprehensive physicochemical characterization confirmed that the CZZ-MCBM catalyst exhibits superior textural properties, higher metal dispersion, stronger metal-support interaction, and enhanced oxygen vacancy concentration compared to catalysts synthesized via other routes. The incorporation of ZrO_2 played a decisive role in improving catalyst stability, surface basicity, and oxygen defect density, and its promotional effect was consistently reflected across structural, activity, stability, and structural analyses.

A clear correlation between oxygen vacancy concentration and methanol yield was established, highlighting the importance of defect-mediated CO_2 activation in governing the reaction performance. Catalytic evaluation revealed that the optimized operating conditions for the CZZ-MCBM catalyst are T = 260°C, P = 40 bar, and WHSV = 5200 $ml/g_{cat}\cdot hr$, under which the catalyst delivered a CO_2 conversion of 14.4%, methanol selectivity of 73%, and methanol STY of 187 $mg_{MeOH}/g_{cat}\cdot hr$.

Long-term stability testing demonstrated the excellent durability of the CZZ-MCBM catalyst, with only ~4.2% performance deviation over 184 hours of time-on-stream, confirming its strong resistance to sintering and deactivation under reaction conditions.

Overall, this work establishes the MCBM route as a simplified, scalable, cost-effective, and highly efficient synthesis strategy for fabricating phase-pure $Cu/ZnO/ZrO_2$ catalysts. The insights gained into precursor engineering, oxygen vacancy control, and metal-support synergy provide valuable guidelines for the rational design of next-generation Cu-based catalysts for high-performance CO_2 hydrogenation to methanol.

While the present chapter establishes the superior performance of the CZZ-MCBM catalyst through precursor engineering and ZrO_2 promotion, a quantitative understanding of the intrinsic reaction steps and rate-controlling phenomena is essential for process-level optimization. Accordingly, the subsequent chapter focuses on detailed kinetic modeling and mechanistic investigations of CO_2 hydrogenation to methanol over the optimized Cu-based catalyst using experimental and spectroscopic insights. This integrated approach provides a direct link between catalyst structure, reaction mechanism, and reactor-scale performance.

Chapter 7 Parameter-driven performance, reaction kinetics, and mechanistic modeling in CO_2 hydrogenation to methanol over the ternary Cu/ZnO/ZrO_2 catalyst

7.1 Overview

Following the demonstration of superior activity, stability, and structural robustness of the ternary Cu/ZnO/ZrO_2 (CZZ-MCBM) catalyst in the preceding chapter, this chapter presents a structured, multi-faceted investigation of CO_2 hydrogenation to methanol, integrating parameter-driven performance analysis, *in-situ* mechanistic insight, and quantitative kinetic modeling into a unified framework. The study is designed to progress systematically from macroscopic performance evaluation to molecular-level mechanistic understanding, ultimately leading to a robust kinetic framework capable of predicting catalytic performance.

The chapter begins with a systematic assessment of the parameter-driven performance landscape, quantifying how process parameters, such as temperature, pressure, and space velocity (WHSV), influence CO_2 conversion, product selectivity, and methanol space-time yield. This analysis establishes the optimal operating window and generates the experimental dataset required for robust kinetic parameter estimation.

Building on this foundation, *in-situ* DRIFTS spectroscopy is employed to elucidate the dynamic evolution of surface intermediates under reaction conditions. The spectroscopic evidence identifies the dominant reaction pathway and clarifies the role of the multifunctional Cu/ZnO/ZrO_2 interface in stabilizing key intermediates during the methanol synthesis process. These mechanistic insights are then integrated into a comprehensive Langmuir-Hinshelwood-Hougen-Watson (LHHW) kinetic framework.

Multiple kinetic models are implemented, parameterized, and rigorously evaluated based on statistical goodness of fit, thermodynamic consistency, and agreement with spectroscopically identified mechanisms. The resulting validated model successfully bridges surface chemistry with reactor-scale observations, providing a quantitative tool for interpreting catalyst behaviour and enabling predictive process modeling for future intensification and scale-up.

In summary, this chapter establishes a direct and quantitative link between operating parameters, reaction mechanism, and intrinsic kinetics for CO_2 hydrogenation to methanol over the CZZ-MCBM catalyst, thereby completing the structure-performance-mechanism-kinetics continuum of this thesis.

7.2 Results and Discussion

7.2.1 Parameter-driven performance: Uncovering the role of temperature, pressure, and WHSV in methanol synthesis

To establish the baseline performance of the CZZ-MCBM catalyst before mechanistic (*in-situ* DRIFTS) and kinetic modeling studies, its catalytic activity was systematically evaluated by varying temperature, pressure, and WHSV at a fixed CO_2/H_2 ratio of 1:3. This screening enabled the identification of the optimal operating window and clarified how each process variable influence CO_2 conversion, CH_3OH/CO selectivity, and methanol yield.

This sequential evaluation not only defined the most favourable operating window but also generated key performance trends that can be directly interpreted through LHHW kinetic models. Such models, including those proposed by Vanden Bussche & Froment (1996) and Graaf et al. (1988), describe methanol synthesis as a competition between CO_2 hydrogenation, CO hydrogenation, and the reverse water-gas shift (RWGS) reactions, governed by adsorption-desorption equilibria. The performance patterns identified here, therefore, serve as the experimental basis against which mechanistic and kinetic interpretations are later developed.

7.2.1.1 Effect of temperature on the catalytic activity

Methanol synthesis is an exothermic reaction that is favoured at low temperatures and high pressures; however, the kinetically inert CO_2 molecule requires sufficient thermal energy for activation [8,59]. Screening experiments revealed that higher temperatures promoted CO_2 activation and conversion but also shifted selectivity towards CO via the RWGS reaction, thereby reducing methanol selectivity [8,22,59,110,137]. The CZZ-MCBM catalyst, however, maintained relatively high methanol selectivity across the investigated range, which translated into higher space-time yields (STY) when both CO_2 conversion and methanol selectivity were considered. An optimum catalytic performance was observed at ~260°C, where the balance between conversion and selectivity yielded the maximum methanol STY. At this condition

(260°C, 40 bar, 5200 ml/g_{cat}·hr), CO_2 conversion, methanol selectivity, and methanol STY reached 14.4%, 73%, and 187 mg_{MeOH}/g_{cat}·hr, respectively, in close agreement with thermodynamic predictions, as illustrated in **Figure 7.1 (a)** and **(b)** [8,22,110,137]. The equations of CH_3OH, CO via CO_2, and CO hydrogenation are written in **Equations (7.1) to (7.3)**.

$$CO_2 + 3H_2 \rightleftharpoons CH_3OH + H_2O, \quad \Delta H_{25°C} = -49.5\ kJmol^{-1} \tag{7.1}$$

$$CO_2 + H_2 \rightleftharpoons CO + H_2O, \quad \Delta H_{25°C} = 41.2\ kJmol^{-1} \tag{7.2}$$

$$CO + 2H_2 \rightleftharpoons CH_3OH, \quad \Delta H_{25°C} = -90.6\ kJmol^{-1} \tag{7.3}$$

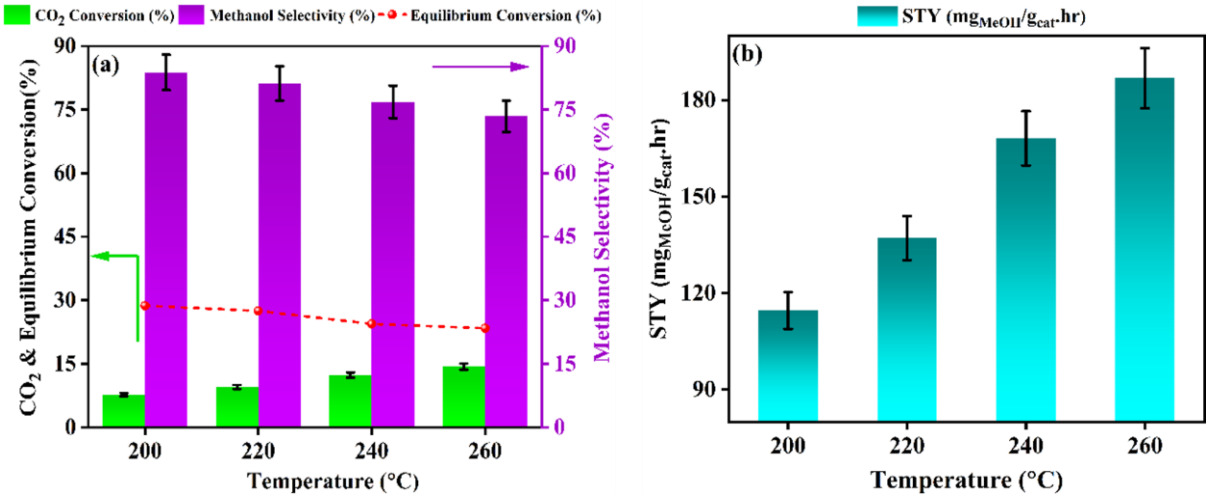


Figure 7.1. *Effect of temperature on* ***(a)*** *CO_2 conversion and methanol selectivity, and* ***(b)*** *methanol space-time yield (STY) at 40 bar and WHSV = 5200 ml/g_{cat}.hr over the CZZ-MCBM catalyst during CO_2 hydrogenation to methanol.*

7.2.1.2 Effect of pressure on the catalytic activity

Following the identification of 260°C as the optimal temperature, the influence of total pressure was evaluated across a range of 20 to 40 bar. As illustrated in the accompanying **Figure 7.2 (a) and (b)**, both CO_2 conversion and methanol selectivity exhibit a strong positive correlation with increasing pressure.

This trend is consistent with the reaction equilibrium, which favours methanol synthesis at higher pressures due to a reduction in the number of gas molecules. More significantly, under the prevailing kinetic regime, elevated pressure enhances the surface coverage of reactants by promoting the adsorption of CO_2 and H_2 onto the catalyst's active sites. This intensified

reactant-catalyst interaction directly drives the observed increase in CO_2 conversion and methanol selectivity, which in turn maximizes the methanol space-time yield (STY) [110,137].

The data conclusively show that 40 bar delivers the highest catalytic performance within the studied range. Therefore, 40 bar was established as the optimum pressure, operating in synergy with the previously determined temperature of 260°C.

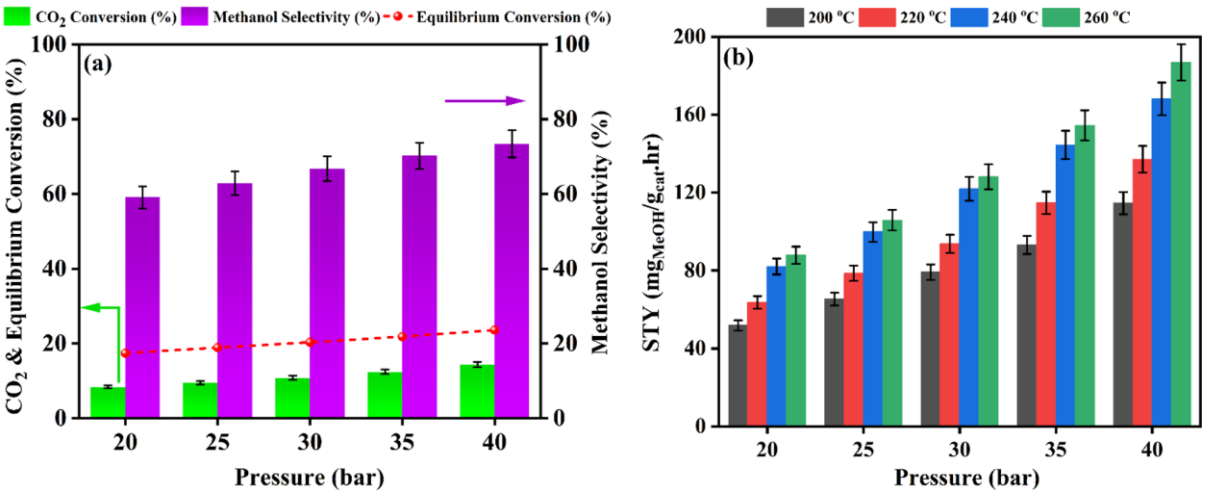


Figure 7.2. *Effect of pressure on* ***(a)*** *CO_2 conversion and methanol selectivity at T = 260°C and WHSV = 5200 ml/g_{cat}.hr, and* ***(b)*** *methanol space-time yield (STY) at varying temperatures and WHSV = 5200 ml/g_{cat}.hr over the CZZ-MCBM catalyst during CO_2 hydrogenation to methanol.*

7.2.1.3 Effect of space velocity on the catalytic activity

The influence of weight hourly space velocity (WHSV) was investigated under the optimized conditions of 260°C and 40 bar. The results, depicted in the accompanying **Figure 7.3 (a) and (b)**, demonstrate that WHSV is a critical operating parameter that directly affects the reactant-catalyst interaction time and thereby governs catalytic performance.

A clear inverse relationship was observed between WHSV and CO_2 conversion. Increasing the WHSV from 2600 to 5200 ml/g_{cat}.hr reduced the CO_2 conversion from approximately 20% to 15%, a decrease of about 25%. A further increase to 10400 ml/g_{cat}.hr led to a conversion of only ~10%, representing a 50% reduction from the initial value. This decline is attributed to the shorter contact time between the reactants and the catalyst at higher space velocities, limiting the opportunity for CO_2 activation. In contrast, methanol selectivity remained largely stable, showing only a slight increase with rising WHSV. However, since the methanol space-time yield (STY) is a function of both conversion and selectivity, the sharp drop in CO_2

conversion became the dominant factor. Consequently, the overall MeOH STY decreased significantly with increasing WHSV. These trends confirm that within the tested range, the residence time, controlled by WHSV, is the primary determinant of catalytic efficiency for CO_2 hydrogenation to methanol [8,22,59,110,137].

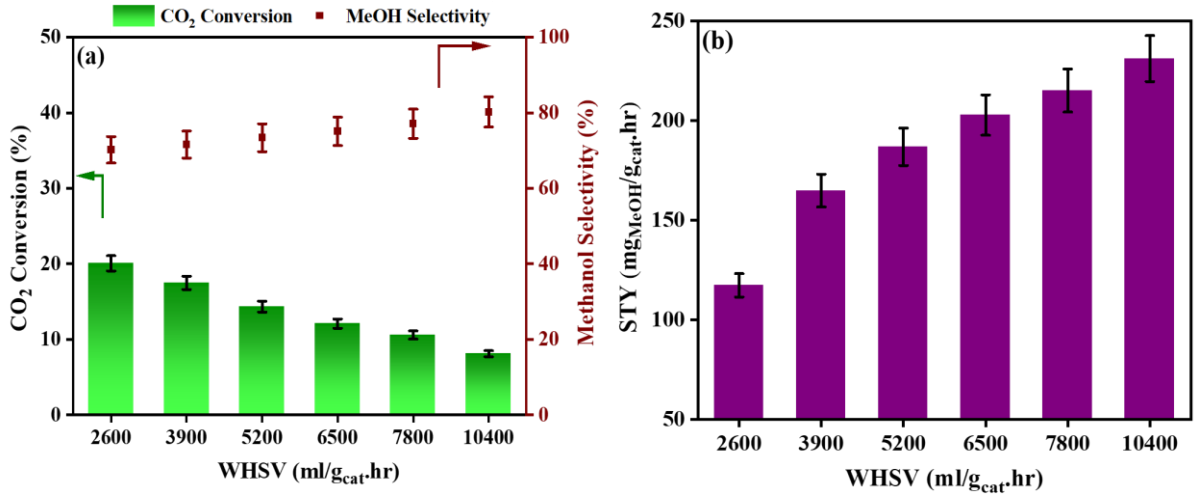


Figure 7.3. *Effect of WHSV on* ***(a)*** *CO_2 conversion and methanol selectivity, and* ***(b)*** *methanol space-time yield (STY) at T = 260°C and P = 40 bar over the CZZ-MCBM catalyst during CO_2 hydrogenation to methanol.*

7.2.1.4 Effect of temperature and pressure on the product distribution

The product distribution, as illustrated in **Figure 7.4 (a) and (b)**, clearly demonstrates the competing effects of temperature and pressure. At lower temperatures (e.g., 200-220°C), the product stream is predominantly composed of methanol, with selectivity exceeding 80%. However, as the temperature increases, the reverse water-gas shift (RWGS) reaction is progressively favoured, leading to a significant rise in CO formation. At 260°C, the CO selectivity increases to approximately 23%, and this trend is accompanied by a slight increase in methane formation at higher temperatures.

Pressure exhibits an opposing effect, strongly favouring methanol formation by shifting the equilibrium. Higher pressure suppresses the RWGS reaction, as evidenced by the increased methanol share in the product slate at 40 bar compared to lower pressures.

Therefore, selecting the optimal operating conditions requires balancing competing effects. Lower temperatures favour high methanol selectivity but result in insufficient CO_2 activation and low overall conversion, whereas higher temperatures boost CO_2 conversion at the expense of undesirable CO production. An optimum was identified at 260°C and 40 bar, providing sufficient energy for CO_2 activation while maintaining sufficiently high methanol selectivity.

Coupled with an optimized WHSV of 5200 ml/g_{cat}.hr, these conditions balance residence time and productivity, maximize the methanol space-time yield, and maintain catalytic stability. While these trends establish the optimal operational window, understanding the underlying molecular pathways and surface intermediates is essential to rationalize the observed performance and guide subsequent kinetic modeling studies.

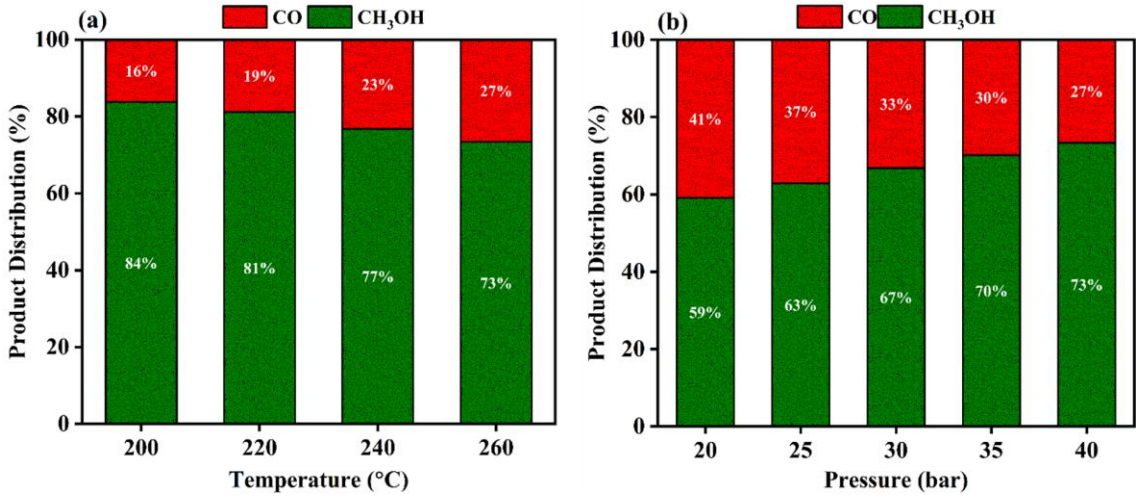


Figure 7.4. *Effect of* ***(a)*** *temperature and* ***(b)*** *pressure on product distribution (CO and CH_3OH) over the CZZ-MCBM catalyst during CO_2 hydrogenation to methanol. Plot* ***(a)*** *corresponds to P = 40 bar and WHSV = 5200 ml/g_{cat}.hr, and plot* ***(b)*** *corresponds to T = 260°C and WHSV = 5200 ml/g_{cat}.hr.*

7.2.2 Mechanistic Insights

To gain deeper insight into the origin of the catalytic performance trends observed under optimized operating conditions, *in-situ* Diffuse Reflectance Infrared Fourier Transform Spectroscopy (DRIFTS) was employed to elucidate the reaction mechanism of CO_2 hydrogenation to methanol over the developed CZZ-MCBM catalyst. The evolution of surface species was monitored under a continuous flow of CO_2 and H_2 as the temperature was ramped from 50°C (T50) to 250°C (T250), as shown in **Figure 7.5 (a)**. These experiments provide direct spectroscopic evidence of transient intermediates, allowing for the identification of the dominant reaction pathway governing methanol formation [110,137,226,227].

With increasing temperature, the spectra reveal a dynamic progression of surface intermediates. The appearance of carbonate species evidences the initial adsorption of CO_2. The bands in the regions of 1650-1300 cm^{-1} and 1100-1000 cm^{-1} can be assigned to various configurations, including unidentate carbonate (~1330 cm^{-1}) and bidentate carbonate (~1580 cm^{-1}). As the temperature is elevated, these carbonate species are progressively hydrogenated. A critical

transition is observed with the emergence and growth of intense bands in the region of 1750-1400 cm^{-1}, characteristic of formate (HCOO*) species. Specifically, the vibrations around ~1530 cm^{-1} and ~1370 cm^{-1} are attributed to the asymmetric and symmetric O-C-O stretching modes of the bidentate formate, which becomes a dominant surface intermediate. The persistence and increasing intensity of these formate bands with temperature underscore their role as a central and stable intermediate. Subsequent hydrogenation of the formate species leads to the formation of methoxy (H_3CO*) groups, identified by the C-H stretching vibrations appearing between ~1100-1170 cm^{-1} and the O-H deformation mode near ~1450 cm^{-1}. The final scission of the C-O bond in the methoxy intermediate results in the desorption of molecular methanol, $H_3COH(g)$ [88,226,227].

This sequence of intermediates, from carbonates to formates to methoxy, and finally to methanol, is schematically summarized in **Figure 7.5 (b)**. The absence of significant signals attributable to CO* adsorbed on metal sites suggests that the CO route (or indirect pathway via the reverse water-gas shift reaction) is not a dominant pathway under these conditions. Therefore, the *in-situ* DRIFTS analysis conclusively demonstrates that methanol synthesis proceeds primarily via the direct hydrogenation of CO_2 through the formate pathway, with formate (HCOO*) and methoxy (H_3CO*) serving as the key stable intermediates [144,226,227].

Our spectroscopic observations are fully consistent with the broader mechanistic understanding established for Cu-based methanol synthesis catalysts. The predominance of formate, persisting across the entire temperature range, mirrors the findings of Grabow and Mavrikakis (2011) [71] and Studt et al. (2015) [142], whose microkinetic analyses identified formate stabilization and subsequent hydrogenation as essential steps in the CO_2-to-methanol pathway. The strong and thermally resilient formate bands observed on the CZZ-MCBM catalyst indicate that our catalyst surface provides the type of multifunctional environment, combining Cu^+, Cu^0, and oxide-derived basic sites, previously emphasized by Behrens et al. (2012) [25] and Chen et al. [236], for efficient CO_2 activation. Moreover, the apparent dominance of the formate pathway over the RWGS-derived CO route is consistent with systems where ZnO-rich interfaces modulate CO_2 binding and suppress CO-mediated channels, as reported by Wang and Kattel (2019) [88]. This stands in contrast to catalysts with stronger Cu-ZrO_2 interactions, where Kattel et al. (2016) [105] observed a shift toward CO-assisted hydrogenation. Thus, our DRIFTS results provide direct experimental validation that, under realistic operating

conditions, the CZZ-MCBM catalyst promotes a classical formate-mediated CO_2 hydrogenation mechanism rather than a RWGS-driven CO pathway.

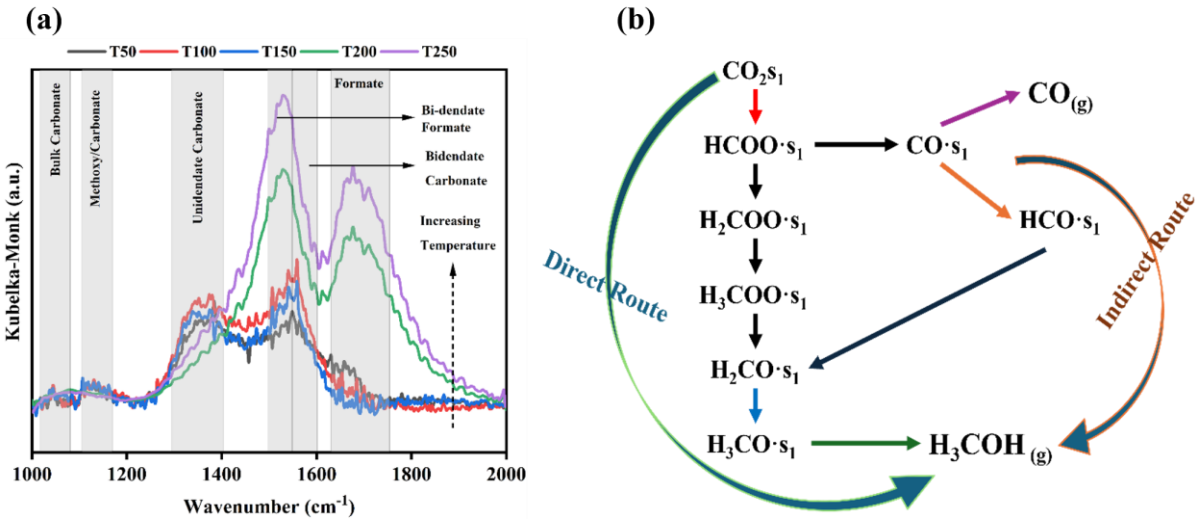


Figure 7.5. (a) *In-situ DRIFTS analysis of surface species formed during CO_2 hydrogenation over the catalyst,* ***(b)*** *schematic representation of the proposed reaction mechanism showing the transformation pathways of surface intermediates leading to methanol formation.*

The identification of this reaction pathway and its associated intermediates provide the mechanistic foundation for the kinetic analysis presented in the following section. The strong spectroscopic evidence for persistent formate species suggests that formate hydrogenation is the most likely rate-determining step, informing the selection of elementary steps included in LHHW-type kinetic models. Moreover, the detection of bidentate carbonates, formates, and methoxy species directly guides the formulation of adsorption-desorption equilibria and reaction pathways in the kinetic rate expressions. In the subsequent kinetic modeling, the estimated activation energies, adsorption enthalpies, and surface coverages are interpreted in direct correlation with this spectroscopic evidence, enabling a coherent link between molecular-level chemistry and reactor-scale rate behaviour.

7.2.3 Kinetic Studies

Building on the performance trends and mechanistic insights obtained from *in-situ* DRIFTS, particularly the identification of formate hydrogenation as the central reaction step, kinetics studies were undertaken to quantitatively describe the intrinsic reaction rates of methanol synthesis over the CZZ-MCBM catalyst. To ensure the validity of the intrinsic kinetics, potential transport limitations were first assessed using the Weisz-Prater and Mears criteria,

confirming the absence of significant internal and external mass transfer effects under all experimental conditions (C_{WP} << 0.3 and C_m << 0.15) [144,145].

With validated intrinsic data, different families of Langmuir-Hinshelwood-Hougen-Watson (LHHW) models were implemented and compared, including the single-site two-reaction model (Model A), the dual-site two-reaction model (Model B), and the extended dual-site three-reaction model (Model C), incorporating CO_2 hydrogenation, CO hydrogenation, and RWGS. These models translate molecular-level processes-adsorption, surface reaction, and product inhibition into macroscopic rate expressions, enabling direct comparison with the experimental data collected in the parameter-variation studies.

7.2.3.1 *Model Comparison and Validation*

The adequacy of each kinetic model was evaluated through both qualitative parity plots and quantitative statistical metrics (R^2, RMSE). A visual inspection of the parity plots for the molar flow rates of CH_3OH and CO reveals a clear progression in predictive accuracy from **Figure 7.6** (Model A) to **Figure 7.7** (Model B) and finally to **Figure 7.8** (Model C), with the latter showing the tightest clustering of data along the parity line over the full range This qualitative assessment is confirmed quantitatively in **Table 7.1,** which summarizes the statistical goodness-of-fit. The dual-site three-reaction model (Model C) yielded the highest R^2 values (0.97-0.98) and the lowest RMSE for key components, thereby establishing its superior predictive accuracy. This statistical superiority underscores a key mechanistic insight: accurately describing our system requires a model that accounts for the contributions of both CO and CO_2 to methanol synthesis, even when CO_2 is the sole carbon source. The strong agreement in Model C's parity plots and its robust statistical performance confirm it as the most reliable representation of the intrinsic kinetics [144].

Table 7.1. *Statistical Goodness-of-Fit Metrics for the Kinetic Models.*

Models	Component	R^2 score	RMSE
Single-site two-reaction model	CH_3OH	0.92	1.54E-7
	CO	0.94	8.63E-8
Dual-site two-reaction model	CH_3OH	0.95	1.42E-7
	CO	0.95	5.59E-8
Dual-site three-reaction model	CH_3OH	0.97	9.65E-8

	CO	0.98	4.31E-8

This statistical superiority is underpinned by robust physical and mechanistic reasoning. While DRIFTS confirmed that CO is not a primary feedstock, it also revealed non-negligible CO selectivity (15-35%). The three-reaction model uniquely captures this complexity by incorporating a pathway for the hydrogenation of this *in-situ* generated CO. This inclusion is critical, as the reaction ($CO + 2H_2 \rightleftharpoons CH_3OH$, $\Delta H_{25°C} = -90.6\ kJmol^{-1}$) is thermodynamically more favourable than direct CO_2 hydrogenation. Therefore, Model C most accurately reflects the actual reaction network: the formate pathway dominates, but CO produced via RWGS is concurrently consumed, a crucial nuance missed by simpler models [95,137,145].

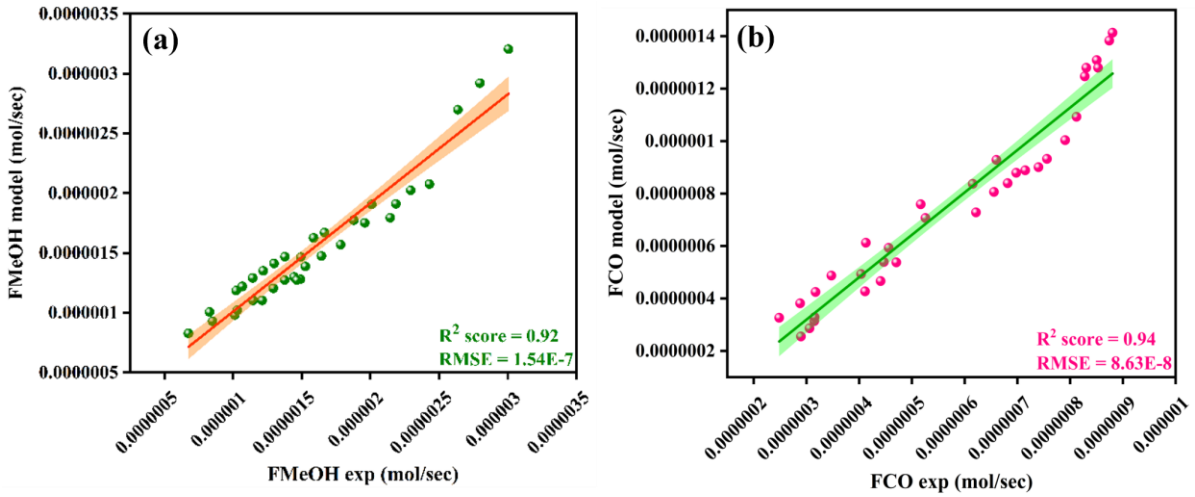


Figure 7.6. *Parity plots comparing experimental and predicted molar flow rates of* ***(a)*** *methanol (MeOH) and* ***(b)*** *carbon monoxide (CO) for Model A.*

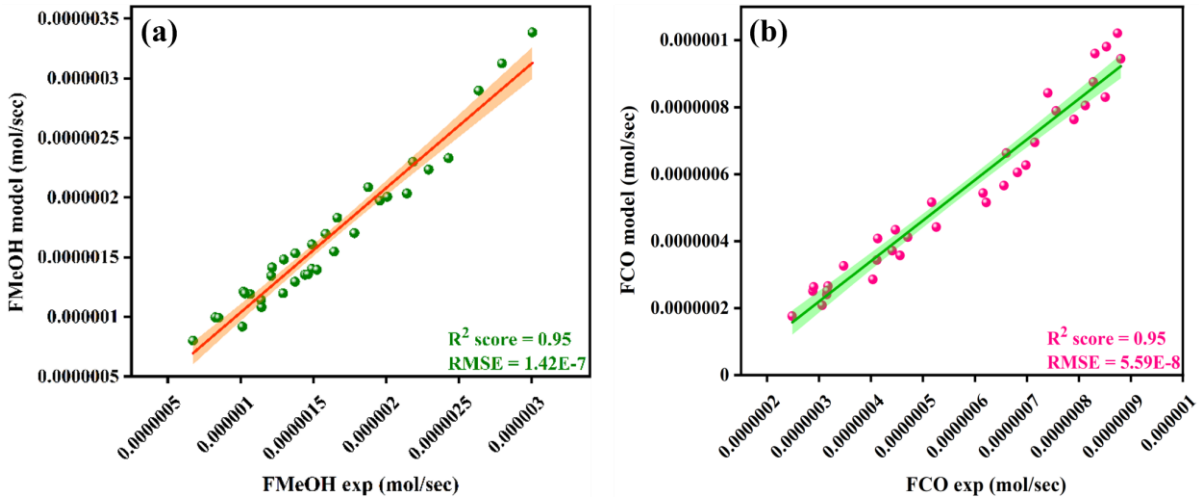


Figure 7.7. *Parity plots comparing experimental and predicted molar flow rates of* ***(a)*** *methanol (MeOH) and* ***(b)*** *carbon monoxide (CO) for Model B.*

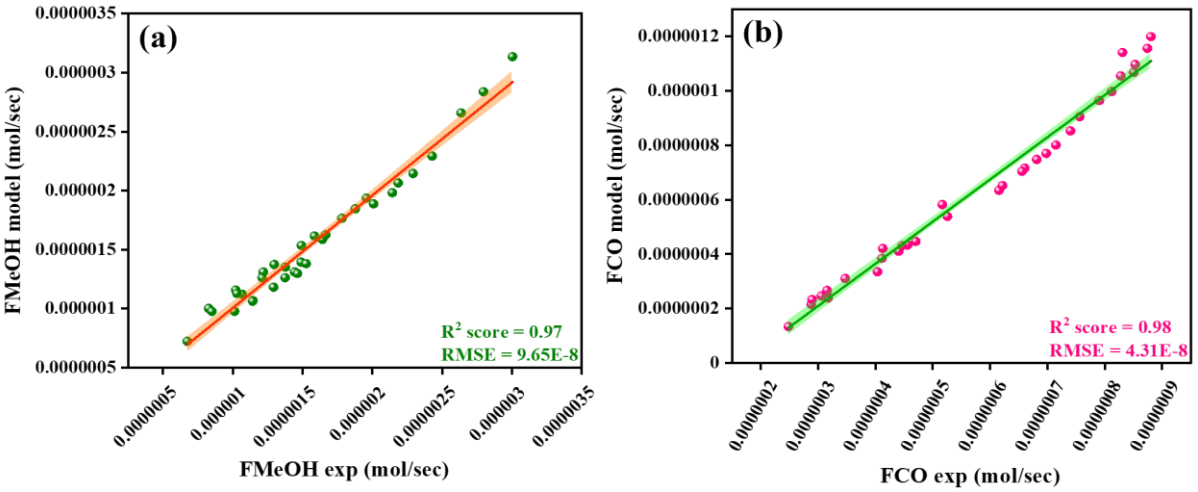


***Figure 7.8**. Parity plots comparing experimental and predicted molar flow rates of **(a)** methanol (MeOH) and **(b)** carbon monoxide (CO) for Model C.*

7.2.3.2. Parameter Estimation and Mechanistic Interpretation

Having statistically established the superiority of the dual-site three-reaction model (Model C), its kinetic and adsorption parameters were estimated via non-linear regression and are presented in **Table 7.2, Table 7.3,** and **Table 7.4** for all tested models. The parameters for the best-performing Model C are expressed in the Arrhenius/Van't Hoff form (Parameter = A × exp(B/RT)), where for rate constants (k), A represents the pre-exponential parameter. B represents the activation energy (E_a) in J/mol. In contrast, for adsorption constants (K), A represents the pre-exponential factor, and B represents the enthalpy of adsorption (ΔH_{ads}) in J/mol.

***Table 7.2.** Estimated Parameters for the Single-Site Two-Reaction Model (Model A).*

Single-Site (Two reaction)		Simulated Values
$k'_{CH_3OH}K'_2K_3K_4K_{H_2}$ (mol/kg$_{cat}$.sec.bar^2)	A	12.74
	B	22468
k'_1 (mol/kg$_{cat}$.sec.bar)	A	2.2×10^3
	B	49528
$\sqrt{K_{H_2}}$ (bar$^{-1/2}$)	A	2.62
	B	-10639
K_{H_2O} (bar^{-1})	A	1.25×10^{-9}
	B	-100200

$\frac{K_{H_2O}}{K_8K_9K_{H_2}}$ (Dimensionless)	A	311.82
	B	-0.0046

Table 7.3. *Estimated Parameters for the Dual-Site Two-Reaction Model (Model B)*

Dual-Site (Two reaction)		**Simulated Values**
k_1 (mol/kg$_{cat}$.sec.bar)	A	24.5
	B	22897
k_2 (mol/kg$_{cat}$.sec.bar$^{1/2}$)	A	3.28×10^4
	B	49780
K_{CO} (bar^{-1})	A	8.8×10^{-4}
	B	-26839
K_{CO_2} (bar^{-1})	A	4.01×10^{-7}
	B	-60016
$\frac{K_{H_2O}}{\sqrt{K_{H_2}}}$ (bar$^{-1/2}$)	A	4.68×10^{-11}
	B	-93833

Table 7.4. *Estimated Parameters for the Dual-Site Three-Reaction Model (Model C).*

Dual-Site (Three reaction)		**Simulated Values**
k_1 (mol/kg$_{cat}$.sec.bar)	A	17.5
	B	23080
k_2 (mol/kg$_{cat}$.sec.bar$^{1/2}$)	A	3.98×10^3
	B	51019
k_3 (mol/kg$_{cat}$.sec.bar)	A	1.25×10^2
	B	41500
K_{CO} (bar^{-1})	A	9.42×10^{-4}
	B	-29000
K_{CO_2} (bar^{-1})	A	1.03×10^{-7}
	B	-67000
$\frac{K_{H_2O}}{\sqrt{K_{H_2}}}$ (bar$^{-1/2}$)	A	9.07×10^{-12}
	B	-100078

Unit of rate constants = Unit of pre-exponential factor = A
Unit of adsorption constants = Unit of pre-exponential factor = A
Unit of B = J/mol

The estimated activation energies provide profound insight into the reaction system. The activation energy for the RWGS reaction (k_2, $CO_2 \rightarrow CO$) is the highest at 51.0 kJ/mol, which is consistent with its endothermic nature. A key finding is the notably low activation energy of 23.1 kJ/mol for the direct CO_2-to-methanol step (k_1), which is the dominant pathway identified by DRIFTS. This low value is a direct kinetic manifestation of the high efficiency of the CZZ-MCBM catalyst in activating and hydrogenating CO_2 via the formate pathway. In contrast, the activation energy for the CO-to-methanol route (k_3) is higher at 41.5 kJ/mol. This suggests that while the hydrogenation of in-situ produced CO is feasible and is rightly included in the model for completeness, the primary route to methanol on this catalyst is the direct CO_2 hydrogenation, which proceeds with a significantly lower energy barrier. The adsorption constants further validate the model's physical realism. The strongly exothermic CO_2 adsorption enthalpy (ΔH_{ads} = -67 kJ/mol) aligns with values reported for catalysts where strong metal-support interactions facilitate CO_2 activation, corroborating the proposed role of the Cu-ZnO-ZrO_2 interface [144,149]. To quantitatively benchmark our catalyst's performance, **Table 7.5** provides a direct comparison of the temperature-dependent rate constants obtained for the CZZ-MCBM catalyst with those reported by Graaf et al. (1988) [149] and Angelo et al. (2022) [144].

Table 7.5. *Comparison of rate constants (mol/kg$_{cat}$.sec) with literature in the temperature range of 200-260°C.*

Rate constant	This work (3 reaction) (200-260°C)	Graaf et al. (200-260°C)	Angelo et al. (200-260°C)
k_1	$(4.95 \times 10^{-2}) - (9.59 \times 10^{-2})$	$(2.99 \times 10^{-5}) - (1.92 \times 10^{-4})$	$(1.32 \times 10^{-4}) - (3.47 \times 10^{-4})$
k_2	$(9.27 \times 10^{-3}) - (3.99 \times 10^{-2})$	$(1.72 \times 10^{-5}) - (5.9 \times 10^{-4})$	$(4.17 \times 10^{-4}) - (1.94 \times 10^{-2})$
k_3	$(3.28 \times 10^{-3}) - (1.07 \times 10^{-2})$	$(1.96 \times 10^{-5}) - (4.5 \times 10^{-4})$	$(7.15 \times 10^{-5}) - (2.24 \times 10^{-3})$

A comparison of the temperature-dependent rate constants reveals clear and mechanistically meaningful trends. Across the investigated temperature window (200-260°C), all three rate constants obtained in this work lie within the same order of magnitude as those reported in earlier studies, confirming the physical realism of the fitted kinetic parameters. The higher absolute values of k_1, k_2, and k_3 relative to Graaf et al. 1988 [149] mirror the enhanced hydrogenation capability of the CZZ-MCBM catalyst, likely attributable to its higher copper dispersion and the presence of synergistic Cu/ZnO/ZrO_2 interfaces. At the same time, the rate

constants remain lower than those reported by Angelo et al. [144], which is consistent with their catalyst's higher concentration of oxygen vacancies and stronger metal-support interactions. Most importantly, when comparing the three rate constants within our catalyst system, a clear hierarchy emerges: $k_1 > k_2 > k_3$. This trend is physically intuitive and highly consistent with the mechanistic picture derived from *in-situ* DRIFTS. The highest rate constant (k_1) corresponds to the direct hydrogenation of CO_2 to methanol, confirming this pathway as the most kinetically favourable over CZZ-MCBM. The intermediate magnitude of k_2 indicates a significant but secondary contribution from the $CO_2 \rightarrow CO$ (RWGS) route, which aligns with the moderate CO formation observed experimentally. Finally, k_3 shows the lowest magnitude, demonstrating that direct CO hydrogenation to methanol is the least favoured among the three reactions, consistent with the minimal spectral signature of adsorbed CO species during DRIFTS and with literature indicating that CO hydrogenation is typically slower on Cu-based systems unless strong CO adsorption sites (e.g., Cu-ZrO_2 interfaces) dominate.

Taken together, these observations highlight that the CZZ-MCBM catalyst preferentially channels CO_2 through the direct methanol pathway, with RWGS acting as a parallel but weaker route, and with CO hydrogenation playing only a minor role. This internal ranking of rate constants therefore reinforces the mechanistic conclusion that the formate-mediated CO_2 hydrogenation pathway is the dominant route on this catalyst, while also confirming the consistency of the derived kinetic parameters with well-established kinetic models in the literature.

7.2.3.2 Interpretation of Adsorption Energetics and Comparison with Literature

The magnitudes of the fitted parameters are consistent with literature values. Although our catalyst system (CZZ-MCBM) differs from the Cu/ZnO/Al_2O_3 catalyst used by Graaf et al. 1988 [149], a fair comparison can be made in terms of the resulting adsorption constants, which reflect the nature of the active sites. For this reason, **Table 7.6** compares our adsorption constants from Model C with those calculated by Graaf et al. (1988) [149] and Angelo et al. (2022) [144] at 200 and 260°C.

Table 7.6. *Comparison of Adsorption Constants with Literature at 200°C and 260°C.*

Adsorption constant	This work (3 reaction) (200-260°C)	Graaf (3 reaction) (200-260°C)	Angelo (3 reaction) (200-260°C)

K_{CO} (bar^{-1})	1.5 – 0.65	3.17 – 0.83	(3.04 – 2.38) $\times 10^{-2}$
K_{CO_2} (bar^{-1})	2.56 – 0.37	4.57 – 0.78	1.12 – 0.22
$\frac{K_{H_2O}}{\sqrt{K_{H_2}}}$ $(bar^{-1/2})$	1.02 – 0.058	(5.38 – 4.238) $\times 10^{-8}$	181.4 – 5.19

From the structure of the reaction rate expressions, it becomes evident that CO_2 and CO adsorption constants influence the driving force (the numerator of the rate law). Consequently, their exact impact on the rate is not straightforward to predict. In contrast, the combined adsorption of H_2O and H_2, represented by the ratio $K_{H_2O}/\sqrt{K_{H_2}}$, contributes only to the denominator of the rate expression, acting as an inhibitory term. Our fitted value of $K_{H_2O}/\sqrt{K_{H_2}}$, which is higher than that of Graaf et al. (1988), yet lower than that reported by Angelo et al. (2022), suggesting that the CZZ-MCBM catalyst displays balanced sensitivity toward H_2O and H_2 adsorption. Similarly, the CO adsorption constant K_{CO} is lower than that of Graaf but slightly higher than that obtained by Angelo, implying that the catalyst exhibits moderate sensitivity to CO adsorption, consistent with a measurable contribution of CO in the methanol formation pathway.

7.2.3.3 *Predictive Validation Under Varied Conditions*

The predictive capability of the kinetic models was rigorously tested by simulating methanol formation rates across the entire experimental matrix of temperature, pressure, and WHSV. A comparative analysis of the simulations, presented in **Figure 7.9 (a-c)** (Model A), **Figure 7.10 (a-c)** (Model B), and **Figure 7.11 (a-c)** (Model C), clearly demonstrates the superior performance of Model C. While all models captured the general positive effect of pressure and the adverse impact of WHSV, only Model C accurately reproduced the complex, non-linear trends, particularly the distinct inflection point in activity around the optimum temperature of 260°C and the precise scaling of the rate with pressure. The ability of Model C **(Figure 7.11 (a-c))** to quantitatively capture these nuanced behaviours, including the trade-off between conversion and selectivity with temperature, the strong kinetic driving force of pressure, and the residence time limitations imposed by WHSV, confirms its robustness. This successful predictive validation under varied and challenging conditions underscores that Model C is not merely a statistical fit but a reliable tool for simulating catalyst performance within and potentially beyond the studied operating window [145,237].

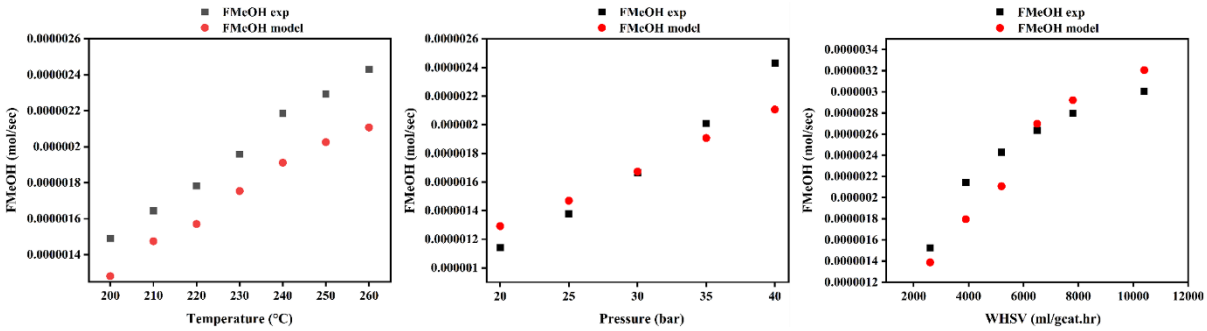


Figure 7.9. *Experimental vs. model-predicted methanol formation rate for the single-site two-reaction model under varying process conditions.*

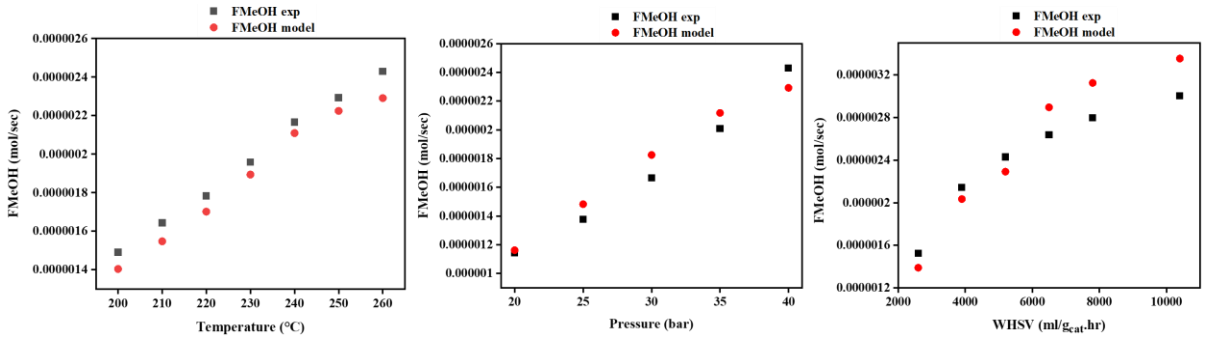


Figure 7.10. *Experimental vs. model-predicted methanol formation rate for the dual-site two-reaction model under varying process conditions.*

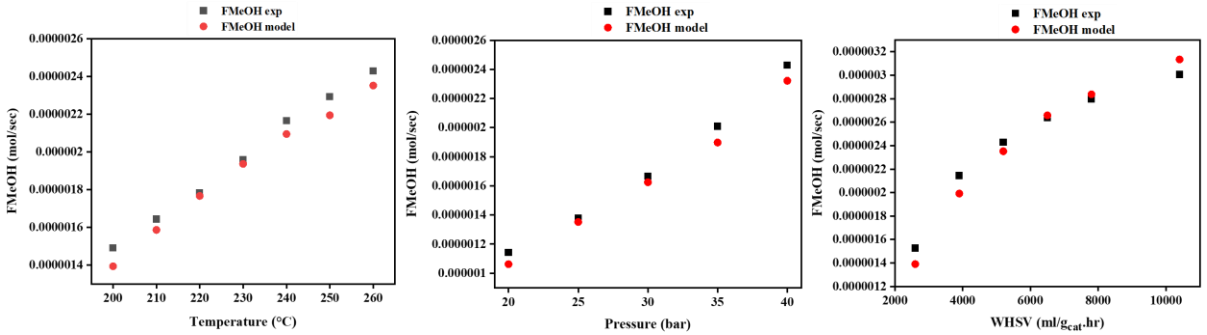


Figure 7.11. *Experimental vs. model-predicted methanol formation rate for the dual-site three-reaction model under varying process conditions.*

7.2.3.4 Mechanistic Integration of Kinetics, Spectroscopy, and Catalyst Architecture

Beyond identifying the statistically best model, this discrimination also provides mechanistic insight. The Graaf-based model assumes the coexistence of two distinct active sites, which aligns with the bifunctional nature of the CZZ-MCBM catalyst. One site corresponds to metallic copper (Cu^0), which hosts the dissociative adsorption of H_2. The second site corresponds to oxygen-vacant Zn/Zr interfacial regions, where CO_2 adsorbs and becomes activated. Hydrogen then spills over from Cu^0 to the activated CO_2, initiating a sequence of hydrogenation steps characteristic of the formate pathway. This bifunctional assignment is

consistent with our H_2-TPR/TPD and XPS analyses **(Chapter 6)** and aligns with literature hypotheses on synergistic Cu^0-oxide interfaces [88,144,227].

This kinetic model complements the *in-situ* DRIFTS analysis perfectly. The reaction sequence illustrated in **Figure 7.5 b** clearly depicts this formate-mediated route. Methanol may form either directly from CO_2 or indirectly from CO generated via the RWGS reaction. These pathways converge at the formation of the H_2CO* intermediate, after which the final hydrogenation steps are identical. However, at the stage where the adsorbed CO* species appear, an equilibrium develops between surface-bound CO and gas-phase CO, explaining the observed selectivity toward CO. The relative contributions of CO and CO_2 to methanol formation, therefore, depend on operating temperature, feed composition, space velocity, and the spatial relationship between Cu^0 sites and oxygen vacancies. For a fixed catalyst formulation, these relative contributions are governed solely by the reaction conditions, and it is this complex interplay that the dual-site three-reaction model (Model C) successfully captures.

7.2.4 Final Discussion and Industrial Implications

This study demonstrates that rational catalyst design, when coupled with mechanistic and kinetic validation, can lead to highly efficient systems for CO_2 valorisation. The CZZ-MCBM catalyst achieves high productivity at a relatively low optimal temperature (260°C), which has direct implications for reducing energy costs in an industrial process. The validated dual-site three-reaction model (Model C) provides a reliable tool for engineers to simulate, scale up, and optimize reactor systems using this catalyst. It accurately predicts performance under a wide range of conditions, enabling the design of more efficient and controllable processes for converting CO_2 into a valuable chemical feedstock, thereby supporting the transition to a circular carbon economy.

7.3 Summary

This chapter systematically decoupled the intrinsic kinetics and reaction mechanism of CO_2 hydrogenation over the CZZ-MCBM catalyst, progressing from macroscopic reactor performance to molecular-level insight. Through controlled parametric studies, the optimal operating window was identified at 260°C and 40 bar, representing the conditions where

kinetic acceleration of CO_2 conversion coincides with thermodynamically favourable methanol selectivity.

Mechanistic interrogation using *in-situ* DRIFTS provided conclusive evidence that the reaction predominantly follows a formate-mediated pathway. The persistent formation of surface formate (HCOO*) and methoxy (CH_3O*) intermediates, coupled with the negligible presence of CO* species, confirmed that the direct CO_2 hydrogenation route is dominant, while the indirect CO-derived pathway plays only a minor role under the investigation conditions.

Kinetic analysis confirmed the absence of transport limitations, allowing for a reliable assessment of the intrinsic reaction behaviour. Among the three LHHW kinetic models evaluated, the dual-site three-reaction model (Model C) showed the highest statistical accuracy ($R^2 > 0.97$) and the strongest mechanistic consistency. Its explicit consideration of parallel CO_2 and CO hydrogenation routes on distinct active sites was essential to reproduce the experimental trends in CO and methanol formation.

The estimated kinetic parameters were physically meaningful and well aligned with reported literature values. Notably, the hierarchy of rate constants, $k_1(CO_2 \rightarrow MeOH) > k_2(RWGS) > k_3(CO \rightarrow MeOH)$, quantitatively substantiated the dominance of the formate pathway. The relatively low activation energy associated with the key CO_2-to-methanol step (E_a = 23.1 kJ/mol), combined with the favourable comparison of rate constants with literature benchmarks, provides quantitative confirmation of the high intrinsic activity of the CZZ-MCBM catalyst.

Overall, the integrated approach adopted in this chapter, combining performance evaluation, *in-situ* spectroscopy, and kinetics modeling, provides a validated, mechanistically transparent, and quantitatively robust understanding of methanol synthesis over the CZZ-MCBM catalyst, thereby laying a solid foundation for rational reactor design and process optimization.

Chapter 8 Overall Conclusion and Future Recommendations

8.1 Conclusion

This thesis presents a systematic, multi-scale investigation of CO_2 hydrogenation to methanol over phase-pure hydroxycarbonate precursor-derived Cu-based catalysts, integrating data-driven catalyst design, advanced precursor engineering, catalyst synthesis, mechanistic studies, and intrinsic kinetic modeling into a unified scientific framework. The work establishes a strong structure-property-performance relationship for Cu-based catalytic systems and demonstrates how rational precursor control, defect engineering, and mechanistically consistent kinetics together enable the development of highly efficient, stable, and scalable methanol synthesis catalysts.

In the first phase of the thesis, a PCA-assisted machine learning framework was developed to predict CO_2 conversion, methanol selectivity, CO selectivity, and methanol space-time yield using a curated dataset of 227 literature data points. Among the applied algorithms (ANN, SVM, and GPR), the Artificial Neural Network (ANN) emerged as the most robust and experimentally relevant model, offering the lowest prediction error and the unique advantage of sensitivity backtracking. Experimental validation using an independent laboratory dataset confirmed the model's strong predictive capability, particularly for methanol and CO selectivity. However, limitations in predicting MeOH STY were attributed to the insufficient representation of low-STY regions in the training database. Sensitivity analysis further identified Cu dispersion and operating pressure as the dominant controlling parameters, thereby providing a rational, data-driven foundation for the design of experimental catalysts [13].

Building on these ML-guided insights, a hydrothermally synthesized Cu/MgO catalyst was developed from a monophasic Mg-rich hydroxycarbonate (mcguinnessite) precursor. This work demonstrated for the first time the stabilization of a highly Mg-substituted rosasite-type precursor and established precursor chemistry as a central design handle for modulating metal dispersion, oxygen vacancy concentration, surface basicity, and metal-support interactions. The resulting Cu/MgO catalyst exhibited enhanced CO_2 activation, improved H_2 adsorption, suppressed RWGS activity, and excellent long-term stability, achieving 15.2% CO_2 conversion, 68.5% methanol selectivity, and 98 mg_{MeOH}/g_{cat}.hr methanol STY under optimized

conditions. *In-situ* DRIFTS confirmed that methanol formation proceeds via formate and methoxy intermediates, consistent with literature-reported dominant pathways [14].

The design philosophy based on phase-pure precursor engineering was then successfully transferred to the industrially relevant Cu/ZnO system and further developed into a ternary Cu/ZnO/ZrO_2 catalyst using a scalable mechanochemical ball milling (MCBM) strategy. This approach enabled the direct formation of phase-pure zincian malachite, avoided multiphase contamination, and significantly enhanced metal dispersion, oxygen vacancy density, surface basicity, and strong metal-support interactions. The optimized CZZ-MCBM catalyst demonstrated superior catalytic performance, achieving 14.4% CO_2 conversion, 73% methanol selectivity, and 187 mg_{MeOH}/g_{cat}.hr STY at 260°C, 40 bar, and WHSV = 5200 ml/g_{cat}.hr, together with excellent durability over 184 hr time-on-stream with only ~4.2% performance decay. A direct correlation between oxygen vacancy concentration and methanol productivity was clearly established.

Finally, the intrinsic reaction kinetics and mechanism of CO_2 hydrogenation over the optimized CZZ-MCBM catalyst were quantitatively resolved. Through rigorous parametric studies, transport limitations were eliminated, enabling reliable intrinsic kinetic analysis. Among the evaluated Langmuir-Hinshelwood-Hougen-Watson (LHHW) models, the dual-site three-reaction model provided the best statistical and mechanistic agreement ($R^2 > 0.97$) with experimental data. In-situ DRIFTS conclusively confirmed the dominance of the formate-mediated direct CO_2 hydrogenation pathway, while the hierarchy of kinetic rate constants: $k_1(CO_2 \rightarrow MeOH) > k_2(CO_2 \rightarrow CO) > k_3(CO \rightarrow MeOH)$, and the low activation energy for the rate-determining step (E_a = 23.1 kJ/mol) quantitatively substantiated the high intrinsic activity of the CZZ-MCBM catalyst.

8.1.1 Overall Significance of the Thesis Work

Collectively, this thesis establishes a holistic, closed-loop research framework in which:

- Machine learning enables predictive catalyst screening,
- Phase-pure precursor chemistry governs catalyst structure,
- Defect and promoter engineering control activity and stability, and

- Mechanistically consistent kinetics bridge surface chemistry with reactor-scale performance.

This integrated approach provides a robust and scalable platform for the rational design of next-generation Cu-based catalysts for sustainable methanol production from CO_2, with direct relevance to carbon capture and utilization (CCU) technologies and net-zero carbon strategies.

8.2 Future Recommendations

- **ML-Guided Catalyst Design and Scale-Up**
    - The ANN-based predictive framework developed in this thesis can be expanded to include larger and more diverse datasets involving structured catalysts, solvent-assisted systems, and long-term deactivation behaviour.
    - The integration of machine learning with automated synthesis and high-throughput experimentation can enable the rapid discovery and optimization of promoter combinations, defect architectures, and precursor compositions under industrially relevant conditions.
- **Reaction System Advancement**
    - The present work is based on isothermal gas-solid fixed-bed reactor studies, which are well suited for intrinsic kinetics and mechanistic investigations.
    - However, such systems do not fully represent the thermal complexities of industrial methanol synthesis, especially under highly exothermic conditions.
- **Transition to Adiabatic Gas-Liquid-Solid Reactor Systems**
    - Future studies should focus on adiabatic gas-liquid-solid reactor configurations, where the presence of a solvent can:
        - Improve heat dissipation,
        - Suppress hotspot formation,
        - Reduce Cu sintering and catalyst deactivation,
        - Enhance long-term catalyst stability.
    - These systems may also facilitate operation under milder temperatures and pressures, which is thermodynamically favorable for CO_2 hydrogenation, potentially improving methanol selectivity and catalyst lifetime.
- **Structured Catalysts for Industrial Stability**

- To overcome deactivation and pressure-drop limitations associated with pelletized catalysts, future work should explore:
  - Monolithic catalysts,
  - Metallic and ceramic foams,
  - Coated structured supports.
- These architectures offer enhanced heat and mass transfer, low pressure drop, and superior mechanical robustness, making them highly suited for continuous industrial operation.

- **Techno-Economic Analysis (TEA)**
  - A comprehensive TEA should be conducted to evaluate:
    - Catalyst synthesis cost using MCBM and hydrothermal routes,
    - Reactor capital and operating costs for gas-solid vs. multiphase systems,
    - Hydrogen production and compression costs,
    - Overall, the economics of methanol production from CO_2.
  - This will help identify economic bottlenecks and guide process optimization for large-scale deployment.
- **Life Cycle Assessment (LCA)**
  - A full cradle-to-grave LCA is recommended to quantify:
    - Net CO_2 footprint of catalyst synthesis and operation,
    - Environmental impact of hydrogen production routes,
    - Energy efficiency and sustainability of CO_2-to-methanol conversion.
  - This will establish the true climate mitigation potential of the developed catalytic systems.

Response to Examiner Comments

Examiner: Prof. Atsushi Urakawa (TU Delft, Netherlands)

Comment 1: DRIFTS depth limited

Rebuttal: The examiner's observation regarding the depth of *in-situ* DRIFTS analysis is acknowledged. While the present study focused on identifying dominant reaction intermediates under realistic conditions, a more detailed quantitative analysis (e.g., time-resolved or isotopic studies) could further strengthen mechanistic interpretation. This is identified as a direction for future work.

Comment 2: Activity not exceptional

Rebuttal: The catalytic activity reported in this work is comparable to that of reported Cu-based systems under similar operating conditions. The primary objective of this study was not only to maximize activity but to establish a clear structure-property-performance relationship and develop a mechanistically consistent kinetic framework. Therefore, the contribution lies in integrating catalyst design and modeling rather than in absolute activity enhancement alone.

Comment 3: Clarity & presentation

Rebuttal: The examiner's suggestion regarding clarity and presentation has been carefully considered. Relevant sections have been revised to improve conciseness, figure readability, and the communication of key findings.

Comment 4: Error/Statistics and Significant Figures

Rebuttal: The numerical values reported in the thesis have been revised to ensure consistency with experimental uncertainties and appropriate significant figures.

References

[1] S. Daneshmand-Jahromi, M. Hashem Sedghkerdar, N. Mahinpey, Synthesis, characterization, and kinetic study of nanostructured copper-based oxygen carrier supported on silica and zirconia aerogels in the cyclic chemical looping combustion process, Chem. Eng. J. 448 (2022) 137756. https://doi.org/10.1016/j.cej.2022.137756.

[2] Y. Chen, B. Robinson, C. Jiang, B.K. Desta, Y. Wang, C.E. Dumitrescu, D. Bhattacharyya, J. Hu, Improved Efficiency of CO_2 Conversion to Olefins in a Thermal-Microwave Hybrid Heating Reactor, ACS Sustain. Chem. Eng. (2025). https://doi.org/10.1021/acssuschemeng.5c01387.

[3] G.A. Olah, A. Goeppert, G.K.S. Prakash, Chemical recycling of carbon dioxide to methanol and dimethyl ether: From greenhouse gas to renewable, environmentally carbon neutral fuels and synthetic hydrocarbons, J. Org. Chem. 74 (2009) 487-498. https://doi.org/10.1021/jo801260f.

[4] G.A. Olah, Beyond oil and gas: The methanol economy, Angew. Chemie - Int. Ed. 44 (2005) 2636-2639. https://doi.org/10.1002/anie.200462121.

[5] H.R. Darji, H.B. Kale, F.F. Shaikh, M.B. Gawande, Advancement and State-of-the-art of heterogeneous catalysis for selective CO_2 hydrogenation to methanol, Coord. Chem. Rev. 497 (2023) 215409. https://doi.org/10.1016/j.ccr.2023.215409.

[6] S.K. Sharma, T.S. Khan, R.K. Singha, B. Paul, M.K. Poddar, T. Sasaki, A. Bordoloi, C. Samanta, S. Gupta, R. Bal, Design of highly stable MgO-promoted Cu/ZnO catalyst for clean methanol production through selective hydrogenation of CO_2, Appl. Catal. A Gen. 623 (2021) 118239. https://doi.org/10.1016/j.apcata.2021.118239.

[7] J. Ye, N. Dimitratos, L.M. Rossi, N. Thonemann, A.M. Beale, R. Wojcieszak, Hydrogenation of CO_2 for sustainable fuel and chemical production, Science. 387 (2025) eadn9388. https://doi.org/10.1126/science.adn9388.

[8] A. Álvarez, A. Bansode, A. Urakawa, A. V. Bavykina, T.A. Wezendonk, M. Makkee, J. Gascon, F. Kapteijn, Challenges in the Greener Production of Formates/Formic Acid, Methanol, and DME by Heterogeneously Catalyzed CO_2 Hydrogenation Processes, Chem. Rev. 117 (2017) 9804-9838. https://doi.org/10.1021/acs.chemrev.6b00816.

[9] IEA, Net Zero Roadmap, Int. Energy Agency. (2023) 1-226.

[10] M.H. Rasool, S.A. Moiz Hashmi, Carbon capture and storage: An evidence-based review of its limitations and missed promises, Pet. Res. (2025). https://doi.org/10.1016/j.ptlrs.2025.09.005.

[11] S.G. Subraveti, E. Rodríguez Angel, A. Ramírez, S. Roussanaly, Is Carbon Capture and Storage (CCS) Really So Expensive? An Analysis of Cascading Costs and CO_2 Emissions Reduction of Industrial CCS Implementation on the Construction of a Bridge, Environ. Sci. Technol. 57 (2023) 2595-2601. https://doi.org/10.1021/acs.est.2c05724.

[12] M. Mirparizi, F. Shakeriaski, F. Salehi, C. Zhang, Available challenges and recent progress in carbon dioxide capture, and reusing methods toward renewable energy, Sustain. Energy Technol. Assessments. 58 (2023) 103365. https://doi.org/10.1016/j.seta.2023.103365.

[13] A. Bhardwaj, A.S. Ahluwalia, K.K. Pant, S. Upadhyayula, A principal component analysis assisted machine learning modeling and validation of methanol formation over Cu-based catalysts in direct CO_2 hydrogenation, Sep. Purif. Technol. 324 (2023) 124576. https://doi.org/10.1016/j.seppur.2023.124576.

[14] M. Pokhriyal, A. Bhardwaj, V. Pandey, K.K. Pant, S. Upadhyayula, Enhanced Methanol Formation over Cu/MgO Catalysts Derived from Mg-Rich Active Hydroxycarbonate Precursors, ACS Appl. Energy Mater. 7 (2024) 5163-5178. https://doi.org/10.1021/acsaem.4c00525.

[15] M.M.J. Li, S.C.E. Tsang, Bimetallic catalysts for green methanol production via CO_2 and renewable hydrogen: A mini-review and prospects, Catal. Sci. Technol. 8 (2018) 3450-3464. https://doi.org/10.1039/c8cy00304a.

[16] X. Jiang, X. Nie, X. Guo, C. Song, J.G. Chen, Recent Advances in Carbon Dioxide Hydrogenation to Methanol via Heterogeneous Catalysis, Chem. Rev. (2020). https://doi.org/10.1021/acs.chemrev.9b00723.

[17] L. Fu, Z. Ren, W. Si, Q. Ma, W. Huang, K. Liao, Z. Huang, Y. Wang, J. Li, P. Xu, Research progress on CO_2 capture and utilization technology, J. CO_2 Util. 66 (2022) 102260. https://doi.org/10.1016/j.jcou.2022.102260.

[18] M.E. Boot-Handford, J.C. Abanades, E.J. Anthony, M.J. Blunt, S. Brandani, N. Mac Dowell, J.R. Fernández, M.C. Ferrari, R. Gross, J.P. Hallett, R.S. Haszeldine, P. Heptonstall, A. Lyngfelt, Z. Makuch, E. Mangano, R.T.J. Porter, M. Pourkashanian,

G.T. Rochelle, N. Shah, J.G. Yao, P.S. Fennell, Carbon capture and storage update, Energy Environ. Sci. 7 (2014) 130-189. https://doi.org/10.1039/c3ee42350f.

[19] G.T. Rochelle, Amine Scrubbing for CO_2 Capture, Science, 325 (2009) 1652-1654.

[20] M. Wang, A. Lawal, P. Stephenson, J. Sidders, C. Ramshaw, Post-combustion CO_2 capture with chemical absorption: A state-of-the-art review, Chem. Eng. Res. Des. 89 (2011) 1609-1624. https://doi.org/10.1016/j.cherd.2010.11.005.

[21] M. Bui, C.S. Adjiman, A. Bardow, E.J. Anthony, A. Boston, S. Brown, P.S. Fennell, S. Fuss, A. Galindo, L.A. Hackett, J.P. Hallett, H.J. Herzog, G. Jackson, J. Kemper, S. Krevor, G.C. Maitland, M. Matuszewski, I.S. Metcalfe, C. Petit, G. Puxty, J. Reimer, D.M. Reiner, E.S. Rubin, S.A. Scott, N. Shah, B. Smit, J.P.M. Trusler, P. Webley, J. Wilcox, N. Mac Dowell, Carbon capture and storage (CCS): The way forward, Energy Environ. Sci. 11 (2018) 1062-1176. https://doi.org/10.1039/c7ee02342a.

[22] J. Zhong, X. Yang, Z. Wu, B. Liang, Y. Huang, T. Zhang, State of the art and perspectives in heterogeneous catalysis of CO_2 hydrogenation to methanol, Chem. Soc. Rev. 49 (2020) 1385-1413. https://doi.org/10.1039/c9cs00614a.

[23] S. Kar, A. Goeppert, V. Galvan, R. Chowdhury, J. Olah, G.K.S. Prakash, A Carbon-Neutral CO_2 Capture, Conversion, and Utilization Cycle with Low-Temperature Regeneration of Sodium Hydroxide, J. Am. Chem. Soc. 140 (2018) 16873-16876. https://doi.org/10.1021/jacs.8b09325.

[24] A. Goeppert, M. Czaun, J.P. Jones, G.K. Surya Prakash, G.A. Olah, Recycling of carbon dioxide to methanol and derived products-closing the loop, Chem. Soc. Rev. 43 (2014) 7995-8048. https://doi.org/10.1039/c4cs00122b.

[25] M. Behrens, F. Studt, I. Kasatkin, S. Kühl, M. Hävecker, F. Abild-Pedersen, S. Zander, F. Girgsdies, P. Kurr, B.L. Kniep, M. Tovar, R.W. Fischer, J.K. Nørskov, R. Schlögl, The active site of methanol synthesis over $Cu/ZnO/Al_2O_3$ industrial catalysts, Science 336 (2012) 893-897. https://doi.org/10.1126/science.1219831.

[26] A. Beck, M.A. Newton, L.G.A. Van de Water, J.A. Van Bokhoven, The Enigma of Methanol Synthesis by $Cu/ZnO/Al_2O_3$-Based Catalysts, Chem. Rev. 124 (2024) 4543-4678. https://doi.org/10.1021/acs.chemrev.3c00148.

[27] J.C.J. Bart, R.P.A. Sneeden, Copper-zinc oxide-alumina methanol catalysts revisited, Catal. Today. 2 (1987) 1-124. https://doi.org/10.1016/0920-5861(87)80001-9.

[28] A. Koushik V, B.C. Dharmalingam, M. Mureddu, F. Ferrara, A. Pettinau, P. Aghalayam, N.S. Kaisare, J.J. Varghese, Cu facet-dependent activity of Cu/ZnOx catalyst during methanol synthesis from industrially relevant CO-CO_2 gas mixtures, Appl. Catal. B Environ. 371 (2025) 125213. https://doi.org/10.1016/j.apcatb.2025.125213.

[29] B.C. Dharmalingam, A. Koushik V, M. Mureddu, L. Atzori, S. Lai, A. Pettinau, N.S. Kaisare, P. Aghalayam, J.J. Varghese, Unraveling the role of metal-metal oxide interfaces of Cu/ZnO/ZrO_2/Al_2O_3 catalyst for methanol synthesis from CO_2: Insights from experiments and DFT-based microkinetic modeling, Appl. Catal. B Environ. 332 (2023) 122743. https://doi.org/10.1016/j.apcatb.2023.122743.

[30] W. Wang, S. Wang, X. Ma, J. Gong, Recent advances in catalytic hydrogenation of carbon dioxide, Chem. Soc. Rev. 40 (2011) 3703-3727. https://doi.org/10.1039/c1cs15008a.

[31] R.P. Ye, J. Ding, W. Gong, M.D. Argyle, Q. Zhong, Y. Wang, C.K. Russell, Z. Xu, A.G. Russell, Q. Li, M. Fan, Y.G. Yao, CO_2 hydrogenation to high-value products via heterogeneous catalysis, Nat. Commun. 10 (2019). https://doi.org/10.1038/s41467-019-13638-9.

[32] É.S. Van-Dal, C. Bouallou, Design and simulation of a methanol production plant from CO_2 hydrogenation, J. Clean. Prod. 57 (2013) 38-45. https://doi.org/10.1016/j.jclepro.2013.06.008.

[33] S. Kar, J. Kothandaraman, A. Goeppert, G.K.S. Prakash, Advances in catalytic homogeneous hydrogenation of carbon dioxide to methanol, J. CO_2 Util. 23 (2018) 212-218. https://doi.org/10.1016/j.jcou.2017.10.023.

[34] L. Tomme, Y. Ureel, M.R. Dobbelaere, I. Lengyel, F.H. Vermeire, C. V. Stevens, K.M. Van Geem, Machine learning applications for thermochemical and kinetic property prediction, Rev. Chem. Eng. (2024) 1-31. https://doi.org/10.1515/revce-2024-0027.

[35] V. V. Yurak, S.A. Fedorov, Review of natural and anthropogenic emissions of carbon dioxide into the earth's atmosphere, Int. J. Environ. Sci. Technol. 22 (2025) 2719-2736. https://doi.org/10.1007/s13762-024-05896-y.

[36] K. Calvin, D. Dasgupta, G. Krinner, A. Mukherji, P.W. Thorne, C. Trisos, J. Romero, P. Aldunce, K. Barrett, G. Blanco, W.W.L. Cheung, S. Connors, F. Denton, A. Diongue-Niang, D. Dodman, M. Garschagen, O. Geden, B. Hayward, C. Jones, F. Jotzo, T. Krug,

R. Lasco, Y.-Y. Lee, V. Masson-Delmotte, M. Meinshausen, K. Mintenbeck, A. Mokssit, F.E.L. Otto, M. Pathak, A. Pirani, E. Poloczanska, H.-O. Pörtner, A. Revi, D.C. Roberts, J. Roy, A.C. Ruane, J. Skea, P.R. Shukla, R. Slade, A. Slangen, Y. Sokona, A.A. Sörensson, M. Tignor, D. van Vuuren, Y.-M. Wei, H. Winkler, P. Zhai, Z. Zommers, J.-C. Hourcade, F.X. Johnson, S. Pachauri, N.P. Simpson, C. Singh, A. Thomas, E. Totin, A. Alegría, K. Armour, B. Bednar-Friedl, K. Blok, G. Cissé, F. Dentener, S. Eriksen, E. Fischer, G. Garner, C. Guivarch, M. Haasnoot, G. Hansen, M. Hauser, E. Hawkins, T. Hermans, R. Kopp, N. Leprince-Ringuet, J. Lewis, D. Ley, C. Ludden, L. Niamir, Z. Nicholls, S. Some, S. Szopa, B. Trewin, K.-I. van der Wijst, G. Winter, M. Witting, A. Birt, M. Ha, IPCC, 2023: Climate Change 2023: Synthesis Report. Contribution of Working Groups I, II, and III to the Sixth Assessment Report of the Intergovernmental Panel on Climate Change. IPCC, Geneva, Switzerland, (2023) 35-115. https://doi.org/10.59327/IPCC/AR6-9789291691647.

[37] V. Davtyan, International Energy Agency, Elgar Encycl. Energy Econ. (2025) 294-296. https://doi.org/10.4337/9781035310371.00082.

[38] International Energy Agency, World Energy Outlook 2023 https://www.iea.org/reports/world-energy-outlook-2023, https://www.Iea.Org/Data-and-Statistics/Data. (2023) 1-355.

[39] IPCC, Mitigation Pathways Compatible with 1.5°C in the Context of Sustainable Development, 2022. https://doi.org/10.1017/9781009157940.004.

[40] IPCC, Impacts of 1.5°C Global Warming on Natural and Human Systems, 2022. https://doi.org/10.1017/9781009157940.005.

[41] F. Hong, Y. Qi, Z. Yang, L. Yu, X. Guan, J. Diao, B. Sun, H. Liu, Recent advances of CO_2 hydrogenation to methanol, DeCarbon. 8 (2025) 100111. https://doi.org/10.1016/j.decarb.2025.100111.

[42] E.S. Sanz-Pérez, C.R. Murdock, S.A. Didas, C.W. Jones, Direct Capture of CO_2 from Ambient Air, Chem. Rev. 116 (2016) 11840-11876. https://doi.org/10.1021/acs.chemrev.6b00173.

[43] K. Sumida, D.L. Rogow, J.A. Mason, T.M. McDonald, E.D. Bloch, Z.R. Herm, T.H. Bae, J.R. Long, Carbon dioxide capture in metal-organic frameworks, Chem. Rev. 112 (2012) 724-781. https://doi.org/10.1021/cr2003272.

[44] R. Guo, J. Wang, L. Bing, D. Tong, P. Ciais, S.J. Davis, R.M. Andrew, F. Xi, Z. Liu, Global Carbon Budget 2023, Earth Syst. Sci. Data. 13 (2023) 1791-1805. https://essd.copernicus.org/articles/13/1791/2021/.

[45] A. Demirbas, Biofuels sources, biofuel policy, biofuel economy and global biofuel projections, Energy Convers. Manag. 49 (2008) 2106-2116. https://doi.org/10.1016/j.enconman.2008.02.020.

[46] G. Pétron, P. Tans, G. Frost, D. Chao, M. Trainer, High-resolution emissions of CO_2 from power generation in the USA, J. Geophys. Res. Biogeosciences. 113 (2008) 1-9. https://doi.org/10.1029/2007JG000602.

[47] S. Shafiee, E. Topal, When will fossil fuel reserves be diminished?, Energy Policy. 37 (2009) 181-189. https://doi.org/10.1016/j.enpol.2008.08.016.

[48] J. Hansen, M. Sato, R. Ruedy, Global Warming Acceleration : Causes and Consequences, (2024) 2-7.

[49] J.G. Olivier, J.A.H. W. Peters, Trends In Global CO_2 and Total Greenhouse Gas: 2020 Report, PBL Netherlands Environ. Assess. Agency, Hague. 2020 (2020).

[50] CO_2-Emissions, Encycl. Sustain. Manag. (2023) 600-600. https://doi.org/10.1007/978-3-031-25984-5_300288.

[51] IPCC, An IPCC Special Report on climate change, desertification, land degradation, sustainable land management, food security, and greenhouse, 2017.

[52] REN21, Renewables in Energy Demand, 2023. https://www.ren21.net/gsr-2023/modules/energy_demand/.

[53] M. Jarraud, A. Steiner, Summary for policymakers, 2012. https://doi.org/10.1017/CBO9781139177245.003.

[54] J. Artz, T.E. Müller, K. Thenert, J. Kleinekorte, R. Meys, A. Sternberg, A. Bardow, W. Leitner, Sustainable Conversion of Carbon Dioxide: An Integrated Review of Catalysis and Life Cycle Assessment, Chem. Rev. 118 (2018) 434-504. https://doi.org/10.1021/acs.chemrev.7b00435.

[55] D. Sheldon, Methanol production - A technical history, Johnson Matthey Technol. Rev. 61 (2017) 172-182. https://doi.org/10.1595/205651317X695622.

[56] P. Sabatier, How I Have Been Led to the Direct Hydrogenation Method by Metallic

Catalysts, Ind. Eng. Chem. 18 (1926) 1005-1008. https://doi.org/10.1021/ie50202a005.

[57] P.J.A. Tijm, F.J. Waller, D.M. Brown, Methanol technology developments for the new millennium, Appl. Catal. A Gen. 221 (2001) 275-282. https://doi.org/10.1016/S0926-860X(01)00805-5.

[58] U. Mondal, G.D. Yadav, Methanol economy and net zero emissions: Critical analysis of catalytic processes, reactors and technologies, Green Chem. 23 (2021) 8361-8405. https://doi.org/10.1039/d1gc02078a.

[59] I.U. Din, M.S. Shaharun, M.A. Alotaibi, A.I. Alharthi, A. Naeem, Recent developments on heterogeneous catalytic CO_2 reduction to methanol, J. CO_2 Util. 34 (2019) 20-33. https://doi.org/10.1016/j.jcou.2019.05.036.

[60] G. Bozzano, F. Manenti, Efficient methanol synthesis: Perspectives, technologies and optimization strategies, Prog. Energy Combust. Sci. 56 (2016) 71-105. https://doi.org/10.1016/j.pecs.2016.06.001.

[61] J. Rostrup-Nielsen and L. J. Christiansen, Concepts in Syngas Manufacture, Catalytic, Imperial College Press, 2019.

[62] F. Manenti, S. Cieri, M. Restelli, Considerations on the steady-state modeling of methanol synthesis fixed-bed reactor, Chem. Eng. Sci. 66 (2011) 152-162. https://doi.org/10.1016/j.ces.2010.09.036.

[63] T. Arthur, Control structure design for methanol process, Norwegia Nor. (2010) 91. http://www.nt.ntnu.no/users/skoge/diplom/Control Structure Design for Methanol Process.pdf.

[64] E.L. Kunkes, F. Studt, F. Abild-Pedersen, R. Schlögl, M. Behrens, Hydrogenation of CO_2 to methanol and CO on $Cu/ZnO/Al_2O_3$: Is there a common intermediate or not? This work is dedicated to the memory and achievements of Dr. Haldor Topsøe. J. Catal. 328 (2015) 43-48. https://doi.org/10.1016/j.jcat.2014.12.016.

[65] G.A. Olah, Towards oil independence through renewable methanol chemistry, Angew. Chemie - Int. Ed. 52 (2013) 104-107. https://doi.org/10.1002/anie.201204995.

[66] R. Guil-López, N. Mota, J. Llorente, E. Millán, B. Pawelec, J.L.G. Fierro, R.M. Navarro, Methanol synthesis from CO_2: A review of the latest developments in heterogeneous catalysis, Materials (Basel). 12 (2019). https://doi.org/10.3390/ma122333902.

[67] J. Wu, M. Saito, M. Takeuchi, T. Watanabe, The stability of Cu/ZnO-based catalysts in methanol synthesis from a CO_2-rich feed and from a CO-rich feed, Appl. Catal. A Gen. 218 (2001) 235-240. https://doi.org/10.1016/S0926-860X(01)00650-0.

[68] A. Bansode, A. Urakawa, Towards full one-pass conversion of carbon dioxide to methanol and methanol-derived products, J. Catal. 309 (2014) 66-70. https://doi.org/10.1016/j.jcat.2013.09.005.

[69] K. Ahmad, S. Upadhyayula, Greenhouse gas CO_2 hydrogenation to fuels: A thermodynamic analysis, Environ. Prog. Sustain. Energy. 38 (2019) 98-111. https://doi.org/10.1002/ep.13028.

[70] K.M. Vanden Bussche, G.F. Froment, A steady-state kinetic model for methanol synthesis and the water gas shift reaction on a commercial $Cu/ZnO/Al_2O_3$ catalyst, J. Catal. 161 (1996) 1-10. https://doi.org/10.1006/jcat.1996.0156.

[71] L.C. Grabow, M. Mavrikakis, Mechanism of methanol synthesis on cu through CO_2 and CO hydrogenation, ACS Catal. 1 (2011) 365–384. https://doi.org/10.1021/cs200055d.

[72] F. Studt, I. Sharafutdinov, F. Abild-Pedersen, C.F. Elkjær, J.S. Hummelshøj, S. Dahl, I. Chorkendorff, J.K. Nørskov, Discovery of a Ni-Ga catalyst for carbon dioxide reduction to methanol, Nat. Chem. 6 (2014) 320–324. https://doi.org/10.1038/nchem.1873.

[73] Y.F. Zhao, Y. Yang, C. Mims, C.H.F. Peden, J. Li, D. Mei, Insight into methanol synthesis from CO_2 hydrogenation on Cu(1 1 1): Complex reaction network and the effects of H_2O, J. Catal. 281 (2011) 199–211. https://doi.org/10.1016/j.jcat.2011.04.012.

[74] Y. Yang, C.A. Mims, D.H. Mei, C.H.F. Peden, C.T. Campbell, Mechanistic studies of methanol synthesis over Cu from $CO/CO_2/H_2/H_2O$ mixtures: The source of C in methanol and the role of water, J. Catal. 298 (2013) 10–17. https://doi.org/10.1016/j.jcat.2012.10.028.

[75] S. Lee, A. Sardesai, Liquid phase methanol and dimethyl ether synthesis from syngas, Top. Catal. 32 (2005) 197–207. https://doi.org/10.1007/s11244-005-2891-8.

[76] A. Smith, A. Keane, J.A. Dumesic, G.W. Huber, V.M. Zavala, A machine learning framework for the analysis and prediction of catalytic activity from experimental data, Appl. Catal. B Environ. 263 (2020) 118257. https://doi.org/10.1016/j.apcatb.2019.118257.

[77] S. Sharma, A. Bhardwaj, S. Upadhyayula, Data-driven design of catalysts for CO_2 hydrogenation to formic acid/formate: Toward sustainable hydrogen carrier and greener fuel, Fuel. 407 (2026) 137331. https://doi.org/10.1016/j.fuel.2025.137331.

[78] K. Kundu, A. Kumar, H. Kodamana, K.K. Pant, Obtaining high H_2-rich syngas yield and carbon conversion efficiency from biomass gasification: From characterization to process optimization using machine learning with experimental validation, Fuel. 378 (2024) 132931. https://doi.org/10.1016/j.fuel.2024.132931.

[79] A. Midilli, H. Kucuk, M.E. Topal, U. Akbulut, I. Dincer, A comprehensive review on hydrogen production from coal gasification: Challenges and Opportunities, Int. J. Hydrogen Energy. 46 (2021) 25385-25412. https://doi.org/10.1016/j.ijhydene.2021.05.088.

[80] G.J. Stiegel, M. Ramezan, Hydrogen from coal gasification: An economical pathway to a sustainable energy future, Int. J. Coal Geol. 65 (2006) 173-190. https://doi.org/10.1016/j.coal.2005.05.002.

[81] A.S. Joshi, I. Dincer, B. V. Reddy, Exergetic assessment of solar hydrogen production methods, Int. J. Hydrogen Energy. 35 (2010) 4901-4908. https://doi.org/10.1016/j.ijhydene.2009.09.067.

[82] A.K. Sahu, X.S. Zhao, S. Upadhyayula, Ceria-based photocatalysts in water-splitting for hydrogen production and carbon dioxide reduction, Catal. Rev. Sci. Eng. 66 (2024) 1400-1477. https://doi.org/10.1080/01614940.2023.2166227.

[83] V. Kumaravel, S. Mathew, J. Bartlett, S.C. Pillai, Photocatalytic hydrogen production using metal-doped TiO_2: A review of recent advances, Appl. Catal. B Environ. 244 (2019) 1021-1064. https://doi.org/10.1016/j.apcatb.2018.11.080.

[84] N.A.M. Razali, K.T. Lee, S. Bhatia, A.R. Mohamed, Heterogeneous catalysts for production of chemicals using carbon dioxide as raw material: A review, Renew. Sustain. Energy Rev. 16 (2012) 4951-4964. https://doi.org/10.1016/j.rser.2012.04.012.

[85] M. Behrens, R. Schlögl, How to prepare a good Cu/ZnO catalyst or the role of solid state chemistry for the synthesis of nanostructured catalysts, Zeitschrift Fur Anorg. Und Allg. Chemie. 639 (2013) 2683-2695. https://doi.org/10.1002/zaac.201300356.

[86] M. Behrens, F. Studt, I. Kasatkin, S. Kühl, M. Hävecker, F. Abild-pedersen, S. Zander, F. Girgsdies, P. Kurr, B. Kniep, M. Tovar, R.W. Fischer, J.K. Nørskov, R. Schlögl,

Industrial Catalysts, 759 (2012) 893-898. https://www.science.org/doi/10.1126/science.1219831.

[87] M. Behrens, Coprecipitation: An excellent tool for the synthesis of supported metal catalysts - From the understanding of the well-known recipes to new materials, Catal. Today. 246 (2015) 46-54. https://doi.org/10.1016/j.cattod.2014.07.050.

[88] Y. Wang, S. Kattel, W. Gao, K. Li, P. Liu, J.G. Chen, H. Wang, Exploring the ternary interactions in Cu-ZnO-ZrO_2 catalysts for efficient CO_2 hydrogenation to methanol, Nat. Commun. 10 (2019). https://doi.org/10.1038/s41467-019-09072-6.

[89] L. Angelo, K. Kobl, L.M.M. Tejada, Y. Zimmermann, K. Parkhomenko, A.C. Roger, Study of CuZn MOx oxides (M = Al, Zr, Ce, CeZr) for the catalytic hydrogenation of CO_2 into methanol, Comptes Rendus Chim. 18 (2015) 250-260. https://doi.org/10.1016/j.crci.2015.01.001.

[90] P. Gao, F. Li, N. Zhao, F. Xiao, W. Wei, L. Zhong, Y. Sun, Influence of modifier (Mn, La, Ce, Zr, and Y) on the performance of Cu/Zn/Al catalysts via hydrotalcite-like precursors for CO_2 hydrogenation to methanol, Appl. Catal. A Gen. 468 (2013) 442-452. https://doi.org/10.1016/j.apcata.2013.09.026.

[91] F. Chen, W. Gao, K. Wang, C. Wang, X. Wu, N. Liu, X. Guo, Y. He, P. Zhang, G. Yang, N. Tsubaki, Enhanced performance and stability of Cu/ZnO catalyst by introducing MgO for low-temperature methanol synthesis using methanol itself as catalytic promoter, Fuel. 315 (2022) 123272. https://doi.org/10.1016/j.fuel.2022.123272.

[92] W. Gao, G. Qu, M. Xu, S. Chang, W. Na, Effect of pH on Co-precipitated Cu-ZnO-ZrO_2 Catalysts Used in CO_2 Hydrogenation: the Role of Zn-malachite in the Precursors, Fuel Cells. 21 (2021) 31-38. https://doi.org/10.1002/fuce.202000032.

[93] G. Behrendt, B. Mockenhaupt, N. Prinz, M. Zobel, E.J. Ras, M. Behrens, CO Hydrogenation to Methanol over Cu/MgO Catalysts and Their Synthesis from Amorphous Magnesian Georgeite Precursors, ChemCatChem. 14 (2022) 1-13. https://doi.org/10.1002/cctc.202200299.

[94] V. Pandey, K.K. Pant, S. Upadhyayula, Combustion-induced synthesis of multicomponent Cu-based catalysts for autocatalytic CO hydrogenation to methanol in a three-phase reactor system, React. Chem. Eng. 8 (2022) 442-454. https://doi.org/10.1039/d2re00427e.

[95] R. Singh, K. Kundu, K.K. Pant, CO_2 hydrogenation to methanol over Cu-ZnO-CeO_2 catalyst: Reaction structure–activity relationship, optimizing Ce and Zn ratio, and kinetic study, Chem. Eng. J. 479 (2024) 147783. https://doi.org/10.1016/j.cej.2023.147783.

[96] R. Singh, V. Pandey, K.K. Pant, Promotional Role of Oxygen Vacancy Defects and Cu-Ce Interfacial Sites on the Activity of Cu/CeO_2 Catalyst for CO_2 Hydrogenation to Methanol, ChemCatChem. 14 (2022). https://doi.org/10.1002/cctc.202201053.

[97] F. Arena, G. Mezzatesta, G. Zafarana, G. Trunfio, F. Frusteri, L. Spadaro, How oxide carriers control the catalytic functionality of the Cu-ZnO system in the hydrogenation of CO_2 to methanol, Catal. Today. 210 (2013) 39-46. https://doi.org/10.1016/j.cattod.2013.02.016.

[98] R. Singh, K. Tripathi, K.K. Pant, Investigating the role of oxygen vacancies and basic site density in tuning methanol selectivity over Cu/CeO_2 catalyst during CO_2 hydrogenation, Fuel. 303 (2021) 121289. https://doi.org/10.1016/j.fuel.2021.121289.

[99] C. Álvarez Galván, J. Schumann, M. Behrens, J.L.G. Fierro, R. Schlögl, E. Frei, Reverse water-gas shift reaction at the Cu/ZnO interface: Influence of the Cu/Zn ratio on structure-activity correlations, Appl. Catal. B Environ. 195 (2016) 104-111. https://doi.org/10.1016/j.apcatb.2016.05.007.

[100] M.M.J. Li, C. Chen, T. Ayvall, H. Suo, J. Zheng, I.F. Teixeira, L. Ye, H. Zou, D. O'Hare, S.C.E. Tsang, CO_2 Hydrogenation to Methanol over Catalysts Derived from Single Cationic Layer CuZnGa LDH Precursors, ACS Catal. 8 (2018) 4390-4401. https://doi.org/10.1021/acscatal.8b00474.

[101] E. Frei, A. Schaadt, T. Ludwig, H. Hillebrecht, I. Krossing, The influence of the precipitation/ageing temperature on a Cu/ZnO/ZrO_2 catalyst for methanol synthesis from H_2 and CO_2, ChemCatChem. 6 (2014) 1721-1730. https://doi.org/10.1002/cctc.201300665.

[102] J. Kim, C. Jeong, J.H. Baik, Y.W. Suh, Phases of Cu/Zn/Al/Zr precursors linked to the property and activity of their final catalysts in CO_2 hydrogenation to methanol, Catal. Today. 347 (2020) 70-78. https://doi.org/10.1016/j.cattod.2018.09.008.

[103] S. Kühl, M. Friedrich, M. Armbrüster, M. Behrens, Cu, Zn, Al layered double hydroxides as precursors for copper catalysts in methanol steam reforming - pH-

controlled synthesis by microemulsion technique, J. Mater. Chem. 22 (2012) 9632-9638. https://doi.org/10.1039/c2jm16138a.

[104] M. Behrens, S. Zander, P. Kurr, N. Jacobsen, J. Senker, G. Koch, T. Ressler, R.W. Fischer, R. Schlögl, Performance improvement of nanocatalysts by promoter-induced defects in the support material: Methanol synthesis over Cu/ZnO:Al, J. Am. Chem. Soc. 135 (2013) 6061-6068. https://doi.org/10.1021/ja310456f.

[105] S. Kattel, B. Yan, Y. Yang, J.G. Chen, P. Liu, Optimizing Binding Energies of Key Intermediates for CO_2 Hydrogenation to Methanol over Oxide-Supported Copper, J. Am. Chem. Soc. 138 (2016) 12440-12450. https://doi.org/10.1021/jacs.6b05791.

[106] N. Narkhede, H. Zheng, H. Zhang, G. Zhang, Z. Li, Isomorphous substitution method to fabricating pure phase Al-doped zinc malachite: defects driven promotion improvement and enhanced synergy between Cu-ZnO, ChemCatChem. 12 (2020) 5697-5709. https://doi.org/10.1002/cctc.202001030.

[107] H. Zheng, N. Narkhede, H. Zhang, Z. Li, Oriented Isomorphous Substitution: An Efficient and Alternative Route to Fabricate the Zn Rich Phase Pure $(Cu_{1-x},Zn_x)_2(OH)_2CO_3$ Precursor Catalyst for Methanol Synthesis, ChemCatChem. 12 (2020) 2040-2049. https://doi.org/10.1002/cctc.201902286.

[108] H. Zhang, J. Chen, X. Han, Y. Pan, Z. Hao, S. Tang, X. Zi, Z. Zhang, P. Gao, M. Li, J. Lv, X. Ma, High-Performance $Cu/ZnO/Al_2O_3$ Catalysts for CO_2 Hydrogenation to Methanol, Ind. Eng. Chem. Res. 63 (2024) 6210-6221. https://doi.org/10.1021/acs.iecr.4c00357.

[109] Z. Chen, J. Wen, Y. Zeng, M. Li, Y. Tian, F. Yang, M.M.J. Li, P. Chen, H. Huang, D. Ye, L. Chen, The origin of the mediocre methanol selectivity of Cu/ZnO-based catalysts for methanol synthesis from CO_2 hydrogenation, Appl. Catal. B Environ. 340 (2024) 123192. https://doi.org/10.1016/j.apcatb.2023.123192.

[110] H. Chen, H. Cui, Y. Lv, P. Liu, F. Hao, W. Xiong, H. Luo, CO_2 hydrogenation to methanol over $Cu/ZnO/ZrO_2$ catalysts: Effects of ZnO morphology and oxygen vacancy, Fuel. 314 (2022). https://doi.org/10.1016/j.fuel.2021.123035.

[111] M. Mureddu, F. Ferrara, A. Pettinau, Highly efficient $CuO/ZnO/ZrO_2$@SBA-15 nanocatalysts for methanol synthesis from the catalytic hydrogenation of CO_2, Appl. Catal. B Environ. 258 (2019). https://doi.org/10.1016/j.apcatb.2019.117941.

[112] X.X. Hou, C.H. Xu, Y.L. Liu, J.J. Li, X.D. Hu, J. Liu, J.Y. Liu, Q. Xu, Improved methanol synthesis from CO_2 hydrogenation over CuZnAlZr catalysts with precursor pre-activation by formaldehyde, J. Catal. 379 (2019) 147-153. https://doi.org/10.1016/j.jcat.2019.09.025.

[113] Z. Shi, Q. Tan, D. Wu, Enhanced CO_2 hydrogenation to methanol over TiO_2 nanotubes-supported CuO-ZnO-CeO_2 catalyst, Appl. Catal. A Gen. 581 (2019) 58-66. https://doi.org/10.1016/j.apcata.2019.05.019.

[114] G. Wang, D. Mao, X. Guo, J. Yu, Methanol synthesis from CO_2 hydrogenation over CuO-ZnO-ZrO_2-M_xO_y catalysts (M = Cr, Mo, and W), Int. J. Hydrogen Energy. 44 (2019) 4197-4207. https://doi.org/10.1016/j.ijhydene.2018.12.131.

[115] S. Chen, J. Zhang, P. Wang, X. Wang, F. Song, Y. Bai, M. Zhang, Y. Wu, H. Xie, Y. Tan, Effect of Vapor-phase-treatment to CuZnZr Catalyst on the Reaction Behaviors in CO_2 Hydrogenation into Methanol, ChemCatChem. 11 (2019) 1448-1457. https://doi.org/10.1002/cctc.201801988.

[116] M.Z. Ramli, S.S.A. Syed-Hassan, A. Hadi, Performance of Cu-Zn-Al-Zr catalyst prepared by ultrasonic spray precipitation technique in the synthesis of methanol via CO_2 hydrogenation, Fuel Process. Technol. 169 (2018) 191-198. https://doi.org/10.1016/j.fuproc.2017.10.004.

[117] X. Dong, F. Li, N. Zhao, F. Xiao, J. Wang, Y. Tan, CO_2 hydrogenation to methanol over Cu/ZnO/ZrO_2 catalysts prepared by precipitation-reduction method, Appl. Catal. B Environ. 191 (2016) 8-17. https://doi.org/10.1016/j.apcatb.2016.03.014.

[118] L. Angelo, M. Girleanu, O. Ersen, C. Serra, K. Parkhomenko, A.C. Roger, Catalyst synthesis by continuous coprecipitation under microfluidic conditions: Application to the preparation of catalysts for methanol synthesis from CO_2/H_2, Catal. Today. 270 (2016) 59-67. https://doi.org/10.1016/j.cattod.2015.09.028.

[119] H. Lei, R. Nie, G. Wu, Z. Hou, Hydrogenation of CO_2 to CH_3OH over Cu/ZnO catalysts with different ZnO morphology, Fuel. 154 (2015) 161-166. https://doi.org/10.1016/j.fuel.2015.03.052.

[120] K. Samson, M. Sliwa, R.P. Socha, K. Góra-Marek, D. Mucha, D. Rutkowska-Zbik, J.F. Paul, M. Ruggiero-Mikoajczyk, R. Grabowski, J. Soczyński, Influence of ZrO_2 structure and copper electronic state on activity of Cu/ZrO_2 catalysts in methanol synthesis from

CO_2, ACS Catal. 4 (2014) 3730-3741. https://doi.org/10.1021/cs500979c.

[121] H. Ban, C. Li, K. Asami, K. Fujimoto, Influence of rare-earth elements (La, Ce, Nd, and Pr) on the performance of Cu/Zn/Zr catalyst for CH_3OH synthesis from CO_2, Catal. Commun. 54 (2014) 50-54. https://doi.org/10.1016/j.catcom.2014.05.014.

[122] G. Bonura, M. Cordaro, C. Cannilla, F. Arena, F. Frusteri, The changing nature of the active site of Cu-Zn-Zr catalysts for the CO_2 hydrogenation reaction to methanol, Appl. Catal. B Environ. 152-153 (2014) 152-161. https://doi.org/10.1016/j.apcatb.2014.01.035.

[123] X.M. Liu, Z.F. Yan, G.Q. Lu, Role of nanosized zirconia on the properties of $Cu/Ga_2O_3/ZrO_2$ catalysts for methanol synthesis, Chinese J. Chem. 24 (2006) 172-176. https://doi.org/10.1002/cjoc.200690033.

[124] M.A. Hossain, B. V. Ayodele, C.K. Cheng, M.R. Khan, Artificial neural network modeling of hydrogen-rich syngas production from methane dry reforming over novel $Ni/CaFe_2O_4$ catalysts, Int. J. Hydrogen Energy. 41 (2016) 11119-11130. https://doi.org/10.1016/j.ijhydene.2016.04.034.

[125] B.V. Ayodele, S.I. Mustapa, M.A. Alsaffar, C.K. Cheng, Artificial intelligence modelling approach for the prediction of CO-rich hydrogen production rate from methane dry reforming, Catalysts. 9 (2019). https://doi.org/10.3390/catal9090738.

[126] M. Suvarna, T.P. Araújo, J. Pérez-Ramírez, A generalized machine learning framework to predict the space-time yield of methanol from thermocatalytic CO_2 hydrogenation, Appl. Catal. B Environ. 315 (2022). https://doi.org/10.1016/j.apcatb.2022.121530.

[127] S. Bahri, S. Pathak, A. Singhahluwalia, P. Malav, S. Upadhyayula, Meta-analysis approach for understanding the characteristics of CO_2 reduction catalysts for renewable fuel production, J. Clean. Prod. 339 (2022) 130653. https://doi.org/10.1016/j.jclepro.2022.130653.

[128] T. Fujitani, J. Nakamura, The chemical modification seen in the Cu/ZnO methanol synthesis catalysts, Appl. Catal. A Gen. 191 (2000) 111-129. https://doi.org/10.1016/S0926-860X(99)00313-0.

[129] L. Martínez-Suarez, N. Siemer, J. Frenzel, D. Marx, Reaction Network of Methanol Synthesis over Cu/ZnO Nanocatalysts, ACS Catal. 5 (2015) 4201-4218. https://doi.org/10.1021/acscatal.5b00442.

[130] G.C. Chinchen, K.C. Waugh, D.A. Whan, The activity and state of the copper surface in methanol synthesis catalysts, Appl. Catal. 25 (1986) 101-107. https://doi.org/10.1016/S0166-9834(00)81226-9.

[131] S. Kuld, M. Thorhauge, H. Falsig, C.F. Elkjær, S. Helveg, I. Chorkendorff, J. Sehested, Quantifying the promotion of Cu catalysts by ZnO for methanol synthesis, Science (80). 352 (2016) 969-974. https://doi.org/10.1126/science.aaf0718.

[132] X. Sun, B. Yan, Emerging Strategies in Engineering Cu-ZnO Interfacial Sites for CO_2-to-Methanol: Mechanistic Advances, Challenges, and Opportunities, ACS Catal. 15 (2025) 18282-18304. https://doi.org/10.1021/acscatal.5c05750.

[133] S.M. Fehr, K. Nguyen, I. Krossing, Realistic Operando-DRIFTS Studies on Cu/ZnO Catalysts for CO_2 Hydrogenation to Methanol - Direct Observation of Mono-ionized Defect Sites and Implications for Reaction Intermediates, ChemCatChem. 14 (2022). https://doi.org/10.1002/cctc.202101500.

[134] G. Pacchioni, From CO_2 to Methanol on Cu/ZnO/Al_2O_3 Industrial Catalyst. What Do We Know about the Active Phase and the Reaction Mechanism?, ACS Catal. 14 (2024) 2730–2745. https://doi.org/10.1021/acscatal.3c05669.

[135] Y. Liu, L. Cui, C. Liu, L. Huang, F. Cao, Enhanced CO_2 hydrogenation to methanol over Cu-ZnO-Al_2O_3 catalyst modified with zirconium: Experimental and theoretical insights, Chem. Eng. J. 511 (2025) 162221. https://doi.org/10.1016/j.cej.2025.162221.

[136] E. Fernández-Villanueva, P.G. Lustemberg, M. Zhao, J. Soriano Rodriguez, P. Concepción, M.V. Ganduglia-Pirovano, Water and Cu+ Synergy in Selective CO_2 Hydrogenation to Methanol over Cu-MgO-Al_2O_3 Catalysts, J. Am. Chem. Soc. 146 (2024) 2024-2032. https://doi.org/10.1021/jacs.3c10685.

[137] F.C.F. Marcos, F.M. Cavalcanti, D.D. Petrolini, L. Lin, L.E. Betancourt, S.D. Senanayake, J.A. Rodriguez, J.M. Assaf, R. Giudici, E.M. Assaf, Effect of operating parameters on H_2/CO_2 conversion to methanol over Cu-Zn oxide supported on ZrO_2 polymorph catalysts: Characterization and kinetics, Chem. Eng. J. 427 (2022). https://doi.org/10.1016/j.cej.2021.130947.

[138] Y. Yang, C.A. Mims, R.S. Disselkamp, J.H. Kwak, C.H.F. Peden, C.T. Campbell, (Non)formation of methanol by direct hydrogenation of formate on copper catalysts, J. Phys. Chem. C. 114 (2010) 17205-17211. https://doi.org/10.1021/jp104068k.

[139] S. Polierer, J. Jelic, S. Pitter, F. Studt, On the Reactivity of the Cu/ZrO_2 System for the Hydrogenation of CO_2 to Methanol: A Density Functional Theory Study, J. Phys. Chem. C. 123 (2019) 26904-26911. https://doi.org/10.1021/acs.jpcc.9b06500.

[140] X. Chang, X. Han, Y. Pan, Z. Hao, J. Chen, M. Li, J. Lv, X. Ma, Insight into the Role of Cu-ZrO_2 Interaction in Methanol Synthesis from CO_2 Hydrogenation, Ind. Eng. Chem. Res. 61 (2022) 6872-6883. https://doi.org/10.1021/acs.iecr.2c00858.

[141] Y. Fang, F. Wang, Y. Chen, Q. Lv, K. Jiang, H. Yang, H. Zhao, P. Wang, Y. Gan, L. Wu, Y. Tang, X. Gao, L. Tan, Realizing methanol synthesis from CO and water via the synergistic effect of Cu^0/Cu^+ over Cu/ZrO_2 catalyst, J. Energy Chem. 93 (2024) 126-134. https://doi.org/10.1016/j.jechem.2024.01.066.

[142] F. Studt, M. Behrens, E.L. Kunkes, N. Thomas, S. Zander, A. Tarasov, J. Schumann, E. Frei, J.B. Varley, F. Abild-Pedersen, J.K. Nørskov, R. Schlögl, The Mechanism of CO and CO_2 Hydrogenation to Methanol over Cu-Based Catalysts, ChemCatChem. 7 (2015) 1105-1111. https://doi.org/10.1002/cctc.201500123.

[143] Y. Slotboom, M.J. Bos, J. Pieper, V. Vrieswijk, B. Likozar, S.R.A. Kersten, D.W.F. Brilman, Critical assessment of steady-state kinetic models for the synthesis of methanol over an industrial Cu/ZnO/Al_2O_3 catalyst, Chem. Eng. J. 389 (2020) 124181. https://doi.org/10.1016/j.cej.2020.124181.

[144] S. Poto, D. Vico van Berkel, F. Gallucci, M. Fernanda Neira d'Angelo, Kinetic modelling of the methanol synthesis from CO_2 and H_2 over a CuO/CeO_2/ZrO_2 catalyst: The role of CO_2 and CO hydrogenation, Chem. Eng. J. 435 (2022) 134946. https://doi.org/10.1016/j.cej.2022.134946.

[145] J.F. Portha, K. Parkhomenko, K. Kobl, A.C. Roger, S. Arab, J.M. Commenge, L. Falk, Kinetics of Methanol Synthesis from Carbon Dioxide Hydrogenation over Copper-Zinc Oxide Catalysts, Ind. Eng. Chem. Res. 56 (2017) 13133-13145. https://doi.org/10.1021/acs.iecr.7b01323.

[146] F. Bisotti, M. Fedeli, K. Prifti, A. Galeazzi, A. Dell'Angelo, M. Barbieri, C. Pirola, G. Bozzano, F. Manenti, Century of Technology Trends in Methanol Synthesis: Any Need for Kinetics Refitting?, Ind. Eng. Chem. Res. 60 (2021) 16032-16053. https://doi.org/10.1021/acs.iecr.1c02877.

[147] F. Bisotti, M. Fedeli, K. Prifti, A. Galeazzi, A. Dell'Angelo, F. Manenti, Impact of

Kinetic Models on Methanol Synthesis Reactor Predictions: In Silico Assessment and Comparison with Industrial Data, Ind. Eng. Chem. Res. 61 (2022) 2206-2226. https://doi.org/10.1021/acs.iecr.1c04476.

[148] K. Klier, V. Chatikavanij, R.G. Herman, G.W. Simmons, Catalytic synthesis of methanol from CO and H_2. IV. The effects of carbon dioxide, J. Catal. 74 (1982) 343-360. https://doi.org/10.1016/0021-9517(82)90040-9.

[149] G.H. Graaf, E.J. Stamhuis, A.A.C.M. Beenackers, Kinetics of low-pressure methanol synthesis, Chem. Eng. Sci. 43 (1988) 3185-3195. https://doi.org/10.1016/0009-2509(88)85127-3.

[150] P. Villa, P. Forzatti, G. Buzzi-Ferraris, G. Garone, I. Pasquon, Synthesis of alcohols from carbon oxides and hydrogen. 1. Kinetics of the low-pressure methanol synthesis, Ind. Eng. Chem. Process Des. Dev. 24 (1985) 12-19. https://doi.org/10.1021/i200028a003.

[151] P.S. T.S. Askgaard, J.K. Norskov, C.V. Ovesen, Askgaard_1995.Pdf, J. Catal. (1995) 229-242.

[152] C. Seidel, A. Jörke, B. Vollbrecht, A. Seidel-Morgenstern, A. Kienle, Kinetic modeling of methanol synthesis from renewable resources, Chem. Eng. Sci. 175 (2018) 130-138. https://doi.org/10.1016/j.ces.2017.09.043.

[153] J. Skrzypek, M. Lachowska, H. Moroz, Kinetics of methanol synthesis over commercial copper/zinc oxide/alumina catalysts, Chem. Eng. Sci. 46 (1991) 2809-2813. https://doi.org/10.1016/0009-2509(91)85150-V.

[154] T.W. and M.S. Takeshi Kubota, Itaru Hayakawa, Hirotaka Mabuse, Kozo Mori, Kenji Ushikoshi, Kinetic study of methanol synthesis from carbon dioxide and hydrogen, Appl. Organomet. Chem. 15 (2001) 121–126. https://doi.org/10.1002/1099-0739(200102)15.

[155] N. Park, M.J. Park, Y.J. Lee, K.S. Ha, K.W. Jun, Kinetic modeling of methanol synthesis over commercial catalysts based on three-site adsorption, Fuel Process. Technol. 125 (2014) 139-147. https://doi.org/10.1016/j.fuproc.2014.03.041.

[156] A. Kouzehli, M. Kazemeini, A. Ashrafi Moghaddam, A robust kinetic modeling of CO_2 hydrogenation to methanol over an industrial copper-zinc oxide catalyst based on a single-active site mechanism, Int. J. Hydrogen Energy. 60 (2024) 756–768.

https://doi.org/10.1016/j.ijhydene.2024.02.176.

[157] K.W. Ting, T. Toyao, S.M.A.H. Siddiki, K.I. Shimizu, R. Gaikwad, A. Bansode, A. Urakawa, J. Xu, X. Su, X. Liu, X. Pan, G. Pei, Y. Huang, X. Wang, T. Zhang, H. Geng, L. Angelo, K. Kobl, L.M.M. Tejada, Y. Zimmermann, K. Parkhomenko, A.C. Roger, A. Bansode, A. Urakawa, Towards full one-pass conversion of carbon dioxide to methanol and methanol-derived products, J. Catal. 309 (2016) 3685-3693. https://doi.org/10.1016/j.jcat.2013.09.005.

[158] S. Arab, J.M. Commenge, J.F. Portha, L. Falk, Methanol synthesis from CO_2 and H_2 in multi-tubular fixed-bed reactor and multi-tubular reactor filled with monoliths, Chem. Eng. Res. Des. 92 (2014) 2598–2608. https://doi.org/10.1016/j.cherd.2014.03.009.

[159] M. Shahrokhi, G.R. Baghmisheh, Modeling, simulation, and control of a methanol synthesis fixed-bed reactor, Chem. Eng. Sci. 60 (2005) 4275-4286. https://doi.org/10.1016/j.ces.2004.12.051.

[160] G. Leonzio, E. Zondervan, P.U. Foscolo, Methanol production by CO_2 hydrogenation: Analysis and simulation of reactor performance, Int. J. Hydrogen Energy. 44 (2019) 7915-7933. https://doi.org/10.1016/j.ijhydene.2019.02.056.

[161] F. Samimi, M.R. Rahimpour, A. Shariati, Development of an efficient methanol production process for direct CO_2 hydrogenation over a $Cu/ZnO/Al_2O_3$ catalyst, Catalysts. 7 (2017). https://doi.org/10.3390/catal7110332.

[162] A. Montebelli, C.G. Visconti, G. Groppi, E. Tronconi, S. Kohler, Optimization of compact multitubular fixed-bed reactors for the methanol synthesis loaded with highly conductive structured catalysts, Chem. Eng. J. 255 (2014) 257-265. https://doi.org/10.1016/j.cej.2014.06.050.

[163] Z. Liang, P. Gao, Z. Tang, M. Lv, Y. Sun, Three-dimensional porous Cu-Zn/Al foam monolithic catalyst for CO_2 hydrogenation to methanol in microreactor, J. CO_2 Util. 21 (2017) 191-199. https://doi.org/10.1016/j.jcou.2017.05.023.

[164] S. Roy, T. Bauer, M. Al-Dahhan, P. Lehner, T. Turek, Monoliths as multiphase reactors: A review, AIChE J. 50 (2004) 2918-2938. https://doi.org/10.1002/aic.10268.

[165] S. Schlüter, A. Steiff, P.M. Weinspach, Modeling and simulation of bubble column reactors, Chem. Eng. Process. 31 (1992) 97-117. https://doi.org/10.1016/0255-2701(92)85004-L.

[166] K. Zhang, Y. Zhao, A scale-up strategy for low-temperature methanol synthesis in a circulating slurry bubble reactor, Chem. Eng. Sci. 61 (2006) 1459-1469. https://doi.org/10.1016/j.ces.2005.08.040.

[167] G.W. Roberts, M.A. Márquez, C.A. Haney, Liquid/catalyst interactions in slurry reactors: Methanol synthesis over zinc chromite, Appl. Catal. A Gen. 183 (1999) 395-410. https://doi.org/10.1016/S0926-860X(99)00076-9.

[168] M. Šetinc, J. Levec, Dynamics of a mixed slurry reactor for the three-phase methanol synthesis, Chem. Eng. Sci. 56 (2001) 6081-6087. https://doi.org/10.1016/S0009-2509(01)00212-3.

[169] H.A. Garona, F.M. Cavalcanti, T.F. de Abreu, M. Schmal, R.M.B. Alves, Evaluation of Fischer-Tropsch synthesis to light olefins over Co- and Fe-based catalysts using artificial neural network, J. Clean. Prod. 321 (2021) 129003. https://doi.org/10.1016/j.jclepro.2021.129003.

[170] Y. Wang, W. Gao, K. Li, Y. Zheng, Z. Xie, W. Na, J.G. Chen, H. Wang, Strong Evidence of the Role of H_2O in Affecting Methanol Selectivity from CO_2 Hydrogenation over Cu-ZnO-ZrO_2, Chem. 6 (2020) 419-430. https://doi.org/10.1016/j.chempr.2019.10.023.

[171] C. Zhang, H. Yang, P. Gao, H. Zhu, L. Zhong, H. Wang, W. Wei, Y. Sun, Preparation and CO_2 hydrogenation catalytic properties of alumina microsphere supported Cu-based catalyst by deposition-precipitation method, J. CO_2 Util. 17 (2017) 263-272. https://doi.org/10.1016/j.jcou.2016.11.015.

[172] A. Bansode, B. Tidona, P.R. Von Rohr, A. Urakawa, Impact of K and Ba promoters on CO_2 hydrogenation over Cu/Al_2O_3 catalysts at high pressure, Catal. Sci. Technol. 3 (2013) 767-778. https://doi.org/10.1039/c2cy20604h.

[173] M.R.K. Estahbanati, M. Feilizadeh, M.C. Iliuta, Photocatalytic valorization of glycerol to hydrogen: Optimization of operating parameters by artificial neural network, Appl. Catal. B Environ. 209 (2017) 483-492. https://doi.org/10.1016/j.apcatb.2017.03.016.

[174] L.A. Baumes, J.M. Serra, P. Serna, A. Corma, Support vector machines for predictive modeling in heterogeneous catalysis: A comprehensive introduction and overfitting investigation based on two real applications, J. Comb. Chem. 8 (2006) 583-596. https://doi.org/10.1021/cc050093m.

[175] J. Eberhard, V. Geissbuhler, Konservative und operative therapie bei harninkontinenz,

deszensus und urogenital-beschwerden, 2000.

[176] S. Zander, E.L. Kunkes, M.E. Schuster, J. Schumann, G. Weinberg, D. Teschner, N. Jacobsen, R. Schlögl, M. Behrens, The role of the oxide component in the development of copper composite catalysts for methanol synthesis, Angew. Chemie - Int. Ed. 52 (2013) 6536-6540. https://doi.org/10.1002/anie.201301419.

[177] S. Kleiber, M. Pallua, M. Siebenhofer, S. Lux, Catalytic hydrogenation of CO_2 to methanol over Cu/MgO catalysts in a semi-continuous reactor, Energies. 14 (2021). https://doi.org/10.3390/en14144319.

[178] R. Singh, K. Tripathi, K.K. Pant, J.K. Parikh, Unravelling synergetic interaction over tandem Cu-ZnO-ZrO_2/hierarchical ZSM5 catalyst for CO_2 hydrogenation to methanol and DME, Fuel. 318 (2022) 123641. https://doi.org/10.1016/j.fuel.2022.123641.

[179] S. Bahri, U. Basak, S. Upadhyayula, Rational design of process parameters for carbon-neutral and sulfur-free motor fuel production from second-generation biomass generated syngas, J. Clean. Prod. 279 (2021) 123559. https://doi.org/10.1016/j.jclepro.2020.123559.

[180] S.J. Clark, M.D. Segall, C.J. Pickard, P.J. Hasnip, M.I.J. Probert, K. Refson, M.C. Payne, First principles methods using CASTEP, Zeitschrift Fur Krist. 220 (2005) 567–570. https://doi.org/10.1524/zkri.220.5.567.65075.

[181] J. Li, H. Zheng, X. Zhang, Z. Li, First-principles investigation on Cu/ZnO catalyst precursor: Energetic, structural and electronic properties of Zn-doped $Cu_2(OH)_2CO_3$, Comput. Mater. Sci. 96 (2015) 1-9. https://doi.org/10.1016/j.commatsci.2014.08.038.

[182] H. Zheng, N. Narkhede, Z. Li, New Theoretical Insights into the Origin of Highly-Effective Dispersion of Cu-Based Catalysts As-Synthesized Using Mg/Zn Doped Malachite as Precursors, ChemistrySelect. 4 (2019) 13271-13279. https://doi.org/10.1002/slct.201903918.

[183] M.D. Segall, P.J.D. Lindan, M.J. Probert, C.J. Pickard, P.J. Hasnip, S.J. Clark, M.C. Payne, First-principles simulation: Ideas, illustrations and the CASTEP code, J. Phys. Condens. Matter. 14 (2002) 2717-2744. https://doi.org/10.1088/0953-8984/14/11/301.

[184] D. Vanderbilt, Vanderbilt(1990), Phys. Rev. B. 41 (1990) 7892.

[185] J.P. Perdew, A. Zunger, Self-interaction correction to density-functional approximations

for many-electron systems, Phys. Rev. B. 23 (1981) 5048-5079. https://doi.org/10.1103/PhysRevB.23.5048.

[186] A.N. Şener, M.E. Günay, A. Leba, R. Yıldırım, Statistical review of dry reforming of methane literature using decision tree and artificial neural network analysis, Catal. Today. 299 (2018) 289-302. https://doi.org/10.1016/j.cattod.2017.05.012.

[187] M.T. Hagan, M.B. Menhaj, Training Feedforward Networks with the Marquardt Algorithm, IEEE Trans. Neural Networks. 5 (1994) 989-993. https://doi.org/10.1109/72.329697.

[188] F.D. Foresee, M.T. Hagan, Gauss-Newton approximation to Bayesian learning, in: Proceedings of International Conference on Neural Networks, Vol. 3, 1997, pp. 1930-1935.

[189] L. Eriksson, D. Louer, P. Werner, Crystal structure determination and rietveld refinement of Zn (OH)(NO_3)·H_2O, J. Solid State Chem. 81 (1989) 9-20.

[190] G. Behrendt, N. Prinz, A. Wolf, L. Baumgarten, A. Gaur, J.D. Grunwaldt, M. Zobel, M. Behrens, S. Mangelsen, Substitution of Copper by Magnesium in Malachite: Insights into the Synthesis and Structural Effects, Inorg. Chem. 61 (2022) 19678-19694. https://doi.org/10.1021/acs.inorgchem.2c01976.

[191] M. Behrens, F. Girgsdies, A. Trunschke, R. Schlögl, Minerals as model compounds for Cu/ZnO catalyst precursors: structural and thermal properties and IR spectra of mineral and synthetic (zincian) malachite, rosasite and aurichalcite and a catalyst precursor mixture, Eur. J. Inorg. Chem. (2009) 1347-1357. https://doi.org/10.1002/ejic.200801216.

[192] Y.J. Heo, S.J. Park, Facile Synthesis of MgO-Modified Carbon Adsorbents with Microwave-Assisted Methods: Effect of MgO Particles and Porosities on CO_2 Capture, Sci. Rep. 7 (2017) 1–9. https://doi.org/10.1038/s41598-017-06091-5.

[193] N. Rui, Z. Wang, K. Sun, J. Ye, Q. Ge, C. jun Liu, CO_2 hydrogenation to methanol over Pd/In_2O_3: effects of Pd and oxygen vacancy, Appl. Catal. B Environ. 218 (2017) 488-497. https://doi.org/10.1016/j.apcatb.2017.06.069.

[194] T.W. van Deelen, C. Hernández Mejía, K.P. de Jong, Control of metal-support interactions in heterogeneous catalysts to enhance activity and selectivity, Nat. Catal. 2 (2019) 955-970. https://doi.org/10.1038/s41929-019-0364-x.

[195] X. Yu, M. Xin, H. Yuan, L. Gao, A. Zheng, E. Xing, X. Zhang, C. Zhang, B. Zong, Cu-Based Catalysts with Enhanced Thermal Stability for Cyclohexyl Acetate Hydrogenation: Studies on Cu^{+} and Cu^{0} Sites at Different Reduction Temperatures, Catalysts. 13 (2023). https://doi.org/10.3390/catal13040737.

[196] M. Xiong, Z. Gao, Y. Qin, Spillover in Heterogeneous Catalysis: New Insights and Opportunities, ACS Catal. 11 (2021) 3159-3172. https://doi.org/10.1021/acscatal.0c05567.

[197] G. Song, X. Zhu, R. Chen, Q. Liao, Y.D. Ding, L. Chen, Influence of the precursor on the porous structure and CO_2 adsorption characteristics of MgO, RSC Adv. 6 (2016) 19069-19077. https://doi.org/10.1039/c5ra26595a.

[198] E.G. Choi, K.H. Song, S.R. An, K.Y. Lee, M.H. Youn, K.T. Park, S.K. Jeong, H.J. Kim, Cu/ZnO/AlOOH catalyst for methanol synthesis through CO_2 hydrogenation, Korean J. Chem. Eng. 35 (2018) 73-81. https://doi.org/10.1007/s11814-017-0230-y.

[199] F. Liao, Y. Huang, J. Ge, W. Zheng, K. Tedsree, P. Collier, X. Hong, S.C. Tsang, Morphology-Dependent Interactions of ZnO with Cu Nanoparticles at the Materials' Interface in Selective Hydrogenation of CO_2 to CH_3OH, Angew. Chemie. 123 (2011) 2210-2213. https://doi.org/10.1002/ange.201007108.

[200] I. Ganesh, Conversion of carbon dioxide into methanol - A potential liquid fuel: Fundamental challenges and opportunities (a review), Renew. Sustain. Energy Rev. 31 (2014) 221–257. https://doi.org/10.1016/j.rser.2013.11.045.

[201] H. Ren, C.H. Xu, H.Y. Zhao, Y.X. Wang, J. Liu, J.Y. Liu, Methanol synthesis from CO_2 hydrogenation over Cu/γ-Al_2O_3 catalysts modified by ZnO, ZrO_2, and MgO, J. Ind. Eng. Chem. 28 (2015) 261-267. https://doi.org/10.1016/j.jiec.2015.03.001.

[202] K. Ahmad, S. Upadhyayula, Conversion of the greenhouse gas CO_2 to methanol over supported intermetallic Ga-Ni catalysts at atmospheric pressure: Thermodynamic modeling and experimental study, Sustain. Energy Fuels. 3 (2019) 2509-2520. https://doi.org/10.1039/c9se00165d.

[203] K. Lee, H. Yan, Q. Sun, Z. Zhang, N. Yan, Mechanism-Guided Catalyst Design for CO_2 Hydrogenation to Formate and Methanol, Accounts Mater. Res. 4 (2023) 746-757. https://doi.org/10.1021/accountsmr.3c00075.

[204] P. Tian, X.Y. Han, G.L. Ning, H.X. Fang, J.W. Ye, W.T. Gong, Y. Lin, Synthesis of

porous hierarchical MgO and its superb adsorption properties, ACS Appl. Mater. Interfaces. 5 (2013) 12411-12418. https://doi.org/10.1021/am403352y.

[205] C. Zhang, L. Wang, Y. Chen, X. He, Y. Song, O.M. Gazit, Z. Zhong, Shifting CO_2 hydrogenation from producing CO to CH_3OH by engineering defect structures of Cu/ZrO_2 and Cu/ZnO catalysts, Chem. Eng. J. 475 (2023). https://doi.org/10.1016/j.cej.2023.146102.

[206] Y. Wang, Y. Liu, L. Tan, X. Lin, Y. Fang, X.F. Lu, Y. Hou, G. Zhang, S. Wang, Confining ultrafine Pt nanoparticles on In_2O_3 nanotubes for enhanced selective methanol production by CO_2 hydrogenation, J. Mater. Chem. A. 11 (2023) 26804-26811. https://doi.org/10.1039/d3ta05938c.

[207] W. Wu, K. Xie, D. Sun, X. Li, F. Fang, $CuO/ZnO/Al_2O_3$ Catalyst Prepared by Mechanical-Force-Driven Solid-State Ion Exchange and Its Excellent Catalytic Activity under Internal Cooling Condition, Ind. Eng. Chem. Res. 56 (2017) 8216-8223. https://doi.org/10.1021/acs.iecr.7b01464.

[208] Z.J. Liu, X.J. Tang, S. Xu, X.L. Wang, Synthesis and catalytic performance of graphene modified $CuO-ZnO-Al_2O_3$ for CO_2 hydrogenation to methanol, J. Nanomater. 2014 (2014). https://doi.org/10.1155/2014/690514.

[209] K. Oshima, Y. Honma, K. Kinoshita, Z. Gao, T. Honma, S. Tada, S. Satokawa, Mechanochemical Effect in Mixing Sponge Copper with Amorphous ZrO_2 Creates Effective Active Sites for Methanol Synthesis by CO_2 Hydrogenation, J. Phys. Chem. C. 125 (2021) 8155-8162. https://doi.org/10.1021/acs.jpcc.0c10917.

[210] L. Huang, G.J. Kramer, W. Wieldraaijer, D.S. Brands, E.K. Poels, H.L. Castricum, H. Bakker, Methanol synthesis over Cu/ZnO catalysts prepared by ball milling, Catal. Letters. 48 (1997) 55-59. https://doi.org/10.1023/a:1019014701674.

[211] X. Fang, Y. Men, F. Wu, Q. Zhao, R. Singh, P. Xiao, T. Du, P.A. Webley, Improved methanol yield and selectivity from CO_2 hydrogenation using a novel $Cu-ZnO-ZrO_2$ catalyst supported on Mg-Al layered double hydroxide (LDH), J. CO_2 Util. 29 (2019) 57-64. https://doi.org/10.1016/j.jcou.2018.11.006.

[212] X. Sun, Y. Jin, Z. Cheng, G. Lan, X. Wang, Y. Qiu, Y. Wang, H. Liu, Y. Li, Dual active sites over $Cu-ZnO-ZrO_2$ catalysts for carbon dioxide hydrogenation to methanol, J. Environ. Sci. (China). 131 (2023) 162-172. https://doi.org/10.1016/j.jes.2022.10.002.

[213] Q. He, Z. Li, D. Li, F. Ning, Q. Wang, W. Liu, W. Zhang, Y. Cui, J. Zhang, C. Liu, Mg enhanced the performance of Cu/ZnO/ZrO_2 for CO_2 hydrogenation to methanol and the mechanism investigation, Mol. Catal. 558 (2024) 114008. https://doi.org/10.1016/j.mcat.2024.114008.

[214] T. Witoon, T. Numpilai, T. Phongamwong, W. Donphai, C. Boonyuen, C. Warakulwit, M. Chareonpanich, J. Limtrakul, Enhanced activity, selectivity, and stability of a CuO-ZnO-ZrO_2 catalyst by adding graphene oxide for CO_2 hydrogenation to methanol, Chem. Eng. J. 334 (2018) 1781–1791. https://doi.org/10.1016/j.cej.2017.11.117.

[215] T. Pinheiro Araújo, G. Giannakakis, J. Morales-Vidal, M. Agrachev, Z. Ruiz-Bernal, P. Preikschas, T. Zou, F. Krumeich, P.O. Willi, W.J. Stark, R.N. Grass, G. Jeschke, S. Mitchell, N. López, J. Pérez-Ramírez, Low-nuclearity CuZn ensembles on ZnZrOx catalyze methanol synthesis from CO_2, Nat. Commun. 15 (2024). https://doi.org/10.1038/s41467-024-47447-6.

[216] X. Fang, Y. Men, F. Wu, Q. Zhao, R. Singh, P. Xiao, T. Du, P.A. Webley, Moderate-pressure conversion of H_2 and CO_2 to methanol via adsorption enhanced hydrogenation, Int. J. Hydrogen Energy. 44 (2019) 21913-21925. https://doi.org/10.1016/j.ijhydene.2019.06.176.

[217] X. Sun, Y. Jin, Z. Cheng, G. Lan, X. Wang, Y. Qiu, Y. Wang, H. Liu, Y. Li, Dual active sites over Cu-ZnO-ZrO_2 catalysts for carbon dioxide hydrogenation to methanol, J. Environ. Sci. (China). 131 (2023) 162-172. https://doi.org/10.1016/j.jes.2022.10.002.

[218] L. Zwiener, F. Girgsdies, D. Brennecke, D. Teschner, A.G.F. Machoke, R. Schlögl, E. Frei, Evolution of zincian malachite synthesis by low temperature co-precipitation and its catalytic impact on the methanol synthesis, Appl. Catal. B Environ. 249 (2019) 218-226. https://doi.org/10.1016/j.apcatb.2019.02.023.

[219] F. Zhang, B. Li, X. Quan, K. Wang, J. Xu, T. Wu, Z. Li, M. Yan, S. Liu, Y. He, Y. Shi, Y. Su, P. Xie, Revealing the Dynamics of Oxygen Vacancy in ZnO_{1-x}/Cu during Robust Methanol Synthesis from CO_2, ACS Catal. 14 (2024) 7136-7148. https://doi.org/10.1021/acscatal.4c01648.

[220] L. Li, D. Mao, J. Yu, X. Guo, Highly selective hydrogenation of CO_2 to methanol over CuO-ZnO-ZrO_2 catalysts prepared by a surfactant-assisted co-precipitation method, J. Power Sources. 279 (2015) 394-404. https://doi.org/10.1016/j.jpowsour.2014.12.142.

[221] F. Arena, G. Mezzatesta, G. Zafarana, G. Trunfio, F. Frusteri, L. Spadaro, Effects of oxide carriers on surface functionality and process performance of the Cu-ZnO system in the synthesis of methanol via CO_2 hydrogenation, J. Catal. 300 (2013) 141-151. https://doi.org/10.1016/j.jcat.2012.12.019.

[222] F. Arena, G. Italiano, K. Barbera, S. Bordiga, G. Bonura, L. Spadaro, F. Frusteri, Solid-state interactions, adsorption sites and functionality of Cu-ZnO/ZrO_2 catalysts in the CO_2 hydrogenation to CH_3OH, Appl. Catal. A Gen. 350 (2008) 16-23. https://doi.org/10.1016/j.apcata.2008.07.028.

[223] N. Kanjanasoontorn, T. Permsirivanich, T. Numpilai, T. Witoon, N. Chanlek, M. Niamlaem, C. Warakulwit, J. Limtrakul, Structure-Activity Relationships of Hierarchical Meso-Macroporous Alumina Supported Copper Catalysts for CO_2 Hydrogenation: Effects of Calcination Temperature of Alumina Support, Catal. Letters. 146 (2016) 1943-1955. https://doi.org/10.1007/s10562-016-1849-8.

[224] Z. Li, T. Du, Y. Li, H. Jia, Y. Wang, Y. Song, X. Fang, Water- and reduction-free preparation of oxygen vacancy rich Cu-ZnO-ZrO_2 catalysts for promoted methanol synthesis from CO_2, Fuel. 322 (2022) 124264. https://doi.org/10.1016/j.fuel.2022.124264.

[225] F. Han, H. Liu, W. Cheng, Q. Xu, Highly selective conversion of CO_2 to methanol on the CuZnO-ZrO_2 solid solution with the assistance of plasma, RSC Adv. 10 (2020) 33620-33627. https://doi.org/10.1039/d0ra00961j.

[226] M. Yang, J. Yu, A. Zimina, B.B. Sarma, L. Pandit, J.D. Grunwaldt, L. Zhang, H. Xu, J. Sun, Probing the Nature of Zinc in Copper-Zinc-Zirconium Catalysts by Operando Spectroscopies for CO_2 Hydrogenation to Methanol, Angew. Chemie - Int. Ed. 62 (2023). https://doi.org/10.1002/anie.202216803.

[227] P. Luo, P. Shi, Z. Yan, J. Han, J. Wang, Y. Li, H. Ban, W. Cai, C. Li, Ternary synergistic interaction of Cu-ZnO-ZrO_2 promoting CO_2 hydrogenation to methanol, Appl. Catal. A Gen. 689 (2025) 120006. https://doi.org/10.1016/j.apcata.2024.120006.

[228] C. Zhang, L. Wang, U.J. Etim, Y. Song, O.M. Gazit, Z. Zhong, Oxygen vacancies in Cu/TiO_2 boost strong metal-support interaction and CO_2 hydrogenation to methanol, J. Catal. 413 (2022) 284-296. https://doi.org/10.1016/j.jcat.2022.06.026.

[229] S. Chen, A.M. Abdel-Mageed, C. Mochizuki, T. Ishida, T. Murayama, J. Rabeah, M.

Parlinska-Wojtan, A. Brückner, R.J. Behm, Controlling the O-Vacancy Formation and Performance of Au/ZnO Catalysts in CO_2 Reduction to Methanol by the ZnO Particle Size, ACS Catal. 11 (2021) 9022-9033. https://doi.org/10.1021/acscatal.1c01415.

[230] K. Sun, C. Shen, R. Zou, C. Jun Liu, Highly active Pt/In_2O_3-ZrO_2 catalyst for CO_2 hydrogenation to methanol with enhanced CO tolerance: The effects of ZrO_2, Appl. Catal. B Environ. 320 (2023) 122018. https://doi.org/10.1016/j.apcatb.2022.122018.

[231] J. Strunk, K. Kähler, X. Xia, M. Comotti, F. Schüth, T. Reinecke, M. Muhler, Au/ZnO as catalyst for methanol synthesis: The role of oxygen vacancies, Appl. Catal. A Gen. 359 (2009) 121-128. https://doi.org/10.1016/j.apcata.2009.02.030.

[232] R. Raudaskoski, M.V. Niemelä, R.L. Keiski, The effect of ageing time on co-precipitated Cu/ZnO/ZrO_2 catalysts used in methanol synthesis from CO_2 and H_2, Top. Catal. 45 (2007) 57-60. https://doi.org/10.1007/s11244-007-0240-9.

[233] F. Arena, K. Barbera, G. Italiano, G. Bonura, L. Spadaro, F. Frusteri, Synthesis, characterization and activity pattern of Cu-ZnO/ZrO_2 catalysts in the hydrogenation of carbon dioxide to methanol, J. Catal. 249 (2007) 185-194. https://doi.org/10.1016/j.jcat.2007.04.003.

[234] G. Bonura, F. Arena, G. Mezzatesta, C. Cannilla, L. Spadaro, F. Frusteri, Role of the ceria promoter and carrier on the functionality of Cu-based catalysts in the CO_2-to-methanol hydrogenation reaction, Catal. Today. 171 (2011) 251-256. https://doi.org/10.1016/j.cattod.2011.04.038.

[235] J. Xiao, D. Mao, X. Guo, J. Yu, Effect of TiO_2, ZrO_2, and TiO_2-ZrO_2 on the performance of CuO-ZnO catalyst for CO_2 hydrogenation to methanol, Appl. Surf. Sci. 338 (2015) 146-153. https://doi.org/10.1016/j.apsusc.2015.02.122.

[236] K. Li, J.G. Chen, CO_2 Hydrogenation to Methanol over ZrO_2-Containing Catalysts: Insights into ZrO_2 Induced Synergy, ACS Catal. 9 (2019) 7840-7861. https://doi.org/10.1021/acscatal.9b01943.

[237] S. Ghosh, J. Sebastian, L. Olsson, D. Creaser, Experimental and kinetic modeling studies of methanol synthesis from CO_2 hydrogenation using In_2O_3 catalyst, Chem. Eng. J. 416 (2021) 129120. https://doi.org/10.1016/j.cej.2021.129120.

Appendix A

Section 5A.1 Optimization of synthetic parameters for ($(CuMg)_2(OH)_2CO_3$)) precursor phase through hydrothermal route

The formation of the McGuinnessite ($(CuMg)_2(OH)_2CO_3$) phase during different hydrothermal treatments with $(NH_4)_2CO_3$ was closely monitored by recording PXRD patterns. Initial experiments conducted at temperatures between 100°C and 180°C for 8-16 hours clearly indicated the formation of a single crystalline phase at 150°C for 16 hours. The products obtained after the reactions at 120°C/16 hr and 150°C/6 hr consisted of both malachite and magnesian malachite phases, respectively. The extension of the reaction for 16 hours at 150°C (CM50) resulted in a phase-pure compound, as seen in the PXRD, which resembles the standard data of rosasite, an analogous mineral to mcguinnessite (Mg-rich copper hydroxycarbonate phase) extracted from the American Mineralogist Crystal Structure Database (AMCSD-0011133). The Subsequent increase in reaction temperature to 180°C for the same duration resulted in phase separation, forming mcguinnessite and $MgCO_3$ (PDF No. 08-0479). It is intriguing to note that when other carbonate sources, such as Na_2CO_3, $NaHCO_3$, and NH_4HCO_3, were used at similar concentrations to form mcguinnessite-analogous compounds, pure-phase formation did not occur consistently. When Na_2CO_3 and $NaHCO_3$ were used, a thermodynamically stable phase, hydromagnesite, a hydrated magnesium carbonate mineral, formed alongside malachite phases, competing. Experiments with NH_4HCO_3 resulted in the formation of biphasic magnesium hydroxy carbonates, specifically magnesian malachite (with Mg substituting for Cu in the malachite structure) and mcguinnessite. The use of $(NH_4)_2CO_3$ as a base proved crucial not only in facilitating the reaction to form the Mg-rich McGuinnessite phase but also in minimizing the competing kinetics of Cu^{2+} oxolation to form CuO. It should be noted that to compensate for the leaching of Cu as $[Cu(NH_3)_4]^{2-}$ complex, a slight excess (~10%) of copper reactant weight was taken initially. These experiments indicate that modifications to the hydrothermal conditions, such as the types of carbonate sources, reaction temperature, and duration, could elucidate the detailed mechanism of mcguinnessite formation.

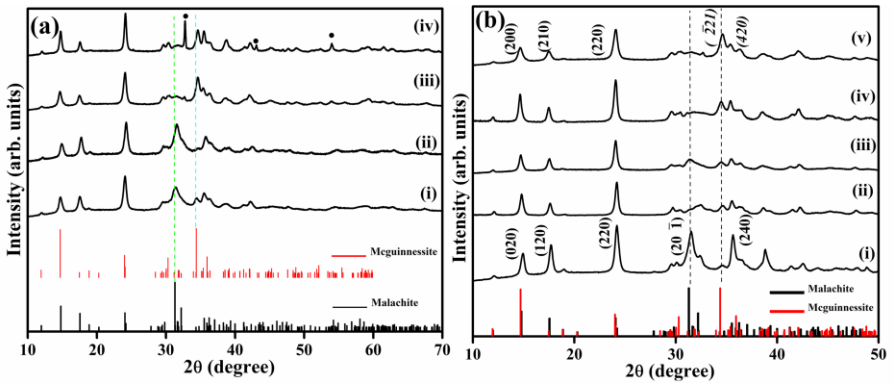


Figure 5A1 (a). *PXRD patterns of the optimization experiments at different conditions carried out for Cu-Mg hydroxycarbonate precursor synthesis, (i) 120°C/16 hr, (ii) 150°C/6 hr, (iii) 150°C/16 hr, and (iv) 180°C/16 hr,* ***(b).*** *PXRD patterns of the different levels of Mg substitutions in ($(Cu_{1-x}Mg_x)_2(OH)_2CO_3$) (i) x = 0 (CM0), (ii) x = 0.125 (CM12.5), (iii) x = 0.25 (CM25), (iv) x = 0.375 (CM37.5), and (v) x = 0.50 (CM50) precursor samples. The line diagram of the standard patterns of Malachite ((PDF No.-41-1390) and McGuinnessite (AMCSD-0011133) is also plotted for reference. • represents the $MgCO_3$ phase (PDF No. 08-0479).*

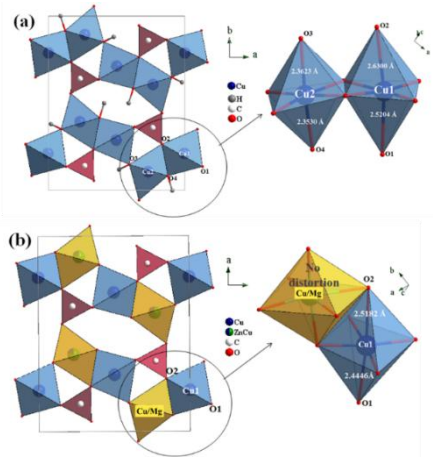


Figure 5A2. *Crystal structure of (a) pure malachite ($Cu_2(OH)_2(CO_3)$), (b) Rosasite analogous mcguinnessite ($(CuMg)_2(OH)_2(CO_3)$) minerals showing the effect of substitution of a non-Jahn-Teller ion (Mg) for a Jahn-Teller ion (Cu).*

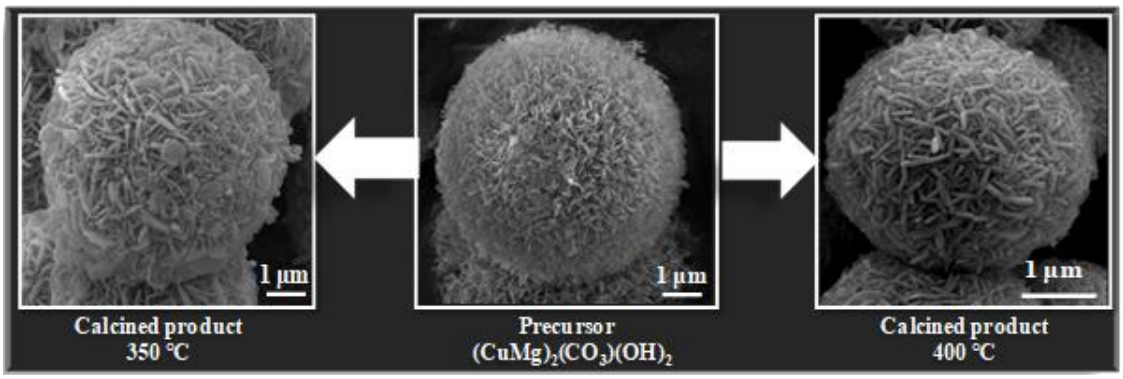


Figure 5A3. *Effect of temperature on the morphology of CM50 precursor sample.*

Table 7A1. *Physical properties of the CZZ-MCBM catalyst.*

Property	Value
Catalyst solid density (g/cm^3)	7.65
Catalyst apparent density (g/cm^3)	3.59
Copper metal composition (wt%)	62.87
Particle size (μm)	300
BET surface area (m^2/g)	32.10
Cu dispersion (%)	5.56
Cu specific surface area (m^2/g)	15.64
Porosity	0.531

Table 7A2. *Catalytic fixed-bed reactor properties.*

Property	Value
Catalyst mass (mg)	1500
Bed volume (cm^3)	3.80
Bed length (cm)	3
Internal reactor diameter (cm)	1.27
External reactor diameter (cm)	1.67
Bed porosity	0.52

Table 7A3. *Experimental reaction conditions and catalytic performance results of CO_2 to methanol over CZZ-MCBM.*

Exp	T (°C)	P(bar)	WHSV ($ml/g_{cat}.hr$)	H_2/CO_2	X_{CO2} (%)	S_{MeOH} (%)	S_{CO} (%)	MeOH STY ($mg_{MeOH}/g_{cat}.hr$)
1	200	40	2600	3	11.3	80.3	19.7	77.87
2	210	40	2600	3	13.1	78.3	21.7	88.03
3	200	40	5200	3	7.71	83.8	16.2	114.59
4	210	40	5200	3	8.63	82.55	17.45	126.35
5	220	40	2600	3	15.2	76.2	23.8	99.40
6	220	40	5200	3	9.52	81.2	18.8	137.11
7	230	40	2600	3	16.41	75.1	24.9	105.76
8	230	40	5200	3	10.73	79.12	20.88	150.57
9	240	40	2600	3	17.64	73.3	26.7	110.97
10	240	40	5200	3	12.34	76.8	23.2	168.09
11	250	40	2600	3	18.63	70.4	29.6	112.56
12	250	40	5200	3	13.22	75.2	24.8	176.33
13	260	40	2600	3	20.08	68.1	31.9	117.36

14	260	40	5200	3	14.35	73.4	26.6	186.81
15	260	40	7800	3	10.6	77.1	22.9	215.09
16	260	40	3900	3	17.5	71.6	28.4	164.88
17	260	40	6500	3	12.1	75.1	24.9	202.76
18	200	20	5200	3	4.18	69.95	30.05	51.86
19	220	20	5200	3	5.37	66.79	33.21	63.61
20	240	20	5200	3	7.32	63.19	36.81	82.04
21	260	20	5200	3	8.38	59.1	40.9	87.84
22	200	25	5200	3	5.01	73.53	26.47	65.34
23	220	25	5200	3	6.34	69.87	30.13	78.57
24	240	25	5200	3	8.47	66.44	33.56	99.81
25	260	25	5200	3	9.49	62.9	37.1	105.87
26	200	30	5200	3	5.83	76.57	23.43	79.17
27	220	30	5200	3	7.22	73.17	26.83	93.69
28	240	30	5200	3	9.83	69.94	30.06	121.94
29	260	30	5200	3	10.81	66.8	33.2	128.07
30	200	35	5200	3	6.62	79.33	20.67	93.15
31	220	35	5200	3	8.51	76.03	23.97	114.75
32	240	35	5200	3	11.17	72.91	27.09	144.45
33	260	35	5200	3	12.41	70.2	29.8	154.52
34	260	40	10400	3	8.12	80.24	19.76	231.12

X_{CO2} = CO_2 Conversion, S_{MeOH} = Methanol Selectivity, S_{CO} = CO Selectivity

Table 7A4. *Initial kinetic model parameters for Model A (Bussche & Froment 1996).*

Model Parameters		**Literature Values**	
		Lower Bounds	**Upper Bounds**
$k'_{CH_3OH}K'_2K_3K_4K_{H_2}$ (mol/kg_{cat}.sec.bar^2)	A	1	1×10^3
	B	1×10^4	6×10^4
k'_1 (mol/kg_{cat}.sec.bar)	A	1×10^2	1×10^6
	B	3×10^4	1×10^5
$\sqrt{K_{H_2}}$ ($bar^{-1/2}$)	A	0.1	1×10^3
	B	-7×10^4	-1×10^3
K_{H_2O}	A	1×10^{-14}	1×10^{-11}

(bar^{-1})	B	-1.2×10^5	-6×10^4
$\frac{K_{H_2O}}{K_8 K_9 K_{H_2}}$ (Dimensionless)	A	1×10^2	1×10^3
	B	-0.005	-0.0001

Table 7A5. *Initial kinetic model parameters for Model B & C (Graaf et al. 1988).*

Model Parameters		**Literature Values**	
		Lower Bounds	**Upper Bounds**
k_1 (mol/kg$_{cat}$.sec.bar)	A	1	1×10^4
	B	1×10^4	8×10^4
k_2 (mol/kg$_{cat}$.sec.bar$^{1/2}$)	A	1×10^3	1×10^6
	B	2×10^4	1.4×10^5
k_3 (mol/kg$_{cat}$.sec.bar)	A	1×10^3	1×10^6
	B	2×10^4	1.3×10^5
K_{CO} (bar^{-1})	A	1×10^{-10}	9×10^{-5}
	B	-1×10^5	-1×10^4
K_{CO_2} (bar^{-1})	A	1×10^{-10}	1×10^{-5}
	B	-1×10^5	-1×10^4
$\frac{K_{H_2O}}{\sqrt{K_{H_2}}}$ (bar$^{-1/2}$)	A	1×10^{-14}	1×10^{-5}
	B	-1×10^5	-1×10^4

Unit of rate constants = Unit of pre-exponential factor = A
Unit of adsorption constants = Unit of pre-exponential factor = A
Unit of activation energy = Unit of adsorption energy = B = J/mol

CURRICULUM VITAE



Aakash Bhardwaj
Department of Chemical Engineering
Indian Institute of Technology Delhi
Phone No: 7987066182, Email Id: bhardwajaakash137@gmail.com
Nationality: Indian
Research gate: http://www.researchgate.net/profile/Aakash Bhardwaj2
Google Scholar: Aakash Bhardwaj - Google Scholar
LinkedIn: www.linkedin.com/in/aakash-bhardwaj-4622b1112.

RESEARCH SUMMARY

I have completed my Ph.D. in Chemical Engineering at IIT Delhi under the joint supervision of Prof. Sreedevi Upadhyayula, Prof. Shantanu Roy, and Prof. Kamal Kishore Pant. My doctoral thesis, **"Comprehensive Investigations into CO_2 Hydrogenation over Cu-based Catalysts: Catalyst Design, Mechanistic Insights, and Kinetic Modeling,"** focuses on heterogeneous catalysis and reaction engineering for sustainable energy applications.

My research involves developing novel catalytic systems for direct CO_2 hydrogenation to methanol in both gas-solid and gas-liquid-solid reactor configurations, with a strong emphasis on understanding structure-activity relationships, reaction mechanisms, and detailed kinetics. I have successfully designed and optimized advanced Cu-based catalytic formulations that deliver stable, long-term performance under industrially relevant conditions. Working across multidisciplinary projects, I have gained extensive experience in high-pressure two- and three-phase reaction systems, chemical reaction engineering, thermodynamic modeling, and kinetic parameter estimation. I am well-versed in a broad suite of catalyst characterization techniques, including XRD, BET, SEM, TEM, XPS, Raman, TPX, and in-situ DRIFTS.

Additionally, I have been actively involved in conceptualizing, drafting, and managing research proposals in collaboration with industrial partners such as Thermax and IIT Delhi, funded by the Government of India (DST), further strengthening my skills in technical communication, project planning, and strategic research execution.

ACADEMIC QUALIFICATIONS

Class	Name of Institution	Subjects	Board/Passing Year	Percentage
Ph.D.	Indian Institute of Technology, Delhi	Chemical Engineering	IIT Delhi (2019-2026)	7.65 CGPA
M.Tech	Indian Institute of Technology (Indian School of Mines), Dhanbad, (Jharkhand), Pincode-826004	Mineral Engineering	IIT(ISM) Dhanbad (2017-2019)	8.57 CGPA
B. Tech	Institute of Technology, GuruGhasidas Vishwavidyalaya, Koni, Bilaspur (C.G.), Pincode-495009	Chemical Engineering	Central Govt. University (2013-2017)	8.06 CGPA

PROJECT WORK

- Project on **"Recovery of heavy metals from effluents of Indian Leather and Tanning Industries by Ion Flotation"** under the guidance of Prof. Shravan Kumar (Fuel and Mineral Engineering Department) IIT (ISM) Dhanbad, during master's program in 2017-2019.
- Major Project on "**Production of ETHANOL from Potato by algae and Saccharomyces Cerevisiae (Baker's Yeast)"** under the guidance of Mr. Gautam Prasad Dewangan (Department of Chemical Engineering) ITGGV Bilaspur during B.Tech (2013-2017).

EXPERIENCE

- Trainee at "Comminution, Dewatering, Leaching, Filtration, Clarification Unit, Ion Exchange, Precipitation Unit, Drying Unit, Peroxide plant, Tailings Disposal, WTP,

ETP, STP" in "URANIUM CORPORATION OF INDIA LIMITED" Jaduguda, East Singhbhum, Jharkhand during master's program.

- Trainee at "R&D, CONCENTRATOR UNIT & TAILINGS DISPOSAL PLANT" in "HINDUSTAN COPPER LIMITED (MCP)" Malanjkhand, Balaghat, M.P., during Master's program.
- Trainee at "DISTILLERY UNIT" in "BAJAJ HINDUSTAN SUGAR LTD." Gola Gokarannath, Lakhimpur (Kheri), U.P., while pursuing B.Tech.

COMPUTER AND SOFTWARE SKILLS

- MS Word, MS PowerPoint, MS Excel, and Adobe Photoshop.
- Basic C and C++, MATLAB, Python, ASPEN PLUS, EDEM Basics, DOE (Minitab), Material Studio.

TECHNICAL AND PROFESSIONAL SKILLS

- Handling the high-pressure fixed-bed, slurry tank, and slurry bubble column reactor.
- Handling and troubleshooting the analytical instruments used for gas and liquid analysis, such as Gas Chromatography GC-TCD/FID.
- UV Spectrophotometer, Atomic Absorption Spectrophotometer, X-ray diffraction, BET Surface Area Analyzer, Thermo-gravimetric Analyzer, Temperature Programmed and Chemisorption Analyzer, CHNS Analyzer, and DRIFTS-FTIR.

EXTRACURRICULAR ACTIVITIES

- Event coordinator of BALLOON-CAR in Equilibrio-2K15, ITGGV, Bilaspur (C.G).
- Attended ASPEN-HYSYS and HAZOP workshop in AZEOTROPY-2K16 at IIT BOMBAY.
- Got 2nd prize in CHEM-E-CAR in Equilibrio-2K16, ITGGV, Bilaspur (C.G).
- Attended the **"Introductory Training on EDEM"** at IIT(ISM) DHANBAD.
- Attended **"A Short-Term Course on Coal to Chemicals"** at IIT(ISM) DHANBAD.
- Attended different catalyst characterization webinars at IIT Delhi.
- Participated in 3-minute Thesis event organized by Research Scholar Forum (RSF) at IIT Delhi, New Delhi, India.

LEADERSHIP AND PROJECT HANDLING EXPERIENCE

- Managed an industrial collaborative research project (with Thermax) awarded by the Government (DST) on "Methanol Production from Indian Coal: Pilot Plant Demonstration, Catalysis, and Scale-up Technologies"; responsible for catalyst synthesis and its characterization, conducting experiments in high-pressure fixed bed reactor system, preparing progress reports, technical presentations, tracking of team's research progress and future research planning.
- Managed an industrial collaborative research project (with Thermax) awarded by Mission Innovations (IC#3), DST on "Integrated CO_2 absorption and conversion to methanol in slurry phase reactors using metal complexes as a catalyst (IITD, Univ. of Calgary, Canada, THERMAX, Pune collaboration) IRD, IIT Delhi"; responsible for catalyst synthesis and its characterization, conducting experiments in high pressure fixed bed reactor system, preparing progress reports, technical presentations, tracking of team's research progress and future research planning.
- Travelled to Hebrew University of Jerusalem Israel (HUJI) as a Visiting Research Scholar (VRF) and simultaneously managed an academic collaborative research project with IITD and HUJI under the Joint Seed Money Funding Scheme (MFIRP) on "Reduction of carbon dioxide using low-cost carbometalated Pincer-Type complexes with appended functionalities," responsible for the catalyst synthesis and characterization of pincer-type metal complexes with its application for the CO_2 reduction to value-added fuels in a high-pressure slurry reactor, preparing progress reports, technical presentations, tracking of team's research progress and future research planning.
- Participated in conceptualizing, drafting, and managing a collaborative research proposal (with Thermax) funded by DST on "A test bench for continuous performance study over the in-house developed catalysts in selective CO_2 hydrogenation to methanol", responsible for catalyst synthesis and its characterization, conducting experiments in a high-pressure fixed bed reactor system, preparing progress reports, technical presentations, and future research planning.
- Mentored two M.Tech., two Dual Degrees, and five B.Tech. students by guiding them in formulating research and work plans, teaching them to conduct experiments and

analyze data, and providing critical feedback and suggestions to improve their research and academic projects.

- Supervised procurement of cutting-edge characterization instruments and high-pressure reactors as a part of the above-mentioned projects; responsible for preparing and finalizing technical specification requirements, installation, and commissioning for high-pressure slurry tank batch reactor, high-pressure slurry-bubble column reactor, high-pressure tubular fixed-bed reactor, Gas Chromatography, TPX, etc.

PUBLICATIONS AND PATENT DISCLOSURES

PUBLICATIONS

1. **Aakash Bhardwaj**[†], Akshdeep S. Ahluwalia[†], K.K. Pant, Sreedevi Upadhyayula*, "A principal component analysis assisted machine learning modeling and validation of methanol formation over Cu-based catalysts in direct CO_2 hydrogenation". *Separation and Purification Technology*, Volume 324, 1 November 2023, 124576.
2. **Aakash Bhardwaj**[a,1], Meenakshi Pokhriyal[a,1], Vaibhav Pandey[a], Kamal Kishore Pant[a], Sreedevi Upadhyayula[a,*], "Enhanced Methanol Formation over Cu/MgO catalyst derived from Mg-Rich Active Hydroxycarbonate Precursor". *ACS Appl. Energy Mater*. 2024, 7, 12, 5163-5178**.**
3. **Aakash Bhardwaj**[a,1]**,** Shriya Sharma[a,1], Sreedevi Upadhyayula[a,*], "Machine Learning Driven Screening of Catalyst and Reaction System for CO_2 Hydrogenation to Formic Acid/Formate: A Greener Fuel and a Liquid H_2 Carrier". *Fuel*, Volume 407, Part B, 1 March 2026, 137331.
4. Tiwari S. C., **A. Bhardwaj**, K. D. P. Nigam, K. K. Pant, and S. Upadhyayula "A Strategy of Development and Selection of Absorbent for Efficient CO_2 Capture: An Overview of Properties and Performance". *Process Safety and Environmental Protection*, Volume 163, July 2022, Pages 244-273.
5. Ambereen A. Niaze[a], **Aakash Bhardwaj**[a], Mahendra K. Sunkara[b], Sreedevi Upadhyayula[a]* "Promotional role of tungstate in the integrated synthesis of C_2-C_3 alcohols and understanding the bond functionality for a series of cascade reaction". *Biofuels, Bioproducts and Biorefining (2023)*.
6. Vaibhav Pandey[a], **Aakash Bhardwaj**[a#]**,** Priyanshu Pratap Singh[b#], Kamal Kishore Pant[a*], Sreedevi Upadhyayula[a*], Siddhartha Sengupta[b], "Low-temperature methanol-

assisted CO_2 hydrogenation populating intermediates on Ce-promoted Cu/ZnO/MgO catalyst in three-phase slurry reactors". *Sustainable Energy Fuels*, 2025, 9, 4889-4893.

7. **Aakash Bhardwaj**, Shantanu Roy, K.K. Pant, Sreedevi Upadhyayula*, "Mechano-chemical synthesis of phase-pure Cu/ZnO-based catalysts from hydroxycarbonate precursors in CO_2 hydrogenation to methanol". (To be communicated)
8. **Aakash Bhardwaj**, Vaibhav Pandey, Shantanu Roy, K.K. Pant, Sreedevi Upadhyayula*, "Parameter-driven performance, reaction kinetics and mechanistic modeling in CO_2 hydrogenation to methanol over the ternary Cu/ZnO/ZrO_2 catalyst". (To be communicated)

PATENT DISCLOSURES

1. "Process for integrated CO_2 capture and conversion to renewable, gasoline blendable fuel in multi-phase reactor". (*Patent Disclosure submitted*)
2. "Process for manufacturing catalyst pellets and structured catalysts and the process for manufacture of methanol using these catalysts in fixed bed tubular reactors". (*Patent Disclosure submitted*)

NATIONAL AND INTERNATIONAL CONFERENCES

1. **Aakash Bhardwaj[1]**, Rohit Sahu[1], and Sreedevi Upadhyayula[1*], Fabrication of Cu-Zn coated structured foam catalysts for CO_2 hydrogenation to methanol in a fixed-bed reactor. 15th European Congress on Catalysis (EUROPACAT), Prague, Czech Republic, August 2023.
2. **Aakash Bhardwaj[1]**, Rohit Sahu[1], Kamal Kishore Pant[1], and Sreedevi Upadhyayula[1*], Experimental and kinetic investigation for CO_2 hydrogenation to methanol over structured foam catalysts. 18th International Congress on Catalysis (ICC Lyon 2024), Lyon, France, July 2024.

PERSONAL INFORMATION

Father's Name - Mr. Devendra Sharma
Date of Birth - 13 March 1994
Nationality - Indian
Sex - Male
Marital Status - Unmarried

Languages Known - English & Hindi

Hobbies - Cooking, Travelling, Reading

Permanent Address - S/O: Devendra Sharma, Near Sahni Deluxe Hotel, Munnuganj, Lakhimpur Road, Gola Gokarannath, Distt-Lakhimpur (Kheri), U.P. Pin code - 262802

DECLARATION

I assure you that the information given above is true to the best of my knowledge and beliefs.



Aakash Bhardwaj